



Universitat Autònoma de Barcelona

**Carbon Xerogel Nanocomposite
Materials for Electrochemical Devices:
Application to Heavy Metal Detection**

PENGFEI NIU

DOCTORAL THESIS

Doctoral Studies in Material Science

Supervised by Dr. César Fernández-Sánchez and Dr. Martí Gich Garcia

Tutor: Dr. Lluís Casas Duocastella

Departament de Geologia, Facultat de Ciències

Universitat Autònoma de Barcelona

2015

Thesis submitted to aspire for the Doctor Degree

Pengfei Niu

Supervisor's Approval

Dr. César Fernández Sánchez

Dr. Martí Gich Garcia

Tutor

Dr. Lluís Casas Duocastella

Bellaterra (Cerdanyola del Vallès), 11 de juny 2015

El **Dr. César Fernández Sánchez** (Científic Titular del CSIC), el **Dr. Martí Gich Garcia** (Científic Titular del CSIC) i el **Dr. Lluís Casas Duocastella** (Professor Agregat de la UAB)

CERTIFIQUEN:

Que en Pengfei Niu, amb un Màster en Ciència i Enginyeria de Polímers per la Universitat de Sichuan (Xina), ha dut a terme aquesta tesi doctoral sota la seva direcció i que porta per títol **“Carbon Xerogel Nanocomposite Materials for Electrochemical Devices: Application to Heavy Metal Detection”**, la qual queda recollida en aquesta memòria per optar al grau de Doctor.

I perquè així consti, signen el present certificat

Dr. César Fernández Sánchez Dr. Martí Gich Garcia Dr. Lluís Casas Duocastella

Pengfei Niu

Bellaterra, 10 de juny de 2015

Acknowledgements

In 2012, I got the funding from Chinese Scholarship Council (CSC) for pursuing my PhD degree in Spain. On Sep. 25th, 2012, I arrived in Barcelona and it was my first time abroad. I did not know what a great experience I was going to have in the following three years. This period really broadened my horizons. I want to thank my home country China for funding me to pursue my PhD degree abroad. In addition, I want to express my deep gratitude to many people.

First of all, I would like to extend my deepest gratitude to my PhD supervisors, **Dr. Martí Gich** and **Dr. César Fernández-Sánchez** for accepting me as a PhD candidate and studying with you. Before I met you, I did not have many experiences about sol-gel chemistry, electrochemistry, and microfabrication techniques. In the beginning, you both taught me little by little in the lab, making me start knowing these powerful techniques, which soon fascinated me. In these three years, both of you have always been available for all kind of discussions. I have learned a lot from you about how to explore the “unknown”, face challenges, and solve scientific problems. Definitely, this period will be very helpful for my professional and personal growth.

Anna Roig, thank you for all your guideline and support. I will never forget the interview between you, Martí and I, with Muling as a “translator” before I came here. You gave me this opportunity to study here and it changed my life.

I also want to thank the clean room technicians at ICMA-B-CSIC: Enrique Irisarri, Neus Romà, Edgar León; at UAB: Maria Angeles Benítez, Raquel Palencia and at IMB-CNM-CSIC, Libertad Solé, who taught me and helped me use the equipment for carrying out experiments and performing structural characterization. Furthermore I would like to thank Ana Esther Carrillo for teaching me using the scanning electron microscopy; Dr. Carlos Ayora from Institut de Diagnòsi Ambiental i Estudis de l'Aigua, IDAEA (CSIC) who provided me with relevant real waters solutions and analyzed them by ICP-MS technique; Carla Navarro-Hernández and Dr. Pablo Fanjul-Bolado from DropSens S.L, who fabricated the screen printed electrodes based on bismuth/carbon nanocomposite powders; Erica Álvarez from IMB-CNM who helped me do the photolithography process on carbon/silica thin-films; Josep Montserrat,

for the assistance with the four-probe conductivity measurements; Raquel Palencia from UAB for helping me with the reactive ion etching process of the carbon/silica films; Xavier Jordà and David Sánchez from the Power Devices group at IMB-CNM-CSIC who did the aluminum layer deposition to produce the contact pads of the carbon/silica electrochemical devices and Hector Cabezas Martínez from IMB-CNM who carried out the wire bonding process on these pads; Guillermo Antorrena from the Instituto de Nanociencias de Aragón for performing and analyzing materials by X-ray Photoelectron Spectroscopy; Frances Pi from the Optics Group at UAB for depositing SiO₂ on the C/SiO₂ films by physical vapor deposition.

In addition, I would like to thank Nídia Santamaria for helping me build up many electrochemical setups; Manuel Gutiérrez, Pablo Giménez, Laura Asturias, María Díaz for all the kind discussions about electrochemistry. Cosmin Cotet, Ayman Zaheer, Miriam Garza, thanks for your earlier work on this project. It made the start of my Thesis much easier and allowed us to progress faster.

People in the group of Nanoparticles and Nanocomposites at ICMAB-CSIC, Anna Laromaine, Elisa Carenza, Nerea Murillo-Cremaes, Muling Zeng, Laura González, Laura Asturias, Siming Yu; members in the group of Chemical Transducers at IMB-CNM-CSIC, Manuel Gutiérrez, María Díaz, Maria Mallén, Pablo Giménez, Erica Álvarez, Nídia Santamaria, Pere Jiménez, Alfredo Cadarso, Juan Manuel Ríos; Thanks for all the helpful discussions with all of you about research, culture, politics, football and everything. I really enjoyed the time spent with you inside and outside the lab.

My friends in Barcelona, Rafael, Pablo, Laura, Jun, Ping, Dong, thanks for always taking care of me, being close and supporting me. Thank you for your friendship and I am so happy to have had you around.

My wife, my dear lover Huanliang, I thank god every day for sending you into my life. Lastly, I want to thank my parents for all your support, understanding and trust in my life.

Foreword and Scope of the Thesis

The detection of heavy metals in waters is of importance since these are highly toxic to living organisms in general and humans in particular. As a result, various regulations are setting maximum allowable concentrations of these pollutants in waters. In comparison with standard methods for monitoring heavy metals, electrochemical sensors provide a unique opportunity for developing a system capable of performing rapid, sensitive and reliable analysis in-situ and at a low cost. Making available such type of sensors would open the door to semi-continuous and remote sensing of heavy metals.

In this context, this Thesis aims at developing cost-effective and easy-to-use miniaturized electrochemical sensors with high accuracy and sensitivity for trace level determination of heavy metals in waters. For that, we have worked on the development of tailored porous carbon composites by sol-gel chemistry and on the fabrication of both thick-film and thin-film sensors with these materials by two available industrial processes: screen-printing and lithography techniques. In the first case, we synthesized bulk nanocomposites consisting of a porous carbon matrix doped with bismuth nanoparticles. These materials were ball-milled into powders of suitable size and electrochemically tested in the lab in the form of paste electrodes before producing a large batch of commercial-like screen-printed electrodes. In the second case, carbon thin-film electrodes were fabricated on SiO₂/Si substrates by both photolithography and soft-lithography processes. Herein, carbon derived films containing silica were processed, with silica enhancing the interfacial adhesion between the carbon film and the SiO₂/Si substrate following a solution chemistry route. Both types of electrochemical sensors were assessed for the sensitive determination of heavy metals.

This Thesis is divided into 10 Chapters. **Chapter 1** is a general introduction that includes the motivation of this Thesis and a state-of-the-art on heavy metal sensing. For a better understanding of the approaches applied to the development of materials and the fabrication of electrodes, in the second section of this chapter we briefly describe general concepts about sol-gel chemistry, electrochemical sensors,

screen-printing and lithographic techniques. In **Chapter 2** the objectives of this Thesis are outlined.

The main body of the Thesis is structured into two parts depending on whether the porous carbon nanocomposites are prepared in bulk or thin-film forms and on the technologies applied for the fabrication of electrochemical sensors.

In the **first part (i.e. Chapters 3, 4 and 5)**, bismuth nanoparticle/porous carbon nanocomposites in bulk were developed and applied to fabricate conventional bismuth/carbon nanocomposite paste electrodes and screen printed electrodes. More specifically, **Chapter 3** is mainly focused on the preparation of bismuth nanoparticle/porous carbon nanocomposites in bulk and their structural characterization. In **Chapter 4**, the preparation of paste electrodes made of these nanocomposites and their electrochemical performance towards the determination of heavy metals both in buffer solutions and in a variety of real water solutions was thoroughly studied. Finally, these bismuth nanoparticle/porous carbon nanocomposites were successfully employed to fabricate electrodes by the screen-printing technique. The fabrication process and electrochemical performance of these miniaturized electrodes are presented in **Chapter 5**.

In the **second part (i.e. Chapters 6, 7, 8)**, the study about the generation, characterization and electrochemical performance of robust carbon/silica films on SiO_2/Si substrates is presented. These films were successfully patterned into thin-film carbon/silica electrodes by both standard photolithography and soft-lithography techniques. More specifically, **Chapter 6** mainly describes the deposition of crack-free carbon/silica thin-films on SiO_2/Si substrates by a one-pot one-step spin-coating process. The electrochemical performance of these films is discussed in detail and the possibility of incorporating metal nanoparticles into C/ SiO_2 films is also presented. **Chapter 7** includes the application of standard photolithography processes to pattern the spin-coated carbon/silica films into thin-film electrodes. In addition, thanks to the flexibility of sol-gel processing, this chapter also includes the application of a soft lithography approach to develop thin-film carbon/silica electrodes. **Chapter 8** reports on the electrochemical performance of these thin-film carbon/silica electrodes and their potential application in the analysis of heavy metals.

Chapter 9 lists the general conclusions of this Thesis and some perspectives for further work. **Chapter 10** contains information about the author and the publications resulting from this PhD work.

The work presented in this Thesis has been achieved through a very close collaboration between the Group of Nanoparticles and Nanocomposite at ICMAB-CSIC, the Group of Chemical Transducers at IMB-CNM-CSIC and DropSens S.L, Spain. Finally it is worth mentioning that the appealing approach and outcomes of this Thesis are currently being exploited within the EU project COMMON SENSE (call FP7-Ocean_2013) with the objective of developing a multisensor platform for the monitoring of different parameters in ocean waters.

Table of Contents

Acknowledgements

Foreword and Scope of the Thesis

Index

Chapter 1 Introduction	1
Summary.....	1
1.1. Motivation and State of the art.....	3
1.1.1. Analysis of Heavy Metals in Waters.....	3
1.1.2. Electrochemical Sensors	4
1.1.3. Electrochemical Sensors for Heavy Metals.....	5
1.1.4. Downsizing Bi Based Electrochemical Devices for Scaling up the Device Fabrication Process	9
1.1.5. Our Approach.....	11
1.2. Sol-Gel Chemistry	12
1.2.1. General Introduction about Sol-Gel Materials	12
1.2.2. Synthesis of Sol-Gel Nanocomposites	13
1.2.3. Sol-Gel Nanocomposites for Heavy Metal Detection	15
1.2.4. Porous Carbon Materials Prepared from Resorcinol- Formaldehyde Gels	15
1.2.5. Thin-films Prepared by Sol-Gel	17
1.3. Screen-printing Technique	19
1.4. Lithographic Techniques.....	20
1.4.1. Photolithography	20
1.4.2. Soft-lithography	24
References.....	25
Chapter 2 Aims and Objectives	31
Chapter 3 Synthesis of Bismuth Nanoparticle-Porous Carbon Nanocomposite	33
Summary.....	33
3.1. General Introduction	35
3.2. Nanocomposite Synthesis	36
3.2.1. Impregnation Approach.....	36
3.2.2. Co-synthesis approach.....	37
3.2.3. Carbonization.....	40
3.3 Structural and Morphological Characterization	41

3.3.1. Assessment of the Presence of Bismuth Nanoparticles	42
3.3.2. Porosity of the Materials	45
3.3.3. Bismuth Nanoparticle Chemical Structure	46
3.4. Conclusion	48
References	48
Chapter 4 Electroanalytical Assessment of Bismuth-Carbon Nanocomposite Materials: Detection of Heavy Metals in Waters	51
Summary	51
4.1. General Introduction to Bi-C CPEs	53
4.1.1. Fabrication of Electrodes	53
4.1.2. Stripping Voltammetric Signals of Bi Using Bi-C CPEs	54
4.1.3. Preliminary Studies on the Performance of the Bi-C CPEs for Heavy Metal Analysis: Reusability of the Electrode	56
4.2. Effect of the Material Synthesis Process on the Electrode Performance	57
4.2.1. Effect of the Applied Material Synthesis Route	57
4.2.2. Effect of Bi Content	59
4.3. Analytical Performance of Bi-C CPEs	62
4.3.1. Pb(II) and Cd(II) Detection	62
4.3.2. Zn(II) Detection	64
4.3.3. Ni(II) Detection	66
4.3.4. Cu(II) Detection with Porous Carbon Electrodes without Bi	69
4.3.5. Interference Study	70
4.4. Analysis of Real Water Samples	73
4.4.1. Description of Water Samples	73
4.4.2. Cd(II), Pb(II) and Ni(II) Analyses in Real Waters	74
4.4.3. Zn(II) and Cu(II) Analyses in Real Waters	79
4.5. Conclusion	80
References	81
Chapter 5 Fabrication and Characterization of Screen Printed Bismuth Nanoparticle-Porous Carbon Nanocomposite Electrodes	83
Summary	83
5.1. Brief Introduction	85
5.2. Electrode Fabrication	85
5.2.1. Nanocomposite Synthesis	85

5.2.2. Fabrication of the Screen Printed Bi-C Nanocomposite Electrodes ...	86
5.3. Electrochemical Characterization of Bi-C SPEs.....	88
5.3.1. Measurement Procedure.....	89
5.3.2. Cyclic Voltammetry.....	89
5.3.3. Cd(II) and Pb(II) Detection.....	90
5.3.4. Comparative Analysis of the Performance of Bi-C SPE with Bi-C-CPE	95
5.4. Cu(II) analysis on SPEs without Bi.....	98
5.5. Application of the SPEs for the Analysis of Heavy Metals in Waters	100
5.6. Conclusion	102
References.....	102

Chapter 6 Deposition of C/SiO₂ Thin-films on SiO₂/Si Substrate by Spin-Coating..... 105

Summary.....	105
6.1. Introduction.....	107
6.2. Development of Carbon Thin-films	108
6.2.1. SiO ₂ /Si Substrates	108
6.2.2. Resorcinol/Formaldehyde Sol Preparation.....	109
6.2.3. Carbon Film Deposition	110
6.2.4. Evaluation of the Interfacial Adhesion between Carbon Film and SiO ₂ /Si Substrate	110
6.3. C/SiO ₂ Thin-films with Enhanced Adhesion to SiO ₂ /Si Substrates	111
6.3.1. RF/APTES Sol Preparation.....	112
6.3.2. C/SiO ₂ Films Deposition on SiO ₂ /Si Substrates	113
6.3.3. Characterization of the Films.....	116
6.4. Electrochemical Performance of C/SiO ₂ Thin-films.....	122
6.4.1. Cyclic Voltammetric Studies of the Responses of C/SiO ₂ Films with Different SiO ₂ Content	123
6.4.2. Estimation of the Electron Transfer Rate at the Film/Electrolyte Interface.....	125
6.5. Doping C/SiO ₂ Films with Bi or Au Nanoparticles.....	127
6.5.1. Synthesis of Bulk Bi/C/SiO ₂ Nanocomposite Materials	127
6.5.2. Deposition of Bi Doped C/SiO ₂ Films on SiO ₂ /Si Substrates	130
6.5.3. Preparation of C/SiO ₂ Films on SiO ₂ /Si Substrates with Gold Nanoparticles.....	135
6.6. Conclusion	136

References	136
Chapter 7 Fabrication of C/SiO₂ Thin-film Electrodes	139
Summary.....	139
7.1. Patterning C/SiO ₂ Films into Thin-film Electrodes by Photolithography....	141
7.1.1. Patterning Process	141
7.1.2. Effect of the photoresist coating on the C/SiO ₂ Film.....	144
7.2. On-chip C/SiO ₂ Film Electrodes Fabricated by Soft lithography	150
7.2.1. Microtransfer Molding Procedure	150
7.2.2. Electrodes Prepared by μ -TM Procedure	152
7.3 Conclusion	159
References	159
Chapter 8 Development and Characterization of Electrochemical Probes Based on C/SiO₂ Thin-film Electrodes	161
Summary.....	161
8.1. Packaging C/SiO ₂ Thin-film Electrodes.....	163
8.2. Electrochemical Characterization of the Electrochemical Probes	165
8.2.1. Common Electroactive Species.....	165
8.2.2. Electrochemical Devices Based on C/SiO ₂ Thin-film Electrodes Patterned by Photolithography	167
8.2.3. C/SiO ₂ Film Chip Electrodes Fabricated by μ -TM Soft-Lithography Approach.....	172
8.3 Conclusion	176
References	177
Chapter 9 Conclusion and Further Work	179
9.1. General Conclusions	179
9.2. Ongoing and Further Work.....	181
Conferences and Publications.....	183
The Author.....	223

Chapter 1

Introduction



Summary

The motivation of the work carried out in this Thesis together with a state-of-the art about electrochemical sensors for heavy metal detection is provided in this chapter. In addition, it includes brief descriptions of sol-gel chemistry, screen-printing and lithographic techniques for a better understanding of the approaches developed to synthesize the materials and fabricate the devices presented in this work.

1.1. Motivation and State of the art

1.1.1. Analysis of Heavy Metals in Waters

Industrialization and agricultural activities have removed a vast quantity of metals from their fairly safe storage deep in the earth to the surface of the earth and caused increased concentrations of heavy metals in our living environment. The detection and monitoring of heavy metals (e.g. lead, cadmium, mercury, or nickel) in waters is of paramount importance since they have long been recognized as very hazardous environmental contaminants that can cause a number of human health effects even at low concentration levels [1]. An increasing number of organizations around the world have defined the maximum allowable concentrations of heavy metal content in drinking water. Table 1.1 summarizes the standards and guidelines for heavy metals in drinking water recommended by the World Health Organization (WHO) [2], the European Union Water Framework Directive (EU-WFD) [3], the US Environmental Protection Agency (US-EPA) [4], and the Ministry of Environmental Protection of China (C-MEP) [5], respectively.

Table 1.1 Maximum allowable concentrations of heavy metals ions in drinking water

Parameter	WHO (ppb)	EU-WFD (ppb)	US-EPA (ppb)	C-MEP (ppb)
Lead (Pb)	10	14	15	10
Cadmium (Cd)	3	0.45-1.5	5	5
Mercury (Hg)	6	0.07	2	1
Nickel (Ni)	70	34	no standard	20

NOTE: ppb = $\mu\text{g/L}$

The standard technique for trace heavy metal analysis is atomic spectroscopy, including three widely accepted analytical methods, namely atomic absorption spectroscopy (AAS), inductively coupled plasma optical emission spectroscopy (ICP-OES), and inductively coupled plasma mass spectrometry (ICP-MS) [6]. These methods exhibit high sensitivity, high selectivity, and provide excellent limit of detection. However, they require expensive and bulk instrumentation placed in centralized laboratories, essential sample preparation, and highly skilled operators. Moreover, water samples must be taken from the field to the laboratory for analysis.

Measuring pollutants in-situ would avoid analytical errors that could be related to the sample collection and transportation. Most importantly, if the analytical protocols were not expensive and could be operated continuously or semi-continuously, one could increase the analysis frequency and provide a more efficient detection of contamination outbreaks, which would be very helpful for making appropriate decisions in time and acting quickly. Accordingly, portable analytical tools that can offer rapid and accurate measurements for heavy metals are currently being developed.

Among the various technological approaches that have been already shown to be applied in this scenario, the electrochemical sensing strategy presents a number of benefits. First of all, electrochemical devices are sensitive and inexpensive, offering rapid analysis and only requiring compact and low-power instrumentation. As such, they can be deployed in field and thus increase the number of locations where water analysis can be carried out as well as the analysis frequency. In addition, the integration of electrochemical devices in automatic fluidic systems, which can enable sample preconditioning and device calibration, makes the automated semi-continuous analysis feasible with these analytical devices [7].

1.1.2. Electrochemical Sensors

An electrochemical sensor is essentially a chemical sensor comprising a selective receptor to the target analyte to be measured, which is in intimate contact with a transducer mainly formed by an electrode structure. This electrode is incorporated in an electrochemical cell showing either a two-electrode or a three-electrode configuration. In both cases, the sensor is the working electrode and includes an extra electrode performing as both reference and counter electrode, or two extra electrodes being individual reference and counter electrodes, respectively [8]. When carrying out measurements, the electrochemical cell is immersed into an electrolyte solution to form a closed electrical circuit. With a supply of electrical energy, the system can undergo chemical reactions, usually an electron transfer process generated as a consequence of the interaction between the target analyte and the working electrode surface, which is easily detected in the form of an electrical signal by the transducer [9]. Figure 1.1 shows the schematic drawing of a

three-electrode electrochemical setup. In this setup, the working electrode (1) is where the electrochemical reaction occurs, counter electrode (2) measures the current flow in the circuit and the reference electrode (3) fixes and keeps constant the potential at the working electrode surface. The electrochemical cell is connected to an electrochemical instrument and potentiostatic or galvanostatic measurements can be carried out.

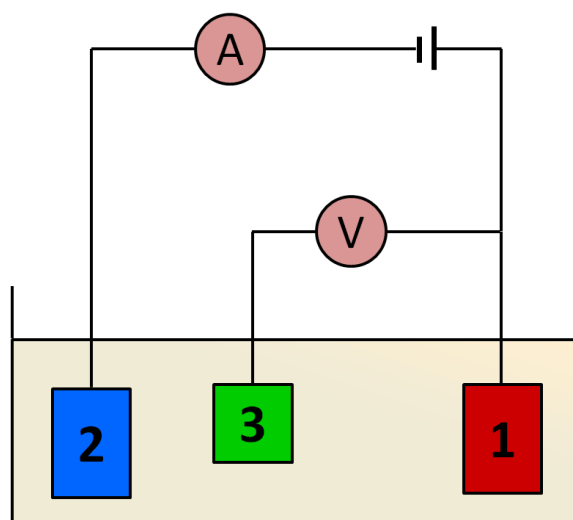


Figure 1.1. Three-electrode electrochemical setup: (1) working electrode, (2) counter electrode and (3) reference electrode

1.1.3. Electrochemical Sensors for Heavy Metals

1.1.3.1. Working principle of the electrochemical detection of heavy metals

When analyzing heavy metals in water using electrochemical sensors, two chemical reactions occur sequentially at the interface between the working electrode and the electrolyte solution during the so-called accumulation and stripping steps of the detection process, as shown in Figure 1.2.

During the accumulation step, which normally lasts a few minutes, the reduction of metal cations at a constant potential occurs. Afterwards, the potential is scanned in a certain potential window, at which the metal deposit gets oxidized and in turn stripped back to the solution. During this process, current signals are recorded in the form of peaks. These peaks appear at a certain potential that is characteristic of each heavy metal, whereas the peak current height reflects the heavy metal

amount deposited on the electrode surface that is proportional to the amount of heavy metal in the solution.

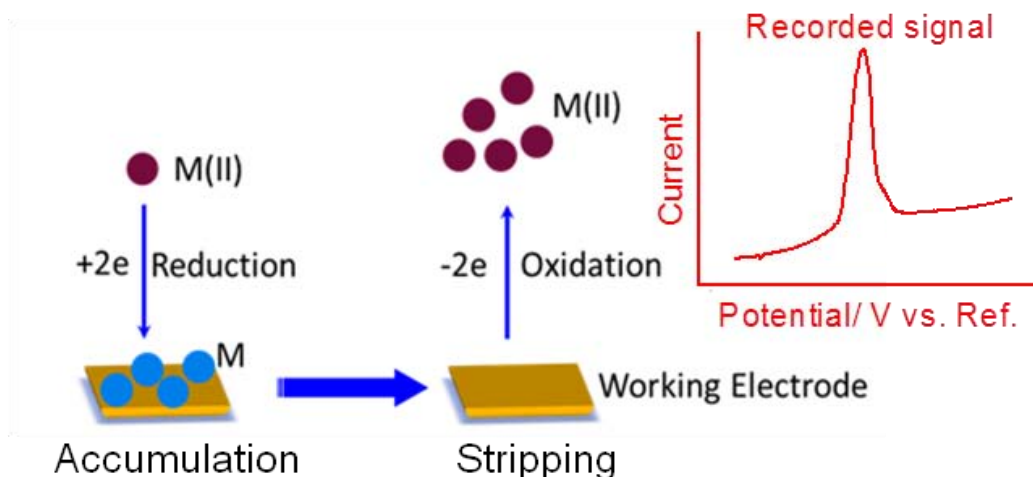


Figure 1.2. Scheme of the chemical reactions commonly taking place at the working electrode for heavy metals analysis

1.1.3.2. Electrochemical approaches

Electrode materials play a critical role in the development of a high performance electrochemical sensing platform. Initial electrochemical devices to detect heavy metals mostly employed hanging Hg drop or Hg film based electrodes, since Hg can form amalgams with many heavy metals during the accumulation step. As a consequence these electrodes offered highly sensitive and reproducible analysis towards several heavy metals. However, owing to the concerns about the toxicity of Hg, new alternative electrode materials are highly desired. Among them, the most commonly used working electrode material is carbon, in the form of glassy carbon, carbon paste, carbon ink among others. The surface of the carbon electrodes made of these materials can be modified following different protocols in order to provide the resulting device with the appropriate selectivity and sensitivity towards a variety of analytes [10].

Regarding the detection of heavy metals, different surface modifiers (receptors) can be applied that interact with the metal analytes by either forming fused alloys and/or complexes, or by promoting their adsorption to the electrode surface. Some representative examples reported in the literature for the determination of $Pb(II)$ and $Cd(II)$ are gathered in Table 1.2, taking into account the receptor structure, the receptor/analyte interaction, the response time and the limit of detection.

Table 1.2 Representative electrochemical approaches for Pb(II) and Cd(II) analysis

Receptor/Analyte interaction	Electrode	Modifier	Response Time (min)	LOD (ppb)		Ref.
				Cd	Pb	
"Fused" Alloy	SPCE	Bi Film	6	0.34	0.03	[11]
	SPCE	Bi Salts	3	1.1	0.9	[12]
	GCE	Nafion/ Graphene/Bi film	3	0.02	0.02	[13]
	Graphite	rGO + Bi Film	3	0.09	0.12	[14]
	SPCE	Bi ₂ O ₃ NPs	3	0.2	0.2	[15]
	SPCE	Bi NPs	3	1.7	1.3	[16]
	Bi SPE	Bi Film	7	0.10	0.16	[17]
Ligand-Metal Complex	SPCE	Functional Porous SiO ₂ NPs	8		0.1	[18]
	GCE	Polymeric Thiadiazole Film	7	0.05	0.3	[19]
	CPE	Cd(II) ion imprinted polymer	22	0.06		[20]
Adsorption	GCE	Graphene	3	1.08	1.82	[21]
	CNTs Film	CNTs	3.5	2.2	0.6	[22]
	GCE	MgSiO ₃ Nano spheres	4	0.02	0.05	[23]

NOTE: SPCE- screen printed carbon electrode; GCE- glassy carbon electrode; Bi SPE- bismuth screen printed electrode; CPE- carbon paste electrode; CNTs- carbon nanotubes; Bi- bismuth; rGO- reduced graphene oxide; NPs- nanoparticles; LOD- limit of detection.

Dielectric materials with high adsorption capacity towards heavy metals ions, even not being electrically conductive [23, 24], can be employed to construct highly sensitive electrochemical heavy metals sensors. These receptors are normally nano-structured materials and are incorporated on the surface of a solid electrode by casting a drop of an appropriate nanomaterial suspension. However, this approach is not compatible with a large scale production of electrodes for practical applications.

Regarding electrochemical sensors based on the formation of ligand-metal complexes, devices offering high selectivity and very low limits of detection have been reported as shown in Table 1.2. Nevertheless, these devices show very long response times due to the time required for ligands to capture heavy metal ions from the solution.

The formation of “fused” alloys between the receptor and the heavy metals has attracted a lot of attention and has been the main approach adopted in the development of electrochemical sensors for these pollutants. Bismuth (Bi) and gold based electrodes have been widely applied in this context. Bi electrodes have shown to perform similarly to Hg electrodes [25] and have the added advantage of Bi being considered as an environmental-friendly metal [26]. Therefore, they are especially popular in the determination of Pb(II), Cd(II) and Ni(II).

1.1.3.3. Bismuth based electrochemical devices

The design and fabrication of Bi-based electrochemical devices, being mainly based on the incorporation of Bi in the form of films or powders, includes two important aspects: **1)** the electrode substrate onto which Bi will be deposited, **2)** the method selected for carrying out the modification of the electrode with Bi.

The most popular working electrodes are based on carbon structures such as commercial glassy carbon electrode (GCE) and screen printed carbon electrode (SPCE). Carbon electrodes show a wide potential window with its limits only determined by the electrolysis of water (no residual faradic process takes place) and very low capacitive currents, which make them ideal for constructing more complex electrode architectures with carbon just performing as the conductive support. These can also be modified with a range of carbon nanomaterials, such as carbon nanotubes and graphene, showing a high surface to volume ratio and excellent conductive properties. These nanomaterials have brought about significant advantages such as large electrode surface areas and high electrical conductivity, thereby increasing analyte mass-transport and electron transfer rates compared to electrodes made by bulk materials [27]. These nanomaterials can be directly adsorbed on the electrode surface [21] or incorporated using polymers like Nafion or Chitosan [13]. The resulting modified carbon based electrodes show enhanced analytical performance and can be applied to the detection of heavy metals [27, 28].

The integration of Bi to carbon electrodes has been carried out by three main strategies.

A) In-situ and ex-situ plating a Bi film – A Bi film is electrochemically deposited on the electrodes in both cases. The difference lies in that the electrochemical deposition of Bi occurs before (**ex-situ** [29]) or during (**in-situ** [25]) the heavy metal analysis.

B) Drop casting Bi/Bi oxide NPs – Bi NPs [16] can be deposited onto the electrode surface by casting a drop of the NP suspension, which is prepared by dispersing pre-synthesized Bi/Bi₂O₃ NPs in an appropriate solvent.

C) “Bulk” modification with Bi – This approach is carried out by mixing carbon materials with a certain amount of a Bi material, such as metallic Bi powders [30] or various Bi chemical components [12] during the fabrication of the electrodes.

1.1.4. Downsizing Bi Based Electrochemical Devices for Scaling up the Device Fabrication Process

In order to carry out measurements in the field and also be able to do analyses in a high number of locations, reduced power and reagent consumption (and in turn waste production) of the applied devices should be carefully considered. In this context, the development of miniaturized electrochemical devices is required for deployment purposes. The size of these devices can be scaled down by using fabrication techniques such as screen-printing or standard photolithography. Both techniques allow the mass production of electrodes of planar configuration based on thick-film or thin-film patterned structures, respectively. Table 1.3 shows a selection of Bi based electrochemical sensors applied to the determination of Pb(II) and Cd(II), which fulfill the above mentioned requirements.

Depending on whether Bi is incorporated to the electrode during its fabrication or afterwards, one can classify the Bi electrodes as prepared by a one-step or two-step methods. The latter includes an additional step to incorporate Bi on the electrode surface after the fabrication of carbon electrodes. The generation of Bi films is carried out by electrodeposition using a concentrated Bi salt solution while the incorporation of nanostructured Bi based active materials is performed mechanically, mainly by a drop casting approach. Such electrode modification

processes normally have to be performed individually, making the sensor fabrication cumbersome and not cost-effective. In order to effectively mass produce devices for heavy metal analysis, several one-step approaches for the fabrication of miniaturized Bi electrodes have been reported. For instance, SPCE containing Bi (or a Bi compound) could be produced by directly screen-printing a mixture of a conductive carbon ink and Bi-based material [12]. Miniaturized sensors based on pure Bi working electrodes, fabricated by combining film deposition techniques, such as sputtering with photolithography processes were also described [31].

Table 1.3 Selected disposable Bi based electrochemical sensors

Miniaturized Electrodes		Fabrication Procedure	LOD(ppb)		Response Time (min)	Ref.
			Cd	Pb		
Screen-printing	Bi Film Modified SPCE	Two step	0.40	0.25	3	[17]
	Bi Film Modified SPC _p E		0.34	0.03	6	[11]
	Bi NPs Modified SPCE		0.40	0.55	4	[32]
	Bi ₂ O ₃ NPs Modified SPCE		0.2	0.2	3	[15]
	Bi Salts Modified SPCE	One-step	1.1	0.9	3	[12]
	Bi ₂ O ₃ Modified SPCE		1.5	2.3	6	[33]
	Sputtered Bi SPE		0.10	0.16	3	[17]
Photolithography	Bi Film Modified DLC Microelectrodes	Two-step	N.R.	4.5	3	[34]
	Bi Film/Nafion Modified PPFE		0.11	0.07	3	[35]
	Bi Film Microelectrode Arrays	One-step	6.7	3.4	3	[31]
	Bi Film Sensor		9.3	8	2	[36]

Note: SPCE- screen printed carbon electrode; SPC_pE- screen printed porous carbon electrode; DLC- diamond like carbon; PPFE- Pyrolyzed photoresist film electrode; N.R. not reported.

1.1.5. Our Approach

In spite of the advantages of the one-step approaches in terms of cost-efficiency and a feasible mass production, the devices prepared by a two-step method show a superior analytical performance, with lower limits of detection towards heavy metals (Table 1.3). Particularly, the use of Bi in the form of nanoparticles or carbon matrices with open porous structures has proved to significantly enhance the sensitivity of the resulting devices because of the increased active sensing area.

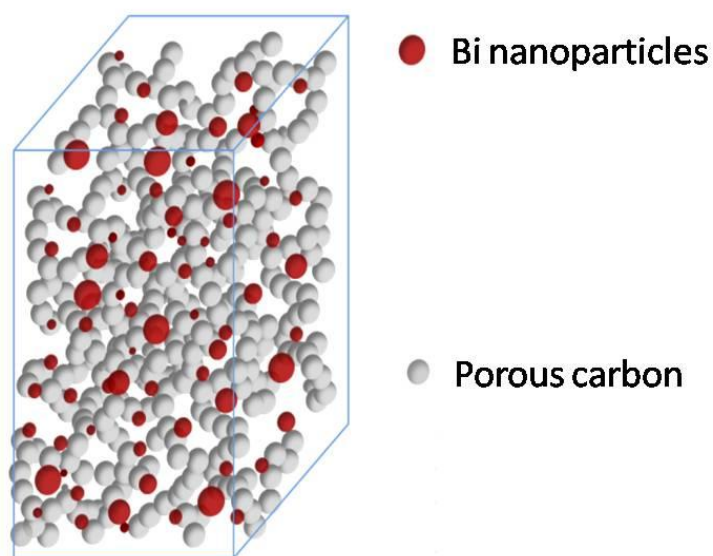


Figure 1.3. Schematic drawing of Bi nanoparticle/porous carbon composite

In an effort to produce highly sensitive Bi based sensors that combined the benefits of both approaches mentioned above, we decided to prepare novel conductive porous nanocomposite materials, consisting of Bi NPs embedded in a porous carbon matrix, as shown in Figure 1.3, and apply them to the development of electrochemical devices for heavy metal detection purposes.

In this context, we explored the synthesis of these composite materials by a sol-gel approach using resorcinol/formaldehyde precursors. Indeed, we anticipated that several features of sol-gel technique could be advantageous for the fabrication of a new generation of Bi electrodes:

- 1) The chemical versatility of the sol-gel chemistry allows for the simultaneous production of porous materials decorated with nanoparticles by introducing slight modifications to well-known sol-gel synthesis processes;
- 2) Sol-gel synthesis starts with the generation of a solution where all the material precursors are thoroughly mixed, which results in a good homogeneity of the final material;
- 3) Sol-gel synthesis processes are compatible with different device fabrication techniques and as such can be combined to produce electrochemical devices. For instance, bulk materials can be prepared and then milled into a powder that can be further used for the development of an ink, which in turn is applied to the fabrication of screen-printed thick-film electrodes. Also, thin-films of these materials can be prepared by a chemical solution deposition process on a substrate, and then patterned by a lithographic technique to produce thin-film electrodes.

For a better understanding of our approach, the basics of sol-gel chemistry, screen-printing and lithographic techniques are given below.

1.2. Sol-Gel Chemistry

1.2.1. General Introduction about Sol-Gel Materials

The term sol-gel refers to process of materials synthesis based on the condensation reaction of certain monomers in solution, often in the presence of acid or basic catalysts. At the initial stage, colloidal particles are formed in the solution containing reagents and solvent, forming the so-called **sol**. These particles agglomerate under controlled conditions and eventually link together to form a network, which eventually percolates and gives rise to a **gel**. In more detail, sol-gel processing includes the following 5 steps: 1) active molecules experience a polymerization reaction to form polymeric particles in a suitable liquid (**sol formation**), 2) these polymeric particles agglomerate and yield a 3-dimensional continuous percolating solid network impregnated by a liquid (**gel formation**), 3) further cross-linking processes and concomitant shrinkage of the formed gel takes place (**ageing process**), 4) the remaining liquid inside the gel is removed (**drying**

process), and 5) the desired materials are produced after an appropriate thermal treatment (**densification**).

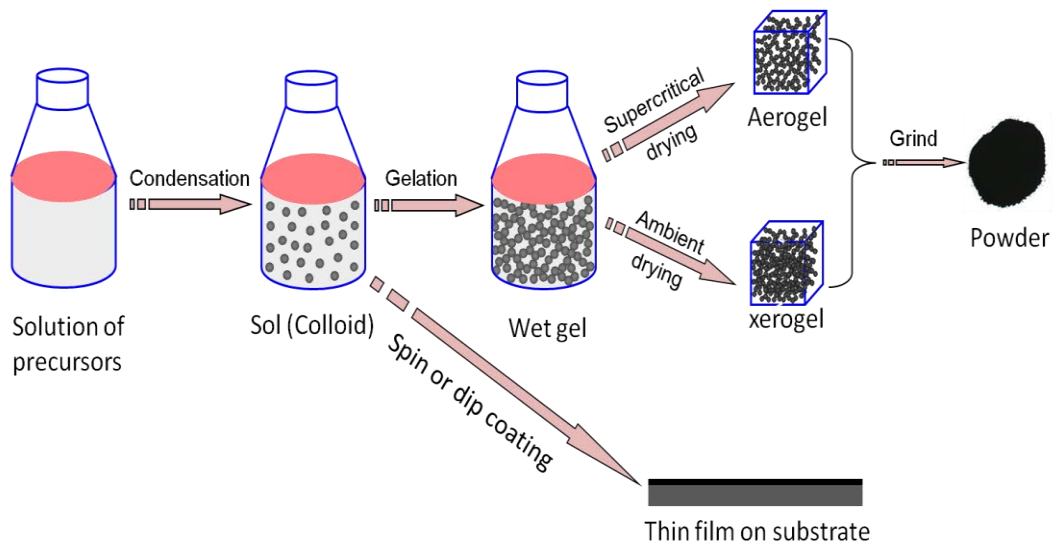


Figure 1.4. Schematic drawing of common sol-gel processes

Common sol-gel processing routes are illustrated schematically in Figure 1.4. The Sol-gel approach offers a number of advantages. The first main advantage is the fact that these materials are processed from a liquid that allows the convenient production of films and bulk materials of the shape of the container. Another advantage is the relatively easy incorporation of additives into a gel matrix for composite preparation, and the possibility of mixing different precursors at the molecular level. The third major advantage of the sol-gel method is that it produces porous materials whose pore-size distributions can be controlled, both by the chemical composition of the starting materials as well as by the processing conditions.

1.2.2. Synthesis of Sol-Gel Nanocomposites

The flexibility of the sol-gel process makes it very powerful to develop new materials such as nanocomposites that feature enhanced properties, these being the synergy of those shown by the different individual material forming the nanocomposite. Figure 1.5 shows three common approaches to produce nanocomposites by a sol-gel process, which is described specifically below in more detail.

Dispersion: It is the simplest method and is achieved by dispersing previously prepared nanomaterials in a sol. After gelation, the nanomaterials are retained within the gel matrix. However, its drawbacks include the possible agglomeration of nanomaterials and in turn the difficulty of obtaining homogeneous nanomaterial dispersion in the gel matrix.

Co-synthesis: In this approach, the gel and the nanomaterial precursors (normally metal salts) are mixed together to produce a sol. After gelation and ageing, a thermal treatment is usually applied in an inert atmosphere that induces the reduction of the nanomaterial precursors into the desired nanoparticles. This route results in well dispersed metal nanoparticles in the gel matrix.

Impregnation: This approach consists of impregnating previously synthesized porous gels with a solution containing nanoparticles or their precursors. Then a thermal treatment such as the one described in the co-synthesis alternative is carried out. Its major drawback is the lack of control over the loading of the gel matrix with the nanomaterial precursors, which is directly related to the gel porosity, the chemical compatibility between the gel and the nanomaterial (precursor) solution, the concentration of nanomaterial precursors and the impregnation time.

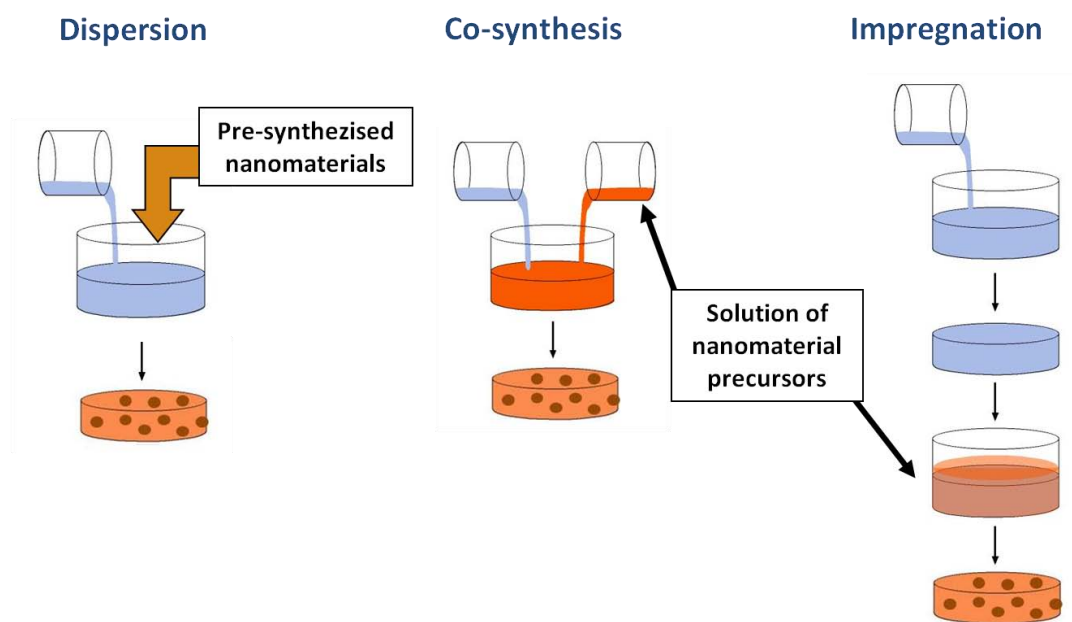


Figure 1.5. Three strategies to encapsulate nanomaterials within a sol-gel matrix

It is worth mentioning that the dispersion approach has been widely employed for the preparation of sol-gel silica/carbon nanomaterial composites, such as

silica/carbon nanotube nanocomposites [37], whereas the co-synthesis and impregnation approaches are more suitable for the introduction of metal nanoparticles into the gel matrix.

1.2.3. Sol-Gel Nanocomposites for Heavy Metal Detection

Sol-gel nanocomposites are promising materials to develop high performance electrochemical sensors [38] for analyzing different substances, including heavy metals, toxic chemicals as well as organic molecules. Regarding the devices developed for heavy metal determination, the few approaches reported so far rely on the use of porous silica matrices that serve as a binder of nanomaterials and are applied for the surface modification of a commercial solid-state electrode. For instance, Jena et al. [39] casted a thin-film of silica-gold nanocomposite on a solid gold electrode for the detection of As(III), Hg(II) and Cu(II). Dimovasilies et al. [40] coated a glassy carbon electrode with (3-mercaptopropyl) trimethoxysilane derived silica gel decorated with Bi nanoparticles and demonstrated its applicability to the detection of Pb(II) and Cd(II). However, this approach shows limitations related to the mass-fabrication of the devices.

1.2.4. Porous Carbon Materials Prepared from Resorcinol-Formaldehyde Gels

In 1989, Pekala et al. [41, 42] pioneered the preparation of resorcinol-formaldehyde gels in aqueous medium using a Na_2CO_3 catalyst. The dried organic gels exhibited a low density, a large surface area and became electrically conductive after pyrolysis in an inert atmosphere. Since then, resorcinol/formaldehyde gels and the porous carbon materials that can be obtained from their pyrolysis, have been receiving considerable attention. The synthesis of resorcinol/formaldehyde gel takes place in two main steps (see Figure 1.6): 1) hydroxymethyl substitution in resorcinol, 2) the polycondensation of hydroxymethyl derivatives [43-45].

The main factors that affect the properties of resorcinol/formaldehyde gels are the initial pH of the solution, the concentration of reactants, and the molar ratio between reactants and catalyst. For the preparation of resorcinol/formaldehyde

gels, the most commonly used catalyst is Na_2CO_3 , and the typical pH values range from 5.4 to 7.6. After gelation and aging, a drying and/or carbonization of these gels is carried out. The drying procedure (e.g., super- or subcritical drying) affects the porosity of the final materials, while their electrical conductivity is dominated by the maximum carbonization temperature. Supercritical drying process will lead to the formation of **aerogels** with a surface area larger than that of the gels dried at room conditions and named **xerogels**. After drying, resorcinol/formaldehyde gels can be transformed into a conductive carbon material normally through carbonization in an inert atmosphere at temperatures above 800°C .

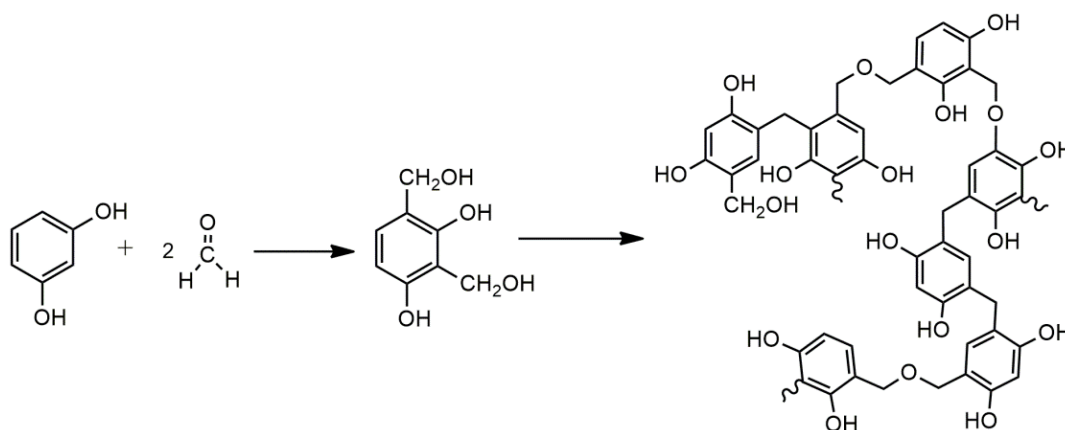


Figure 1.6. Initial reaction of resorcinol/formaldehyde sol-gels

Resorcinol/formaldehyde sol-gels also offer an easy and versatile route to prepare porous carbon based nanocomposites. In principle, these nanocomposites could be produced by all the three approaches presented in Figure 1.5. Regarding the impregnation approach, it can be performed either with resorcinol/formaldehyde gels followed with a carbonization step, or with carbon gels plus a thermal treatment process to form nanoparticles. As we mentioned above, it is extremely difficult to achieve carbon nanocomposites with highly uniform distribution of nanoparticles in a gel matrix through mixing pre-prepared nanoparticles into a sol mixture and therefore this approach is not preferred.

Baumann et al. [46] prepared resorcinol/formaldehyde gels containing Cu(II) by impregnating this organic gel in a Cu(II) solution and found that Cu(II) inside the organic gel was reduced into Cu(0), forming Cu nanoparticles during carbonization of the material. Employing a similar approach, Martínez et al. [47] synthesized carbon aerogel nanocomposites with Ni and Pb nanoparticles. Cotet et al. [48]

prepared carbon aerogels with Fe, Co, Ni, Cu, Pb nanoparticles, also by impregnation with metal salts. However, as already mentioned, this process is less controllable in terms of metal uptake and material homogeneity.

The co-synthesis approach is a powerful alternative for producing metal/carbon nanocomposites by directly adding metal salts into the resorcinol/formaldehyde sol mixture [49, 50]. In this case, the entire experimental process is simplified, consisting of a one-pot synthesis approach. The metal content in the final materials can be controlled and its homogeneity is significantly improved. The obtained hybrid materials are promising material candidates for various applications such as catalysts [51], or adsorbents [52]. However, so far porous carbon nanocomposites have scarcely been exploited in the field of sensors and in particular, the synthesis of carbon aerogels and xerogels doped with Bi has not been reported in the abundant literature of porous carbon nanocomposites.

1.2.5. Thin-films Prepared by Sol-Gel

Spin-coating is a procedure used to deposit uniform thin-films on a flat substrate. Usually, a suspension of the coating material is applied on the center of a substrate. The substrate is then rotated at high speed in order to spread the coating material by centrifugal force and cover the whole substrate while the solvent is being evaporated and gelation takes place. Rotation is stopped when the desired film thickness is achieved.

Sol-gel processing is especially adaptable for spin-coating thin-films on substrate. For the formation of highly reliable coatings, a chemical bonding between the film and the substrate must take place [53]. In the case of coating sol-gel silica films on thermally grown silicon oxide substrates (SiO_2/Si), the film/substrate adhesion is achieved by the formation of siloxane chemical bonds ($-\text{Si}-\text{O}-\text{Si}-$), also produced during the condensation reactions of SiO_2 precursors.

Due to the poor interfacial adhesion between carbon films and most substrates, sol-gel derived pure carbon films have scarcely been investigated. Silicon substrates have been widespread in microfabrication processes. Most of them are modified by a layer of silicon dioxide grown by a thermal process and whose thickness can be

strictly controlled. Such substrates are the starting point of most microelectronic processes. Using the same kind of substrates, we designed novel carbon/silica composite materials derived from a resorcinol-formaldehyde sol-gel route. Here, the incorporation of silica to the sol-gel synthesis was done to improve the interfacial adhesion between the resulting carbon film and the SiO₂/Si substrate. An alternative could be the addition of silica nanoparticles to the resorcinol/formaldehyde sol mixture. However, this was not considered, owing to the possible aggregation of nanoparticles during the gelation that would result in non-homogeneous composite materials and in turn non-stable carbon films [54].

In this work, novel hybrid resorcinol/formaldehyde/silica materials for thin-film deposition were prepared by a co-synthesis approach to yield an interpenetrating network of a carbonizable polymeric gel and a silica gel. A hybrid carbon/silica composite xerogel was produced after a carbonization process [55]. This approach offers a facile route to produce robust and uniform carbon/silica thin-films on SiO₂/Si substrates. Previous synthesis approaches to get this type of films have been reported. For instance, Song et al. [56] obtained a hybrid porous carbon/silica film on SiO₂/Si substrates by spin-coating a sol mixture composed of both silica and phenol/formaldehyde (resol-silica), followed by a carbonization step. It is shown how the addition of silica gel into the carbon matrix significantly improved the film/substrate adhesion. Moreover, the conductivity of a carbon/silica film with ~40 wt% silica content was still comparable to that of carbon inks commonly used for the preparation of screen printed electrodes, thus indicating the potential application of these films in electrochemical sensing. However, the resol-silica sol preparation process mentioned in this approach was very complex and time-consuming and made use of expensive block co-polymers. Due to the undesired interaction of catalysts as well as very different gelation times of the organic and the silica networks, the carbonaceous and silica sols used in this system were synthesized separately and then mixed together. As a matter of fact, this procedure requires a multiple-step sol-gel process carried out over several days.

Recently, Li et al. [57] proposed a very simple approach to prepare carbon/silica composite aerogel materials in bulk. In this synthesis, resorcinol and formaldehyde were used as the source of carbon gel and aminopropyltriethoxysilane (APTES) was selected as a silica source. A homogeneous composite material was obtained in a

few hours at room temperature through mixing these three reagents in ethanol. However, the application of this material for the generation of thin-films has not been investigated.

1.3. Screen-printing Technique

Screen-printing is a patterning technique whereby a mesh screen containing a stencil placed to define the patterns, is used to transfer an ink onto a substrate as illustrated in Figure 1.7. A blade is moved across the screen, to push inks pass through the screen and deposit on a substrate. The smallest pattern that can be easily developed using this technique shows a minimum dimension of 70 μm , though most recent developments are pushing the limits down to 30 μm .

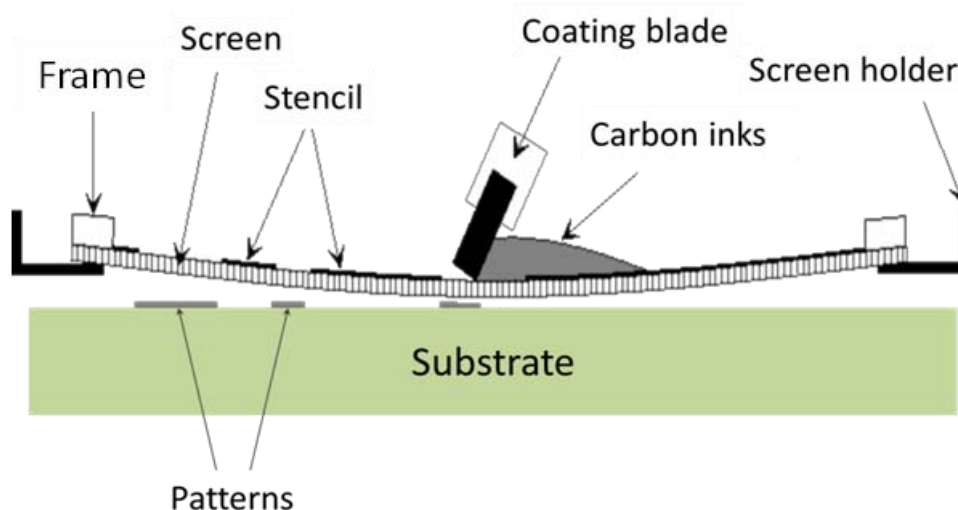


Figure 1.7. Screen-printing process

Screen-printing is widely employed for the fabrication of cost-effective miniaturized electrochemical devices, which are commonly used in a disposable fashion. The whole electrochemical cell, including working, reference and counter electrodes can be printed on the same substrate surface by sequential screen printing of the different inks. Figure 1.8 represents the stepwise fabrication of a screen printed electrode, comprising the printing of 1) transducer electrical tracks, 2) working, counter and reference electrodes, and 3) an insulation layer to define working cell area. The ink formulation and composition used for the fabrication of screen-printed electrodes are usually proprietary information of the respective companies. An ink commonly includes material particles, polymeric binders and other additives

for improved particle dispersion, printing and adhesion processes. In general, silver and graphite based inks are used to fabricate reference and counter electrodes, respectively. An increasing amount of materials are employed for the preparation of active inks to produce working electrodes, including graphite, gold, platinum, silver and carbon nanotubes, among others. This is a versatile process that enables the fabrication of a great variety of screen printed sensors, which are widely used for a high number of electrochemical applications [58].

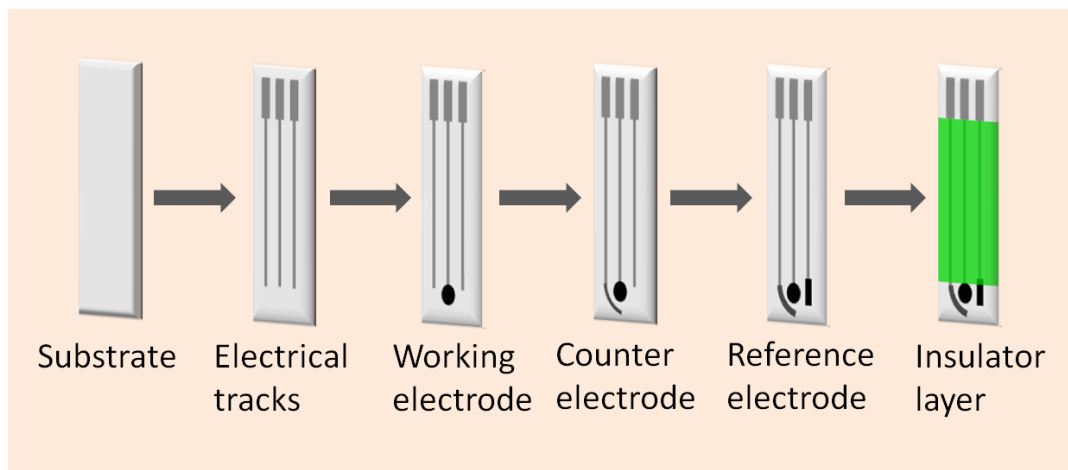


Figure 1.8. Stepwise fabrication of a screen printed electrode

1.4. Lithographic Techniques

1.4.1. Photolithography

1.4.1.1. General Introduction

Photolithography is a microfabrication process used to produce micro- and nano-patterns onto a light-sensitive chemical photoresist film by light exposure through a patterned mask. Upon light exposure, the photoresist may cross-link or not, thus becoming insoluble or soluble in certain solvents, respectively. A thermal baking process carried out after the light exposure step is also introduced. The effect of both the light exposure and thermal treatment steps is different depending on the resist chemical composition. In the case of the so-called positive photoresists, the exposed resist becomes more soluble and is removed from the substrate in the so-called development step. Conversely, in the case of negative photoresist, the exposed areas become insoluble, with the non-exposed ones being removed during

the development step. Photolithography is at the heart of the microelectronics industry and is thus a very mature technology. The book "Fundamentals of Microfabrication: the Science of Miniaturization" [59] gives a comprehensive introduction to the photolithography technique. The smallest features that can be produced by conventional photolithography show sizes down to 1 μm .

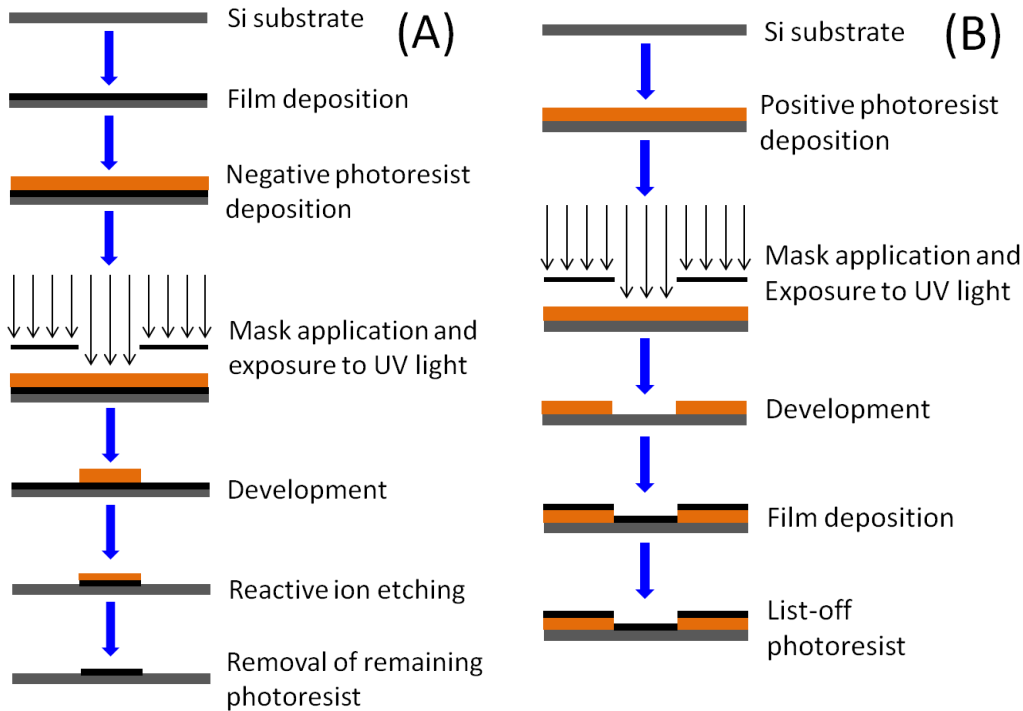


Figure 1.9. Schematic drawing of common photolithography processes

Two commonly used photolithographic fabrication routes are illustrated in Figure 1.9. In both cases, a standard silicon substrate with a thermally grown silicon oxide layer is used. The first one combines photolithography and etching processes (Figure 1.9(A)). A thin-film is firstly grown onto a SiO_2/Si substrate. A photoresist layer is then coated on top of the film and exposed to UV light through a mask. In this figure, a negative photoresist has been used. After development, an etching process is performed to remove the part of the film non-coated by the photoresist. Finally, the remaining photoresist was removed from the substrate, leaving the desired film pattern on the SiO_2/Si substrate. In the second approach (Figure 1.9 (B)), a photoresist layer is firstly deposited and photolithographically patterned on a SiO_2/Si substrate. A positive photoresist has been used in this case. A film of the material to be patterned is then grown on top. Afterwards, a lift-off process is carried out in which the photoresist is removed and thus that part of film deposited

on top of the photoresist patterns is also removed, which eventually produces the desired film patterns on the substrate.

Photolithography can be considered as another powerful technique to commercially produce disposable miniaturized electrochemical sensors. In this context, film deposition plays an important role in the entire process. Up to now, a number of techniques have been developed to grow uniform thin films on a substrate, including chemical vapor deposition [60] and physical vapor deposition [61]. Materials processed as films range from metals (e.g., iridium, gold, platinum [62], and bismuth [63]) to carbon [64]. A brief summary about the recent developments of electrochemical devices fabricated by photolithography that have been applied to the detection of heavy metals is given below.

1.4.1.2. Patterned Thin-film Electrodes by Photolithography

The most commonly reported photolithographically patterned thin-film electrochemical devices for heavy metal detection are made of metals (e.g., platinum [62], iridium [65], gold [62, 66] and bismuth [31, 67]). They are normally deposited on a substrate by a physical vapor deposition approach. Since heavy metals cannot be alloyed with platinum and iridium, therefore the surfaces of these two metal based electrodes had to be modified in order to make them sensitive in this application. Metal thin-film electrodes that can be directly applied to heavy metal detection are those made of bismuth and gold.

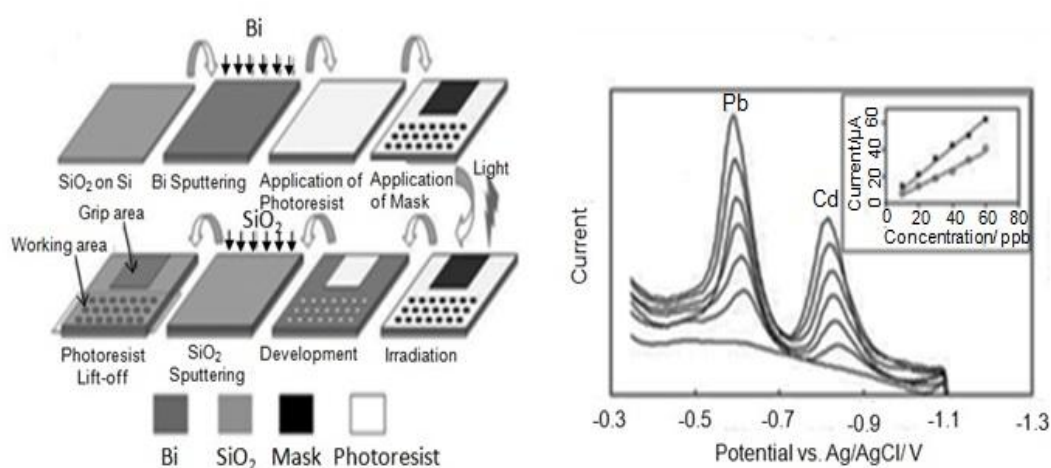


Figure 1.10. Bi microelectrode array fabricated by photolithography and application to heavy metal detection (reprint from [31])

Figure 1.10 shows a representative Bi thin-film microelectrode array fabricated by a photolithographic approach that includes the deposition of a Bi film by a sputtering process followed by a photolithographic step using a positive photoresist and the definition of the electrode areas by the deposition of a SiO₂ layer and the lift-off process of the patterned photoresist. Using these devices [31, 67] LODs of 0.6 , 0.7 and 0.7 ppb for Pb(II), Cd(II) and Ni(II), respectively, were attained. Thin-film gold microelectrodes fabricated by a similar process were reported for the analysis of Pb and Hg in waters with limits of detection in the 0.5-10 ppb range [62, 68].

As mentioned above, carbon electrodes feature several advantages in electrochemistry compared to metal electrodes. Therefore, the fabrication of carbon thin-film electrodes has also been explored. Carbon films generated by chemical vapor deposition using methane as carbon source, have been produced and patterned on SiO₂/Si substrates and then applied for electrochemical applications [69].

In other approaches, films of carbonaceous materials have been produced and then carbonized on SiO₂/Si substrates for the development of carbon thin-films. For instance, Rojo et al. [70] deposited continuous carbon films on 4-inch SiO₂/Si wafers by the pyrolysis of 3,4,9,10-perylenetetracarboxylic dianhydride in a vacuum tube. The resulting carbon film was patterned into interdigitated electrodes by photolithography and then applied to various electrochemical applications, including heavy metal analysis [71, 72]. Wei et al. [73] spin coated sucrose on 4-inch Si/SiO₂ wafer and the resulting film was carbonized and successfully patterned by photolithography to produce carbon thin-film devices. A commonly used starting material for developing carbon patterns on SiO₂/Si substrates is a photoresist. One advantage of using photoresists is the well-known and standard patterning process available, which is carried out before the carbonization step. Kim et al. [74] firstly reported pyrolyzed photoresist derived film electrodes (PPFE) that showed a comparable electrochemical behavior to that of GCE. Sánchez et al. [75] micro-fabricated PPFEs and applied them for Hg(II) detection. Rehacek et al. [76] modified PPFEs with a Bi film for the analysis of Pb(II) and Cd(II) in waters.

Nevertheless, these films show an important shortcoming related to the weak film/substrate interaction, which is manifested by the possible film detachment

from the substrate once the films were immersed in solutions. A weak film/substrate interaction is a serious limitation for sensor applications. Therefore, carbon-based thin-film electrochemical devices that were robust and whose fabrication process could be strictly controlled are still to be developed. This has been one of the objectives of this Thesis.

1.4.2. Soft-lithography

Soft-lithography is another technological process for the production of micro- and nano-patterns of different materials, which has emerged as a cost-effective alternative to photolithography for certain applications. Photolithography is an expensive process and makes use of bulky equipment that must be located in a room under controlled atmosphere, making it less accessible to many people. By contrast, soft lithography includes a group of non-photolithographic fabrication techniques based on printing, molding and embossing processes simply carried out with an elastomeric stamp. The stamp, which is normally made of polydimethylsiloxane (PDMS), is a key element in soft lithography since it presents relief structures patterned on its surface that are used to generate the desired structures. For a comprehensive understanding of various soft lithography methods, such as micro-contact printing, replica molding, micro-molding in capillaries, among others, we refer the reader to the review articles from Whitesides's group [77, 78].

In this Thesis, microtransfer molding method (μ TM) sketched in Figure 1.11 has been applied and is described in more detail. μ TM processes make use of a stamp containing the desired structures, which can be filled with a liquid precursor of the material to be patterned, such as a sol. Then, the filled stamp is brought into contact with a substrate and a certain pressure is applied. After solidification of the liquid, the stamp is peeled off the substrate and the desired patterns on the substrate are released. A continuous residual layer that contacted all the patterns is always generated due to the excess of liquid used to ensure that the patterns in the stamp are completely filled. In this context, the applied pressure is important in order to minimize the thickness of this layer but without deforming the stamp. This residual layer can eventually be removed by applying different etching processes depending on the patterned material.

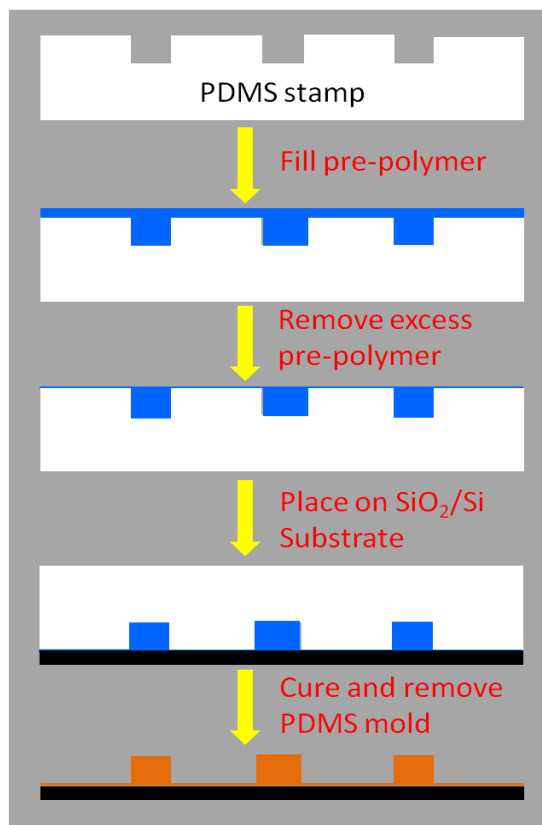


Figure 1.11. Schematic drawing of the microtransfer molding process

Recently, Li et al. [79] reported on a patterning process of reduced graphene oxide microelectrode arrays on indium tin oxide substrates, produced by a soft lithographic approach. Using a resorcinol/formaldehyde sol-gel process, Sharma et al. [80] developed free-standing carbon micro-patterns by an adaptation of a microtransfer molding process. These are very preliminary studies that have to be further explored. In this context, the application of the μ -TM soft lithographic techniques that could be used to produce carbon-based structures on SiO₂/Si substrates and could be directly used for electroanalytical applications has also been studied in this Thesis.

References

- [1] Hu H. Human Health and heavy metals exposure. In: McCally M, editor. life support: The environment and human health: MIT press; 2002. p. 1-13.
- [2] WHO Guidelines for Drinking Water Quality 2011.
- [3] Directive 2013/39/EU of the European Parliament and of the Council.
- [4] U.S. EPA National Primary Drinking Water Regulations 2009.

- [5] GB 5749-2006 Standards for Drinking Water Quality. 2006.
- [6] Standard methods for the examination of water & wastewater, 22nd Edition: American Public Health Association (APHA), American Water Works Association (AWWA) & Water Environment Federation (WEF); 2012.
- [7] Ninwong B, Chuanuwatanakul S, Chailapakul O, Dungchai W, Motomizu S. On-line Preconcentration and Determination of Lead and Cadmium by Sequential Injection/anodic Stripping Voltammetry. *Talanta*. 2012;96:75-81.
- [8] Liu CC. Electrochemical Sensors. In: Bronzino JD, editor. *The Biomedical Engineering Handbook: Second Edition*: CRC Press LLC; 2000.
- [9] Power AC, Morrin A. Electroanalytical Sensor Technology. In: Khalid MAA, editor. *Electrochemistry: InTech*; 2013.
- [10] Cui L, Wu J, Ju H. Electrochemical Sensing of Heavy Metal Ions with Inorganic, Organic and Bio-materials. *Biosensors and Bioelectronics*. 2015;63:276-286.
- [11] Chen C, Niu X, Chai Y, Zhao H, Lan M. Bismuth-Based Porous Screen-Printed Carbon Electrode with Enhanced Sensitivity for Trace Heavy Metal Detection by Stripping Voltammetry. *Sensors and Actuators B: Chemical*. 2013;178:339-342.
- [12] Lezi N, Economou A, Dimovasilis PA, Trikalitis PN, Prodromidis MI. Disposable Screen-Printed Sensors modified with Bismuth Precursor Compounds for the Rapid Voltammetric Screening of Trace Pb(II) and Cd(II). *Analytical Chimica Acta*. 2012;728:1-8.
- [13] Li J, Guo S, Zhai Y, Wang E. High-Sensitivity Determination of Lead and Cadmium based on the Nafion-Graphene Composite Film. *Analytica Chimica Acta*. 2009;649:196-201.
- [14] Pokpas K, Zbeda S, Jahed N, Mohamed N, Baker PG, Iwuoha EI. Electrochemically Reduced Graphene Oxide Pencil-Graphite in situ Plated Bismuth-Film Electrode for the Determination of Trace Metals by Anodic Stripping Voltammetry. *International Journal of Electrochemical Science*. 2014;9:736-759.
- [15] Riman D, Jirovsky D, Hrbac J, Prodromidis MI. Green and Facile Electrode Modification by Spark Discharge: Bismuth Oxide-screen Printed Electrodes for the Screening of Ultra-race Cd(II) and Pb(II). *Electrochemistry Communications*. 2015;50:20-23.
- [16] Rico MÁG, Olivares-Marín M, Gil EP. Modification of Carbon Screen-printed Electrodes by Adsorption of Chemically Synthesized Bi Nanoparticles for the Voltammetric Stripping Detection of Zn(II), Cd(II) and Pb(II). *Talanta*. 2009;80:631-635.
- [17] Sosa V, Serrano N, Arino C, Diaz-Cruz JM, Esteban M. Sputtered Bismuth Screen-printed Electrode: a Promising Alternative to Other Bismuth Modifications in the Voltammetric Determination of Cd(II) and Pb(II) Ions in Groundwater. *Talanta*. 2014;119:348-352.
- [18] Sánchez A, Morante-Zarcero S, Pérez-Quintanilla D, Sierra I, del Hierro I. Development of Screen-Printed Carbon Electrodes Modified with Functionalized Mesoporous Silica Nanoparticles: Application to Voltammetric Stripping Determination of Pb(II) in Non-pretreated Natural Waters. *Electrochimica Acta*. 2010;55:6983-6990.
- [19] Zhao C, Liu H, Wang L. Simultaneous Determination of Pb(ii) and Cd(ii) Using an Electrode Modified with Electropolymerized Thiadiazole Film. *Analytical Methods*. 2012;4:3586-3592.
- [20] Alizadeh T, Amjadi S. Preparation of Nano-sized Pb²⁺ Imprinted Polymer and its Application as the Chemical Interface of an Electrochemical Sensor for Toxic Lead

Determination in Different Real Samples. *Journal of Hazardous Materials*. 2011;190:451-459.

[21] Liu G, Chen J, Hou X, Huang W. A Highly-Sensitive Electrochemical Sensor for the Simultaneous Detection of Cd²⁺ and Pb²⁺ Using Liquid Phase-Exfoliated Graphene. *Analytical Methods*. 2014;6:5760-5765.

[22] Bui M-PN, Li CA, Han KN, Pham X-H, Seong GH. Electrochemical Determination of Cadmium and Lead on Pristine Single-Walled Carbon Nanotube Electrodes. *Analytical Science*. 2012;28:699-704.

[23] Xu R-X, Yu X-Y, Gao C, Jiang Y-J, Han D-D, Liu J-H, et al. Non-conductive Nanomaterial Enhanced Electrochemical Response in Stripping Voltammetry: The Use of Nanostructured Magnesium Silicate Hollow Spheres for Heavy Metal Ions Detection. *Analytical Chimica Acta*. 2013;790:31-38.

[24] Wei Y, Yang R, Zhang Y-X, Wang L, Liu J-H, Huang X-J. High Adsorptive γ -AlOOH(boehmite)@SiO₂/Fe₃O₄ Porous Magnetic Microspheres for Detection of Toxic Metal Ions in Drinking Water. *Chemical Communication (Cambridge, U K)*. 2011;47:11062-11064.

[25] Wang J, Lu J, Hocevar SB, Farias PAM, Ogorevc B. Bismuth-Coated Carbon Electrodes for Anodic Stripping Voltammetry. *Analytical Chemistry*. 2000;72:3218-3222.

[26] Rohr O. Bismuth – the New Ecologically Green Metal for Modern Lubricating Engineering. *Industrial Lubrication and Tribology*. 2002;54:153-164.

[27] Aragay G, Merkoci A. Nanomaterials Application in Electrochemical Detection of Heavy Metals. *Electrochimica Acta*. 2012;84:49-61.

[28] Li M, Gou H, Al-Ogaidi I, Wu N. Nanostructured Sensors for Detection of Heavy Metals: A Review. *ACS Sustainable Chemistry and Engineering*. 2013;1:713-723.

[29] Pauliukaitė R, Brett CMA. Characterization and Application of Bismuth-Film Modified Carbon Film Electrodes. *Electroanalysis*. 2005;17:1354-1359.

[30] Niu X, Zhao H, Lan M. Disposable Screen-Printed Bismuth Electrode Modified with Multi-walled Carbon Nanotubes for Electrochemical Stripping Measurements. *Analytical Science*. 2011;27:1237-1241.

[31] Malakhova NA, Mysik AA, Saraeva SY, Stozhko NY, Uimin MA, Ermakov AE, et al. A Voltammetric Sensor on the Basis of Bismuth Nanoparticles Prepared by the Method of Gas Condensation. *Journal of Analytical Chemistry*. 2010;65:640-647.

[32] Hwang G-H, Han W-K, Park J-S, Kang S-G. An Electrochemical Sensor Based on the Reduction of Screen-Printed Bismuth Oxide for the Determination of Trace Lead and Cadmium. *Sensors and Actuators B: Chemical*. 2008;135:309-316.

[33] Rehacek V, Hotovy I, Vojs M. Bismuth-Coated Diamond-Like Carbon Microelectrodes for Heavy Metals Determination. *Sensors and Actuators B: Chemical*. 2007;127:193-197.

[34] Rehacek V, Hotovy I, Vojs M. Bismuth Film Voltammetric Sensor on Pyrolyzed Photoresist/Alumina Support for Determination of Heavy Metals. *Electroanalysis*. 2014;26:898-903.

[35] Kokkinos C, Economou A, Raptis I. Microfabricated Disposable Lab-on-a-chip Sensors with Integrated Bismuth Microelectrode Arrays for Voltammetric Determination of Trace Metals. *Analytica Chimica Acta*. 2012;710:1-8.

- [36] Zou Z, Jang A, MacKnight E, Wu P-M, Do J, Bishop PL, et al. Environmentally Friendly Disposable Sensors with Microfabricated on-chip Planar Bismuth Electrode for in situ Heavy Metal Ions Measurement. *Sensors and Actuators B: Chemical*. 2008;134:18-24.
- [37] Gong K, Zhang M, Yan Y, Su L, Mao L, Xiong S, et al. Sol-gel-Derived Ceramic-Carbon Nanotube Nanocomposite Electrodes: Tunable Electrode Dimension and Potential Electrochemical Applications. *Analytical Chemistry*. 2004;76:6500-6505.
- [38] Pengfei Niu, Martí Gich, César Fernández-Sánchez, Roig A. Sol-Gel Nanocomposites for Electrochemical Sensor Applications. In: Zayat DLAM, editor. *The Sol-Gel Handbook: Synthesis, Characterization, and Applications: Wiley-VCH Verlag GmbH & Co. KGaA*; 2015; 1413-1434
- [39] Jena BK, Raj CR. Gold Nanoelectrode Ensembles for the Simultaneous Electrochemical Detection of Ultratrace Arsenic, Mercury and Copper. *Analytical Chemistry*. 2008;80:4836-4844.
- [40] Dimovasilis PA, Prodromidis MI. Bismuth-Dispersed Xerogel-Based Composite Films for Trace Pb(II) and Cd(II) Voltammetric Determination. *Analytica Chimica Acta*. 2013;769:49-55.
- [41] Pekala RW. low Density, Resorcinol-Formaldehyde Aerogels. US 4873218, 1989.
- [42] Pekala RW. Low Density, Resorcinol-Formaldehyde Aerogels. US 4997804 A, 1991.
- [43] Al-Muhtaseb SA, Ritter JA. Preparation and Properties of Resorcinol-Formaldehyde Organic and Carbon Gels. *Advanced Materials*. 2003;15:101-114.
- [44] ElKhatat AM, Al-Muhtaseb SA. Advances in Tailoring Resorcinol-Formaldehyde Organic and Carbon Gels. *Advanced Materials*. 2011;23:2887-2903.
- [45] Taylor SJ, Haw MD, Sefcik J, Fletcher AJ. Gelation Mechanism of Resorcinol-Formaldehyde Gels Investigated by Dynamic Light Scattering. *Langmuir*. 2014;30:10231-10240.
- [46] Baumann TF, Fox GA, Satcher JH, Yoshizawa N, Fu R, Dresselhaus MS. Synthesis and Characterization of Copper-Doped Carbon Aerogels. *Langmuir*. 2002;18:7073-7076.
- [47] Martínez S, Vallribera A, Cotet CL, Popovici M, Martín L, Roig A, et al. Nanosized Metallic Particles Embedded in Silica and Carbon Aerogels as Catalysts in the Mizoroki-Heck Coupling Reaction. *New Journal of Chemistry*. 2005;29:1342-1345.
- [48] Cotet LC, Gich M, Roig A, Popescu IC, Cosoveanu V, Molins E, et al. Synthesis and Structural Characteristics of Carbon Aerogels with a High Content of Fe, Co, Ni, Cu, and Pd. *Journal of Non-Crystalline Solids*. 2006;352:2772-2777.
- [49] Czakkel O, Geissler E, Szilagyí IM, Székely E, László K. Cu-doped Resorcinol-Formaldehyde (RF) Polymer and Carbon Aerogels. *Journal of Colloid Interface Science*. 2009;337:513-22.
- [50] Czakkel O, Geissler E, Moussaïd A, Koczka B, László K. Copper-Containing Resorcinol-Formaldehyde Networks. *Microporous and Mesoporous Materials*. 2009;126:213-221.
- [51] Job N, Heinrichs B, Lambert S, Pirard J-P, Colomer J-F, Vertruyen B, et al. Carbon Xerogels as Catalyst Supports: Study of Mass Transfer. *AIChE Journal*. 2006;52:2663-2676.
- [52] Kharissova OV, Dias HVR, Kharisov BI. Magnetic Adsorbents Based on Micro- and Nano-Structured Materials. *RSC Advances*. 2015;5:6695-6719.
- [53] Sakka S. Preparation and Properties of Sol-Gel Coating Films. *Journal of Sol-Gel Science and Technology*. 1994;2:451-455.

- [54] Lee J, Han S, Hyeon T. Synthesis of New Nanoporous Carbon Materials using Nanostructured Silica Materials as Templates. *Journal of Materials Chemistry*. 2004;14:478-486.
- [55] Müller H, Rehak P, Jäger C, Hartmann J, Meyer N, Spange S. A Concept for the Fabrication of Penetrating Carbon/Silica Hybrid Materials. *Advanced Materials*. 2000;12:1671-1675.
- [56] Song L, Feng D, Campbell CG, Gu D, Forster AM, Yager KG, et al. Robust Conductive Mesoporous Carbon–Silica Composite Films with Highly Ordered and Oriented Orthorhombic Structures from Triblock-copolymer Template Co-assembly. *Journal of Materials Chemistry*. 2010;20:1691-1701.
- [57] Ye L, Ji Z-H, Han W-J, Hu J-D, Zhao T. Synthesis and Characterization of Silica/Carbon Composite Aerogels. *Journal of the American Ceramic Society*. 2010;93:1156-1163.
- [58] Li M, Li Y-T, Li D-W, Long Y-T. Recent Developments and Applications of Screen-Printed Electrodes in Environmental Assays—A review. *Analytica Chimica Acta*. 2012;734:31-44.
- [59] Madou MJ. *Fundamentals of Microfabrication: The science of Miniaturization*: CRC press; 2002.
- [60] Pierson HO. *Handbook of Chemical Vapor Deposition (CVD)* William Andrew Inc.; 1999.
- [61] Mattox DM. *Handbook of Physical Vapor Deposition (PVD) Processing*: Elsevier Inc; 2010.
- [62] Uhlig A, Schnakemberg U, Hintsche R. Highly Sensitive Heavy Metal Analysis on Platinum- and Gold-Ultramicroelectrode Arrays. *Electroanalysis*. 1997;9:125-129.
- [63] Jothimuthu P, Wilson RA, Herren J, Haynes EN, Heineman WR, Papautsky I. Lab-on-a-chip Sensor for Detection of Highly Electronegative Heavy Metals by Anodic Stripping Voltammetry. *Biomedical microdevices*. 2011;13:695-703.
- [64] Kumar M, Ando Y. Chemical Vapor Deposition of Carbon Nanotubes: A Review on Growth Mechanism and Mass Production. *Journal of Nanoscience and Nanotechnology*. 2010;10:3739-3758.
- [65] Xie X, Berner Z, Albers J, Stueben D. Electrochemical Behavior and Analysis Performance of Iridium-based Ultramicroelectrode Array (UMEA) Sensor. *Microchimica Acta*. 2005;150:137-45.
- [66] Wan H, Ha D, Zhang W, Zhao H, Wang X, Sun Q, et al. Design of a Novel Hybrid Sensor with Microelectrode Array and LAPS for Heavy Metal Determination using Multivariate Nonlinear Calibration. *Sensors and Actuators B: Chemical*. 2014;192:755-761.
- [67] Kokkinos C, Economou A, Raptis I, Speliotis T. Disposable Lithographically Fabricated Bismuth Microelectrode Arrays for Stripping Voltammetric Detection of Trace Metals. *Electrochemistry Communications*. 2011;13:391-395.
- [68] Wan H, Ha D, Zhang W, Zhao H, Wang X, Sun Q, et al. Design of a Novel Hybrid Sensor with Microelectrode Array and LAPS for Heavy Metal Determination using Multivariate Nonlinear Calibration. *Sensors and Actuators B: Chemical*. 2014;192:755-761.
- [69] Niwa O. Electroanalytical Chemistry with Carbon Film Electrodes and Micro and Nano-Structured Carbon Film-Based Electrodes. *Bulletin of the Chemical Society of Japan*. 2005;78:555-571.

- [70] Rojo A, Rosenstratten A, Anjo D. Characterization of a Conductive Carbon Film Electrode for Voltammetry. *Analytical Chemistry*. 1986;58:2988-2991.
- [71] Tabei H, Morita M, Niwa O, Horiuchi T. Fabrication and Electrochemical Features of New Carbon based Interdigitated Array Microelectrodes. *Journal of Electroanalytical Chemistry*. 1992;334:25-33.
- [72] Wang J, Luo D-B, Horiuchi T. Anodic Stripping with Collection at Interdigitated Carbon Film Microelectrode Arrays. *Electroanalysis*. 1998;10:107-110.
- [73] Wei L, Nitta N, Yushin G. Lithographically Patterned Thin Activated Carbon Films as a New Technology Platform for On-Chip Devices. *ACS Nano*. 2013;7:6498-6506.
- [74] Kim J, Song X, Kinoshita K, Madou M, White R. Electrochemical Studies of Carbon Films from Pyrolyzed Photoresist. *Journal of The Electrochemical Society*. 1998;145:2314-2319.
- [75] Sánchez-Molas D, Cases-Utrera J, Godignon P, Javier del Campo F. Mercury Detection at Microfabricated Pyrolyzed Photoresist Film (PPF) Disk Electrodes. *Sensors and Actuators B: Chemical*. 2013;186:293-299.
- [76] Řeháček V, Hotový I, Vojs M, Kotlár M, Kups T, Spiess L. Pyrolyzed Photoresist Film Electrodes for Application in Electroanalysis. *Journal of Electrical Engineering*. 2011;62:49-53.
- [77] Xia Y, Whitesides GM. *Soft Lithography*. *Angewandte Chemie International Edition*. 1998;37:550-575.
- [78] Qin D, Xia Y, Whitesides GM. *Soft Lithography for Micro- and Nanoscale Patterning*. *Nature Protocols*. 2010;5:491-502.
- [79] Li F, Xue M, Ma X, Zhang M, Cao T. Facile Patterning of Reduced Graphene Oxide Film into Microelectrode Array for Highly Sensitive Sensing. *Analytical Chemistry*. 2011;83:6426-6430.
- [80] Sharma CS, Verma A, Kulkarni MM, Upadhyay DK, Sharma A. Microfabrication of Carbon Structures by Pattern Miniaturization in Resorcinol-Formaldehyde Gel. *ACS Applied Materials & Interfaces*. 2010;2:2193-2197.

Chapter 2

Aim and Objectives

The aim of this Thesis is to develop novel environmentally-friendly electrochemical devices for the sensitive analysis of trace concentration of heavy metal ions in aqueous solutions. In particular, the general objective was the development of porous carbon electrode materials by a sol-gel approach that could be readily applied to the fabrication of miniaturized screen-printed electrodes and thin-film electrodes.

To attain this general objective, we have pursued the following specific objectives:

- I. Developing bismuth nanoparticle-porous carbon composites in bulk by the pyrolysis of resorcinol/formaldehyde gels containing bismuth precursors;
- II. Processing the bulk bismuth-carbon nanocomposites as conventional paste electrodes and characterizing the performance of these materials in the electrochemical analysis of heavy metals in aqueous solution;
- III. Conditioning the bulk nanocomposites for its processing as an ink applied to the production of screen printed electrodes and analyzing water samples with the developed electrodes;
- IV. Adapting the resorcinol/formaldehyde sol-gel route to prepare porous carbon films on silicon substrates and fabricating carbon thin-film electrodes by both photolithography and soft-lithography processes;
- V. Investigating the performance of these thin-film electrodes and their electrochemical application in heavy metal detection.

Figure 2.1 presents an outline of the Thesis work in accordance with the above objectives. It starts from the synthesis of resorcinol/formaldehyde gels, which is the thread that runs through the entire report, and ends with the final aim, which is the

application of the materials in heavy metal sensing. The two branches of the figure correspond to the two parts in which the work is divided.

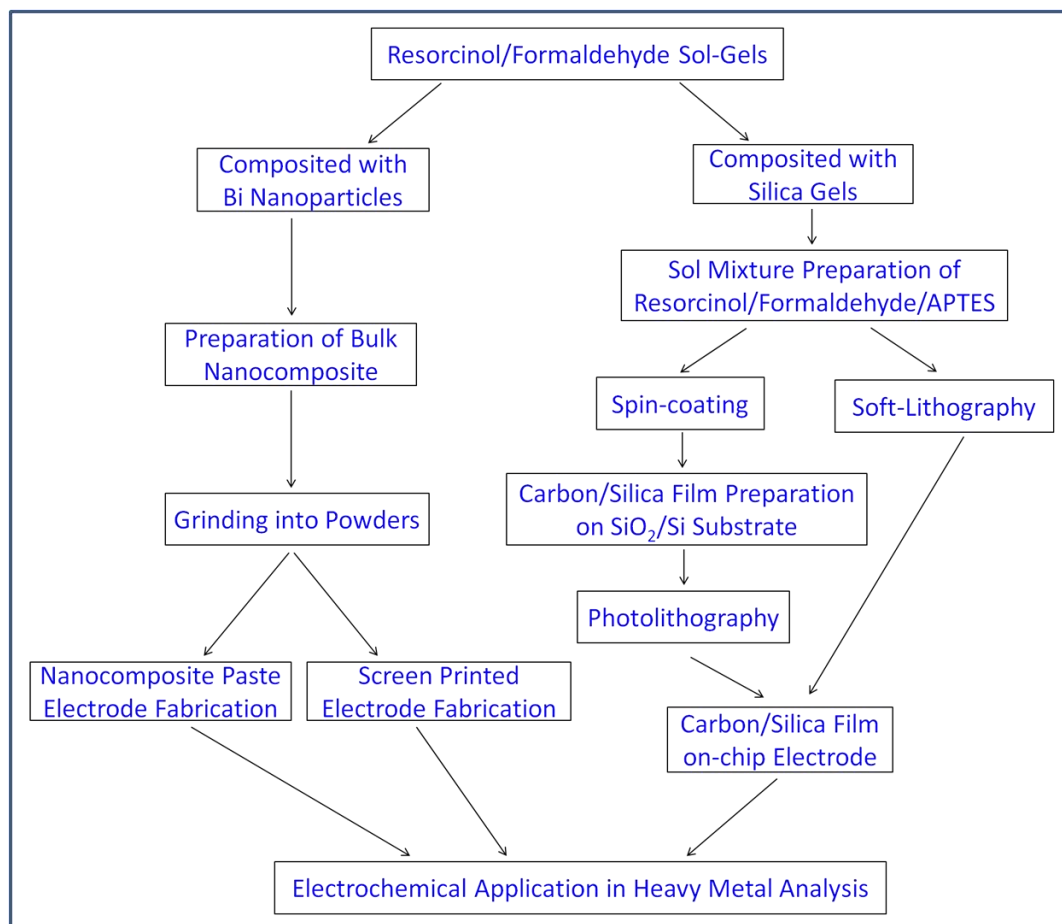
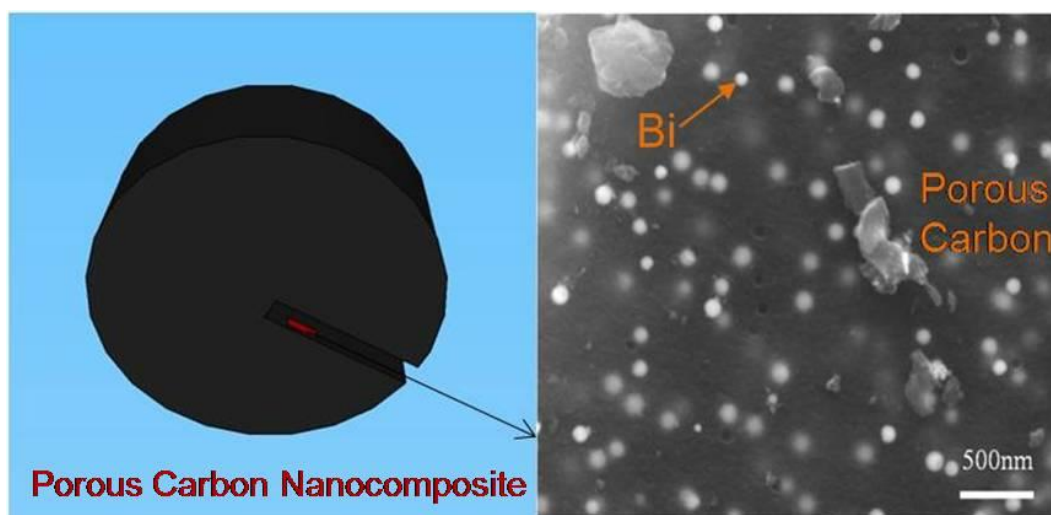


Figure 2.1. Thesis Outline

Chapter 3

Synthesis of Bismuth Nanoparticle-Porous Carbon Nanocomposites



Summary

This chapter describes the synthesis of bismuth nanoparticle/carbon xerogel composites from resorcinol/formaldehyde gels. The synthesis conditions by impregnation and co-synthesis approaches were studied systematically. The microstructure of the resulting nanocomposites was characterized by scanning electron microscopy (SEM), nitrogen adsorption-desorption isotherms, X-ray diffraction (XRD), transmission electron microscopy (TEM), and X-ray photoelectron spectroscopy (XPS).

The work presented in this chapter has been included in one paper entitled “**Facile synthesis of porous bismuth-carbon nanocomposites for the sensitive detection of heavy metals**”, by Martí Gich, César Fernández-Sánchez, Livin Cosmin Cotet, **Pengfei Niu**, and Anna Roig, *Journal of Materials Chemistry A*, 2013, 1, p 11410-11418.

3.1. General Introduction

Figure 3.1 shows a schematic diagram of our concept to prepare bismuth nanoparticle (Bi NP)/porous carbon composites. A homogeneous organic resorcinol/formaldehyde gel containing Bi cations should be firstly synthesized. During carbonization step by a thermal treatment at high temperature in an inert atmosphere, this organic gel is transformed into a porous carbon material and, simultaneously, adjacent Bi(III) cations are reduced into zero valent Bi, which coalesce to form Bi nanoparticles. This results in Bi NPs-porous carbon composite materials. Herein, the incorporation of Bi(III) in a resorcinol/formaldehyde gel is critical for the successful preparation of the nanocomposites.

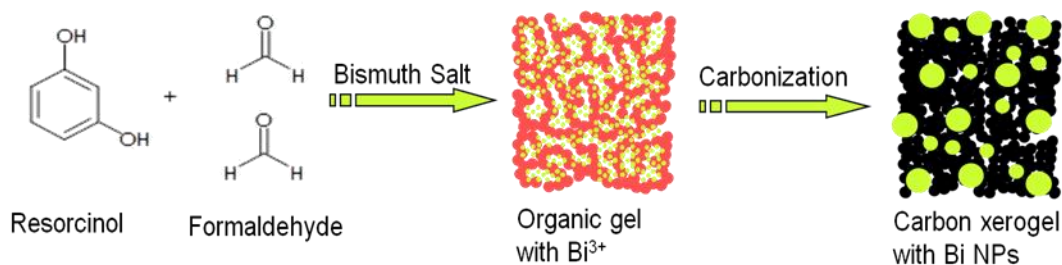


Figure 3.1. Schematic drawing of the synthesis process for Bi NPs/porous carbon nanocomposite

As we mentioned in the Introduction section (Chapter 1), we can consider several strategies to prepare a composite consisting of a dispersion of nanoparticles in a porous matrix. In particular, we have only considered two of these approaches. The first one consists in adding Bi(III) salt to the sol prior to the formation of the resorcinol/formaldehyde gel (co-synthesis), and the second one is based on the incorporation of Bi(III) salt to a previously formed resorcinol/formaldehyde gel (impregnation). However, in both cases, the preparation of a homogeneous bismuth salt solution is necessary. A brief discussion about the solubility of bismuth nitrate ($\text{Bi}(\text{NO}_3)_3$) and bismuth chloride (BiCl_3) which are the most commonly used bismuth salts, in common solvents is given below.

First of all, bismuth salts are known to be readily hydrolyzed in dilute aqueous solutions, forming a white precipitate, when the pH increases above 0 [1, 2]. This is due to the fact that Bi(III) oxide is a weak base and thus its salts are highly acidic and prone to hydrolysis. In order to prevent hydrolysis and prepare a clear aqueous

solution of a Bi(III) salt, the presence of an excess of acid is required. Besides the use of strongly acidic aqueous media, some Bi salts are also soluble in specific organic solvents. The solubility and prices of $\text{Bi}(\text{NO}_3)_3$ and BiCl_3 in some common solvents are listed in Table 3.1. It can be seen that $\text{Bi}(\text{NO}_3)_3$ presents a better solubility in common solvents and much lower cost than BiCl_3 . Therefore, $\text{Bi}(\text{NO}_3)_3$ was employed as a reagent to synthesize the nanocomposites studied in this Thesis.

Table 3.1 Solubility of bismuth salt in organic solvent

	Acetic Acid	Glycerol Formal	Acetone	Ethanol	Prices(€/100g)
$\text{Bi}(\text{NO}_3)_3$	soluble	soluble	soluble	not soluble	61.7
BiCl_3	not soluble	not soluble	soluble	soluble	191.5

It is known that resorcinol/formaldehyde gels can be synthesized in water and organic solvents, such as ethanol and acetone [3]. When co-synthesis approach is employed to prepare the desired Bi containing nanocomposite, the miscibility of the reagents in the selected solvent must be considered. In principle, there are two routes, which are carrying out the synthesis in water and organic solvent, respectively. However, when water is used as the solvent, a very strong acidic aqueous solution must be used to stabilize Bi(III), as described above. In order to avoid producing the resorcinol/formaldehyde gel in a very strong acid solution, the synthesis was selected to be performed in an organic solvent that is glycerol formal. By contrary, when the impregnation route is used, the incorporation of Bi(III) takes place after the formation of the resorcinol/formaldehyde gel. In this case, the gel preparation step is not limited by the solubility of Bi(III) and therefore we chose the most commonly reported approach that is using water as a solvent to prepare it. A full detailed description of the synthesis procedures are given in the following section.

3.2. Nanocomposite Synthesis

3.2.1. Impregnation Approach

3.2.1.1. Synthesis of resorcinol/formaldehyde gel

Resorcinol/formaldehyde xerogels were synthesized following the Pekala method [4], in which the polycondensation of resorcinol and formaldehyde and the

following covalent cross-linking of the formed clusters occurred in water using Na_2CO_3 as catalyst. The molar ratios of resorcinol/formaldehyde and resorcinol/catalyst were set to be 2 and 100, respectively. In a typical synthesis, 6 g resorcinol and 0.057 g Na_2CO_3 were firstly dissolved in 13 ml distilled water. Then 8.2 ml formaldehyde solution (37 wt. % in H_2O , containing 10-15 % methanol as stabilizer) was added to the solution. This mixture was transparent and colorless, with a mass concentration of reagents with respect to water of ca.35 wt%. After sufficient stirring, the mixture was sealed in a glass container and placed in a stove at 60°C . Gelation occurred in about 1 h but the gels were aged in the stove for ~24 h.

3.2.1.2. Impregnation of gels with Bi(III)

The impregnation process was performed after the formation of resorcinol/formaldehyde gels. However, a wet resorcinol/formaldehyde gel contains a large amount of water. If the water containing gel was directly immersed in a Bi(III) solution, we would not obtain a homogeneous distribution of Bi(III) at the molecular scale, since Bi(III) is readily hydrolyzed in water, yielding white precipitates. Hence, a solvent exchange step was performed to replace water inside the gel with an organic solvent that can dissolve $\text{Bi}(\text{NO}_3)_3$. Herein, the organic gels were taken out from the glass container where the gelation took place and immersed immediately in CH_3COOH (98%) bath which is known to solubilize $\text{Bi}(\text{NO}_3)_3$. To exchange the solvent completely from water to CH_3COOH , the gels were cut into irregular pieces of about 2 cm and soaked in a fresh CH_3COOH for at least one hour. The same washing process was repeated by soaking the pieces in a second fresh CH_3COOH bath. Then, the gels were transferred to a 0.2 M solution of $\text{Bi}(\text{NO}_3)_3$ in CH_3COOH and kept for 1 h to incorporate Bi(III) in the organic gel. The bismuth/carbon nanocomposite material obtained after carbonization was labeled $(\text{Bi-C})_{\text{IM}}$.

3.2.2. Co-synthesis approach

The impregnation route can be successfully employed to incorporate Bi(III) into resorcinol/formaldehyde gel, but it presents several drawbacks. 1) It is a time-consuming process. 2) Bi concentration in the final material cannot be controlled. 3) The distribution of Bi(III) in the gel after the impregnation process is not completely

homogeneous, which results in non-homogeneity of the resulting bismuth/carbon nanocomposite. To avoid these disadvantages, we developed the co-synthesis approach, in which $\text{Bi}(\text{NO}_3)_3$ is added to the initial resorcinol-formaldehyde sol. As shown in Table 3.2, the resorcinol/formaldehyde gels containing Bi(III) were prepared by the co-synthesis approach following two different routes (herein labeled as routes A and B), depending on which solvent was used for the dissolution of $\text{Bi}(\text{NO}_3)_3$. The appearances of the sol mixtures during preparation are illustrated in Figure 3.2.

Table 3.2 Bismuth/carbon nanocomposite materials synthesized by co-synthesis

Route A					Route B		
Reagents	Labels			TM	Reagents	Label	TM
	C_B	$(\text{Bi-C})_{\text{CS-L}}$	$(\text{Bi-C})_{\text{CS-H}}$			$\text{M-(Bi-C)}_{\text{CS}}$	
Glycerol Formal (ml)	5	5	5		Acetic Acid (ml)	2	
$\text{Bi}(\text{NO}_3)_3$ (g)	0	0.1	0.6	50	$\text{Bi}(\text{NO}_3)_3$ (g)	0.2	10
Resorcinol (g)	1	1	1	10	Glycerol Formal (ml)	5	10
Formaldehyde (ml)	1.36	1.36	1.36	10	Resorcinol (g)	1	10
NH_4OH (10wt%) (ml)	2	2	2	10	Formaldehyde (ml)	1.36	10
CH_3COOH (ml)	2	2	4	10			

Note: the order in which the reagents are listed in the columns of the table from top to bottom is the same in which these were added into the beaker. TM expressed in minutes refers to the stirring time after the addition of each reagent.

Regarding **route A**, glycerol formal was selected as a solvent for $\text{Bi}(\text{NO}_3)_3$. NH_4OH and CH_3COOH were used to adjust the pH of the sol. As it can be seen in Figure 3.2 (A), a colorless glycerol formal solution containing both $\text{Bi}(\text{NO}_3)_3$ and resorcinol was obtained. However, the mixture became slightly turbid due to the generation of a white suspension after the introduction of formaldehyde solution. With the subsequent addition of NH_4OH solution, it became an opaque orange suspension. Finally, the mixture turned to be a clear yellow sol when a certain amount of

CH_3COOH was added. The required amount of CH_3COOH was related to the $\text{Bi}(\text{NO}_3)_3$ content in the system. This clear yellow solution was poured into a sealed glass container and placed in a stove at 60°C . Gelation occurred in about 15 h but the gels were kept in the oven for at least 24 h for aging.

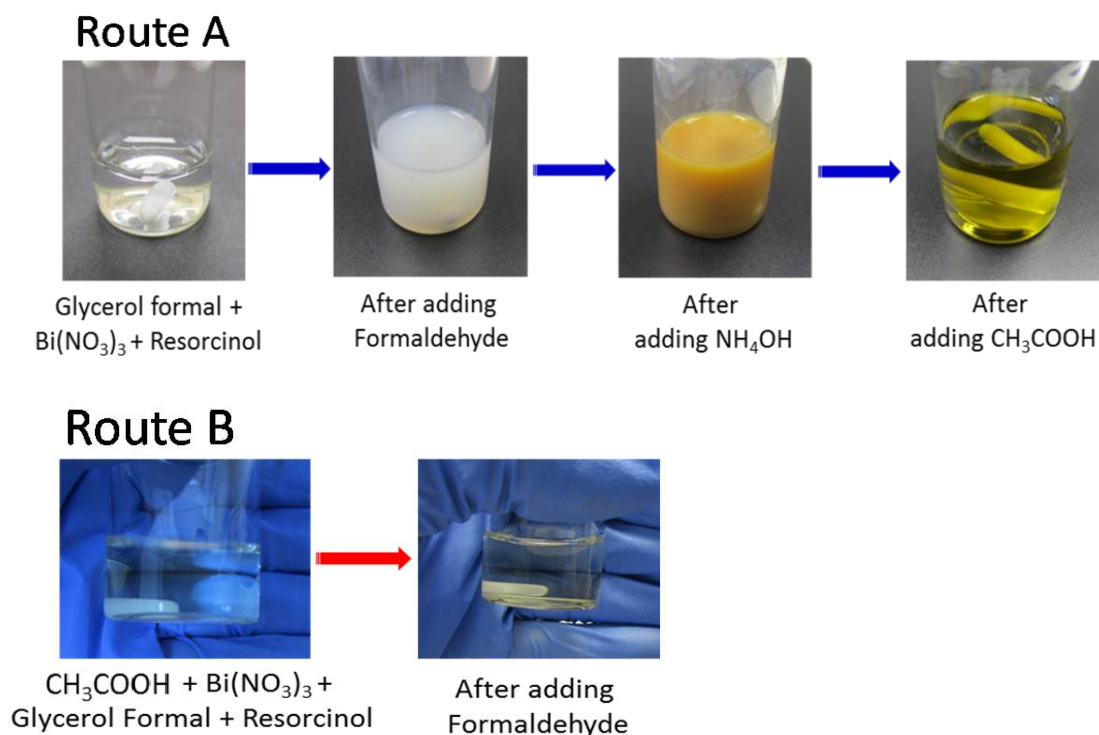


Figure 3.2. Images of the mixtures during sol preparation procedures through different co-synthesis paths

In the case of the gels prepared according to **route B**, CH_3COOH was used to dissolve $\text{Bi}(\text{NO}_3)_3$. Compared to the previous approach, there are several obvious differences observed in this sol-gel process. Firstly, the mixture was transparent and colorless (Figure 3.2(B)) throughout the whole procedure of sol preparation. Secondly, since $\text{Bi}(\text{NO}_3)_3$ dissolves much faster in CH_3COOH than in glycerol formal, the entire sol preparation step was more than two times faster than in the case of route A. Thirdly, the absence of NH_4OH in the system lowered the pH of the initial sol, leading to a much faster gelation. The gel was formed in ~ 8 h at 60°C . Additionally, as it is shown in Table 3.1, $\text{Bi}(\text{NO}_3)_3$ is also soluble in acetone. However, here it is worth mentioning that when glycerol formal was replaced by acetone, the derived gels were not completely homogeneous.

3.2.3. Carbonization

Wet resorcinol/formaldehyde gels doped with Bi(III) prepared by impregnation and co-synthesis paths were dried under a fume hood at ambient conditions for at least 24 h to allow the evaporation of the volatile species. Afterwards, these organic gels were converted into electrically conductive carbon xerogel composites through a carbonization process.

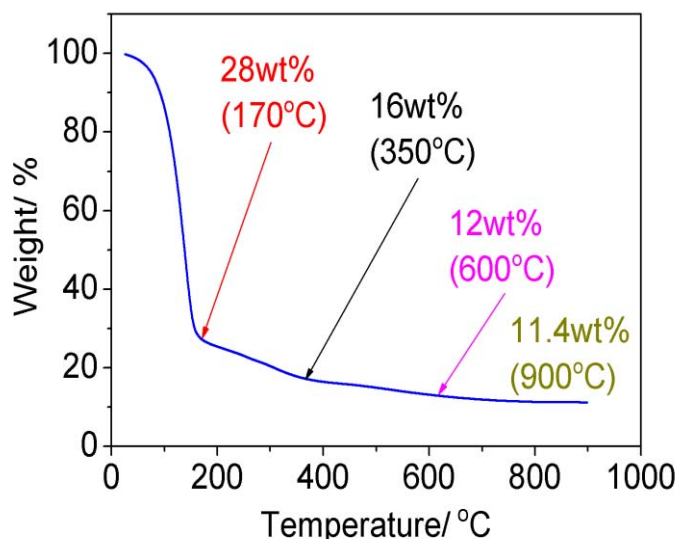


Figure 3.3. TGA of Bi(III)-containing resorcinol/formaldehyde gel

A thermogravimetric analysis (TGA) was performed on Bi(III) containing resorcinol/formaldehyde gels to help us set the adequate pyrolysis treatment. Figure 3.3 shows the corresponding TGA curve. There are two main processes of mass loss in the temperature range of 100-170°C and 170-350°C, respectively. The former with a loss of around 70% of the initial mass is related to the solvent evaporation while the latter showing a mass loss of ~10% is probably associated with the release of organic compounds. Also, a slight mass reduction occurs with the increase of temperature from 360°C to 800°C. A carbonization treatment program was defined based on the TGA curve. The materials were firstly heated up to 350°C at 100°C/h from room temperature and maintained at that temperature for 30 min to release all the solvents and volatile organic compounds. Subsequently, the temperature was increased to 900°C with a ramp of 200°C/h for carbonization. After 2 hours at 900°C, the system was cooled down to room temperature at 350°C/h. During the entire pyrolysis process, which was carried out in a tube with inner

diameter of 55 mm, a constant N₂ or Ar flow with a rate of 120 cm³/min was applied.

Here it is important to note that some of the Bi initially present in the resorcinol/formaldehyde gels was lost during carbonization, especially when initial gel pieces were very small. In fact, we have found that the larger the pieces of Bi(III) containing resorcinol/formaldehyde xerogel used in the pyrolysis, the larger the content of Bi found in the resulting material. On the contrary, almost all Bi was lost when we pyrolyzed xerogel pieces smaller than 100 μm. Thus, in order to preserve as much Bi as possible in the carbon xerogel materials, the co-synthesized resorcinol/formaldehyde gels doped with Bi(III) were not crushed after being removed from the glass container where the gelation takes place (a cylinder with diameter of 1 cm and height of 2 cm). After carbonization, the obtained materials were ball-milled in a Retsch Mixer Mill to obtain micrometer scale powders for structural characterization and further application.

In addition, it must be strongly emphasized that during the pyrolysis of large quantities (around 100 g) of Bi(NO₃)₃/resorcinol/formaldehyde gels, synthesized by co-synthesis using route B, the Mullite tube (OD 65 mm X ID 55 mm X 1000 mm) got ruptured at the area where the materials were placed, when the temperature was around 400°C. We think that an explosion took place probably because of the vigorous exothermic reactions between NO₃⁻ and glycerol formal occurred during the pyrolysis process [5]. Nevertheless, when small amounts (around 5 g) of this material were carbonized, the exothermic reaction did not appear to produce any damage on the tubes. In this Thesis, all the bulk nanocomposite materials were synthesized using both Bi(NO₃)₃ and glycerol formal. Alternative synthesis processes us are being explored.

3.3 Structural and Morphological Characterization

The obtained materials were thoroughly characterized by scanning electron microscopy (SEM), nitrogen adsorption-desorption isotherms, X-ray diffraction (XRD), transmission electron microscopy (TEM) and X-ray photoelectron spectroscopy (XPS) techniques.

3.3.1. Assessment of the Presence of Bismuth Nanoparticles

Energy dispersive X-ray spectroscopy (EDS) performed in Quanta FEI 200F scanning electron microscope (SEM) was used to determine the elemental composition of the materials. To do this measurement, thick layers of the milled powders were coated on an aluminum SEM holder with the aid of silver paint. For each sample, EDS spectra were acquired for more than 120 s at 4 different locations of a 500 x 500 μm^2 substrate area.

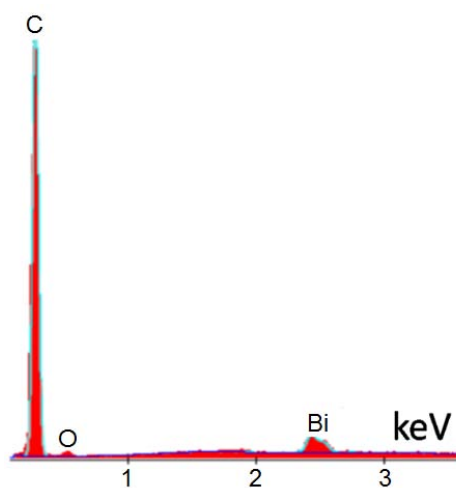


Figure 3.4. Typical EDS analysis of bismuth/carbon nanocomposite

Figure 3.4 shows a typical EDS analysis obtained from the sample of $(\text{Bi-C})_{\text{CS-L}}$. It can be seen that the developed material only contains carbon, oxygen and Bi. Among them, carbon and Bi are the main elements whereas the amount of oxygen is residual. Table 3.3 gives the relative content of Bi in the different materials.

Comparing the Bi content of samples $(\text{Bi-C})_{\text{CS-L}}$ and $(\text{Bi-C})_{\text{CS-H}}$, we found that a 6-fold increase of Bi(III) in resorcinol/formaldehyde gel only results in a 4-fold increase of Bi in the bismuth/carbon composite materials. We believe that this is associated with the loss of Bi during pyrolysis at high temperature as mentioned above.

Table 3.3. Bismuth content in different bismuth/carbon nanocomposites

Samples	$(\text{Bi-C})_{\text{IM}}$	C_B	$(\text{Bi-C})_{\text{CS-L}}$	$(\text{Bi-C})_{\text{CS-H}}$	$\text{M}-(\text{Bi-C})_{\text{CS}}$
Bi (wt. %)	7.0 ± 0.3	0	4.05 ± 0.03	16.4 ± 0.5	6.0 ± 0.2

Note: the associated error corresponds to the standard deviation of 4 measurements

The morphology of Bi in bismuth/carbon composites prepared both by co-synthesis

and impregnation approaches was studied by SEM. It can be seen in Figure 3.4 that spherical white Bi nanoparticles are well dispersed in a gray carbon matrix in both cases.

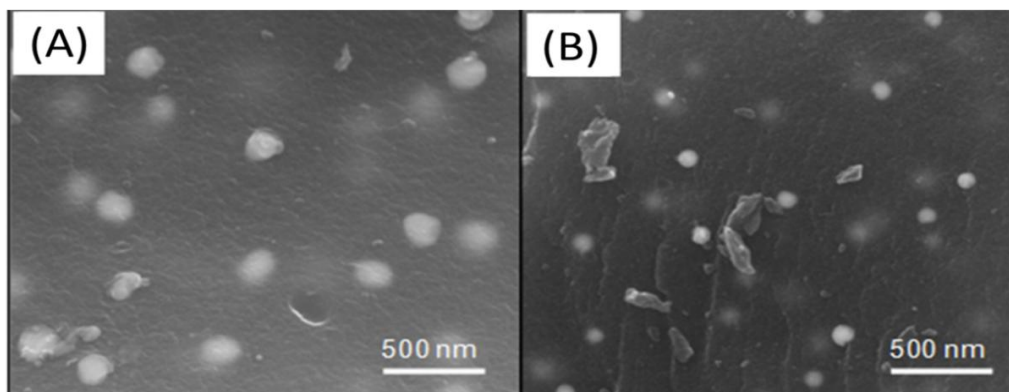


Figure 3.4. Secondary electron SEM images of bismuth/carbon nanocomposites, (A) (Bi-C)_{IM}, and (B) (Bi-C)_{CS-L}.

Nevertheless, the homogeneity of Bi dispersion in co-synthesized samples is much better than that prepared by impregnation route as shown in Figure 3.5. To estimate the size distribution of Bi nanoparticles in the composites, the sizes of more than 150 particles were measured using the imageJ software from at least 10 different SEM images [6] and the histograms of particle size distribution were drawn. This analysis shows that the nanocomposite prepared by the impregnation approach ((Bi-C)_{IM}) shows a very wide particle size distribution ranging from 10 nm up to 250 nm with most of the particles in the diameter range between 15 nm and 50 nm. The inhomogeneity of Bi dispersion and wide polydispersity of particle sizes in (Bi-C)_{IM} is probably due to the concentration gradient of Bi(III) from the surface to the core of the impregnated resorcinol/formaldehyde gel, caused by non-homogeneous impregnation. Regarding the nanocomposites synthesized by co-synthesis method, the dispersion of Bi in the carbon matrix is more homogeneous and the size distribution of Bi particles is clearly bimodal and can be fit by two Gaussians. In the case of the (Bi-C)_{CS-L} sample, the two Gaussian peaks are centered at around 29 nm and 90 nm with a full width at half maximum (FWHM) of 10 nm and 25 nm, respectively. With the increase of Bi concentration, the nanoparticles grow bigger and their size distribution becomes wider. For instance, the two Gaussian peaks obtained from the particle size distribution of sample (Bi-C)_{CS-H} are centered at 85 nm and 155 nm respectively with FWHMs above 30 nm. As a result, the active

surface area of Bi in the nanocomposite cannot be strictly proportional to its concentration. Comparing the samples prepared by the two different co-synthesis paths (route A and B), we could not find significant differences in the morphology of the nanocomposite.

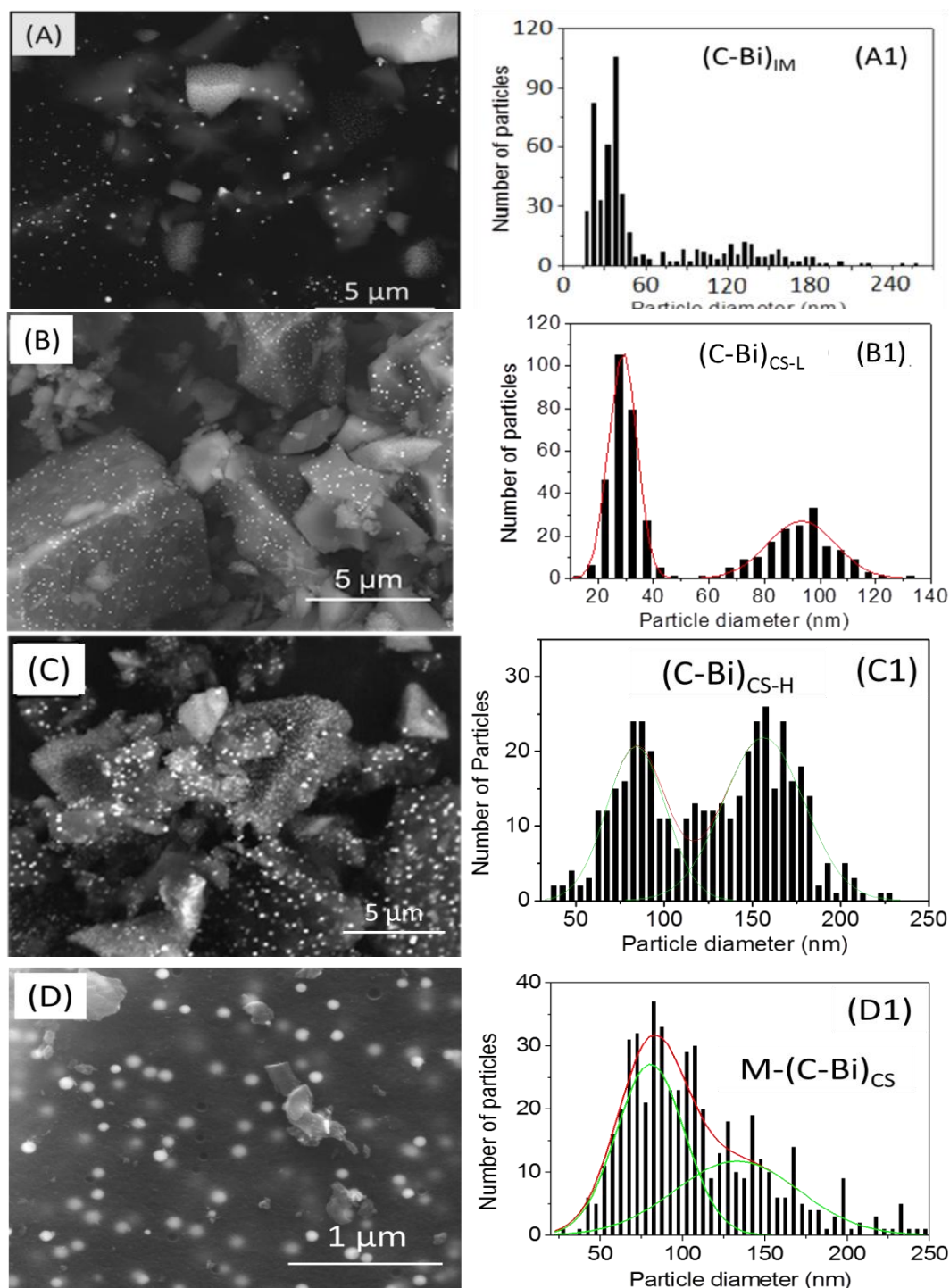


Figure 3.5. SEM images of bismuth/carbon nanocomposites: (A) (Bi-C)_{IM}, (B) (Bi-C)_{CS-L}, (C) (Bi-C)_{CS-H}, and (D) M-(Bi-C)_{CS} as well as the corresponding size distributions of

bismuth nanoparticles.

3.3.2. Porosity of the Materials

In order to study the porosity of the materials, nitrogen adsorption-desorption isotherms were recorded with a Malvern Micromeritics equipment after degassing around 100 mg of nanocomposite powders for 24h at 150°C in vacuum (<1 mPa).

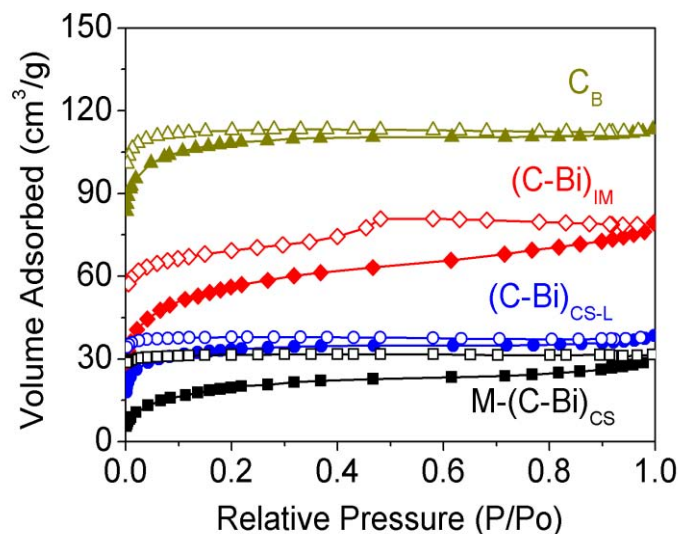


Figure 3.6. Nitrogen adsorption and desorption isotherms of the Bi-C nanocomposites: solid symbols: adsorption and hollow symbols: desorption.

Figure 3.6 displays the recorded isotherms for the different nanocomposites. Very similar N_2 adsorption trends are observed for both carbon blank xerogel and bismuth/carbon xerogel nanocomposites prepared by different approaches. The volume of adsorbed N_2 displays a sharp increase at very low relative pressures, indicating that the porosity is mainly due to micropores (i.e. pores of diameters below 2 nm). The non-negligible slope of the curve at intermediate relative pressures and the increase in adsorbed volume at relative pressures above 0.95 respectively, denotes the existence of some mesopores (i.e. pores of diameters between 2 nm and 50 nm) and macropores (i.e. pores of diameters above 50 nm). Nevertheless, at the same relative pressure, very big differences are observed in the volume of N_2 adsorbed by the different materials, indicating significant differences in their porosity. The Brunauer-Emmet-Teller (BET) model was applied to calculate the specific surface area of the materials. Large BET surface areas of 420 m^2/g were obtained for carbon blank xerogel material. However, this value decreased to 200

m^2/g for $(\text{Bi-C})_{\text{IM}}$ and $120 \text{ m}^2/\text{g}$ for $(\text{Bi-C})_{\text{CS-L}}$. This means that the presence of Bi nanoparticles remarkably reduced the porosity of the carbon xerogel. The reason for this decrease in surface area is probably associated to the lower initial pH of Bi(III) containing sol, which has a decisive influence in the final gel structure [7]. The absence of NH_4OH lowered the pH of the initial sol, and caused a further decrease of the surface area of sample M- $(\text{Bi-C})_{\text{CS}}$ to $71.5 \text{ m}^2\cdot\text{g}^{-1}$.

3.3.3. Bismuth Nanoparticle Chemical Structure

It is well known that Bi is easily oxidized, forming native oxide layers once it comes into contact with air. The crystal structure (crystalline properties) of Bi nanoparticle as well as carbon matrix were studied by X-ray diffraction in the 2θ range of $10\text{-}70^\circ$, using a Siemens diffractometer (CuK α radiation). The chemical composition of the surface of Bi nanoparticles was determined by X-ray photoelectron spectroscopy (XPS) (Kratos analytical spectrometer) using $\text{AlK}\alpha$ X-rays source. Also, Z-contrast imaging of Bi nanoparticles was performed on a Tecnai F20 HRTEM/STEM. For TEM observations, a thin lamella of the nanocomposite was embedded into an epoxy matrix and then cut into a film of an electron transparent thickness in frozen state using a freezing microtome.

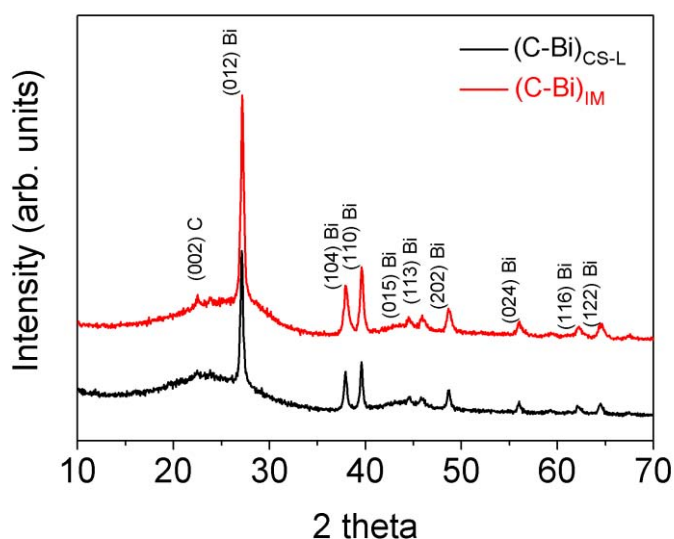


Figure 3.7. XRD pattern of the $(\text{Bi-C})_{\text{CS-L}}$ and $(\text{Bi-C})_{\text{IM}}$ composite

Figure 3.7 compares the XRD patterns of $(\text{Bi-C})_{\text{CS-L}}$ and $(\text{Bi-C})_{\text{IM}}$ nanocomposites. No differences in the crystal structure were observed between samples prepared through impregnation and co-synthesis approaches. The patterns show the

presence of an important background with broad bumps at $2\theta \sim 25^\circ$ originating from the scattering of amorphous carbon whereas all the diffraction peaks could be indexed with the structure of rhombohedral Bi (ICSD PDF 044-1246) [8].

Figure 3.8 shows the Bi 4f XPS spectrum of $(\text{Bi-C})_{\text{IM}}$. The observed peaks correspond to Bi $4f_{7/2}$ and Bi $4f_{5/2}$ at around 159 eV and 164.5 eV, respectively, these being characteristic energies of Bi(III) in the form of Bi_2O_3 [9]. No trace of a photoelectron signal characteristic of metallic Bi is observed (Bi $4f_{7/2}$ and Bi $4f_{5/2}$ peaks at 156.7 and 162 eV, respectively). This observation indicates that the surface of Bi nanoparticles is covered by an oxide layer. The sampling depth ($3\lambda_e$) in XPS was taken to estimate the thickness of the native oxide layer. λ_e is the inelastic mean free path of a photoelectron from AlK_α radiation and the estimated oxide layer thickness is above 3 nm. This oxide outer layer on Bi nanoparticle is probably caused by spontaneous surface passivation once the sample comes into contact with air.

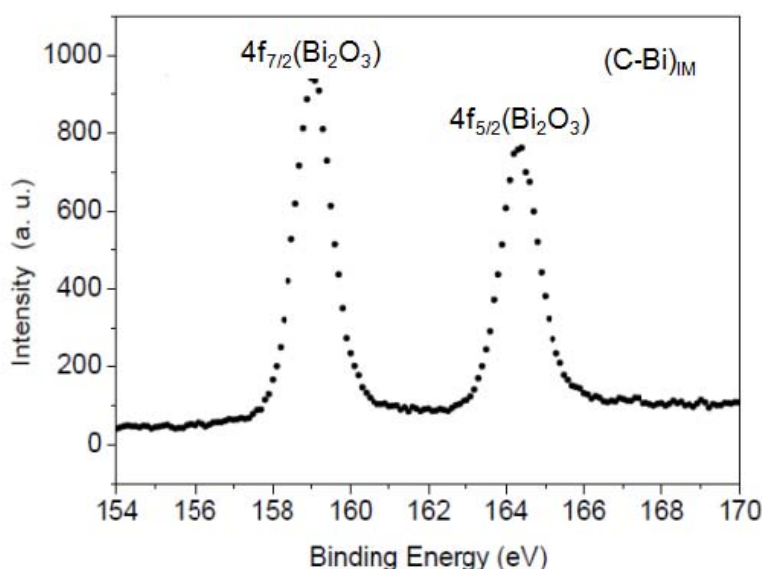


Figure 3.8. Bi 4f XPS spectrum of $(\text{Bi-C})_{\text{IM}}$

The core-shell nature of the Bi nanoparticles in the nanocomposite was also confirmed by Z-contrast imaging in a STEM mode using a high angle annular dark field detector. In this imaging mode, differences in density are visualized as differences in brightness. Figure 3.9 shows the TEM image and it is clearly observed that a less dense shell, corresponding to Bi oxide, surrounds the nanoparticle core.

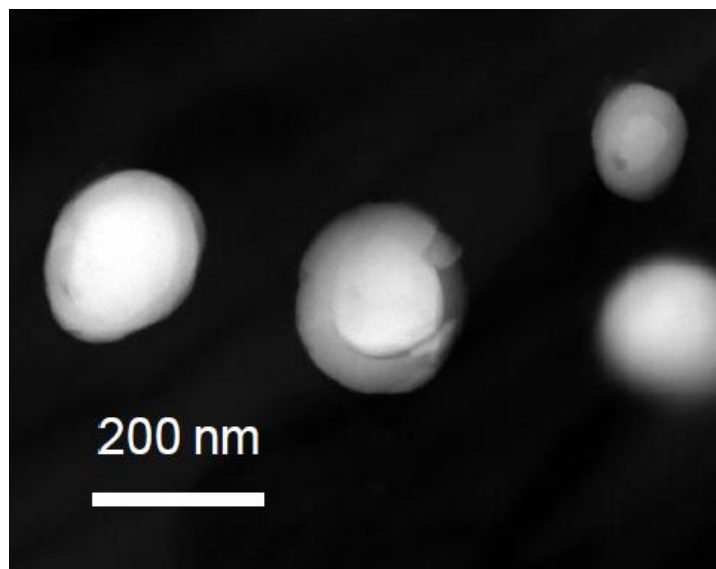


Figure 3.9. Z-contrast TEM image of Bi nanoparticles in $(\text{Bi-C})_{\text{CS-L}}$ composite

3.4. Conclusion

Based on resorcinol/formaldehyde sol-gel chemistry, we have synthesized composites of porous carbon containing bismuth nanoparticles both by impregnation and co-synthesis procedures. The co-synthesis route brought about nanocomposites with homogeneous dispersion of bismuth nanoparticles in the carbon matrix. Higher bismuth content leads to the formation of bigger nanoparticles. Furthermore, it is found that the surface of bismuth nanoparticles is oxidized. The electrochemical performances of these nanocomposites for the analysis of heavy metals are going to be presented in the following chapters using carbon paste electrode and screen printed electrode configurations.

References

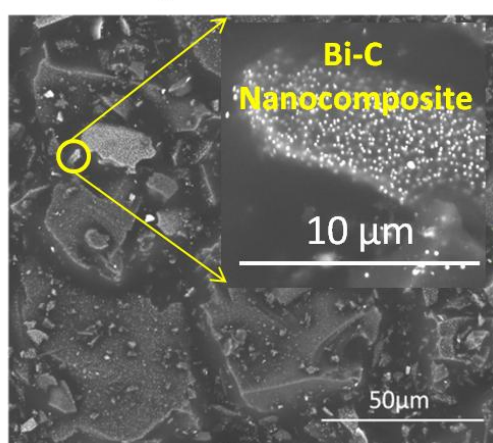
- [1] Norman NC. Chemistry of Arsenic, Antimony and Bismuth: Springer Netherlands; 1998.
- [2] Miersch L, Ruffer T, Schlesinger M, Lang H, Mehring M. Hydrolysis Studies on Bismuth Nitrate: Synthesis and Crystallization of Four Novel Polynuclear Basic Bismuth Nitrates. *Inorganic Chemistry*. 2012;51:9376-9384.
- [3] Elkhatat AM, Al-Muhtaseb SA. Advances in Tailoring Resorcinol-Formaldehyde Organic and Carbon Gels. *Advanced Materials*. 2011;23:2887-2903.
- [4] Pekala RW. Organic Aerogels from the Polycondensation of Resorcinol with Formaldehyde. *Journal of Materials Science*. 1989;24:3221-3227.

- [5] Chick LA, Pederson LR, Maupin GD, Bates JL, Thomas LE, Exarhos GJ. Glycine-Nitrate Combustion Synthesis of Oxide Ceramic Powders. *Materials Letters*. 1990;10:6-12.
- [6] Schneider CA, Rasband WS, Eliceiri KW. NIH Image to ImageJ: 25 years of Image Analysis. *Natural Methods*. 2012;9:671-675.
- [7] Lin C, Ritter JA. Effect of Synthesis pH on the Structure of Carbon Xerogels. *Carbon*. 1997;35:1271-1278.
- [8] Zhao Y, Zhang Z, Dang H. A Simple Way to Prepare Bismuth Nanoparticles. *Materials Letters*. 2004;58:790-793.
- [9] Dharmadhikari VS, Sainkar SR, Badrinarayan S, Goswami A. Characterisation of Thin-films of Bismuth Oxide by X-ray Photoelectron Spectroscopy. *Journal of Electron Spectroscopy and Related Phenomena*. 1982;25:181-189.

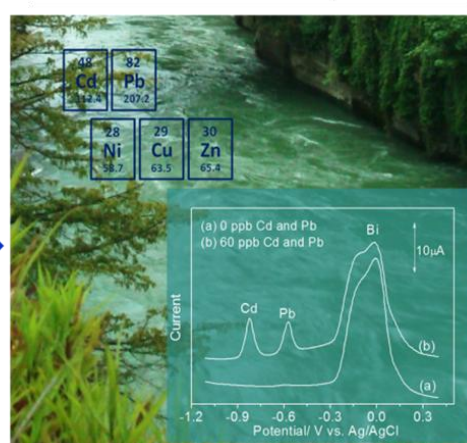
Chapter 4

Electroanalytical Assessment of Bismuth-Carbon Nanocomposite Materials: Detection of Heavy Metals in Waters

Bismuth-Carbon
Nanocomposite Paste Electrode



Electrochemical
Detection of Heavy Metals



Summary

In this Chapter, it is reported how the bismuth/carbon nanocomposite powders prepared by sol-gel were applied to the fabrication of bismuth/carbon nanocomposite paste electrodes (Bi-C CPEs). Electrochemical detection of heavy metals, including Zn(II), Cd(II), Pb(II), Ni(II) and Cu(II), using these nanocomposite based paste electrodes was thoroughly studied both in standard solutions and real water samples.

The work presented in this chapter has been included in one paper entitled “Electroanalytical assessment of heavy metals in waters with bismuth nanoparticle-porous carbon paste electrodes”, by Pengfei Niu, César Fernández-Sánchez, Martí Gich, Carlos Ayora, and Anna Roig, *Electrochemical Acta*, 2015, 165, p 155-161.

4.1. General Introduction to Bi-C CPEs

4.1.1. Fabrication of Electrodes

The preparation of nanocomposite paste electrodes is as follows:

1 g of nanocomposite powder was thoroughly mixed in a mortar with 0.4 ml spectroscopic grade paraffin liquid (Uvasol® from Merck) to produce a paste. This paste was then packed into one end of a 3 mm inner diameter Teflon body which included a 3-mm diameter stainless steel rod to make the electrical contact (as shown in Figure 4.1). The filled paste was polished on a sheet of white paper before each measurement to obtain a smooth electrode surface.

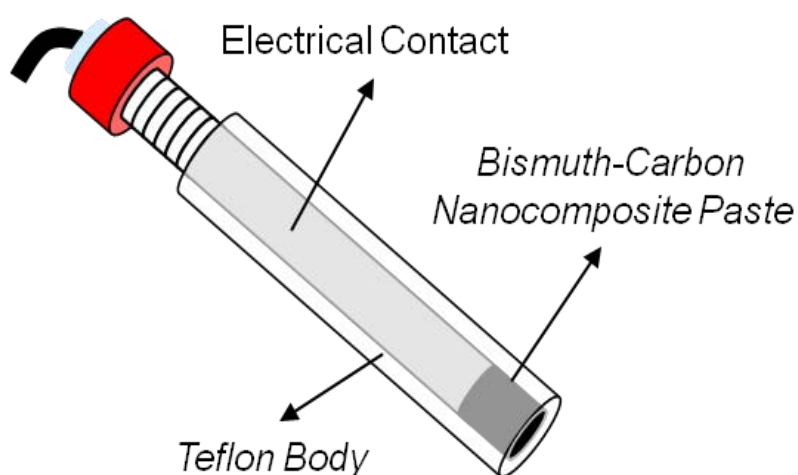


Figure 4.1. Drawing of bismuth/carbon nanocomposite paste working electrode

The Bi-C CPE was implemented in a conventional three-electrode electrochemical cell, which also included a platinum counter electrode and a Ag/AgCl reference electrode (both from Metrohm AG). The three electrodes were immersed in a 10 mL plastic cell. All measurements were carried out at room temperature using an Autolab PGSTAT30 potentiostat (Ecochemie, Netherlands) controlled by GPES software version 4.3. Square wave anodic or cathodic stripping voltammetric techniques (SWASV and SWCSV, respectively) were applied for the detection of heavy metals. Specifically, SWASV was applied to the analysis of Zn(II), Cd(II), Pb(II), and Cu(II), while SWCSV was used for the analysis of Ni(II). The selected square wave parameters were 20Hz frequency, 25mV amplitude and 5mV step potential.

The supporting electrolyte for Zn(II), Cd(II), Pb(II) and Cu(II) was a 0.1 M acetate

buffer solution pH 4.5, unless stated otherwise, whereas a 0.1 M ammonia buffer solution pH 9.2 containing 0.1 mM dimethylglyoxime (DMG) chelating agent was used for Ni(II) analysis. An accumulation step was applied by setting the working electrode at a constant potential for a pre-determined time, while the solution was kept under vigorous magnetic stirring, during this accumulation step. Thus, Zn(II), Cd(II) and Pb(II) were electrochemically reduced and alloyed with Bi whereas Ni(II)-DMG was adsorbed on the surface of the Bi nanoparticles. In the case of Cu(II) analysis, this species was reduced and accumulated on the surface of carbon xerogel electrode without Bi. Afterwards, stirring was stopped. Following a 20 s equilibration step, a potential scan was carried out to strip the heavy metals from the electrode surface and thus produced the corresponding electrochemical signals.

4.1.2. Stripping Voltammetric Signals of Bi Using Bi-C CPEs

From the discussion in Chapter 3, we know that the surface of Bi nanoparticles is covered by an oxide layer. Therefore, an electrochemical reduction step may be required to reduce this oxide layer and thus activate the Bi nanoparticles surface for the accumulation of heavy metals. This step could be implemented by applying a reduction step taking place at a suitable cathodic potential.

Figure 4.2 (A) presents the stripping signals of Bi-C CPE after electrochemical activation at -1.4 V (vs. Ag/AgCl) for different time periods. No stripping signal of Bi is observed before activation, once again indicating the presence of the oxide shell on the Bi nanoparticles. However, the Bi signals are increasingly higher when an electrochemical activation at -1.4 V was carried out for longer time periods. Not only the time, but also the applied potential plays an important role in the activation of Bi nanoparticles. As shown in Figure 4.2 (B), the Bi stripping signals are smaller when the activation potential is larger than -1.0 V, probably because of a non-completed reduction of the oxide shell.

It should be mentioned that the oxide layer on the surface of Bi nanoparticles did not affect the analytical performance of these bismuth/carbon nanocomposites towards the determination of Zn(II), Cd(II) and Pb(II), since its reduction can be concomitantly carried out when these heavy metals are reduced and accumulated on the Bi nanoparticle surface. Using an accumulation potential of -1.4 V vs. Ag/AgCl

not only reduces the oxide layer to Bi, but also effectively reduces the metals ions to produce an alloy with Bi. However, regarding the Ni(II) detection, Ni(II)-DMG complex is adsorbed at a less negative potential, at which the activation of the Bi nanoparticles does not effectively take place. Consequently, an additional step to activate the Bi nanoparticles is required in this case.

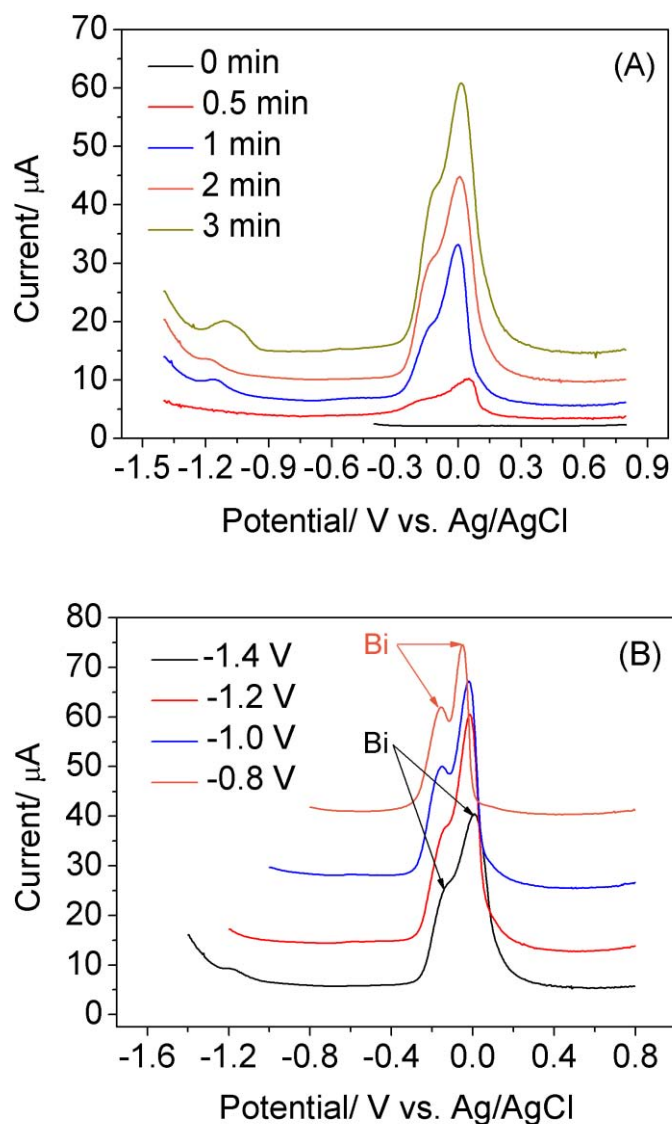


Figure 4.2. SWASV signals recorded with the Bi-C nanocomposite paste electrodes in 0.1 M acetate buffer solutions pH 4.5 after different reduction times at a set potential of -1.4 V (A) and after reduction for 2 min at different potentials (B).

The stripping process of electrodeposited Bi film electrodes in 0.1 M acetate buffer pH 4.5 results in a single sharp peak ascribed to the oxidation of Bi^0 to Bi(III) [1]. However, two Bi stripping peaks were recorded in this work (Figure 4.2). Previous reports of sensing devices based on Bi [2] and Bi_2O_3 [3] nanoparticles did not show

the oxidation peak of Bi and we could not find studies about the electrochemical oxidation of Bi nanoparticles in slightly acidic media like the one used in this work. However, related studies on the oxidation of Bi in alkaline solutions presented two anodic peaks ascribed to Bi(III) oxide and hydroxide species [4]. Also, the electrochemical oxidation in strong acidic solution displays the formation of different Bi(III) species also giving rise to two anodic peaks [5]. These studies may also explain the two peaks observed in our work.

4.1.3. Preliminary Studies on the Performance of the Bi-C CPEs for Heavy Metal Analysis: Reusability of the Electrode

Figure 4.3 shows the stripping voltammetric signals recorded in a solution containing 50 ppb Zn(II), Cd(II) and Pb(II) after 3 min accumulation at -1.4 V. Three peaks at -1.11, -0.80 and -0.56 V are clearly shown that can be ascribed to the stripping of Zn, Cd, and Pb, respectively. This demonstrates the possibility of using these electrodes for detecting such heavy metals.

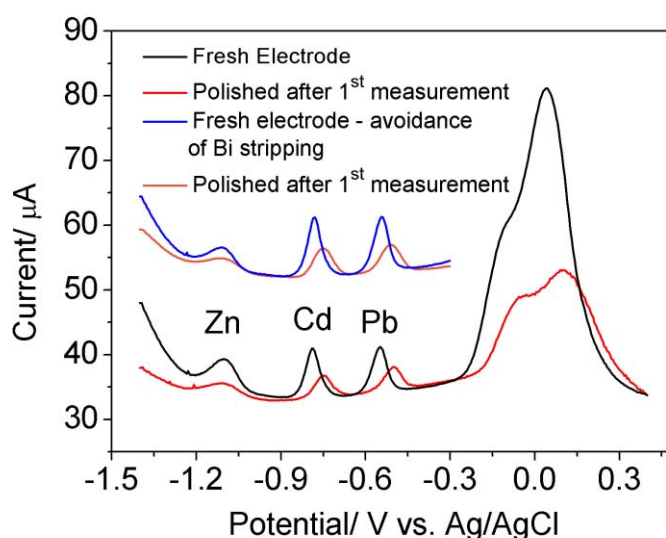


Figure 4.3. SWASV signals recorded consecutively in a 0.1 acetate buffer solution pH 4.5, containing 50 ppb Pb(II), Cd(II), and Zn(II) using freshly prepared and polished CPEs. Voltammetric signals recorded in two different potential windows so that the Bi stripping signal was or was not recorded. Accumulation was carried out at -1.4 V for 3 min. An offset was applied to some of the voltammograms in order to better compare them.

Generally, the surface of carbon paste electrodes can be renewed by mechanical polishing on a white paper sheet following each measurement. However, since the

electrode material studied in this work is porous, it soaks up water and therefore after one measurement, the whole paste inside the Teflon body is wet. Indeed, we found that renewing the electrode by mechanical polishing did not result in a fresh electrode surface and this fact could affect the reproducibility of the electrode signal. Figure 4.3 shows that, even by narrowing the potential window to that at which the heavy metal stripping process took place but avoided the oxidation of Bi, the recorded signals were still not reproducible if the electrode surface was just renewed by mechanical polishing. Therefore, in this Thesis, Bi-C CPEs were systematically renewed by packing a fresh paste after each measurement.

4.2. Effect of the Material Synthesis Process on the Electrode Performance

4.2.1. Effect of the Applied Material Synthesis Route

Figure 4.4 shows typical voltammograms for the detection of 0 and 50 ppb Zn(II), Cd(II) and Pb(II) at Bi-C CPEs made using materials prepared by impregnation (IM) and co-synthesis (CS). Both of them can be used to detect heavy metals. However, the stripping peak intensities obtained from the electrode prepared with the (Bi-C)_{CS-L} nanocomposite are slightly larger than the ones obtained with the electrodes based on the (Bi-C)_{IM} nanocomposite which even contains a higher amount of Bi. This appears to be related to a more inhomogeneous Bi distribution in (Bi-C)_{IM} composite, as discussed in Chapter 3.

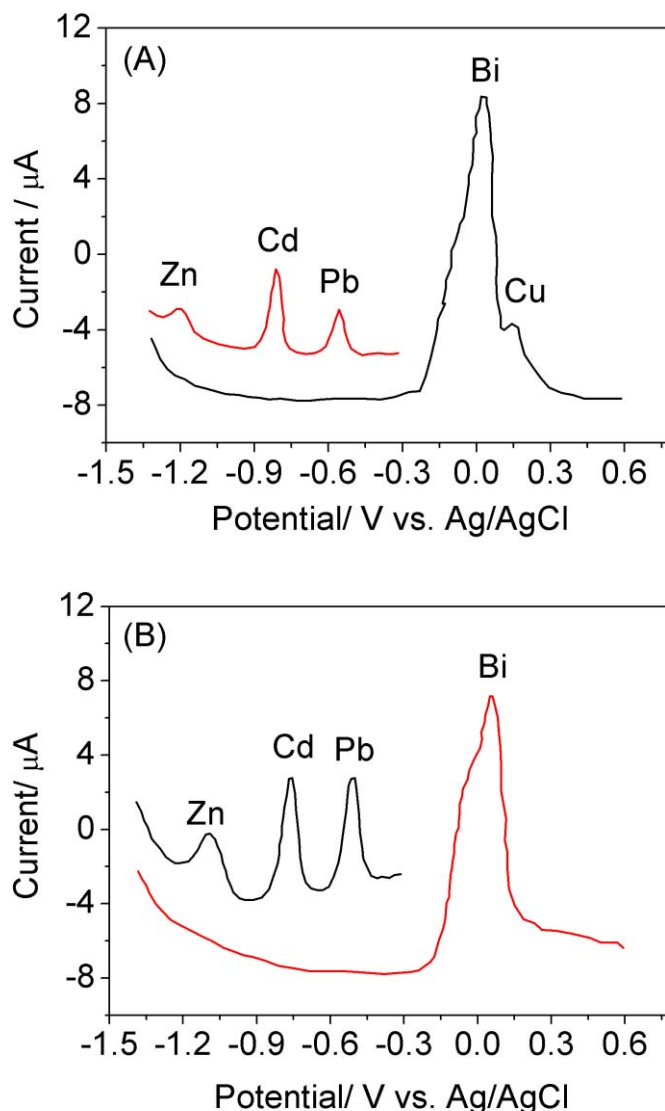


Figure 4.4. SWASV signals recorded in 0.1 M acetate buffer solution pH 4.5 containing 0 and 50 ppb of Zn(II), Cd(II) and Pb(II) at Bi-C CPEs made with $(\text{Bi-C})_{\text{IM}}$ (A) and $(\text{Bi-C})_{\text{CS-L}}$ (B) materials, after accumulation at -1.4 V for 2 min.

In addition, we also recorded the cyclic voltammograms in 0.1 M KNO_3 solutions containing 1mM ferri/ferrocyanide electroactive species using $(\text{Bi-C})_{\text{CS-L}}$ and $(\text{Bi-C})_{\text{IM}}$ CPEs (Figure 4.5). It is known that the peak current is proportional to the active area of the electrode. Smaller peak currents recorded with $(\text{Bi-C})_{\text{IM}}$ CPE could directly be associated to a smaller electrochemical active area of this material.

Because of the increased complexity of the impregnation process, requiring additional preparative steps, as well as the worse electrochemical performance of the resulting material, $(\text{Bi-C})_{\text{CS}}$ materials were chosen for all further measurements. Nevertheless, the impregnation approach could be useful for preparing porous

carbon materials containing other metal nanoparticles when all the precursors cannot be dissolved in the same solvent or when the gelification process produces the segregation of one of the components from the gel matrix.

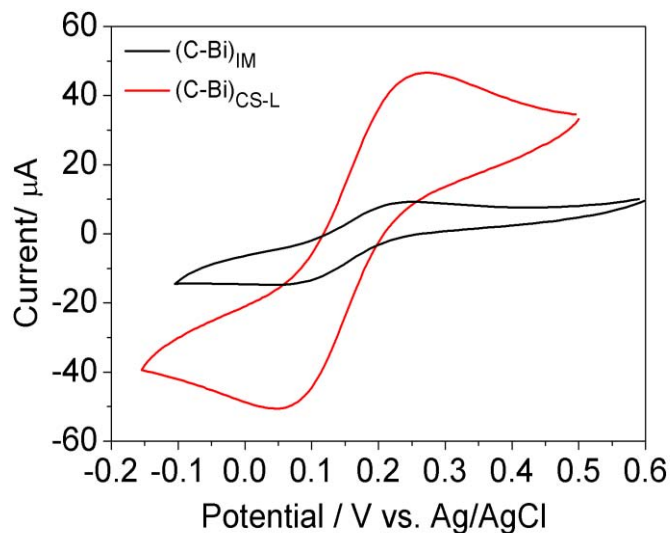


Figure 4.5. Cyclic voltammograms recorded with Bi-C CPEs fabricated with $(\text{Bi-C})_{\text{IM}}$ and $(\text{Bi-C})_{\text{CS-L}}$ in a 0.1 M KNO_3 solution containing 1 mM ferri-/ferrocyanide. Scan rate: 50 mV/s

4.2.2. Effect of Bi Content

Using $(\text{Bi-C})_{\text{CS}}$ materials prepared following the co-synthesis path A (please refer to Chapter 3), we studied the influence of Bi content on the analytical performance of the resulting electrodes. Figure 4.6 shows the voltammograms recorded under the same experimental conditions using materials with different amount of Bi. It can be seen that the 4-fold increase in the Bi amount results in an increased charge transfer related to the oxidation of the Bi nanoparticles (area under the Bi peaks) also by about 4-fold. It was anticipated that the peak current intensities of the heavy metals would be proportional to the Bi amount of the different materials. However, these only increased by around 2-fold. The reason for that is related to the fact that increasing the Bi concentration did not just result in an increase in the number of Bi nanoparticles having the same size but also brought about larger particles as presented in Chapter 3. Figure 4.6 (A) also shows the voltammogram recorded using a carbon xerogel material without Bi. Only very small peaks of Cd(II) and Pb(II) are visible in this case, indicating that the heavy metal signals recorded at Bi-containing electrodes are directly related to the presence of Bi nanoparticles.

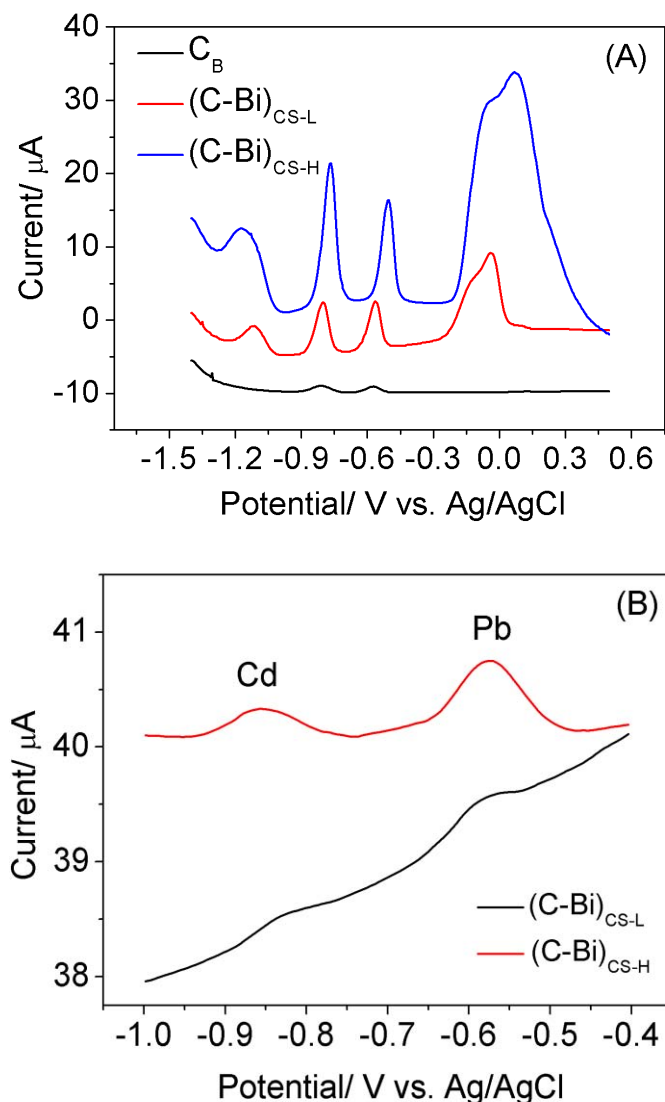


Figure 4.6. SWASV signals recorded with Bi-C CPEs made with materials containing 0 wt% Bi (C_B), 4 wt% Bi (CS-L) and 16 wt% Bi (CS-H) in 0.1 M acetate solutions pH 4.5, (A) with 50 ppb Zn(II), Cd(II) and Pb(II), after accumulation at -1.4 V for 2 min; (B) with 1 ppb Cd(II) and Pb(II) after accumulation at -1.4 V for 3 min

The enhancement of electrode responses, using materials with higher amount of Bi, also has a direct influence on the limits of detection that could be achieved. Figure 4.6 (B) shows the SWASV signals recorded in a solution with only 1 ppb of Cd(II) and Pb(II). The larger signals recorded with the $(\text{Bi-C})_{\text{CS-H}}$ material evidence that higher amounts of Bi are more convenient for the determination of such low concentrations of these pollutants. Therefore, the limits of detection of these devices can be improved by increasing the amount of Bi in the nanocomposite. Using electrodes made with the material of $(\text{Bi-C})_{\text{CS-H}}$ nanocomposite, the minimum concentration that was readily measured was 0.6 ppb for both Cd(II) and Pb(II) after

3 min accumulation (Figure 4.7). These values are considerably lower than those recorded with most of the already reported Bi-based sensor devices [3, 6, 7].

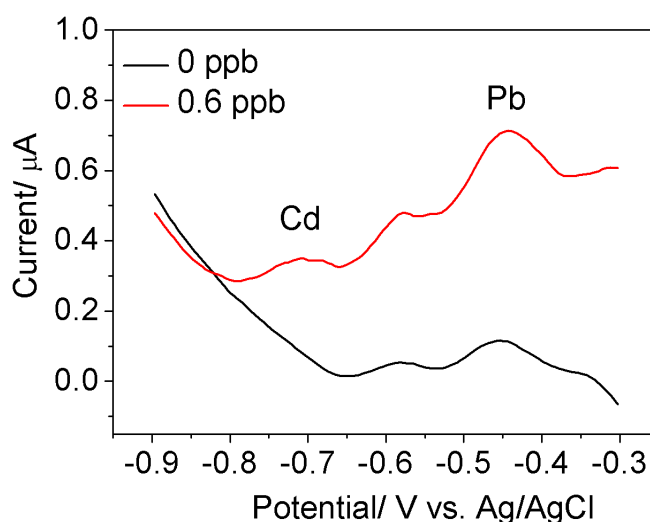


Figure 4.7. SWASV signals recorded in 0.1 M acetate buffer solution pH 4.5 containing 0 and 0.6 ppb Pb(II) and Cd(II) using $(\text{Bi-C})_{\text{CS-H}}$ nanocomposite based electrodes, accumulation at -1.4 V for 3 min.

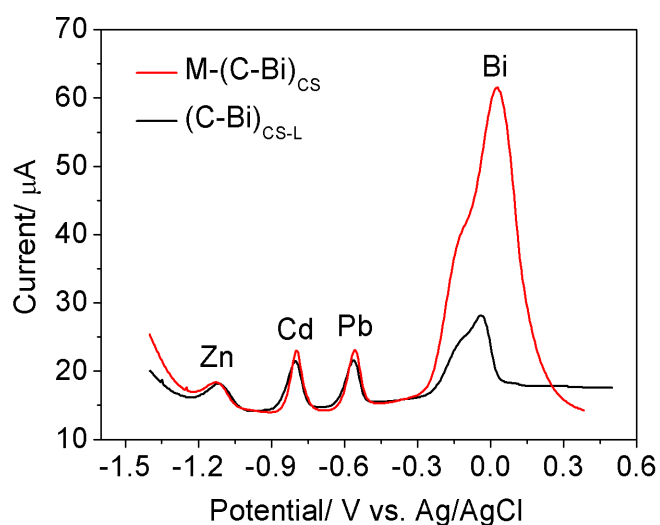


Figure 4.8. SWASV signals recorded at Bi-C CPEs made with $(\text{Bi-C})_{\text{CS-L}}$ and $\text{M}-(\text{Bi-C})_{\text{CS}}$ in 0.1 M acetate solution pH 4.5 containing 50 ppb Zn(II), Cd(II) and Pb(II) after accumulation at -1.4 V for 2 min

Since these porous nanocomposites show high sensitivity towards the detection of heavy metals, a thorough study about the material analytical performance and practical application was performed. Taking into account a more simple synthesis procedure that was named path B co-synthesis approach in Chapter 3, $\text{M}-(\text{Bi-C})_{\text{CS}}$

was selected for the fabrication of Bi-C CPEs. Figure 4.8 shows typical SWASV signals of 50 ppb Zn(II), Cd(II) and Pb(II) recorded with M-(Bi-C)_{CS} (6wt. % Bi) and (Bi-C)_{CS-L} (4wt. % Bi) based CPEs. It confirms that M-(Bi-C)_{CS} and (Bi-C)_{CS} offer comparable responses towards heavy metal determination. So, in the following section, M-(Bi-C)_{CS} was employed as the electrode material.

4.3. Analytical Performance of Bi-C CPEs

Calibration curves for each heavy metal were constructed by plotting the stripping peak currents against the corresponding metal concentration. The simultaneous detection of Zn(II), Cd(II) and Pb(II) is possible, as shown in Figure 4.8. However, as it will be discussed in detail below, the calibration for Zn(II) using this sensor approach proved to be difficult. Therefore, in this Thesis, Cd(II) and Pb(II) were calibrated simultaneously whereas Zn(II) was calibrated individually in acetate buffer standard solutions. Ni(II) was analyzed in 0.1 M ammonia buffer solutions pH 9.2 containing 0.1 mM DMG chelating agent. In addition, since the stripping peak of Cu appears at a potential very similar to that of Bi, resulting in an overlap of both Cu and Bi signals, Cu(II) was analyzed using a carbon xerogel material without Bi. Each point in all the calibration curves was the mean of three measurements with the error bars showing the corresponding standard deviation.

4.3.1. Pb(II) and Cd(II) Detection

Figure 4.9 (A) shows an example of the SWASV signals recorded for the determination of Pb(II) and Cd(II) in a concentration range from 1 ppb to 100 ppb after 3 min accumulation. Two peaks at around -0.8 V and -0.5 V are clearly visible and are ascribed to Cd(II) and Pb(II) stripping processes, respectively.

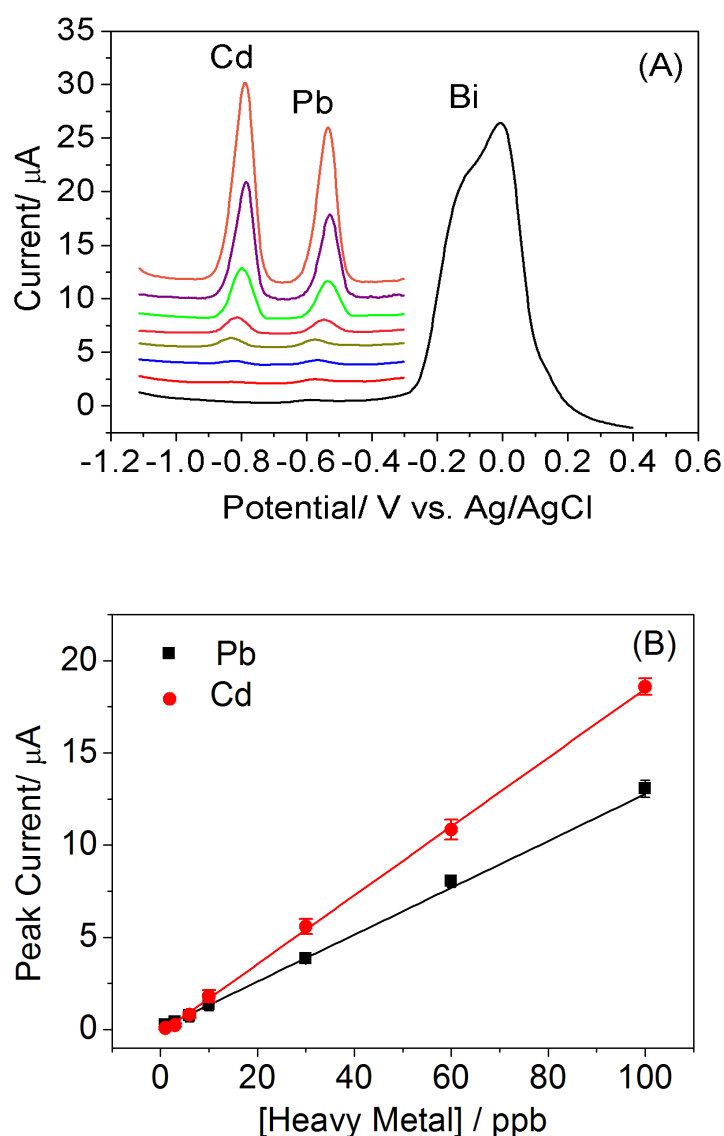


Figure 4.9. (A) SWASV signals recorded in standard 0.1M acetic buffer solutions pH 4.5 containing different concentrations of Pb(II) and Cd(II) (from bottom to top signals: 0, 1, 3, 6, 10, 30, 60 and 100 ppb), and (B) the corresponding calibration curves. Electrodeposition at -1.4 V for 3 min and potential scanned from -1.4 V to +0.8 V. The potential windows of the different voltammograms shown in the figure were cut and an offset was applied to them for clarity of presentation.

The corresponding calibration curves shown in Figure 4.9 (B) are linear in the whole concentration range tested. The limit of detection (LOD) was calculated according to the formula: $\text{LOD} = 3 (\text{SD}/S)$, where SD is the standard deviation of the 3 intercepts obtained from 3 different calibration curves and S is the mean of the corresponding slopes. The calculated LOD values are 0.65 ppb and 0.81 ppb for Pb(II) and Cd(II), respectively. These values are lower than those previously reported on Bi film based electrodes [8], a Bi powder modified carbon paste electrode [6], and a Bi

nanoparticle modified screen printed carbon electrode [7], using similar or longer accumulation times. Among previously reported Bi nanoparticle based electrodes, Malakhora et al. [9] achieved similar values (0.55 ppb for Pb(II) and 0.40 ppb for Cd(II)) using a 180 s accumulation time. Lee et al. [2] reported the lowest LOD of 0.07 ppb and 0.15 ppb for Pb(II) and Cd(II), respectively, but using an accumulation time of 600 s. However, in comparison with our proposed sol-gel approach, these reported systems have the drawback of using complex electrode fabrication procedures. Moreover, as it is mentioned in the previous section, it should be noted that the LODs of this proposed Bi-C CPEs could be improved by increasing the Bi content in the nanocomposites, which can be easily achieved by adding more $\text{Bi}(\text{NO}_3)_3$ in the initial sol preparation stage.

4.3.2. Zn(II) Detection

The Bi-C CPEs were also applied to the detection of Zn(II). However, this proved to be unsuccessful. Several experimental conditions that could negatively influence these measurements were studied. Among them, the presence of Cu(II) in the nanocomposite material, introduced as an impurity of the $\text{Bi}(\text{NO}_3)_3$ reagent during the synthesis process, could interfere in the accurate measurement of Zn(II), since Cu(II) appears to form an intermetallic compound with Zn(II). It has been previously reported that Ga(III) preferentially forms an intermetallic with Cu(II) [10]. In order to avoid this interference, 2000 ppb Ga(III) were added to the acetate buffer solution, following a previously reported approach that described the successful detection of Zn(II) in the presence of Cu(II) [10]. Figure 4.10 shows the voltammetric signals recorded in the absence and presence of Ga(III). It can be observed how the Zn(II) signal is greatly enhanced when Ga(III) is present in solution. The voltammograms in Figure 4.4 and Figure 4.6 show that Zn (II) could be measured in the same buffer solution together with Pb(II) and Cd(II) when Ga(III) was not present in solution. However, it is clear from Figure 4.10 that the simultaneous detection of Zn(II), Cd(II) and Pb(II) is not possible with the presence of Ga(III) in the solution because the stripping peak of Ga(III) overlaps that of Cd(II). Thus, the Zn(II) detection was attempted separately.

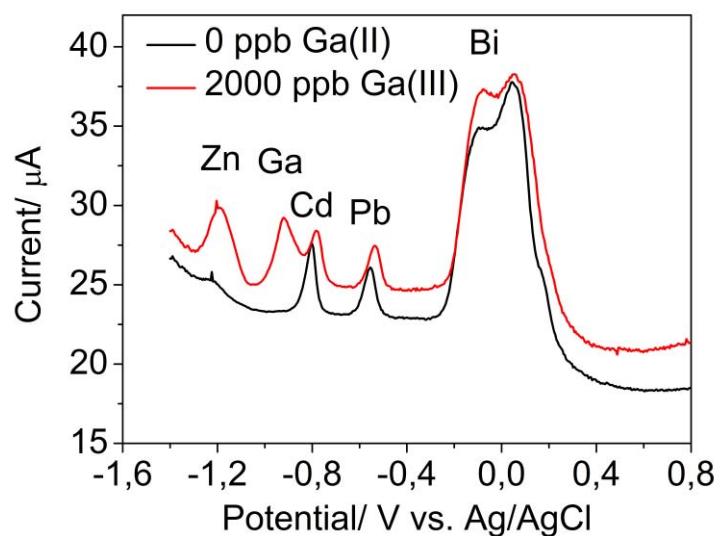


Figure 4.10. SWASV signals for simultaneous detection of 5 ppb Zn(II), and 50 ppb Cd(II), Pb(II) with or without the presence of 2000 ppb Ga(III) in 0.1 M acetate buffer solution pH 4.5. Accumulation at -1.4V for 3 min.

Figure 4.11 (A) shows the SWASV signals recorded in acetate buffer solutions containing different concentrations of Zn(II). Three peaks are clearly visible at around -1.15, -1.05 and -0.93 V, with the first one being ascribed to the stripping of Zn and the other two being related to the stripping of Ga, respectively. The three calibration curves shown in Figure 4.11 (B) were recorded in different moments within the same day and reflect the lack of stability of the Zn analyses. Zn calibration curves were repeated in triplicate more than 10 times during different days, and in all cases, they show such dispersion, with the sensor sensitivity varying within about 0.5 orders of magnitude. However, linear ranges between 1 ppb and 20 ppb were always observed. Different studies were carried out to ascertain such lack of signal stability. It can be seen in the voltammograms of Figure 4.10 (A) that the Zn signal appears at potentials close to the low limit of the sensor potential window and one can vary this value by changing the pH of the buffer solution. Thus, analyses were carried out in buffer solutions with pH values ranging from 3.5 to 5.5. However, no improvement was achieved in the analysis of this heavy metal. Nevertheless, it is worth mentioning that the electrochemical sensor unambiguously detected Zn(II) at concentrations down to 1 ppb and could be used as an alarm analytical device for this pollutant.

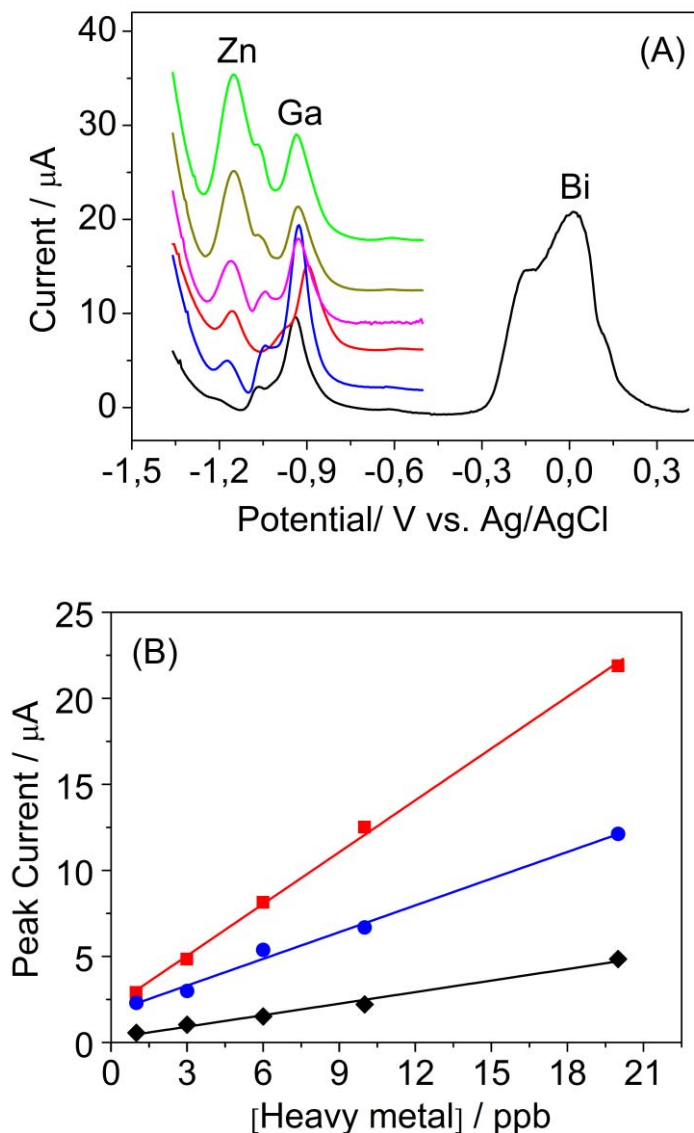
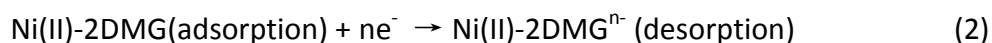


Figure 4.11. (A) SWASV signals recorded in standard 0.1 M acetate buffer solutions pH 4.5 containing different concentrations of Zn(II) (from bottom to top signals: 0, 1, 3, 6, 10, and 20 ppb) and 2000ppb Ga(III). Electrodeposition at -1.4 V for 3min and potential scanned from -1.4 V to +0.4 V. The potential windows of the different voltammograms shown in the figure were cut for clarity of presentation. (B) Calibration curves carried out three times in one day.

4.3.3. Ni(II) Detection

The Bi-C CPEs sensor was also applied to the detection of Ni(II) by SWCSV in an 0.1 M ammonia buffer solution pH 9.2, containing 0.1 mM DMG as a chelating agent for this heavy metal. As proposed by Ma et al. [11], the mechanism for the adsorption and cathodic stripping voltammetry of Ni(II)-2DMG complexes can be explained as follows:



Herein, the accumulation step was firstly carried out at -0.8 V for 180 s, at which the corresponding Ni(II)-DMG complex was adsorbed onto the electrode surface (Equation 1). After adsorption, the Ni(II)-DMG was reduced by applying a cathodic potential scan from -0.8 V to -1.4 V, inducing fast desorption of the Ni(II)-DMG complex from the electrode surface (Equation 2). In the reduction step, not only the DMG ligand but also some of the metal ions may also be reduced (Equation 3).



Hence, in order to guarantee a good reproducibility of the device response, fresh solutions were used for each measurement. Figure 4.12 shows the stripping voltammograms for different Ni(II) concentrations displaying a stripping cathodic peak at around -1.2 V. The absolute value of the stripping peak current increases linearly with the analyte concentration in a range from 10 ppb to 150 ppb (see Figure 4.12 (B)).

A LOD of 5.47 ppb according to the formula of $\text{LOD} = 3 (\text{SD}/\text{S})$ was obtained. This LOD value is much higher than those obtained using Bi films or Bi nanoparticle modified carbon electrodes prepared by two-step processes. For instance, Dal Borgo et al. [12] obtained a LOD of 0.027 ppb for Ni(II) using macro-porous bismuth modified screen printed carbon electrodes. Piankova et al. [13] reported a LOD of 0.2 ppb on screen printed carbon electrodes coated with Bi NPs. Nevertheless, the obtained LOD is still much lower than the recommended maximum allowable concentration following the EU-EQS standards of 34 ppb in drinking water and is therefore of practical use for the detection of Ni(II) in water samples, as will be shown below.

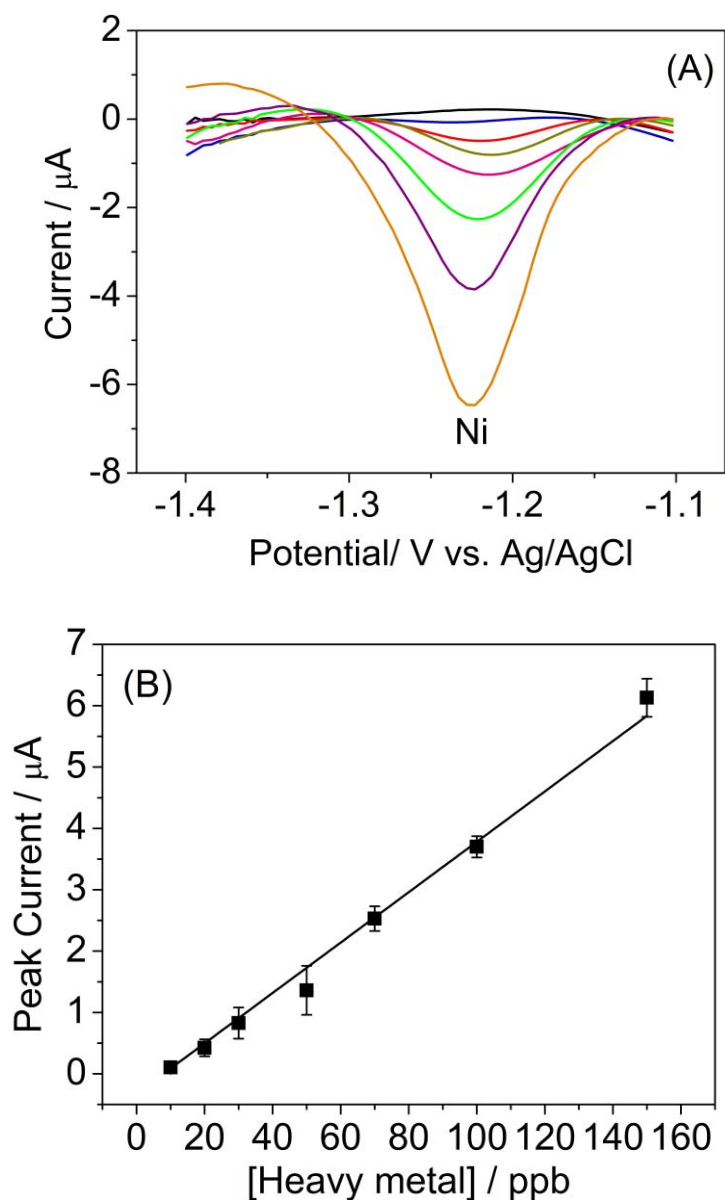


Figure 4.12. (A) SWCSV signals recorded in standard 0.1 M ammonia buffer solutions pH 9.2 containing different concentrations of Ni(II) (from top to bottom signals: 0, 10, 20, 30, 50, 70, 100, and 150 ppb) and 0.1 mM DMG (A). Activation at -1.4 V for 2 min followed by electrodeposition at -0.8 V for 3 min. The potential windows of the different voltammograms shown were cut for clarity of presentation. (B) Calibration curve. Each point represents the mean value of three replicates. The error bars are the corresponding standard deviation.

4.3.4. Cu(II) Detection with Porous Carbon Electrodes without Bi

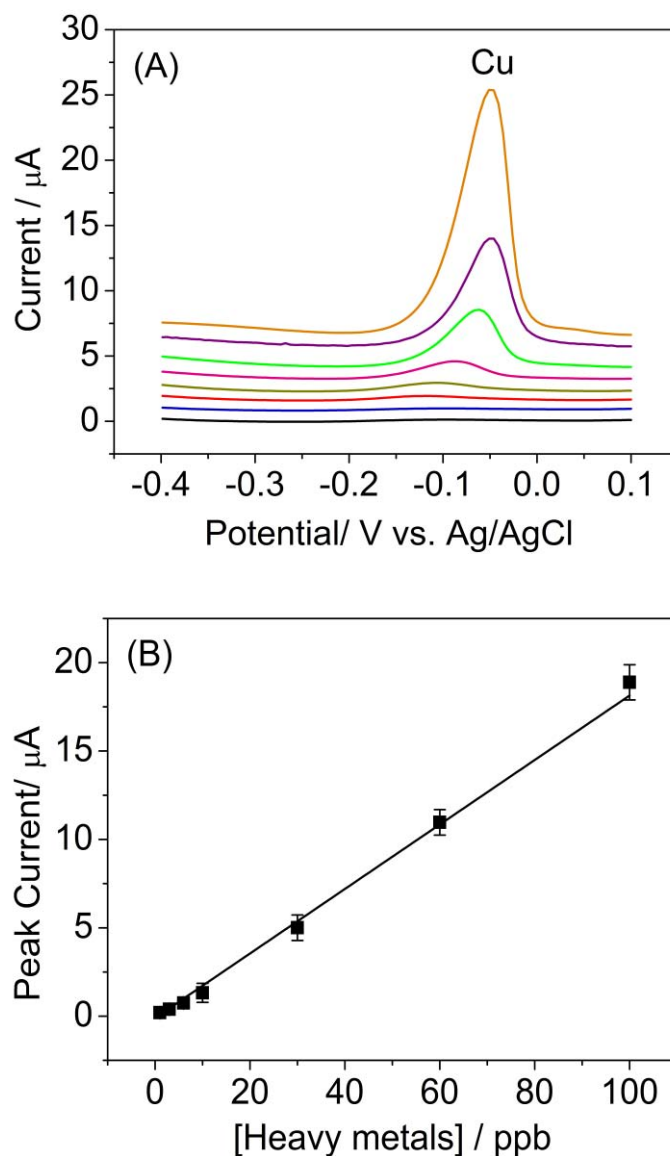


Figure 4.13. (A) SWASV signals recorded in standard 0.1 M acetate buffer solutions pH 4.5 containing different concentrations of Cu(II) (from bottom to top signals: 0, 1, 3, 6, 10, 30, 60 and 100 ppb). Accumulation was carried out at -0.7 V for 3 min. The potential windows of the different voltammograms shown were cut for clarity of presentation. (B) Calibration curve. Each point represents the mean value of three replicates. The error bars are the corresponding standard deviation.

Besides Pb(II), Cd(II), Zn(II) and Ni(II), herein the calibration curve for Cu(II) was also obtained using porous carbon materials synthesized by the same sol-gel process but without Bi. Figure 4.13 (A) shows the SWASV signals recorded in solutions containing Cu(II) in a concentration range from 1 ppb to 100 ppb after an accumulation step of 3 min at -0.7 V. The electrode response is linear in the whole

concentration range tested (Figure 4.13 (B)), and the LOD was calculated to be 0.65 ppb, with the same formula used for other heavy metals.

Table 4.1 Parameters of calibration curves plotted for different heavy metals

Heavy Metals	Linear Range (ppb)	Sensitivity ($\mu\text{A/ppb}$)	LOD (ppb)	Number of Points (n)	Correlation Coefficient (R)
Cd	1-100	0.19 \pm 0.04	0.81	7	0.997
Pb	1-100	0.13 \pm 0.02	0.65	7	0.999
Ni	10-150	0.04 \pm 0.01	5.47	7	0.993
Cu	1-100	0.19 \pm 0.02	0.65	7	0.999

Table 1 gathers all the analytical parameters extracted from the corresponding calibration curves for the four heavy metals (Pb(II), Cd(II), Ni(II) and Cu(II)) that were successfully tested. The obtained LODs for Pb(II), Cd(II) and Ni(II) are lower than the maximum allowable concentrations in surface waters set by European Union [14], the US Environmental Protection Agency [15] and the World Health Organization [16]. In addition, the nanocomposite material was obtained from a homogeneous bulk gel and the paste electrode was single use. Hence, good reproducibility of the electrochemical signals was obtained, indicated by the small relative standard deviations of the electrode responses for most of the heavy metals.

4.3.5. Interference Study

Before undertaking the analysis of real water samples, the effect on the electrochemical signal of possible interfering substances that may be present in water, should be considered. Apart from the organic matter, which has long been identified to mask to a certain degree the presence of heavy metals [17] and after carrying out a literature search, we studied the effect of two metal ions.

4.3.5.1. Cu(II) interference on the detection of Pb(II) and Cd(II)

From the chemical point of view, previous works on Bi film electrodes showed that one of the main interferents in the detection of Pb(II) and Cd(II) is Cu(II). For instance, Yang et al. [18] found that by adding Cu(II) at concentration levels 10 times higher than those of Pb(II) and Cd(II) would result in an approximately 70% and 90% decrease in the peak signals of Pb(II) and Cd(II), respectively. They report

that this effect was likely to be related to the formation of Cu(II)/Pb(II) and Cu(II)/Cd(II) intermetallic compounds and the deposition competition between Cu(II) and Cd(II), Pb(II) on the electrode surface. Jia et al. [19] found that even a Cu(II) concentration only doubling that of Cd(II) and Pb(II) would affect the determination of these pollutants on carbon nanotubes-polystyrene sulfonate (CNTs-PSS)/Bi composite film electrodes.

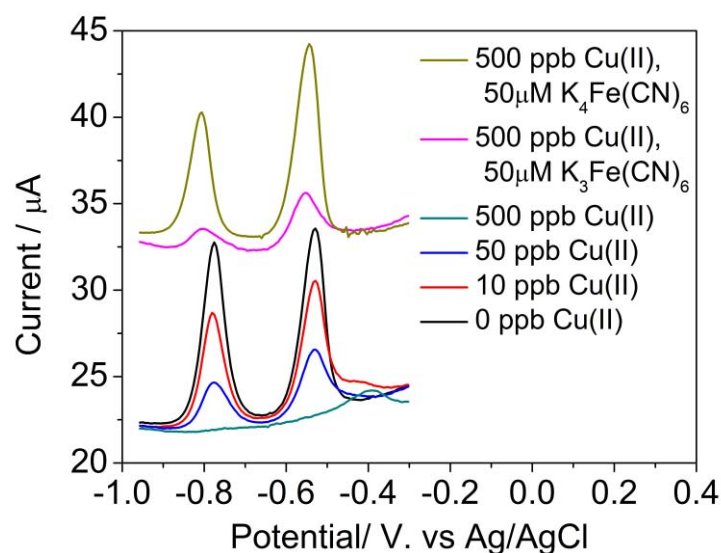


Figure 4.14. SWASV signals showing the Cu(II) interference on Pb(II) and Cd(II) and the effect of the addition of ferricyanide or ferrocyanide to reduce this interference. Accumulation at -1.4 V for 3 minutes in 0.1 M acetate buffer solution pH 4.5 containing 50 ppb Cd(II) and 50 ppb Pb(II). An offset was applied to some voltammograms for clarity of presentation.

Figure 4.14 displays the SWASV signals recorded in solutions containing 50 ppb Pb(II) and Cd(II) and different concentrations of Cu(II). With increasing the Cu(II) concentration, the signals of Pb(II) and Cd(II) were rapidly attenuated and even no signals were recorded when 500 ppb Cu(II) were present in solution (i.e. 10 times higher than that of Pb(II) or Cd(II)), evidencing the serious interfering effect. To alleviate this interference, potassium ferricyanide and potassium ferrocyanide were selected as masking agents for Cu(II). Both of them form relatively stable complexes and therefore may help neutralize the effect of Cu(II) on the analysis of Pb(II) and Cd(II). Our results show that potassium ferrocyanide is a more efficient masking agent than potassium ferricyanide (see Figure 4.14). Using potassium ferrocyanide, 100% and 70% signal recoveries for Pb(II) and Cd(II) were achieved, respectively.

From the electrochemical point of view, other heavy metals that may simultaneously accumulate on the Bi-C CPE surface and whose corresponding stripping signals are recorded at potentials lower than those of Cd(II) and Pb(II) could also interfere. Depending on the relative concentrations of the different heavy metals in solution, Mn(II) and Zn(II) have been identified as possible interferents and their effect should be studied for every particular sample to be analyzed.

4.3.5.2. Co(II) interference on Ni(II) determination

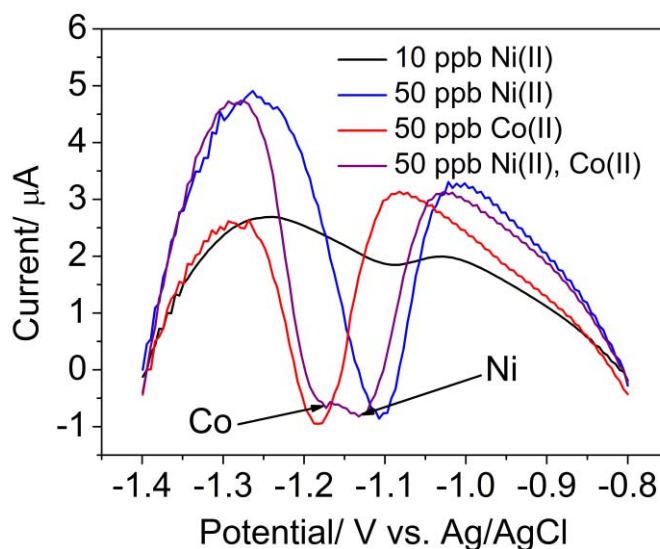


Figure 4.15. SWCSV signals showing the interference of Co(II) on the measurement of Ni(II). Activation at -1.4 V for 2 min and accumulation at -0.8 V for 3 min in 0.1 M ammonia buffer solution pH 9.2.

Regarding the detection of Ni(II), other heavy metals that may be complexed by DMG could have a negative effect on the electrode response to this target analyte. Divalent cations such as Co(II), Cu(II) and Zn(II) should be taken into account when they are present in the measuring sample. From the electrochemical point of view, the Ni(II) stripping voltammetric signal can be hampered by the presence of Co(II), which also forms a complex with DMG and whose stripping peak appears at a potential close to that of Ni. A study was conducted with the Bi-C CPEs in ammonia buffer solutions containing different relative concentrations of Ni(II) and Co(II). Figure 4.15 shows SWCSV signals for Ni(II) or Co(II) recorded individually with Bi-C CPE and those recorded when both metals were present in the buffer solution. It is clearly observed that both signals are overlapped but the peak currents are similar

to those of the individual signals. This behavior was observed in all the concentration range studied. Well-resolved peaks for both metals were previously reported using bismuth film electrodes [20] and macro-porous bismuth electrodes [12].

4.4. Analysis of Real Water Samples

To test the practical applicability of the Bi-C CPEs, several real water samples from different locations were collected and analyzed.

4.4.1. Description of Water Samples

Sample 1- drinking water from the Materials Science Institute of Barcelona (ICMAB, Bellaterra, Spain); **Sample 2** – wastewater containing a high organic load from an urban wastewater treatment plant (WWTP) located in Terrassa (Spain); **Sample 3** – ground water certified reference material BCR[®] 61, purchased from Sigma-Aldrich; **Sample 4** – treated water from an effluent of an urban WWTP located in el Prat (Barcelona, Spain); **Sample 5** – heavily polluted river water from the Meca river due to acid drainages from Tharsis mine (Huelva, Spain). These samples were analyzed as follows. Sample 1 was analyzed immediately after collection. Sample 2 contained a high amount of organic matter in suspension and was stored in the freezer. In order to carry out the measurements, the sample was thawed and left for the organic matter to deposit before use. Sample 3 was stored in the fridge and analyzed as received. Samples 4 and 5 were filtered immediately after collection through 0.2 µm Millipore filters, acidified in the field to pH < 2 with Suprapur[®] HNO₃ and stored at 4°C in sterile polypropylene containers until analysis.

Water sample analyses were carried out in triplicate with the Bi-C CPEs sensor. Prior to the electrochemical measurements, they were diluted using the appropriate buffer. The degree of dilution necessary to obtain a heavy metal concentration falling within the range of the calibration curves was determined from the stripping currents and peak shapes in preliminary measurements. The analyses were carried out according to the standard addition, unless stated otherwise.

4.4.2. Cd(II), Pb(II) and Ni(II) Analyses in Real Waters

Sample 1 and 2 did not contain any detectable concentration of the three heavy metals under study. Then, they were spiked with known amounts of the heavy metals and the recovery was calculated. Results obtained in Sample 3 were compared with those provided by the certificate of analysis of this reference material. Sample 4 and 5 contain different concentrations of heavy metals and the results were compared with those obtained with the ICP-MS standard method performed by an external laboratory. ICP-MS analyses were carried out using a Thermo Scientific XSERIES II instrument with detection limits of about 1 ppb for all the tested heavy metals. Multi-element standard solutions prepared from single certified standards supplied by SCP SCIENCE were used for calibration and run at the beginning and at the end of each analytical series. Certified Reference Material SRM-1640 NIST fresh-water-type and inter-laboratory standard IRMM-N3 wastewater test material (European Commission Institute for Reference Materials and Measurements) were also intercalated in between samples for accuracy checking. Precision error was higher than accuracy and was always around 5%.

Sample 1 and sample 2 were first analyzed. Different aliquots of both samples were diluted with either 0.2 M acetate buffer or 0.2 M ammonia buffer, in a 1:1 volume ratio, depending on the heavy metal to be analyzed. No detectable amounts of the three heavy metals under study were found. Then, two aliquots of both samples diluted with 0.2 M acetate buffer were spiked with 10 ppb (Sample 1) and 5 ppb (Sample 2) of both Cd(II) and Pb(II). Figure 4.16 (A) and (B) show representative stripping voltammograms before and after the addition of different concentrations of Cd(II) and Pb(II) for the two samples, together with the corresponding calibration curves. In addition, two aliquots already diluted with 0.2 M ammonia buffer, were spiked with 10 ppb Ni(II). Figure 4.16 (C) shows the voltammograms of the standard addition method and the corresponding calibration curve carried out for the detection of Ni(II) in Sample 1. Table 2 shows the concentration values recovered for the three heavy metals in both samples. A good agreement between the added values and the estimated ones was found in all cases except for the Ni(II) in Sample 2. The detection of this heavy metal in the spiked sample did not produce any signal. As discussed in section 4.3.5., the presence in the sample of other divalent metal

cations or a high content of organic matter, to which Ni(II) could be strongly adsorbed, may be the reason for this negative result. By contrast, the Cd(II) and Pb(II) detection did not appear to be affected.

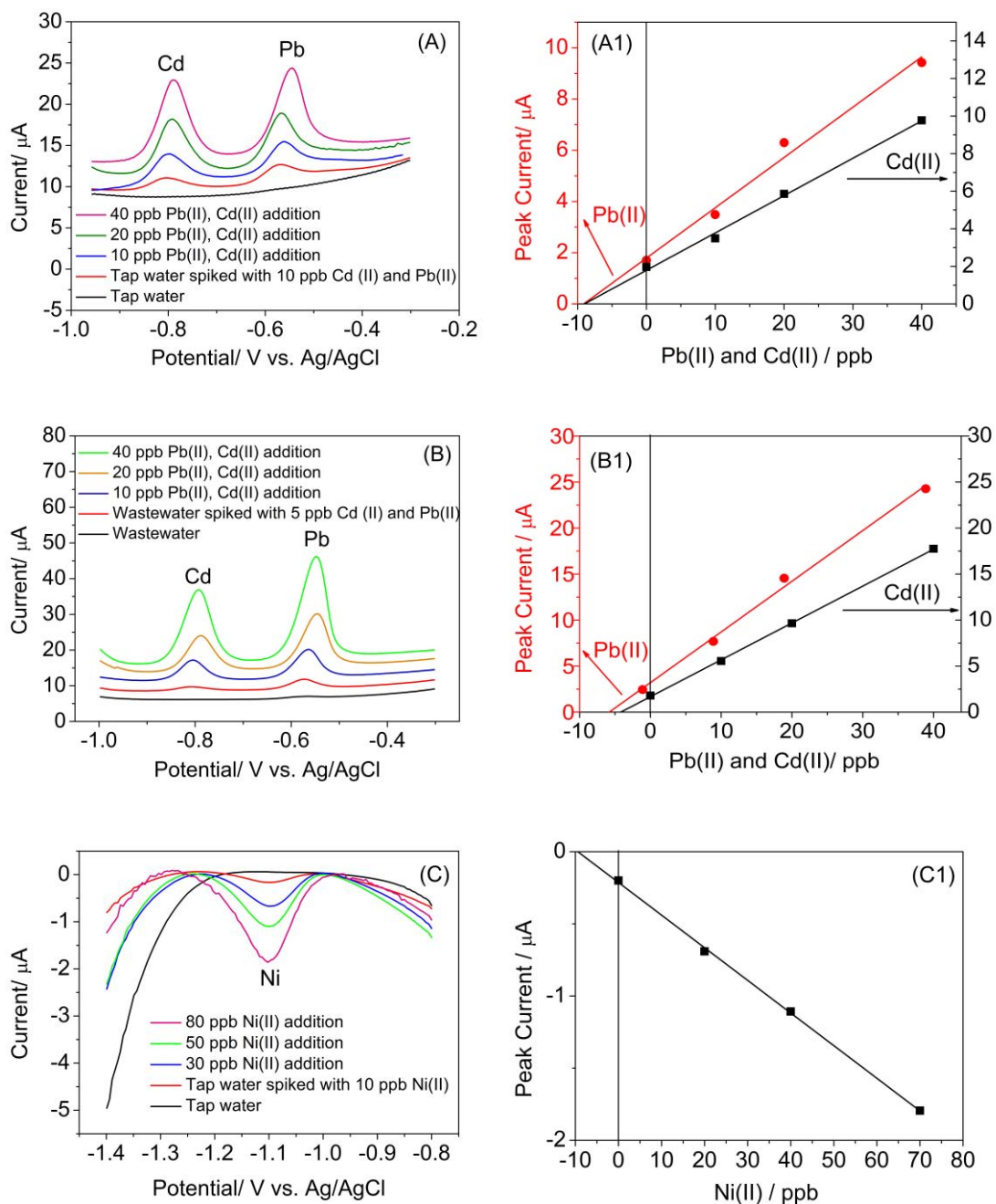


Figure 4.16. SWASV and SWCSV signals recorded for the analysis of Cd(II) and Pb(II) using standard addition method in (A) sample 1, (B) sample 2 and (C) Ni(II) in sample 1. A1, B1, and C1 are the corresponding linear regression curves.

Afterwards, the Bi-C CPE was used to analyze two water samples containing the three heavy metals under study. Namely, Sample 3 is a certified reference

groundwater with relatively high concentrations of the heavy metals under study and Sample 4 is another waste water collected in an effluent of a WWTP with relatively wide spectrum of heavy metals (Mn, Ba, Cu, Zn) but a low amount of Cd(II), Pb (II) and Ni(II). Both samples were diluted and analyzed following the same protocol as for the previous samples. The concentration values measured with the Bi-C CPE are presented in Table 2. The values of Pb(II) and Ni(II) in Sample 3 showed a good agreement with the reference values. Cd(II) detection proved to be more difficult.

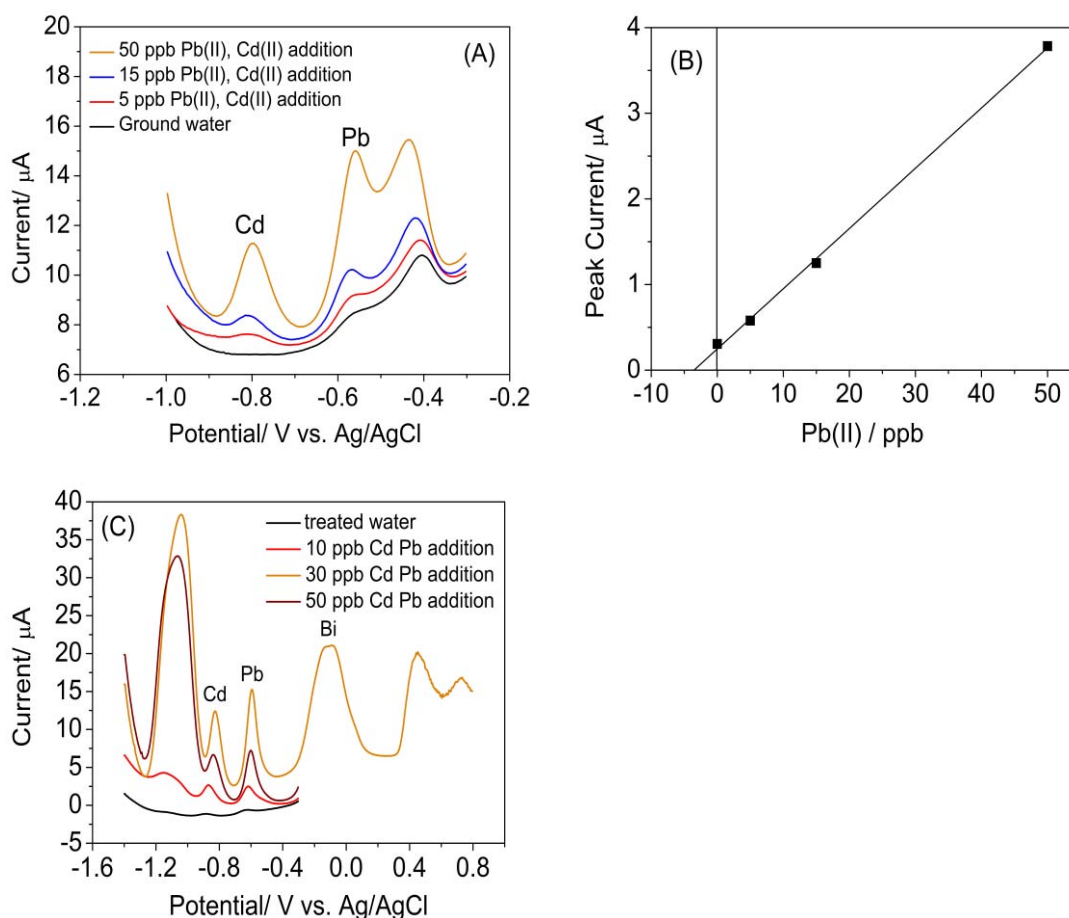


Figure 4.17. (A) SWASV signals recorded in Sample 3 together with those ones recorded after addition of 5, 15 and 50 ppb of Cd(II) and Pb(II) (standard addition method). (B) Corresponding linear regression curve for Pb(II).

Figure 4.17 shows representative stripping voltammograms of Pb(II) and Cd(II) for Sample 3 and sample 4, recorded following the standard addition method. Although the Cd(II) concentration of 1.4 ppb after the 1:1 dilution was still slightly higher than the estimated LOD of Bi-C CPE, the presence of 22 ppb Cu(II) negatively affected the Cd(II) determination, as shown below. Following the results of the interference

study previously carried out, 0.1 mM $K_4Fe(CN)_6$ was added to the solution in order to alleviate the Cu(II) interference. The recorded peak currents were significantly enhanced, but the recovery appeared to be well below the 100%, which still resulted in the non-detectability of this analyte. The analyses of Sample 4 showed that the Bi-C CPE detected Cd(II) and Pb(II) at very low concentrations, at which the ICP-MS standard technique just provided with estimated values below 2 ppb for both heavy metals. However, Ni(II) could not be measured with our device because its concentration appeared to be below the estimated LOD after carrying out the 1:1 dilution, required to pre-condition the sample.

Finally, the analysis of Sample 5, a heavily polluted river water sample due to acid mine drainages was attempted with the aim of assessing the potential of the Bi-C CPEs in the analysis of very complex water samples. This sample contained ppm-levels of Zn (II), Cu(II) and Mn(II) but ppb-levels of Pb(II), Cd(II) and Ni(II). Sample dilution was adjusted to a 1:10 volume ratio with the corresponding buffer solution, this being the highest feasible dilution in an attempt to minimize the matrix effects while the target analytes could still be detected.

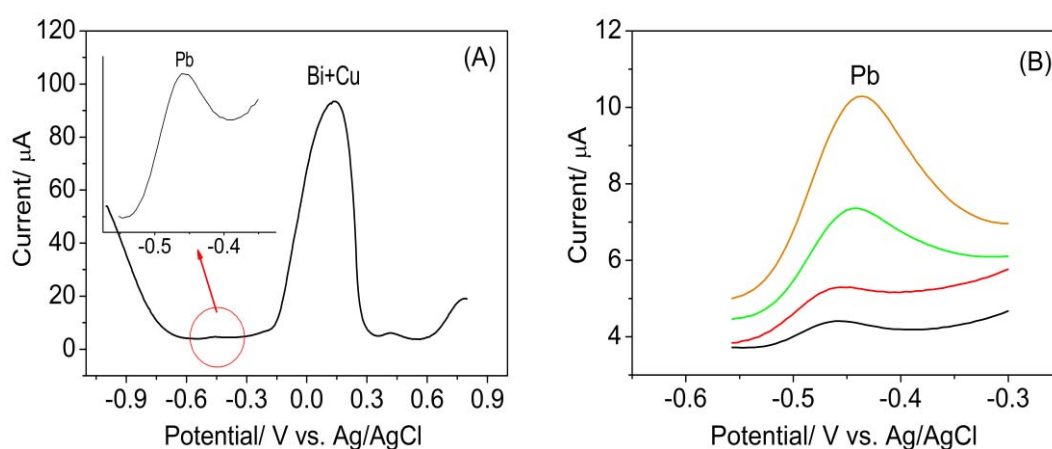


Figure 4.18. (A) SWASV signals recorded in sample 5. (B) Close-up view of the signals in the potential window where the Pb(II) stripping peak was recorded in Sample 5 and after the addition of 10, 30, and 60 ppb of Pb(II). Deposition was carried out at -1.0 V for 3 min. Sample dilution factor: 5, in 0.1 M acetate buffer at pH 4.5.

Figure 4.18 shows the stripping voltammograms of Pb(II) and Cd(II) in this sample. They displayed a step background signal at potentials below -0.6 V that significantly reduced the potential window and hindered the detection of the stripping peak of Cd(II). This effect may be related to the presence of Mn(II) and

Zn(II) at concentrations above 10 ppm in the original sample and whose stripping peaks are usually recorded at potentials lower than that of Cd(II). A Bi stripping peak at around 0 V was recorded, which is wider, rounder and much bigger than the Bi peak recorded in the solutions with a lower content of Cu(II). This peak shape is likely to be related to the overlapping of Bi (III) and Cu(II) stripping peaks. Cu(II) was present in the original sample at concentrations around 10 ppm and its interference on the detection of Cd(II) was described above. Surprisingly, the Pb(II) signals did not seem to be affected by the presence of Cu(II) and increased linearly with the standard additions of Pb(II) into the solution.

Table 4.2. Results of the analyses of five water samples using the Bi-C CPEs

Sample	Added/Reference/ICP-MS values (ppb)			Electrochemical analyzed values (ppb)		
	Cd(II)	Pb(II)	Ni(II)	Cd(II)	Pb(II)	Ni(II)
Tap water (1)	10	10	10	9.2±1.0	9.1±0.7	9.4±0.9
Polluted water-influent (2)	5	5	10	4.7±0.6	5.1±0.8	N.D.
Certified ground water (3)	2.78	7.98	27	<LOD	7±2	25±4
Polluted water-effluent (4)	<2	<2	7.8	3.7±0.8	1.3±0.4	<LOD
Heavily polluted- mine drainages (5)	55±3	38±2	273±14	<LOD	40.9±0.6	262±73*

*- analyzed by interpolation method; N.D.- not detected.

Regarding the Ni(II) detection, DMG was added in the ammonia buffered solution for the formation of the Ni(II)-DMG complex. However, DMG forms complexes with many metallic cations, such as Mn(II), Zn(II), Pb(II), Co (II), and Cu (II), some of which are also present at high concentrations in Sample 5. The Ni(II) current signals did not increase linearly with the standard additions of Ni(II) into the solution. We believe that all the DMG added to the solution was complexing the different heavy metals and then could not chelate the added Ni(II). However, increasing the concentration of DMG in the solution resulted in the production of a clearly visible white precipitate making the measurements unreliable. For all this, the Ni(II) concentration was measured by interpolating the signal recorded in the sample into the corresponding sensor calibration curve. From Table 2, the ICP-MS results and

the values of the electrochemical analysis are in reasonable good agreement. However, this last analysis proves that the performance of electrochemical devices, such as the one presented here, for analysis of complex samples containing a variety of heavy metals in a wide range of concentrations, should be studied in detail for any particular case. Nevertheless, alarm systems based on this kind of sensors with the ability to detect increased concentrations of these pollutants due to sudden spills, could be implemented.

4.4.3. Zn(II) and Cu(II) Analyses in Real Waters

Zn(II) and Cu(II) are not as toxic as Pb(II) and Cd(II) and these two metal cations are not in the list of priority substances included in the water directive released by the European Commission. However, as we discussed above, the proposed nanocomposite sensors could be used as an alarm for Zn(II), and the blank carbon xerogel material electrode also shows superior performance for the detection of Cu(II). Hence, in this work, three real water samples from different locations were also collected and analyzed for the detection of these two heavy metals.

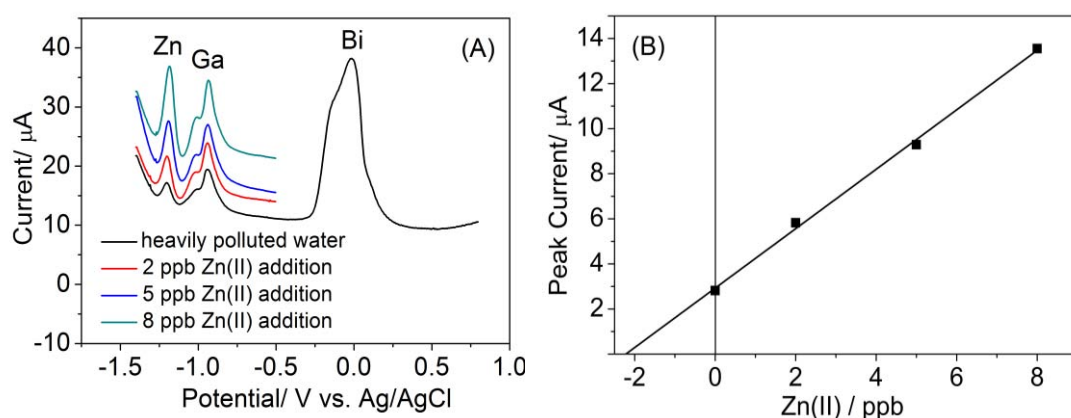


Figure 4.19. SWASV signals describing the determination of Zn(II) in the polluted river water sample due to acid mine drainages (A) and the corresponding linear standard addition plot (B). Accumulation at -1.4 V for 3 min. Sample dilution factor: 10000, in 0.1 M acetate buffer pH 4.5 containing 2000 ppb of Ga.

Firstly, a heavily polluted water sample containing very high amounts of Zn(II) and Cu(II) was analyzed. This sample was analyzed after a 10^4 dilution in acetate buffer solution. The formation of Cu(II)-Zn(II) intermetallic will probably influence the determination of Zn(II). Herein, similarly to the measurements performed to obtain the calibration curve for Zn(II), 2000 ppb of Ga(III) were added to the solutions in

order to avoid the Cu(II) interference. Figure 4.19 displays the SWASV signals of Zn(II) recorded by applying the standard addition in this sample and the corresponding linear calibration regression, indicating the potential application to the detection of Zn(II) using this Bi-C CPEs devices.

The amount of Cu(II) in this heavily polluted water was also quantitatively analyzed using the carbon xerogel electrode without Bi. Two additional water samples, a treated wastewater and an unpolluted river water, which contain relatively low concentration of Zn(II) and Cu(II) were also analyzed. The calculated values are gathered in Table 4.3. A relatively good agreement is obtained between the reference ICP-MS results and the values obtained with the electrochemical sensors, indicating the applicability of the proposed sensors for Zn(II) and Cu(II) analyses.

Table 4.3 Zn(II) and Cu(II) analyses in real waters using Bi-C CPEs

Samples	ICP-MS values (ppb)		Electrochemical analyzed values (ppb)	
	Cu(II)	Zn(II)	Cu(II)	Zn(II)
Mine drainages polluted water	10070±500	25650±1280	14700 ± 2100	20300 ± 4700
Treated waste water	12.9 ±0.6	92.4±4.6	12 ± 4	50 ± 7
Non-polluted river water	8.9±0.4	135±7	9 ± 1	71 ± 5

4.5. Conclusion

Sol-gel derived bismuth carbon nanocomposite materials successfully performed as working electrode materials for the electrochemical analysis of heavy metal pollutants in water. The materials consist of an open porous structure of carbon matrix with well distributed bismuth nanoparticles, and the resulting electrodes provide a large active area and in turn a superior sensitivity for the electrochemical reduction of heavy metals in waters, compared to other common bismuth based electrode architectures. Among them, electrodes made with materials prepared by a one-pot co-synthesis approach offer higher sensitivity because of the homogeneous nanocomposite structure compared to those prepared by the impregnation method.

Low limits of detection and wide linear calibration ranges were obtained for Cd(II), Pb(II), and Ni(II) as well as for Cu(II), meeting the requirements of water regulations established by the EU and the US-EPA. In addition, one could in principle enhance the analytical performance of the presented electrochemical devices by increasing the bismuth amount in the materials. Studies carried out in real water samples of different origin and varied heavy metal concentrations confirmed the good performance of these nanocomposite materials for the fabrication of electrochemical sensors applied to heavy metals analysis.

References

- [1] Wang J, Lu J, Hocevar SB, Farias PAM, Ogorevc B. Bismuth-Coated Carbon Electrodes for Anodic Stripping Voltammetry. *Analytical Chemistry*. 2000;72:3218-3222.
- [2] Lee G-J, Lee H-M, Rhee C-K. Bismuth Nano-powder Electrode for Trace Analysis of Heavy Metals Using Anodic Stripping Voltammetry. *Electrochemistry Communications*. 2007;9:2514-2518.
- [3] Kadara RO, Jenkinson N, Banks CE. Disposable Bismuth Oxide Screen Printed Electrodes for the High Throughput Screening of Heavy Metals. *Electroanalysis*. 2009;21:2410-2414.
- [4] Espinosa AM, San José MT, Tascón ML, Vázquez MD, Sánchez Batanero P. Electrochemical Behaviour of Bismuth(V) and Bismuth(III) compounds at a Carbon Paste Electrode. Application to the Study of the Superconductor BiSrCaCuO. *Electrochimica Acta*. 1991;36:1561-1571.
- [5] Li WS, Long XM, Yan JH, Nan JM, Chen HY, Wu YM. Electrochemical Behaviour of Bismuth in Sulfuric Acid Solution. *Journal of Power Sources*. 2006;158:1096-1101.
- [6] Hočevár SB, Švancara I, Vytřas K, Ogorevc B. Novel Electrode for Electrochemical Stripping Analysis based on Carbon Paste Modified with Bismuth Powder. *Electrochimica Acta*. 2005;51:706-710.
- [7] Rico MÁG, Olivares-Marín M, Gil EP. Modification of Carbon Screen-printed Electrodes by Adsorption of Chemically Synthesized Bi Nanoparticles for the Voltammetric Stripping Detection of Zn(II), Cd(II) and Pb(II). *Talanta*. 2009;80:631-635.
- [8] Khan AAA, Abdullah MA. Bismuth-modified Hydroxyapatite Carbon Electrode for Simultaneous in-situ Cadmium and Lead Analysis. *International Journal of Electrochemical Science*. 2013;8:195-203.
- [9] Malakhova NA, Mysik AA, Saraeva SY, Stozhko NY, Uimin MA, Ermakov AE, et al. A Voltammetric Sensor on the Basis of Bismuth Nanoparticles Prepared by the Method of Gas Condensation. *Journal of Analytical Chemistry*. 2010;65:640-647.
- [10] Wang J, Lu J, Kirgöz ÜA, Hocevar SB, Ogorevc B. Insights into the Anodic Stripping Voltammetric Behavior of Bismuth Film Electrodes. *Analytica Chimica Acta*. 2001;434:29-34.
- [11] Ma F, Jagner D, Renman L. Mechanism for the Electrochemical Stripping Reduction of the Nickel and Cobalt Dimethylglyoxime Complexes. *Analytical Chemistry*. 1997;69:1782-1784.

- [12] Dal Borgo S, Sopha H, Smarzewska S, Hočevár SB, Švancara I, Metelka R. Macroporous Bismuth Film Screen-Printed Carbon Electrode for Simultaneous Determination of Ni(II) and Co(II). *Electroanalysis*. 2015;27:209-216.
- [13] Piankova LA, Malakhova NA, Stozhko NY, Brainina KZ, Murzakaev AM, Timoshenkova OR. Bismuth Nanoparticles in Adsorptive Stripping Voltammetry of Nickel. *Electrochemistry Communications*. 2011;13:981-984.
- [14] Directive 2013/39/EU of the European Parliament and of the Council.
- [15] U.S. EPA National Primary Drinking Water Regulations 2009.
- [16] Daud N, Yusof NA, Tee TW. Development of Electrochemical Sensor for Detection of Mercury by Exploiting His-Phe-His-Ala-His-Phe-Ala-Phe Modified Electrode. *International Journal of Electrochemical Science*. 2011;6:2798-2807.
- [17] Ahmaruzzaman M. Industrial Wastes as Low-cost Potential Adsorbents for the Treatment of Wastewater Laden with Heavy Metals. *Advances in Colloid and Interface Science*. 2011;166:36-59.
- [18] Yang D, Wang L, Chen Z, Megharaj M, Naidu R. Investigation of Copper(II) Interference on the Anodic Stripping Voltammetry of Lead(II) and Cadmium(II) at Bismuth Film Electrode. *Electroanalysis*. 2013;25:2637-2644.
- [19] Jia X, Li J, Wang E. High-Sensitivity Determination of Lead(II) and Cadmium(II) Based on the CNTs-PSS/Bi Composite Film Electrode. *Electroanalysis*. 2010;22:1682-1687.
- [20] Morfobos M, Economou A, Voulgaropoulos A. Simultaneous Determination of Nickel(II) and Cobalt(II) by Square Wave Adsorptive Stripping Voltammetry on a Rotating-disc Bismuth-film Electrode. *Analytica Chimica Acta*. 2004;519:57-64.

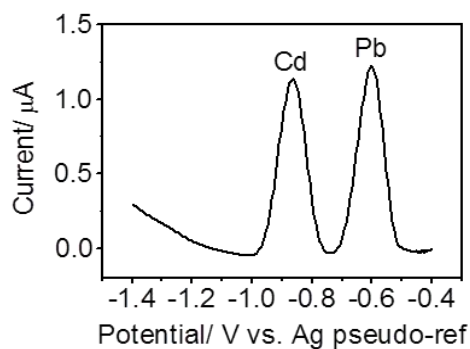
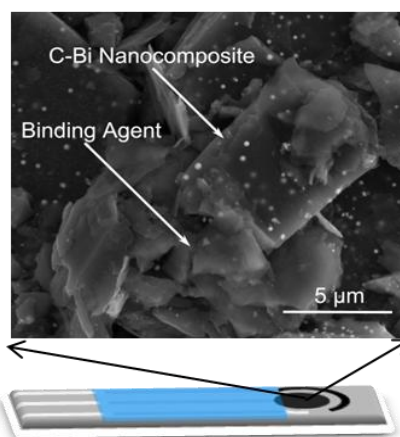
Chapter 5

Fabrication and Characterization of Screen Printed Bismuth Nanoparticle–Porous Carbon Nanocomposite Electrodes

Ink Preparation



Screen Printed Electrode



Summary

In Chapter 4, the excellent electrochemical performance of novel bismuth nanoparticle-porous carbon composite materials applied as carbon paste electrodes (CPEs) in the detection of heavy metals in both buffered and real water samples, is shown. CPEs are laboratory devices intended for characterization and optimization

studies. However, in order to make a device that could be mass-produced and commercialized, other alternatives should be sought. Among them, the fabrication of electrodes by screen-printing has long been recognized as a simple and cost-effective mass-production process. Electrodes of planar configuration can be defined on the same substrate together with reference and counter electrodes. Thus, this technique enables the production of compact electrochemical cells that could be deployed and used in a real scenario. In this Chapter, the sol-gel derived bismuth-carbon nanocomposite material was milled and then made into a custom ink, which is eventually applied to the fabrication of commercial-like screen printed electrodes. The electrode fabrication process is firstly discussed. Afterwards, the electrochemical performance of these electrodes towards heavy metals analysis is investigated. A comparison study between the bismuth/carbon nanocomposite screen printed electrodes (Bi-C SPEs) and the Bi-C CPEs presented in Chapter 4 is also described. Finally, the practical application of these electrodes is demonstrated in real water samples.

The work presented in this chapter has been included in one paper entitled “**One-step fabrication of screen printed bismuth nanoparticle carbon nanocomposite electrodes for heavy metal detection**”, by Pengfei Niu, César Fernández-Sánchez, Martí Gich, Carla Navarro-Hernández, Pablo Fanjul-Bolado and Anna Roig, submitted to Sensors and Actuators B: Chemical.

5.1. Brief Introduction

As we described in Chapter 1, so far, two approaches have been previously reported for the fabrication of screen printed electrodes with both carbon and bismuth components, depending on the method selected for the incorporation of bismuth into carbon electrodes. On one hand, **two-step fabrication processes** based on the addition of Bi after printing the carbon ink that defines the electrode has been extensively described. Overall, these processes give rise to Bi-modified screen printed carbon electrodes displaying low limits of detection. However, the required additional processing step to incorporate Bi hinders a cost-effective mass production process. On the other hand, a **one-step bulk modification** process has also been developed, in which carbon and Bi precursor powders are thoroughly mixed to prepare the ink employed to print the working electrodes. Even though this methodology is simple in terms of electrode production, the process relies on a mechanical mixing step for the ink preparation and the analytical performance of the resulting devices strongly depends on the Bi precursor and some analytical parameters such as the Bi reduction potential. Herein, the fabrication of screen printed electrochemical sensors using the sol-gel derived bismuth/carbon composite material aims at achieving the mass production of devices using a simpler and more cost-effective process than those reported so far and taking advantage of the nanocomposite material developed in this Thesis for the sensitive detection of heavy metals.

5.2. Electrode Fabrication

5.2.1. Nanocomposite Synthesis

The ink for printing the working electrode was made of M-(Bi-C)_{CS} nanocomposite powders. The material was prepared in bulk following the co-synthesis procedure (class B) described in Chapter 3, but scaling it up 20 times. In brief, 4 g Bi(NO₃)₃, 20 g resorcinol, 27.2 ml formaldehyde, 100 ml glycerol formal, and 40 ml CH₃COOH were mixed thoroughly for 30 min and a transparent sol was formed. Afterwards, the sol was transferred into a closed glass container and kept at 60°C for 8 hours to form an organic gel. After carbonization of the organic gel at 900°C for 2 h in N₂ or Ar

atmosphere, around 20 g of bismuth nanoparticle-porous carbon nanocomposite material was obtained. For comparative studies, the same sol-gel procedure but without adding $\text{Bi}(\text{NO}_3)_3$, was followed to synthesize a porous carbon material and fabricate screen printed carbon electrodes.

5.2.2. Fabrication of the Screen Printed Bi-C Nanocomposite Electrodes

Screen printed electrochemical cells were fabricated onto ceramic substrates (L 34 mm x W 10 mm x H 0.5 mm) and included a porous Bi-C nanocomposite working electrode with a diameter of 4 mm (Bi-C SPE), a graphite counter electrode and a silver pseudo-reference electrode (Figure 5.1). These cells were fabricated by DropSens S.L. (Oviedo, Spain) and show the same geometry as the commercially available DRP-110 SPEs.

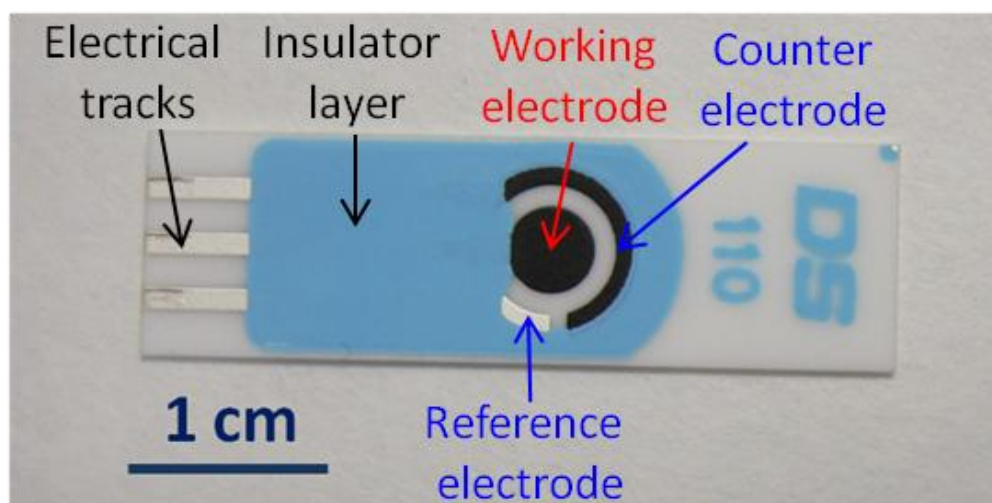


Figure 5.1. Image of the Bi-C SPE

The screen-printing of the working electrode included the preparation of an ink using the $\text{M}-(\text{Bi-C})_{\text{CS}}$ material. For that, the material was ball-milled in a Retsch Mixer Mill to obtain powders with the required particle size and distribution. Particle size distributions were carried out by analyzing more than 10 scanning electron microscopy (SEM) images using imageJ software. The material particle size was critical in order to get an adequate ink that could be printed and give rise to stable electrode devices. The optimum particle size distribution was found to be between 2 μm and 50 μm as shown in Figure 5.2, with an average size below 10 μm . Particle sizes above these values produced inks that could not be printed as they did

not go through the mesh of the mask whereas narrower particle size distributions not containing a small fraction of bigger particles produced electrodes that easily detached from the ceramic substrate.

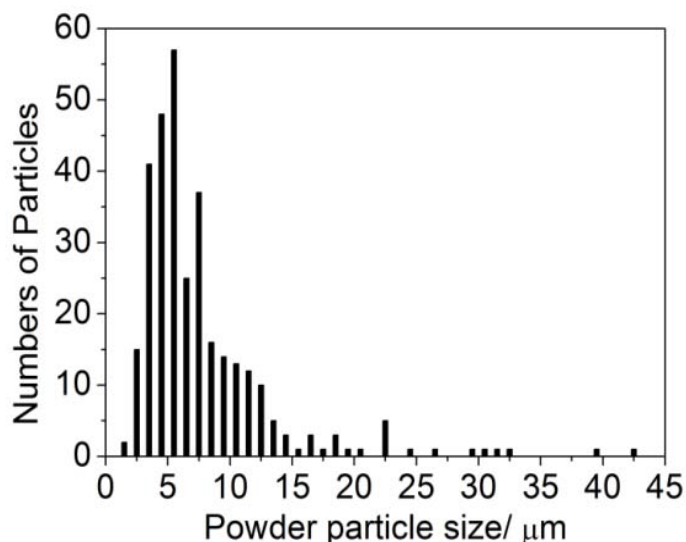


Figure 5.2. Particle size distribution of M-(Bi-C)_{cs} nanocomposite for screen-printing

Then, these powders were mixed with other components in order to get the required ink, following a formulation set by the company (proprietary information). The ink curing process was carried out in an oven at 120°C for 10 min and then at 80°C for 2 min. Micro-structural characterization of the fabricated electrodes was performed with a FEI Quanta 200F SEM equipped with an energy-dispersive X-ray spectroscopy (EDX) analysis system. Using the amount of material obtained in the synthesis process mentioned in the previous section (about 20 g), 450 electrochemical cells containing the Bi-C electrodes were fabricated in one batch. The resulting paste ink contained 60 % of the Bi-C material while the remaining 40 % corresponded to the required binding agent and other additives used in its preparation.

For comparative studies, a porous carbon material was prepared following the same sol-gel procedure but without adding Bi(NO₃)₃ from which screen printed carbon electrodes were also fabricated.

Figure 5.3 (A) presents the backscattered electron SEM image of the rough surface of a screen-printed Bi-C working electrode, this being similar to the surface of any carbon (graphite) screen-printed electrode. A close-up SEM image recorded using

the secondary electron detector is shown in Figure 5.3 (B). Both the carbon and the Bi nanoparticle components were observed to be dispersed in the ink. EDX analysis of the electrode surface revealed the presence of 93 wt% carbon, 2.8 wt% bismuth, 2.0wt% chlorine and 2.2 wt% oxygen, with chlorine being part of the binding agent. The percentage of Bi in the SPE is in reasonable agreement with the percentage of the Bi in the initial Bi-C material ($\approx 6\%$) and the proportion of this material in the ink used in the printing process ($\approx 60\%$).

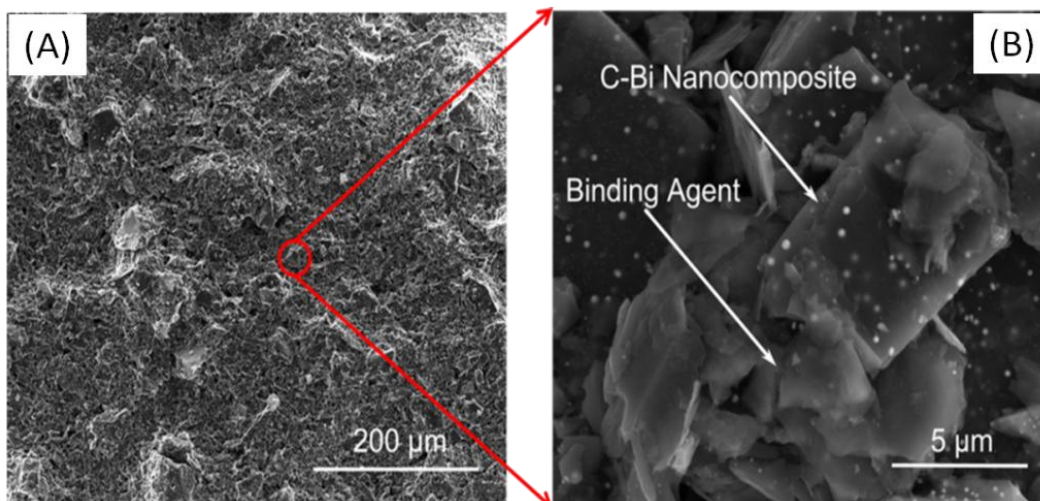


Figure 5.3. SEM images of the surface of a screen printed Bi nanoparticle porous carbon composite electrode

5.3. Electrochemical Characterization of Bi-C SPEs



Figure 5.4. Bi-C SPE connector to the potentiostat

Electrochemical characterization of Bi-C SPEs was performed on an Autolab PGSTA30 potentiostat (EcoChemie, Netherlands) controlled by GPES software version 4.3 at room temperature. An electrical connector as shown in Figure 5.4 was used to connect the electrode to a potentiostat.

5.3.1. Measurement Procedure

The analysis of Pb(II) and Cd(II) at Bi-C SPEs was carried out at room temperature in a 20 mL plastic cell using square wave anodic stripping voltammetric technique (SWASV) operated by an Autolab PGSTAT30 potentiostat (EcoChemie, the Netherlands). The supporting electrolyte was 0.1 M acetate buffer solution pH 4.5. No pretreatment of the Bi-C SPE surface was applied. Pb(II) and Cd(II) were simultaneously reduced to their zero valence state onto the electrode surface by applying a deposition potential of -1.7 V under stirring at 700 rpm for a set time. Then, the stirring was stopped and the system equilibrated for 20 s. Stripping voltammograms were recorded in the potential window from -1.4 V to -0.3 V. The squared-wave potential scan was applied with an amplitude of 25 mV, a frequency of 20 Hz and a step potential of 5 mV. All the screen printed electrodes were single-use. Calibration curves were constructed by plotting the stripping peak current against the corresponding metal ion concentration. Each point in the calibration curves was the mean of three measurements with the error bars showing the corresponding standard deviation, unless stated otherwise.

5.3.2. Cyclic Voltammetry

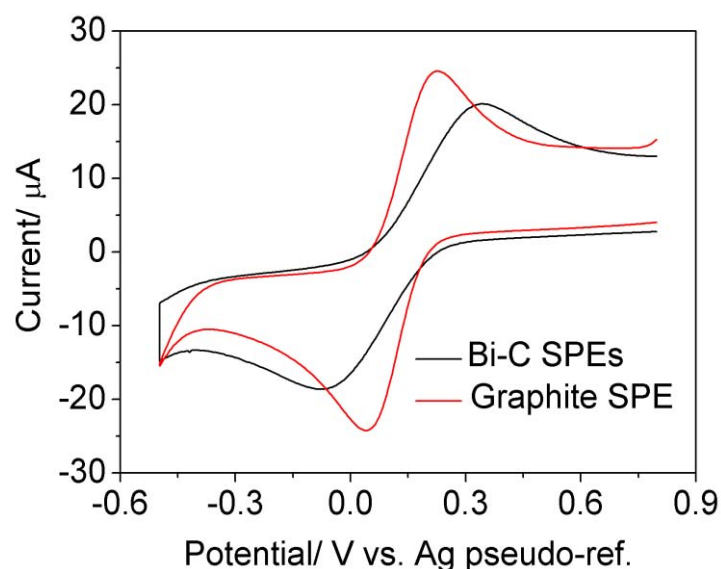


Figure 5.5. Cyclic voltammograms recorded in 0.1 M KNO_3 solution containing 1 mM ferri-/ferrocyanide redox couple at 0.04 V/s with the Bi-C SPE and a commercial graphite SPE.

Figure 5.5 shows the cyclic voltammograms recorded in a solution containing 1 mM ferri-/ferrocyanide electroactive redox pair using the Bi-C SPE. A quasi-reversible signal is observed with a formal potential ($E^{0'}$) and peak-to peak potential separation (ΔE_p) of ca. 200 mV and of 400 mV, respectively. A commercial graphite based screen printed carbon electrode (DRP 110 from DropSens) showed a ΔE_p of ca. 190 mV at the 0.04 V/s scan rate. The higher ΔE_p value of the Bi-C SPE indicates a slower electron transfer at the electrode solution interface. This was the expected behavior taking into account that the resistance of the Bi-C and commercial graphite screen-printed electrode were found to be around 5000 Ω and 300 Ω , respectively, for electrodes of similar areas. Nevertheless, the Bi-C SPEs were suitable for the development of electrochemical sensors, as demonstrated with the studies presented below.

5.3.3. Cd(II) and Pb(II) Detection

Figure 5.6 (A) shows the SWASV signal for the determination of Pb(II) and Cd(II) in a concentration range from 5 ppb to 100 ppb after an accumulation time of 90 s at -1.7 V in acetate buffer solutions. Two clearly visible peaks at around -0.85 V and -0.60 V were ascribed to the stripping process of Cd^0 and Pb^0 , which were originated from the reduction of metal ions and accumulation on the surface of Bi in the deposition step, to produce Pb(II) and Cd(II), respectively.

In order to demonstrate that the Pb(II) and Cd(II) stripping responses originated from the presence of Bi nanoparticles in the electrode material, Figure 5.7 compares the SWASV signals recorded with the Bi-C SPE in acetate buffer solutions containing 10 ppb and 50 ppb Pb(II) and Cd(II), using 90 s accumulation time and those responses recorded with screen printed porous carbon electrodes without Bi after accumulation times even longer than 300 s. The results indicate that the presence of Bi in the carbon electrodes is required for heavy metal analysis.

The peak current is directly proportional to the added Pb(II) and Cd(II) in the whole concentration range studied. The corresponding linear calibration curves for Pb(II) and Cd(II) are shown in Figure 5.6 (B). The relatively small standard deviations of the electrode current response, indicated by the error bars of the calibration curves, illustrate the good reproducibility of the Bi-C SPE. The limit of detection (LOD) was

calculated according to the formula: $\text{LOD} = 3 (\text{SD}/S)$, where SD is the standard deviation of the intercept obtained from 3 different calibration curves recorded successively and S is the mean of the corresponding slopes. The estimated values were 1.15 ppb and 2.04 ppb for Pb(II) and Cd(II), respectively.

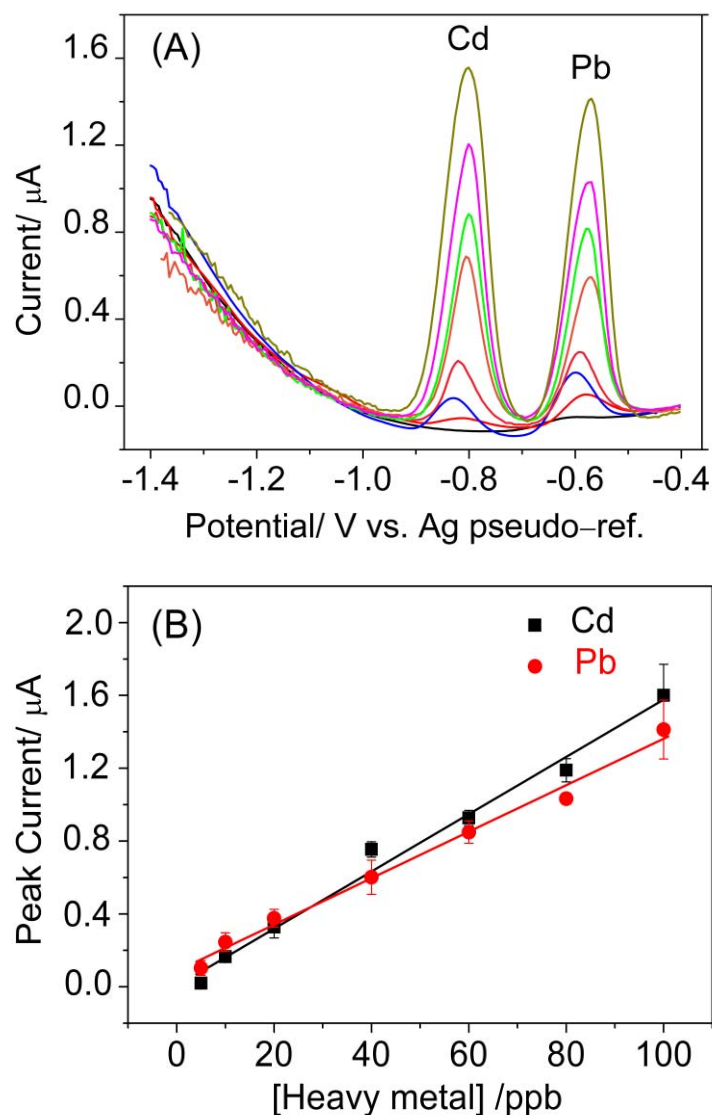


Figure 5.6. (A) SWASV signals recorded in 0.1 M standard acetate buffer solutions pH 4.5 containing different concentrations of Pb(II) and Cd(II), (from bottom to top 0, 5, 10, 20, 40, 60, 80, 100 ppb). (B) Corresponding calibration curves. Accumulation was carried out at -1.7 V for 1.5 min.

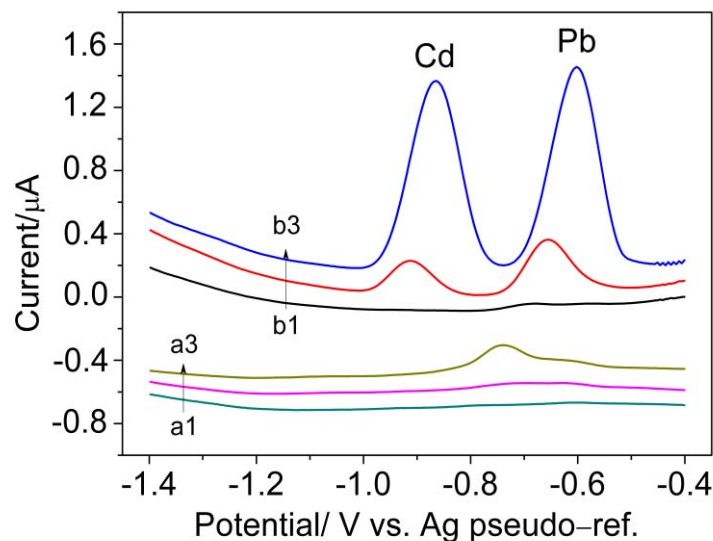


Figure 5.7. SWASV signals recorded in standard 0.1 M acetate solutions pH 4.5 containing 0, 10, 50 ppb of both Pb(II) and Cd(II) at (a1 to a3)- SPEs without Bi nanoparticles (C-SPE), and (b1 to b3) – Bi-C SPEs. Electro-deposition was carried out at -1.7 V for 1.5min and at -1.7 V for 5min with Bi-C SPEs and C-SPEs, respectively. An offset was applied for clarity of presentation.

The LOD of our fabricated Bi-C SPE could be enhanced by, 1) increasing the Bi content during the material synthesis process, or 2) simply using longer accumulation times. In the present work, the accumulation time was increased up to 300 s. Figure 5.8 (A) shows the SWASV signals recorded in acetate buffer solutions containing Pb(II) and Cd(II) in the concentration range of 1-100 ppb after a 300 s accumulation at -1.7 V. The corresponding calibration curves (Figure 5.8 (B)) were plotted in the linear concentration range of 1-50 ppb. A comparison of the calibration curves of Figure 5.6 (B) and Figure 5.8 (B) reveals that a longer accumulation time results in an increased slope (from $1.4 \times 10^{-8} \mu\text{A/ppb}$ to $2.5 \times 10^{-8} \mu\text{A/ppb}$) and thus in a better sensitivity. The LOD calculated from 3 different calibration curves recorded successively and using the formula mentioned above were 0.60 ppb for Pb(II) and 1.28 ppb for Cd(II). These are about 50 % and 40 % lower than those estimated using a 90s accumulation time, respectively, thus demonstrating the validity of this strategy for improving the analytical performance of these electrochemical sensors without compromising the rapidity of the analyses.

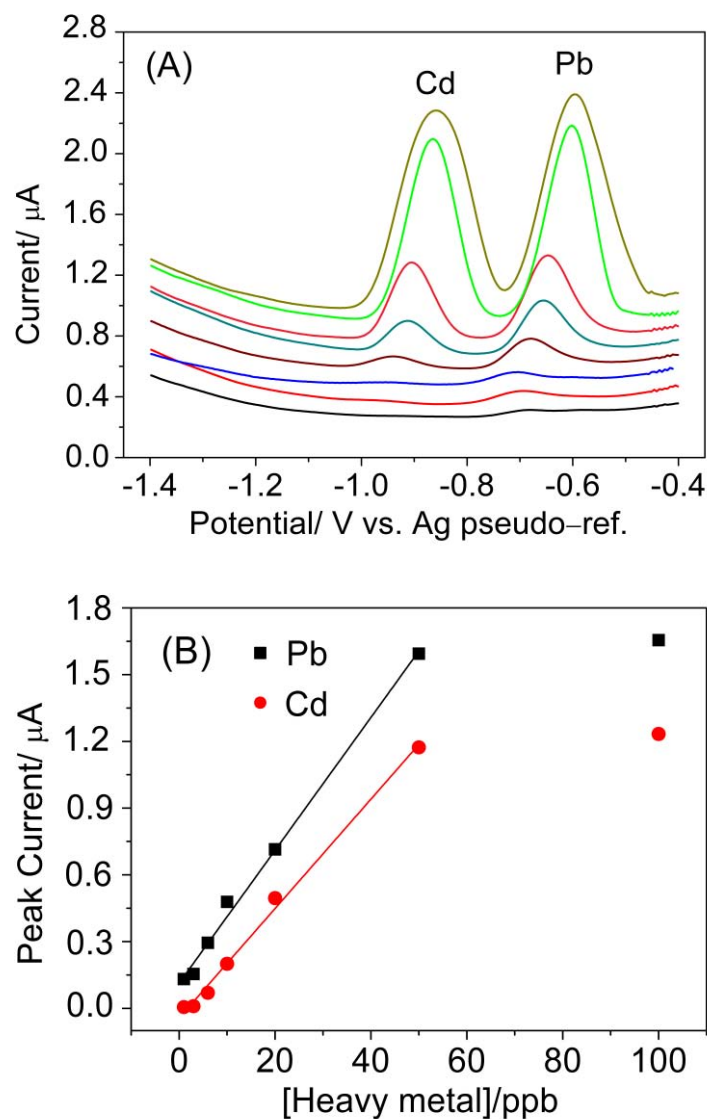


Figure 5.8. SWASV signals recorded in standard 0.1 M acetate buffer solutions pH 4.5 containing different concentrations of Pb(II) and Cd(II) from bottom to top 0, 1, 3, 6, 10, 20, 50, 100 ppb, respectively (A), and the corresponding calibration curves (B). Electrodeposition was carried out at -1.7 V for 5 min.

Overall, the Bi-C SPE approach presented here clearly outperforms different approaches reported in the literature as summarized in Table 1.3 (Chapter 1) if the fabrication process is taken into consideration. Firstly, this is a simple one-step approach for the development of Bi nanoparticle modified screen printed electrode, in contrast with other works, in which the incorporation of the Bi nanoparticle is performed through an additional step after the electrode is fabricated [1-3]. Secondly, the resulting Bi-C SPE offers better analytical performance compared with other bismuth based screen printed sensors fabricated in one-step [4-6] and

displays a performance which is comparable to that of a two-step fabricated Bi based sensor [2] towards the detection of Pb(II) and Cd(II) in waters. It is important to compare the LOD values of the Bi-C SPE to the threshold values recommended by the European Commission [7] and US Environmental Protection Agency [8] in surface waters (i.e. 0.45-5 ppb for Cd(II) and 10-15 ppb for Pb(II)). It is found that in the case of Cd(II), the LOD of Bi-C SPEs fall within the same order of magnitude of the maximum regulated concentrations while in the case of Pb(II) those are more than one order of magnitude lower, thereby demonstrating the application potential of the sensor for the monitoring of these pollutants in water.

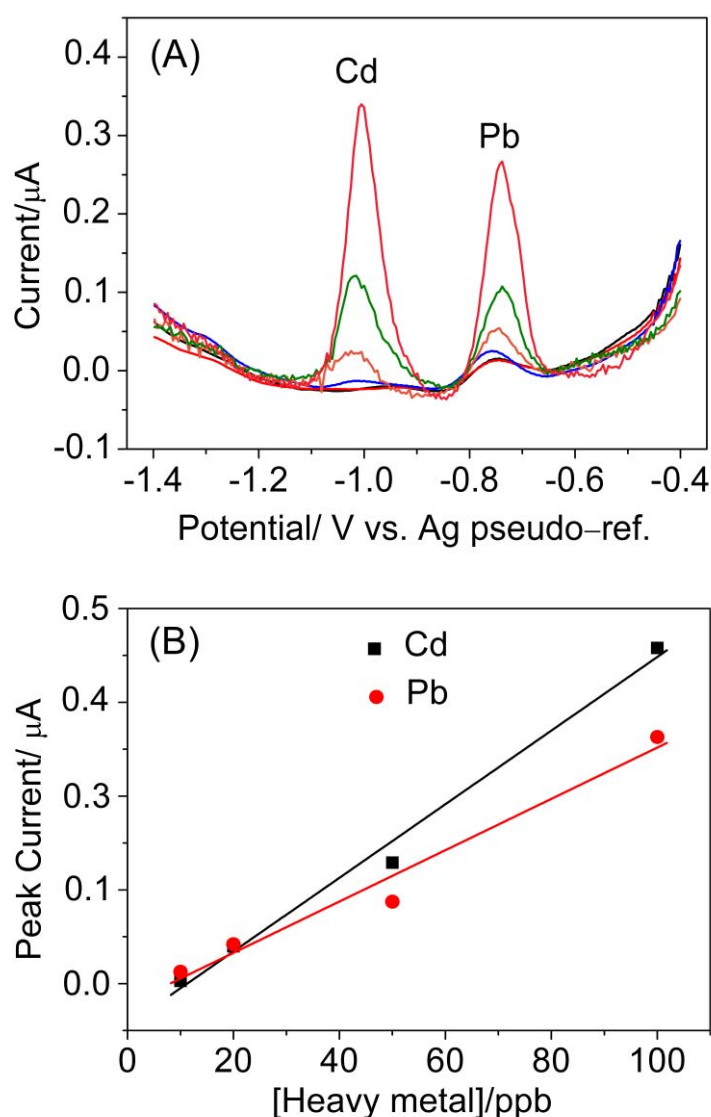


Figure 5.9. SWASV signals recorded in 80 μl of standard 0.1 M acetate buffer solutions pH 4.5 with different concentrations of Pb(II) and Cd(II), from bottom to top 0, 5, 10, 20, 50, 100 ppb (A), and the corresponding calibration curves (B). Electrodeposition was carried out at -1.7 V for 5 min.

One advantage of the screen printed electrodes is the small sample volume required for carrying out the measurements. Herein, we also investigated the electrochemical analysis of a single solution drop containing Pb(II) and Cd(II), by coating the entire area of the screen printed electrochemical cell. Figure 5.9 presents the SWASV signals and the corresponding calibration curves extracted from the voltammograms recorded in 80 μ L drops of the acetate buffer solution containing Pb(II) and Cd(II) in a concentration range from 0 to 100 ppb, after 300s deposition at -1.7 V. Signals for 10 ppb of Pb(II) and Cd(II) were clearly visible and the peak current increased linearly with the concentration of heavy metal ions, demonstrating the applicability of our Bi-C SPE for the analysis of small volume samples.

5.3.4. Comparative Analysis of the Performance of Bi-C SPE with Bi-C CPE

However, it is worth noting that the LODs for Cd(II) and Pb(II) obtained with Bi-C SPEs are higher than those achieved with Bi-C CPEs using the same material (see Table 5.1).

Table 5.1 Comparison study between Bi-C CPE and Bi-C SPE on Pb(II) and Cd(II) analysis

Samples	Linear Range (ppb)		Sensitivity (μ A/ppb per cm^2)		LOD (ppb)		Accumulation time (s)
	Pb(II)	Cd(II)	Pb(II)	Cd(II)	Pb(II)	Cd(II)	
Bi-C CPE	1-100	1-100	1.8×10^{-8}	2.5×10^{-8}	0.65	0.81	180
Bi-C SPE	5-100	5-100	1.2×10^{-9}	1.0×10^{-9}	1.15	2.04	90
	1-50	1-50	2.0×10^{-9}	2.0×10^{-9}	0.60	1.28	300

Under the same experimental conditions, stripping peaks are shifted towards more negative potentials at Bi-C SPEs compared to those recorded with Bi-C CPEs. This is related with the use of a Ag pseudo-reference electrode instead of a Ag/AgCl reference electrode. However, smaller peak currents for both Cd(II) and Pb(II) are recorded (Figure 5.10) with Bi-C SPEs. These results indicate that the performance of Bi-C SPE is not as good as those of Bi-C CPE.

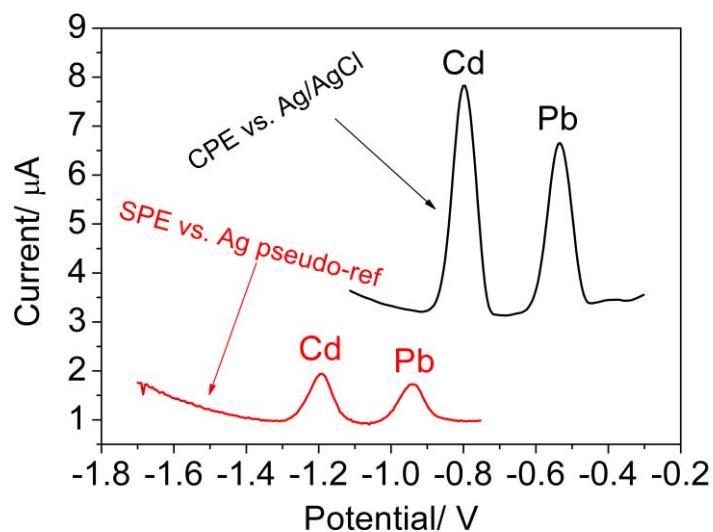


Figure 5.10. SWASV signals recorded in 0.1 M acetate buffer solution pH 4.5 solution containing 30 ppb Pb(II) and Cd(II) at Bi-C CPE and Bi-C SPE. Accumulation was carried at -1.7 V for 3 min at Bi-C SPE (against Ag pseudo-ref) and -1.4 V for 3 min at Bi-C CPE (against Ag/AgCl ref).

One possible explanation for that is the relatively lower Bi content in Bi-C SPEs compared to Bi-C CPEs, which plays a decisive role in the electrode responses.

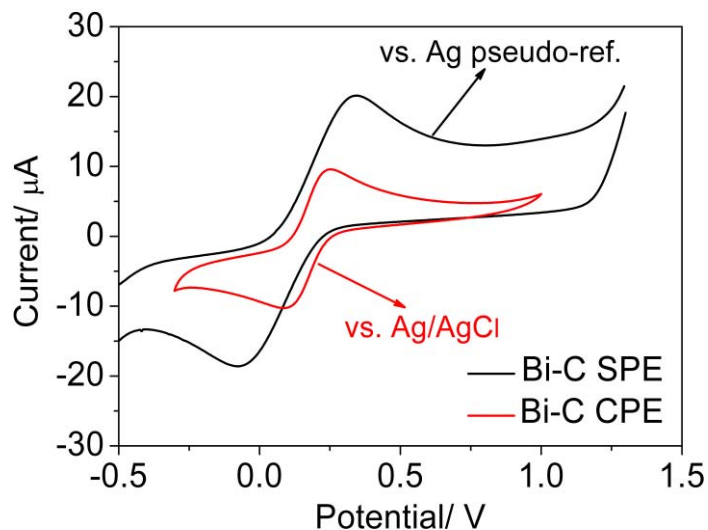


Figure 5.11. Cyclic voltammograms recorded in 0.1 M KNO_3 solution containing 1 mM ferro/ferricyanide redox couple at a potential scanrate of 40 mV/s using Bi-C CPE (3 mm in diameter) and SPE (4 mm in diameter) electrodes.

However, around 40% decrease of Bi amount from Bi-C CPE (4.8 wt%) to Bi-C SPE (2.8 wt%) caused an almost 90% decrease in the peak currents recorded. Besides that, the different conductivity of both electrode surfaces could also have an

influence on such a different behavior. This could also be tested by cyclic voltammetry. Figure 5.11 compares the cyclic voltammograms of ferro/ferricyanide electroactive redox couple recorded at Bi-C CPE and Bi-C SPE at a scan rate of $0.04 \text{ V}\cdot\text{s}^{-1}$. The peak-to-peak potential separation (ΔE_p) at Bi-C CPE is found to be $\sim 150 \text{ mV}$, whereas this value increases to around 400 mV on Bi-C SPE, revealing a much slower electron transfer rate at the surface of Bi-C SPE. This is likely to be related to lower relative content of bismuth/carbon nanocomposite material in Bi-C SPE than in Bi-C CPE, giving rise to a higher electrode resistance of around 5000Ω of Bi-C SPE compared to approximate 500Ω of Bi-C CPE, for electrodes of similar areas.

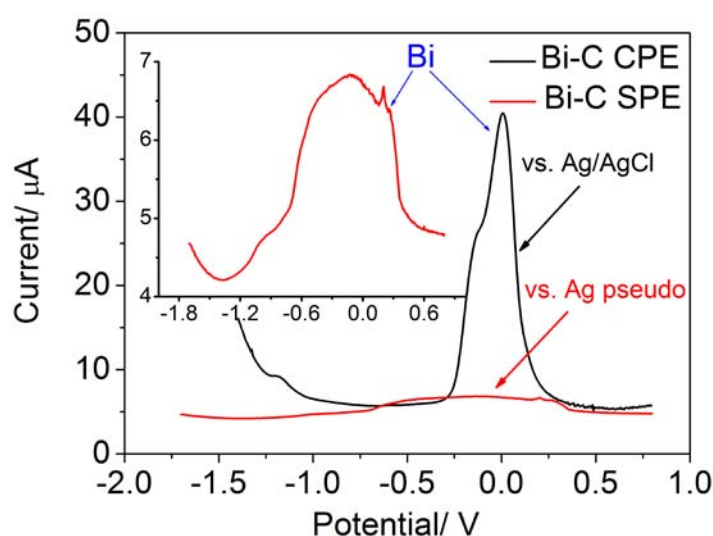


Figure 5.12. SWASV signals of Bi in 0.1 M acetate buffer solution pH 4.5 at Bi-C SPE and Bi-C CPE. Electrochemical reduction was performed for 3 min at -1.4 V (vs. Ag/AgCl) for Bi-C CPE and at -1.7 V (vs. Ag pseudo) for Bi-C SPE respectively.

Apart from displaying a higher resistance, ink formulations also have an unavoidable effect on the performance of the sensor [9]. Figure 5.12 compares the stripping signals of Bi at Bi-C CPE (black curve) and Bi-C SPE (red curve). For Bi-C CPE, a very strong sharp signal ascribed to the stripping of Bi is recorded between -0.3 V and 0.2 V centered at around 0 V and showing a peak height of around $35 \mu\text{A}$. However, for Bi-C SPE, a wide Bi stripping signal was recorded from -0.7 V to 0.5 V centered at around -0.3 V and showing a much smaller peak height of around $2 \mu\text{A}$. Several pretreatment processes were applied on the working electrode aiming at circumventing this negative effect, including electrochemical activation, cleaning by chloride acid solution and even using oxygen plasma. Unfortunately, no clear improvement was observed in the Bi stripping signals after these pretreatments.

Taking into account the different reference electrodes used when recording voltammograms at Bi-C CPEs and SPEs, the integrated Ag-pseudo reference electrode in SPEs was replaced by an Ag/AgCl reference electrode. No obvious change about the shape of Bi stripping process is observed except a ~ 300 mV shift to more positive potentials, as expected.

Although the Bi-C SPE do not perform as well as Bi-C CPE, it should be stressed the practical application of both kinds of electrodes. Bi-C CPEs have been proved to be useful for the analysis of water samples in the laboratory using a conventional three-electrode electrochemical cell. But Bi-C CPEs have to be prepared manually, and thus a scaling up in electrode production is not realistic. By contrast, Bi-C SPEs could be prepared in large quantities in a parallel process which results in more cost-effective, and robust devices that could be deployed in order to carry out measurements in situ [10]. An optimization study of bismuth/carbon nanocomposite ink preparation should be made to improve the stripping process of Bi nanoparticles and the analytical performance of these devices.

5.4. Cu(II) analysis on SPEs without Bi

As we discussed in Chapter 4, a porous carbon material synthesized by the same sol-gel approach but without Bi showed excellent features for the determination of Cu(II). The obtained porous carbon material was used to fabricate screen printed carbon electrodes (C SPE) for the analysis of Cu(II). Figure 5.13 displays the SWASV signals recorded in solutions containing Cu(II) concentrations in the range of 0-70 ppb and the corresponding Cu(II) calibration curve. Two stripping peaks at around -0.22 V and 0 V are clearly visible. The peak appearing at around 0 V originates from the carbon ink itself and not from the accumulation of other metal ions in the acetate solution. This was concluded after observing the same stripping peak when the experiment was repeated using commercial screen printed graphite electrodes supplied by DropSens that were fabricated using an ink formulation similar to the ones applied in this work. The corresponding calibration curve shown in Figure 5.13 (B) exhibits a linear concentration range between 5 ppb and 70 ppb with the LOD being 2.5 ppb, estimated using the same formula as above.

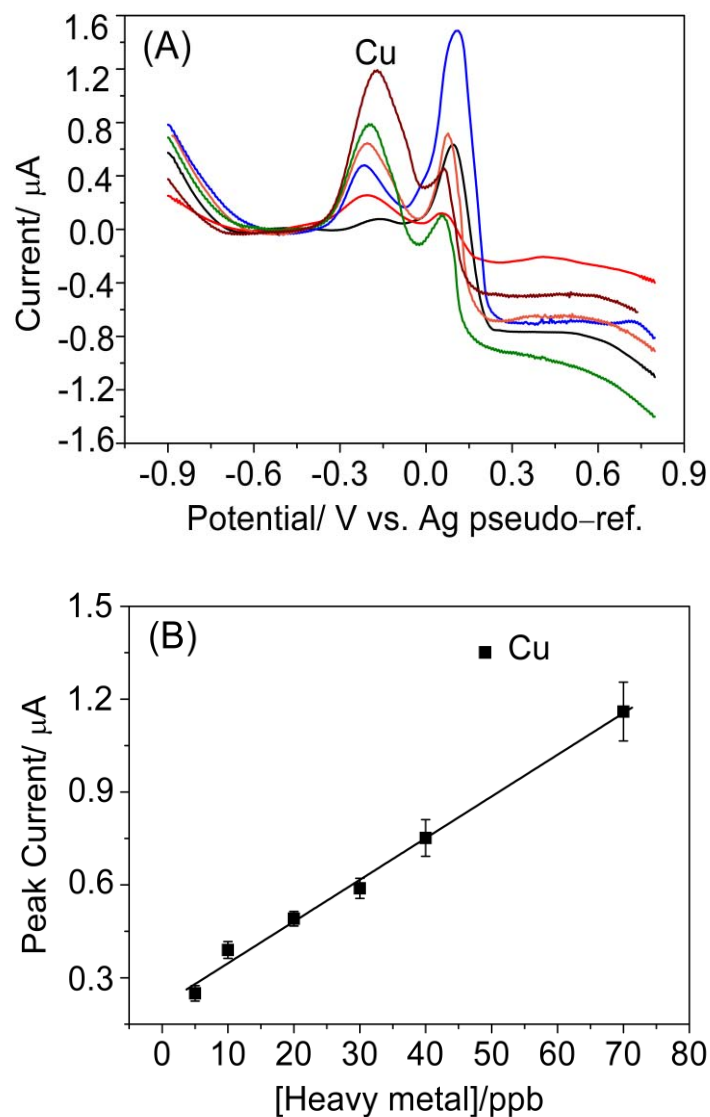


Figure 5.13. (A) SWASV signals recorded in standard 0.1 M acetate buffer solutions pH 4.5 containing different concentrations of Cu(II) from bottom to top 0, 5, 10, 20, 30, 40, 70 ppb, and (B) the corresponding calibration curves. Electrodeposition was carried out at -0.9 V for 5 min.

By carrying out a comparative study with the corresponding CPE counterparts, it can be seen that the carbon based CPE electrodes outperform the SPE presented here as it was also shown in the comparative study between Bi-C CPE and Bi-C SPE. Similarly, an optimization of the ink formulation is expected to improve such analytical behavior.

5.5. Application of the SPEs for the Analysis of Heavy Metals in Waters

Tap water sample from our lab and wastewater sample from an influent of an urban waste water treatment plant located in Terrassa (Barcelona, Spain), were collected aiming at investigating the potential application of our proposed Bi-C SPE for water analysis. The two samples were known to be free of heavy metals. The waste water sample contained a high load of organic matter. A 1:1 dilution of these two samples using a 0.2 M acetate buffer solution pH 4.5 was carried out before doing the analysis. Afterwards, the buffered solution was spiked with known concentrations of Cd(II), Pb(II) and Cu(II) and the recovery values for each heavy metal was calculated.

A preliminary study was performed in tap water by interpolating the recorded peak currents of Cd(II) and Pb(II) into the corresponding calibration curves, and comparing the difference between the interpolated concentration and the added concentration. The buffered tap water sample was spiked in order to get 20 ppb and 50 ppb concentration of Cd(II) and Pb(II). Then, the obtained peak current values after 1.5 min accumulation were interpolated in the calibration curves in Figure 5.6 (B) and the fitting results are summarized in Table 5.2. Recovery values between 89 and 117 % were obtained revealing the good analytical performance of the Bi-C SPEs.

Table 5.2 Results of the analysis of real waters (mean values of three replicates)

Water Samples	Heavy Metals Elements	Known Concentration (ppb)	Analyzed Concentration (ppb)	Recovery (%)	Standard Deviation (ppb)
Tap Water	Pb(II)	20.0	22.9	115	2.5
		50.0	58.5	117	4.6
	Cd(II)	20.0	17.8	89	3.7
		50.0	44.9	90	5
Waste Water	Pb(II)	5.0	5.3	106	0.6
	Cd(II)	5.0	6.0	120	0.9
	Cu(II)	10.0	12.5	125	2.1

Urban waste water with a high load of organic compounds was also analyzed. Although the 1.5 min accumulation time, set for all the previous experiments, was applied in the first place, this was further increased to 5 min in order to make sure that no measurable concentrations of Cd(II), Pb(II) and Cu(II), were present in the sample. Afterwards, 5 ppb of Cd(II) and Pb(II) were simultaneously added to one water sample while a second sample was spiked with 10 ppb of Cu(II). Both of them were analyzed by the standard addition method, and so the possible matrix effects could be taken into account.

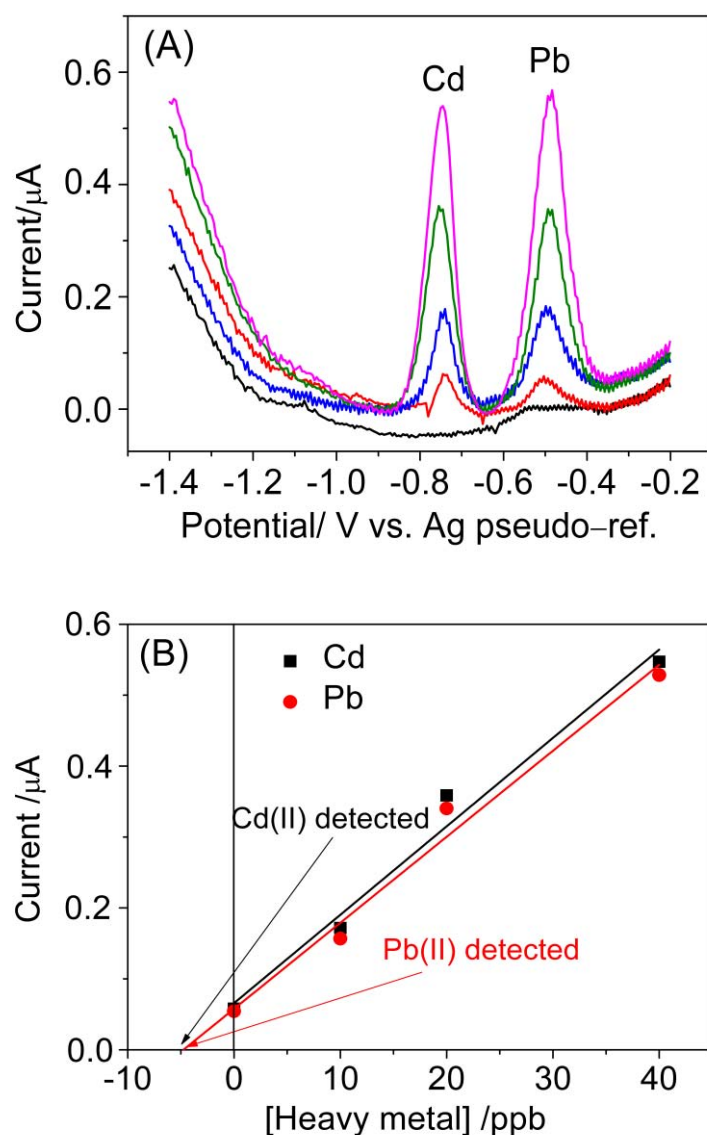


Figure 5.14. SWASV responses recorded in the waste water before and after the addition of different concentrations of Cd(II) and Pb(II), from bottom to top 0, 5, 15, 25, 45 ppb (A), and the corresponding standard addition plots (B). Accumulation was carried out at -1.7 V for 3 min

Figure 5.14 shows the typical SWASV responses recorded in the waste water before and after the addition of Cd(II), Pb(II) and the corresponding standard addition plots. A good agreement between the measured heavy metal concentrations and the added ones was found and results are shown in Table 2. Overall, these results show the adequate analytical performance and practical applicability of the fabricated Bi-C SPEs for the detection of the studied heavy metal pollutants in water samples, even when containing complex matrices.

5.6. Conclusion

In this chapter, the sol-gel derived bismuth/carbon nanocomposite material was successfully implemented for the fabrication of novel disposable miniaturized thick-film electrodes. Powders with an adequate particle size distribution were used to produce robust electrochemical devices. These electrochemical sensors offer competitive analytical performance towards the detection of both Cd(II) and Pb(II) and their adequacy for the analysis of these pollutants in real waters could be demonstrated.

Even though the bismuth/carbon nanocomposite screen printed electrodes did not perform as good as the carbon paste electrodes presented in Chapter 4, it is important to stress that this is a first attempt in the fabrication of bismuth nanoparticle porous carbon screen printed sensor devices using a one-step approach that shows the potential for the cost-effective mass-production of such devices. Further investigation should be directed towards the optimization of the bismuth/carbon nanocomposite ink formulation for further enhancing the analytical performance of the resulting disposable devices and the analytical assessment of other trace heavy metals, such as Ni(II), in water samples.

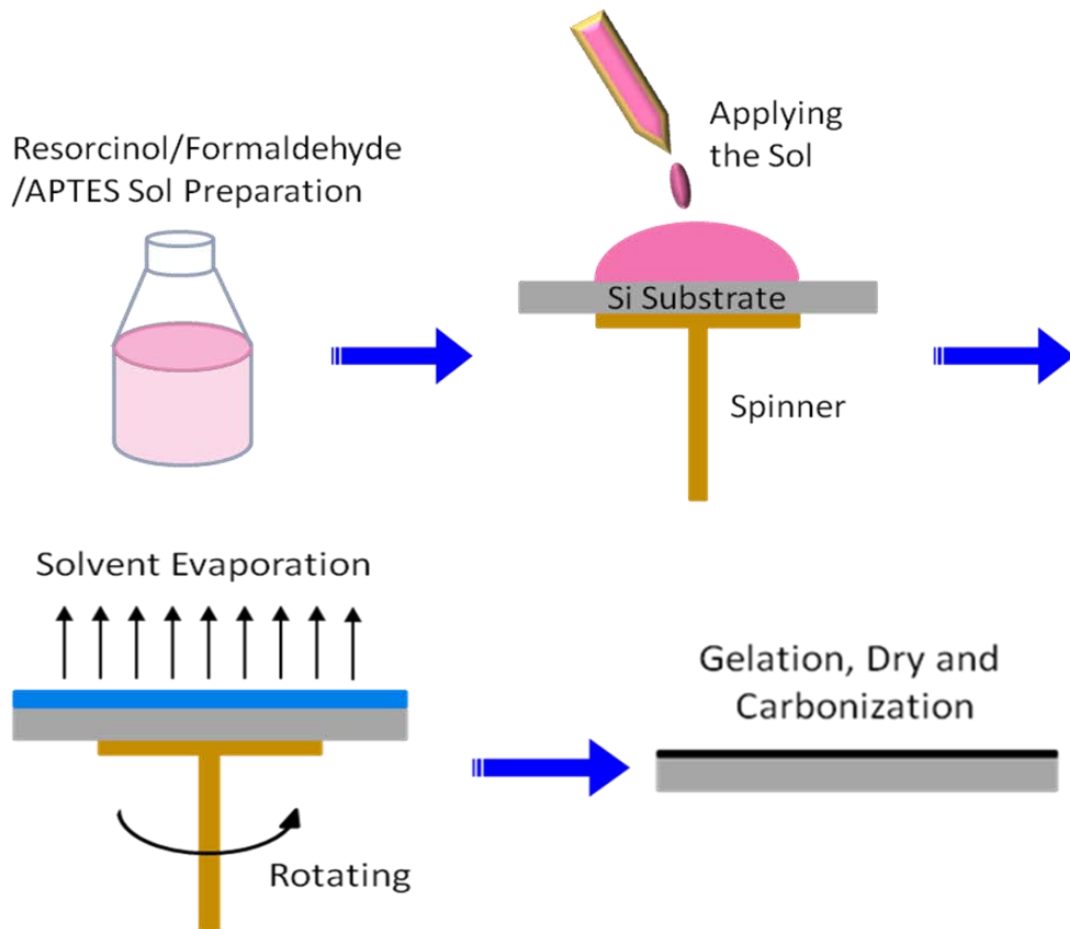
References

- [1] Hwang G-H, Han W-K, Park J-S, Kang S-G. An Electrochemical Sensor Based on the Reduction of Screen-printed Bismuth Oxide for the Determination of Trace Lead and Cadmium. *Sensors and Actuators B: Chemical*. 2008;135:309-316.
- [2] Malakhova NA, Mysik AA, Saraeva SY, Stozhko NY, Uimin MA, Ermakov AE, et al. A Voltammetric Sensor on the Basis of Bismuth Nanoparticles Prepared by the Method of Gas Condensation. *Journal of Analytical Chemistry*. 2010;65:640-647.

-
- [3] Riman D, Jirovsky D, Hrbac J, Prodromidis MI. Green and Facile Electrode Modification by Spark Discharge: Bismuth Oxide-Screen Printed Electrodes for the Screening of Ultra-trace Cd(II) and Pb(II). *Electrochemistry Communications*. 2015;50:20-23.
- [4] Lezi N, Economou A, Dimovasilis PA, Trikalitis PN, Prodromidis MI. Disposable Screen-Printed Sensors Modified with Bismuth Precursor Compounds for the Rapid Voltammetric Screening of Trace Pb(II) and Cd(II). *Analytical Chimica Acta*. 2012;728:1-8.
- [5] Kadara RO, Tothill IE. Development of Disposable Bulk-modified Screen-printed Electrode Based on Bismuth Oxide for Stripping Chronopotentiometric Analysis of Lead (II) and Cadmium (II) in Soil and Water Samples. *Analytica Chimica Acta*. 2008;623:76-81.
- [6] Kadara RO, Jenkinson N, Banks CE. Disposable Bismuth Oxide Screen Printed Electrodes for the High Throughput Screening of Heavy Metals. *Electroanalysis*. 2009;21:2410-2414.
- [7] Zou Z, Jang A, MacKnight E, Wu P-M, Do J, Bishop PL, et al. Environmentally Friendly Disposable Sensors with Microfabricated on-chip Planar Bismuth Electrode for in situ Heavy Metal Ions Measurement. *Sensors and Actuators B: Chemical*. 2008;134:18-24.
- [8] U.S. EPA National Primary Drinking Water Regulations 2009.
- [9] Wang J, Tian B, Nascimento VB, Angnes L. Performance of Screen-printed Carbon Electrodes Fabricated from Different Carbon Inks. *Electrochimica Acta*. 1998;43:3459-3465.
- [10] Wilson D, del Valle M, Alegret S, Valderrama C, Florido A. Potentiometric Electronic Tongue-flow Injection Analysis System for the Monitoring of Heavy Metal Biosorption Processes. *Talanta*. 2012;93:285-292.

Chapter 6

Deposition of C/SiO₂ Thin-films on SiO₂/Si Substrates by Spin-coating



Summary

The results presented in Chapter 5 demonstrate that sol-gel derived bismuth nanoparticles-carbon xerogel nanocomposite powder can be easily applied to the fabrication of screen printed bismuth/carbon nanocomposite electrodes performing as electrochemical sensors for heavy metal detection. As highlighted previously in

this Thesis, sol-gel synthesis is a highly versatile technique and derived materials can be processed in a variety of configurations.

This chapter describes how a carbon based material can be processed as thin-films on planar substrates by a sol-gel process. We explored the possibility of depositing uniform carbon based hybrid films on SiO₂/Si substrates and at wafer level. Firstly, silica gel was incorporated into resorcinol/formaldehyde gels in order to improve the interfacial adhesion between the resulting carbon film and the SiO₂/Si substrate. A series of carbon/silica (C/SiO₂) films of several hundred nanometers thick were deposited on SiO₂/Si substrates of 2 x 2 cm² or on 4-inch wafers by spin-coating technique under optimized conditions. The properties of these C/SiO₂ thin-films were thoroughly investigated, including their electrical conductivity, surface morphology, and electrochemical performance.

Once uniform C/SiO₂ films showing enhanced adhesion to SiO₂/Si substrate were available, we attempted to incorporate metal nanoparticles (Bi or Au) into these films. To this aim, bulk Bi/C/SiO₂ nanocomposites were firstly synthesized using a co-synthesis approach. Afterwards, research was focused on the generation of Bi/C/SiO₂ and Au/C/SiO₂ nanocomposite thin-films on SiO₂/Si substrates.

Part of the work presented in this chapter is being included in a paper under preparation whose tentative title is "**Deposition of Carbon Films on SiO₂/Si Substrates with Enhanced Interfacial Adhesion**", by Pengfei Niu, César Fernández-Sánchez, Martí Gich, and Anna Roig.

6.1. Introduction

From the discussion in Chapter 5, we know that our bismuth/carbon nanocomposite prepared by a sol-gel approach is compatible with the screen-printing technique and can be applied to the one-step fabrication of miniaturized bismuth/carbon thick-film electrodes. However, it should be reminded that, to fabricate screen printed electrodes, an ink formulation should be done that incorporated the bismuth/carbon material together with a curable polymeric binder and other additives. More importantly, the presence of these components made the percentage of the bismuth/carbon material in the electrode to be around 60 % and also they were responsible for the recording of unknown electrochemical signals. Both effects had a negative influence on the performance of the fabricated electrodes. With the aim of overcoming these drawbacks and also reducing the size of the electrodes as well as demonstrating other potential alternative for the processing of these materials as electrochemical devices, the generation of thin-films on solid substrates that could be further patterned to get electrode structures, has been attempted.

Over the past decade, there has been a growing interest in the development of low cost carbon thin-film based miniaturized electrochemical sensing devices. Photolithography technique enables accurate and robust mass-production device manufacturing. However, as mentioned in the general introduction of this Thesis, the so far reported patterned thin-film electrodes using photolithographic approaches are mainly made of metals, particularly gold [1] and bismuth [2]. Carbon is one of the most commonly used working electrode materials, showing allotropic forms, such as graphite, glassy carbon, carbon nanotubes, and graphene as well as amorphous structures. Recently, attention has also been drawn to the mass-scale fabrication of low-cost carbon thin-film electrodes.

Carbon thin-film could be deposited on various substrates. Provided that silicon is the most commonly used starting substrate in microelectronic and microfabrication technologies, this has also been applied to the deposition of carbon thin-films and the fabrication of carbon-based structures. Up to now, several methods have been reported for depositing carbon films on SiO_2/Si substrates, including pyrolysis of carbonaceous thin-films [3, 4], chemical vapor deposition [5-7], sputtering and

electron beam evaporation [8-10]. These can be further processed into carbon thin-film electrodes using different lithographic approaches.

However, as we also mentioned in the Chapter 1 (Introduction section), the films developed by these approaches show several drawbacks, including the weak interaction between carbon film and substrate in all cases, with the pyrolyzed photoresist electrodes also suffering from the serious loss of dimensions both in lateral and vertical directions during carbonization.

With the motivation of developing bismuth/carbon nanocomposite films on SiO₂/Si substrates and patterning it by photolithography to produce miniaturized electrodes, a resorcinol/formaldehyde sol-gel process was employed to grow them by spin-coating technique followed by a carbonization step. Specifically, resorcinol/formaldehyde sol containing Bi metal ions was firstly spin-coated onto a SiO₂/Si substrate. After complete gelation and ageing in an oven, this organic film was converted into a conductive carbon film via pyrolysis under inert atmosphere.

6.2. Development of Carbon Thin-films

A detailed discussion regarding the deposition of carbon films is being presented in detail below. This study has comprised several systematic steps: 1) production, cleaning and activation of SiO₂/Si substrate, 2) preparation of resorcinol/formaldehyde sol, 3) deposition of carbon film through spin-coating process, and 4) evaluation of interfacial attachment.

6.2.1. SiO₂/Si Substrates

4-inch silicon wafers were thermally oxidized at 1000°C to get a 1 μm thick SiO₂ layer. Then, they were diced into 2 x 2 cm² substrates, when required. Before spin-coating, these SiO₂/Si substrates were thoroughly cleaned by immersing them into a ready-prepared piranha solution for at least 30 min. The piranha solution was prepared by adding 7 volume parts of sulfuric acid (98 % H₂SO₄) to 3 volume parts of hydrogen peroxide (30% H₂O₂). The mixing of these two chemicals is highly exothermic and the solution can reach temperatures above 100°C. After cleaning, the substrates were transferred into a fresh mixture of H₂O:H₂O₂:NH₄OH (5:1:1 by

volume) for 10 min to render the SiO₂/Si hydrophilic. Then, the substrates were thoroughly rinsed with deionized (DI) water and ethanol. Finally, the treated substrates were kept in DI water, until use.

6.2.2. Resorcinol/Formaldehyde Sol Preparation

For the synthesis of bulk bismuth/carbon nanocomposite material (Chapter 3), glycerol formal was selected as a solvent for synthesizing resorcinol/formaldehyde gels. However, for the preparation of carbon films on SiO₂/Si substrates, glycerol formal was replaced by water or ethanol because besides being expensive, it also has a high boiling point (~200°C), that would prevent its evaporation during a spin-coating process at room temperature. The chemical formulations of the sol used in the preparation of carbon films are listed in Table 6.1.

Table 6.1 Formula for generating carbon film from resorcinol/formaldehyde sol-gels

Sol	H ₂ O	Ethanol	Na ₂ CO ₃	Acetic Acid	Resorcinol	Formaldehyde
A	1 ml ⁽¹⁾		0.004 g ⁽²⁾		0.4 g ⁽³⁾	0.54 ml ⁽⁴⁾
B		2 ml ⁽¹⁾		0.785 ml ⁽²⁾	0.4 g ⁽³⁾	0.54 ml ⁽⁴⁾

Note: The number in brackets indicates the order in which the different reagents were incorporated to the sol.

Here two sol systems were used for the preparation of resorcinol/formaldehyde sols. The former was a common methodology for synthesizing resorcinol/formaldehyde gels, whereas the later was developed to attain a faster evaporation of solvent during the spin-coating process. The viscosity of resorcinol/formaldehyde sols plays an important role in the morphology and uniformity of the deposited film. If the spin-coating process was carried out readily after sol mixture preparation, no continuous films or even no films at all were obtained due to the absence of colloidal resorcinol/formaldehyde particles in the sol. To obtain a sol with the suitable viscosity for spin-coating, the prepared mixture was sealed in a glass bottle, placed in a hood for 7 days at room temperature, and afterwards spin coated on a substrate.

6.2.3. Carbon Film Deposition

Spin-coating process was performed using a WS-650SZ-6NPP/LITE spinner. For each coating, 500 μl of sol were firstly casted on a 2 x 2 cm² SiO₂/Si substrate. After the substrate was completely covered by the corresponding liquid, the rotation got started at a set rotation speed and duration time of 4000 rpm and 45 s, respectively. However, it must be emphasized that polymerization of resorcinol-formaldehyde gel did not form completely when the rotation was stopped. For a further polymerization and aging of these films, the substrates were placed in an oven at 60°C for more than 4 hours. Finally, they were pyrolyzed at 1000°C for 2 hours under Ar+H₂ (95% + 5%) atmosphere with a flow rate of 100 cm³/min (in a tube of 20 mm in diameter) to convert them into carbon films. The heating rate from room temperature to 1000°C was set to 200°C/h.

6.2.4. Evaluation of the Interfacial Adhesion between Carbon Film and SiO₂/Si Substrate

The interfacial adhesion of carbon film and SiO₂/Si substrate was assessed by ultrasonic treatment in an acetone bath. Figure 6.1 shows images of the films after treatments for 3 min and 10 min, in an ultrasonic bath. A remarkable poor adhesion between pure carbon film and SiO₂/Si substrate is clearly seen in the pictures of Figure 6.1 for both tested times. Due to this weak interaction, the resulting carbon films could not be further used for developing patterned electrode structures by photolithography.

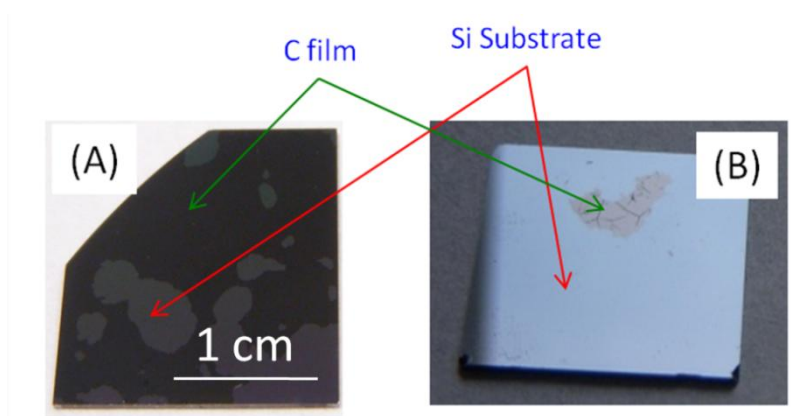


Figure 6.1. Ultrasonically treated carbon film (on 2 x 2 cm² substrate) in acetone for (A) 3 min, (B) 10 min.

A weak interfacial adhesion between resorcinol/formaldehyde derived carbon film and SiO_2/Si substrate is also confirmed by the SEM image shown in Figure 6.2. In addition, the surface morphology displays a very irregular macroporous structure, which may cause a non-uniformity of this carbon film in terms of sheet resistance and electrochemical properties. Some efforts could have been made to grow uniform films by adjusting the conditions to prepare the resorcinol/formaldehyde sol. However, the poor attachment of these films made us leave this approach and try other alternatives.

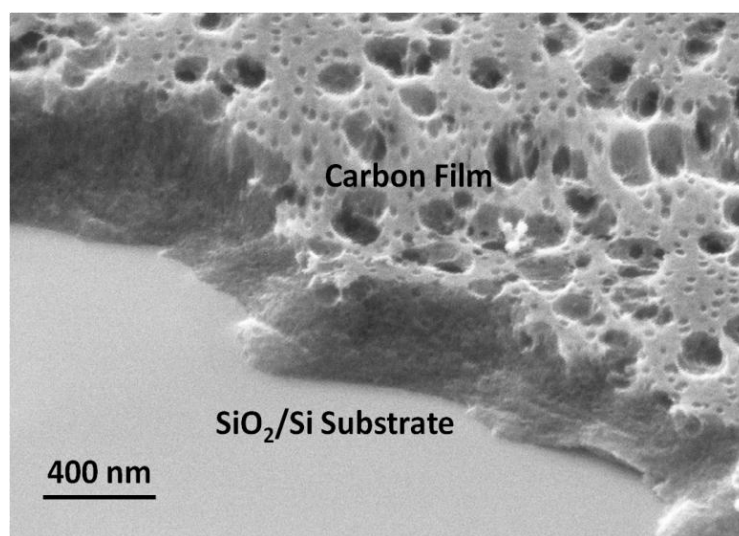


Figure 6.2. SEM image of pure carbon film on SiO_2/Si substrate

6.3. C/ SiO_2 Thin-films with Enhanced Adhesion to SiO_2/Si Substrates

Taking into account the top SiO_2 layer on SiO_2/Si substrates, one possible route to improve the film attachment would be to introduce silica into the carbon precursors, considering the possible formation of covalent Si-O-Si chemical bonds between C/ SiO_2 film and SiO_2/Si substrate. Combining the benefits of producing porous carbon and silica materials individually via a sol-gel process, C/ SiO_2 composite films could also be grown by spin-coating a homogeneous sol containing both carbonaceous and silica precursors. One expected benefit of this approach is that simultaneous gelation of silica and resorcinol/formaldehyde gels would result in an interpenetrating network, giving rise to homogeneous hybrid materials at the macroscopic and even microscopic scale. After a literature review, which has

already been presented in Chapter 1, we followed the approach proposed in 2010 by Ye et al. [11] in which the bulk C/SiO₂ aerogel composite were synthesized by simply mixing resorcinol, formaldehyde, and aminopropyltriethoxysilane (APTES) in ethanol solvent but with a slight modification, with the aim of producing carbon based films fast and effectively.

6.3.1. RF/APTES Sol Preparation

Table 6.2 lists the composition of the sols employed for synthesizing the C/SiO₂ films. Reagents were added in the following order: 1) ethanol (or ethanol/acetic acid mixture), 2) APTES, 3) resorcinol and then 4) formaldehyde. More specifically, a certain amount of APTES was firstly dissolved in ethanol (E) (or ethanol/acetic acid mixture). Then, resorcinol (R) was added into the mixture. After obtaining a clear colorless solution, formaldehyde (F) was incorporated, and the mixture was vigorously stirred for 5 minutes. We found that the systems without acetic acid gelled quite fast, especially when the molar ratio between R and APTES was equal to 1.

In this Thesis, the R/APTES molar ratio for synthesizing C/SiO₂ composite film was varied between 1 and 4 and this is indicated in the labeling of the prepared materials by the two digits following CS, these being the relative molar content of resorcinol and APTES, respectively (see 1st and 5th columns of Table 6.2). Acid is always considered as catalyst of both RF and silica sol-gel processes. However, we observed accidentally that the gelation rate of RF/APTES system was significantly slowed down after adding even a small quantity of acetic acid and the required entire gelation time also increased with the content of acetic acid in the system. It is known that the presence of amine group in APTES show base properties and thus can catalyze the inter- or intra-molecular reactions between silane molecules and silanol groups to form siloxane bonds [12], which is one of the steps of the RF/APTES gelation process. With the addition of acetic acid, the gelation turns to be slower. We think that the incorporation of acetic acid neutralizes the base properties of amino group and thus weaken its catalytic effect, correspondingly slowing down the gelation of RF/APTES system.

Table 6.2 Composition of the sols used in the preparation of C/SiO₂ films

Samples	R (g)	F (ml)	APTES (ml)	Molar Ratio (R:F:APTES)	E (ml)	Acetic Acid (μ l)	GT	AT	Thickness (nm)
C-A	0.4	0.54			2	785	7 days	5 days	300-400
CS41	0.4	0.54	0.21	1:2:0.25	2		0.5 h	0.15 h	700-800
CS41-A _L	0.4	0.54	0.21	1:2:0.25	2	50	10 h	1 or 5 h	400-500 or 700-800
CS41-A _H	0.4	0.54	0.21	1:2:0.25	2	785	3 days	1 day	400-500
CS21-A1	0.4	0.54	0.42	1:2:0.5	2	785	1 day	1 h	400-500
CS21-A2	0.4	0.54	0.42	1:2:0.5	4	785	2 days	1 h or 1 day	360-420 or 600-700
CS11-A	0.4	0.54	0.84	1:2:1	4	785	10 h	1 h	400-500

Note: GT, gelation time of the system; AT, aging time before coating

6.3.2. C/SiO₂ Films Deposition on SiO₂/Si Substrates

In order to obtain C/SiO₂ thin-films, a homogeneous RF/APTES sol was spin-coated on SiO₂/Si substrates. Herein, the selection of appropriate sols plays a key role in the success of spin-coating a continuous and uniform film on a substrate. As we have mentioned in section 6.1, it was very difficult to generate a uniform and continuous RF film on a SiO₂/Si substrate by spin-coating RF sols either in water or ethanol solvents, since on the one hand these systems gel quite slowly, and on the other hand, RF gels exhibit very weak interactions with Si/SiO₂ substrate. The incorporation of APTES into RF sols allows preparing films of better quality, both due to the faster gelation time as listed in Table 6.2 and the enhanced interfacial interaction between RF/SiO₂ film and SiO₂/Si substrate. After coating, these films aged and were dried in an oven at 60°C for more than 4 hours. Dried RF/SiO₂ films were converted to C/SiO₂ films by carbonization under Ar+H₂ (95%+5%) atmosphere at 1000°C for 2 h. A reducing gas was used with the aim of producing a highly conductive film. During pyrolysis, RF/SiO₂ film underwent significant changes. Firstly,

the films turned from transparent to black. Secondly, they experienced a significant reduction in thickness.

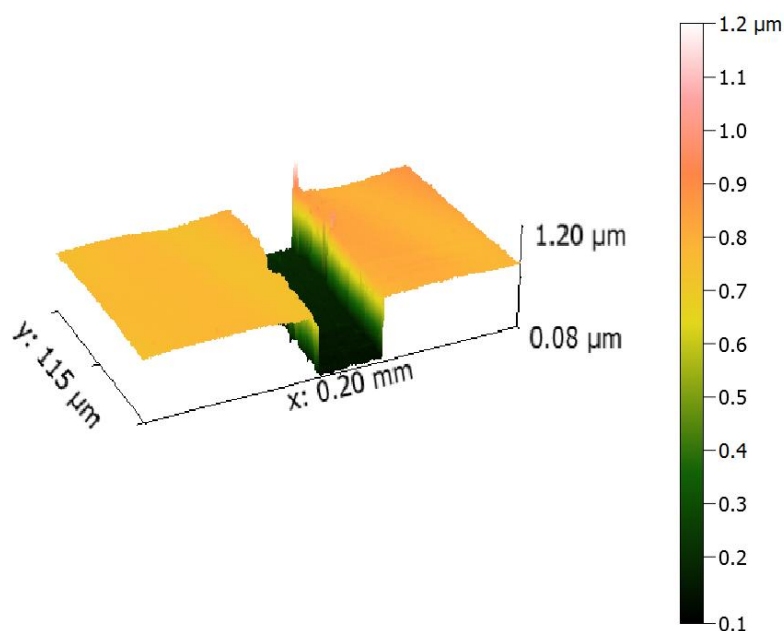


Figure 6.3. Typical profilometer image for measuring film thickness

The thickness of the film was measured using a KLA profilometer. For carrying out measurements, 3 nicks were firstly made with steel tweezers at different zones from the center to the border of the film and a square of $200 \times 200 \mu\text{m}^2$ on each nick was scanned. Taking into account the results obtained in these three zones, the thickness variation of the entire film was estimated. A typical analytical profilometer image for testing film thickness is displayed in Figure 6.3. The results obtained for all the studied materials are summarized in Table 6.2.

When depositing the films, we observed that the average thickness of RF/SiO₂ film deposited from the same sol decreases by increasing the spin-coating speed from 1000 rpm to 3000 rpm (for 30 s of spinning) as expected, and then tends to level off at higher speeds. To obtain a reproducible and homogeneous film, in this Thesis the selected spin-coating conditions were 4000 rpm for 45 s.

Besides the spinning conditions, sol viscosity plays a key role in the final thickness of the film. In principle, it increases with reaction time and a more viscous sol results in a thicker C/SiO₂ film. However, thicker films tend to present cracks. Moreover, the differential shrinkage behavior of RF and silica during the drying and carbonization stages increases the likelihood of crack formation. Herein, sols with viscosities

ranging from 6 to 10 mPa·s resulted in crack-free C/SiO₂ films with thickness of around 400-800 nm. Using sols with viscosities higher than 11 mPa·s would produce C/SiO₂ films thicker than 1000 nm but with cracks as shown in Figure 6.4.

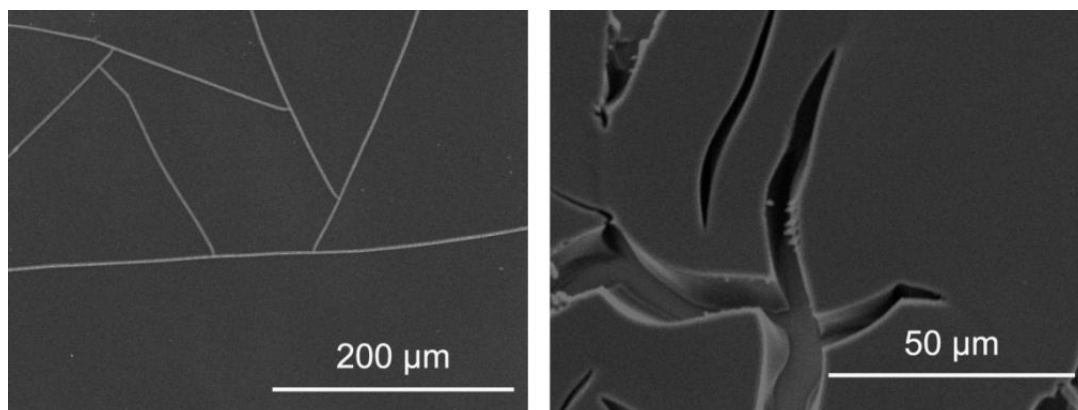


Figure 6.4. Cracks observed in C/SiO₂ films having thickness above 1000 nm

Using the optimized conditions mentioned above, a series of C/SiO₂ films with different SiO₂ content and thicknesses were obtained. Regarding thickness reduction after carbonization, taking sample CS21-A2 as an example, the average film thickness decreased from ~1450 nm to ~650 nm, this being an almost 55% reduction in thickness. Taking into account the fact that the SiO₂ xerogel shrinks less than the RF xerogel during pyrolysis, it is expected that the thickness would decrease less for samples containing more SiO₂. Indeed, in the case of sample CS11-A, which contains the largest amount of SiO₂, approximately a 50% reduction in thickness was observed. Although the presence of acetic acid in the CS41 sample series appeared to significantly slow down the gelation, we did not observe an obvious influence of this parameter on the shrinkage of the film and in turn the final film thickness. Finally it is worth mentioning that even though a large reduction of the vertical dimensions of C/SiO₂ films was observed after carbonization process, none of the presented C/SiO₂ films shows shrinkage of the lateral dimensions no matter whether these films were prepared on 2 x 2 cm² squared substrates or 4 inch wafers.

By comparison with pure carbon films, the remarkable improvement in interfacial adhesion between C/SiO₂ films and SiO₂/Si substrates is illustrated by Figure 6.5 (A), which shows an image of C/SiO₂ film after being treated ultrasonically in an acetone bath for 3 min compared to the carbon film after the same treatment. We believe

that the enhanced adhesion is directly related to the formation of Si-O-Si covalent bonds between SiO₂ xerogel and SiO₂ layer on SiO₂/Si substrate. In addition, no film detachment took place with any of the samples listed in Table 6.2 after ultrasonic treatment in acetone. This indicates that a molar concentration of 20% of APTES in the sol is already sufficient to create a C/SiO₂ film with strong interfacial adhesion to SiO₂/Si substrates. The focused ion beam scanning electron microscopy (FIB-SEM) image displayed in Figure 6.5 (B) shows a good homogeneity of C/SiO₂ film without macro-phase separation and an apparent strong adhesion to the SiO₂/Si substrate.

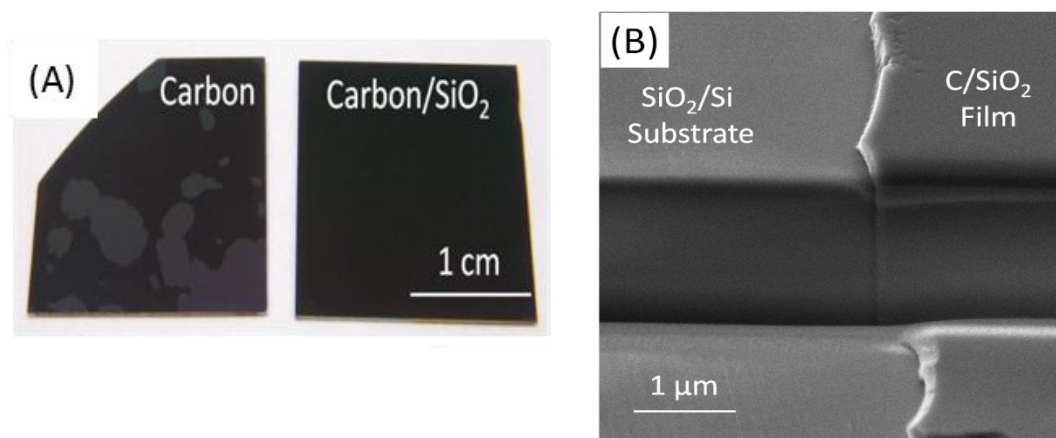


Figure 6.5. Representative images of carbon and C/SiO₂ films after ultrasonic treatment in acetone bath for 3 min (A) and FIB-SEM image of C/SiO₂ film on SiO₂/Si substrate (B).

Thin-film residual stress caused from the deposition process may have drastic effects on the device performance. For instance, during an experiment, we found that the contact with solvents such as ethanol or acetone lead to size reduction and folding of pure carbon film. However, this phenomenon did not occur in SiO₂ containing carbon films, once again revealing a much stronger film/substrate interfacial strength.

6.3.3. Characterization of the Films

After the preparation of C/SiO₂ films, their surface morphology and electrical conductivity were firstly characterized.

6.3.3.1. Film topography

A representative optical image of film surface is shown in Figure 6.6 (A) and a surface profile recorded with a profilometer is illustrated in Figure 6.6 (B).

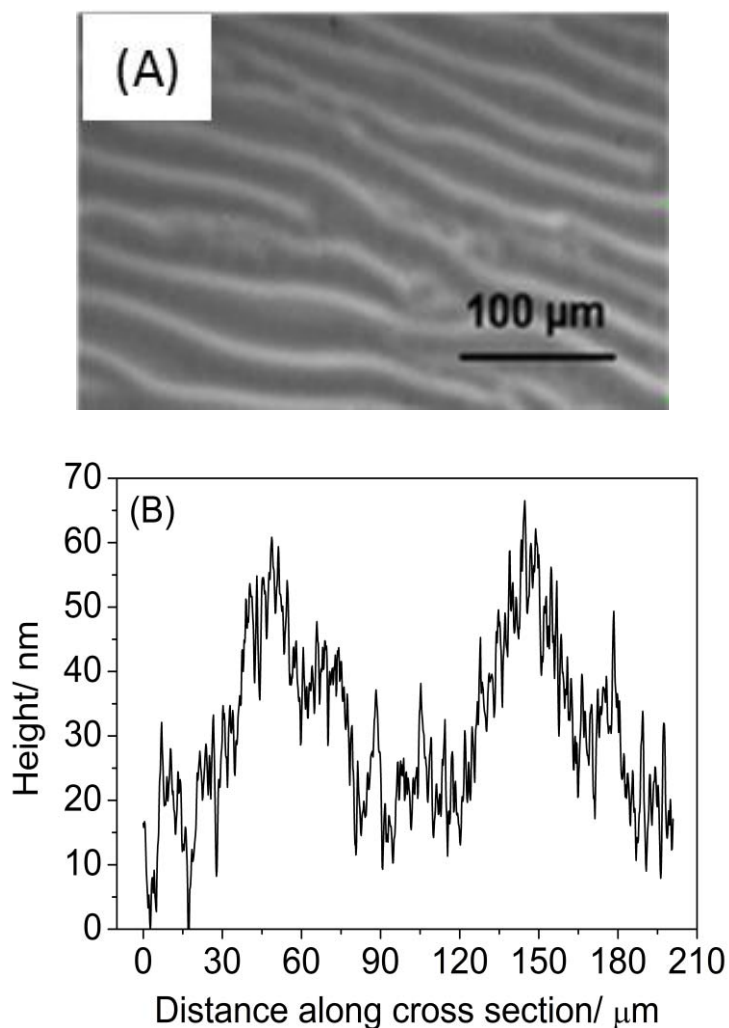


Figure 6.6. Optical image (A) and profilometer trace (B) of C/SiO₂ film surface

This shows that the C/SiO₂ film surface was not flat. It presents roughness at two scales: that is a wave-like morphology with amplitude of about 50 nm and a smaller scale roughness superimposed to that. This is a common feature of spin-coated films and has been related to the rapid drying of the deposited film during the spin-coating process, especially when a low boiling and volatile solvent such as ethanol is employed [13]. However, in comparison with a 400-800 nm thick C/SiO₂ film and a ~1700 nm thick photoresist coated afterwards for carrying out photolithography process, the ~50 nm wave amplitude height difference shows a negligible influence on the photolithography patterning process as will be presented in Chapter 7. In addition, wave topography is expected to be advantageous for electrochemical sensor applications because of a significantly larger surface area exposed to the electrolyte compared to that of a flat surface.

AFM was used to analyze surface roughness of C/SiO₂ film. A 1 μm² squared area was scanned. Figure 6.7 shows a typical AFM image recorded with CS21-A sample and a surface roughness value of less than 0.6 nm was obtained. Such small roughness indicates the excellent homogeneity of these sol-gel derived C/SiO₂ films. In addition, roughness values below 1 nm obtained in a 1 μm² area for all the samples listed in Table 6.2 indicate a negligible effect of the chemical composition and film thickness on film surface roughness.

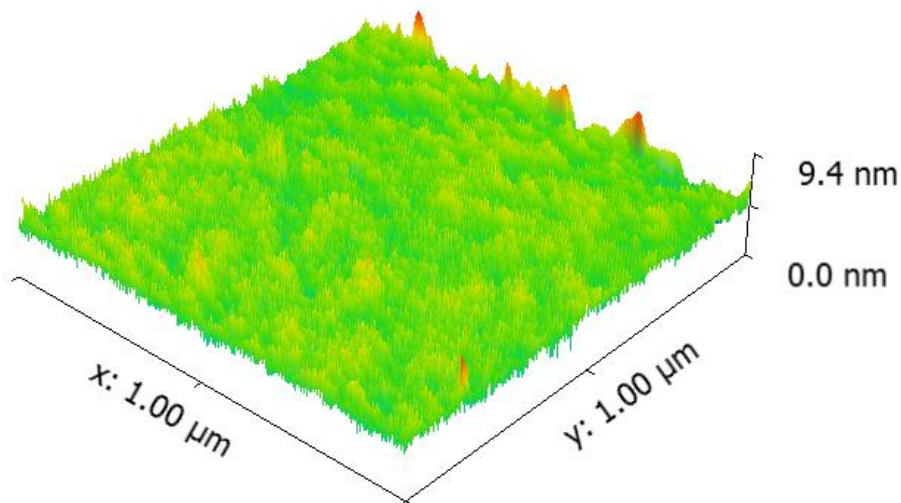


Figure 6.7. Representative AFM image of C/SiO₂ film

6.3.3.2. Sheet Resistance of the C/SiO₂ Films

Table 6.3 Sheet resistance of films with different SiO₂ amount

Sample	C-A	CS41	CS41-A _L	CS41-A _H	CS21-A1	CS11-A
T(nm)	300	800	400/800	400	400	400
R(Ω/□)	652±410	510±82	1280±95 or 750±110	1360±130	1900±190	5200±320
C(S/cm)		20.8-29.7	17.8-20.8	16.7-20.5	11.9-14.7	4.5-5.1

Note: C-electrical conductivity; R- sheet resistance; T-thickness; C falls into the ranges because of the associated error of R.

The addition of APTES makes the deposition of carbon films much easier and strongly improves their interfacial adhesion to SiO₂/Si substrate. However, the presence of SiO₂ also hinders the charge transport through carbon phases, resulting in a higher resistance of C/SiO₂ film compared to pure carbon film. Table 6.3

summarizes the sheet resistance as a function of SiO₂ content in C/SiO₂ films measured by a general purpose four point probe setup. C/SiO₂ films with an average thickness of ~400 nm were selected for comparison, except for the pure carbon film with a thickness of ~300 nm. The sheet resistance increases with the increase of the non-conducting SiO₂ content. The highest sheet resistance value was measured to be 5200Ω/□ on CS11-A film. Assuming an average thickness of 400 nm, the conductivity was calculated to be ~5 S·cm⁻¹. This conductivity value is comparable to that of typical screen printed carbon inks used in electrochemical sensing (1-10 S·cm⁻¹). Regarding the CS41-A film sample (400 nm thick), the calculated conductivity value is nearly 4 times higher than that of CS11-A.

Interestingly, when comparing samples CS41 (700-800 nm thick) and CS41-A (700-800 nm thick) sample, it is noticeable that the film generated from a sol containing acetic acid shows a somewhat higher sheet resistance than that prepared from sol solutions without acetic acid. We think that this is due to the differences in the surface chemical composition of C/SiO₂ films generated under different environment. To find evidences that supported this hypothesis we performed XPS analysis that was carried out in an ultrahigh vacuum Kratos Analytical spectrometer using Al K_α X-rays. Figure 6.8 shows XPS spectra and Table 6.4 lists the elemental composition of the films, showing a relative higher content of Si and O but a lower C content on the surface of the sample made from a sol containing acetic acid.

Table 6.4 Surface elemental composition of CS41 and CS41-A film

Sample	C 1s %	O 1s%	Si 2p%		Si 2p (103.4 eV)	Si 2p (101.9 eV)
CS41	80.6	14.9	4.5		82.8	17.2
CS41-A	76.8	17.6	5.6		93.5	6.5

Among the three peaks of C(1s), O(1s), and Si(2p), the Si(2p) spectra shows a quite different shape in these two samples. Both of them can be decomposed into two peaks using Gaussian curve fitting ascribed to oxidized silicon and centered at around 103.4 and 101.9 eV (Figure 6.8 (C)), in which the 103.4eV peak is for silicon dioxide and the 101.9 eV falls in the binding energy range of suboxides (SiO_x, with x<2) [14], But as can be seen from Table 6.4, the relative content of SiO_x in CS41 film is much higher than that in CS41-A film. It confirms our previous hypothesis

that the presence of acetic acid changes the gelation process of APTES by blocking the catalytic effect of amino group and makes the material to gel more slowly.

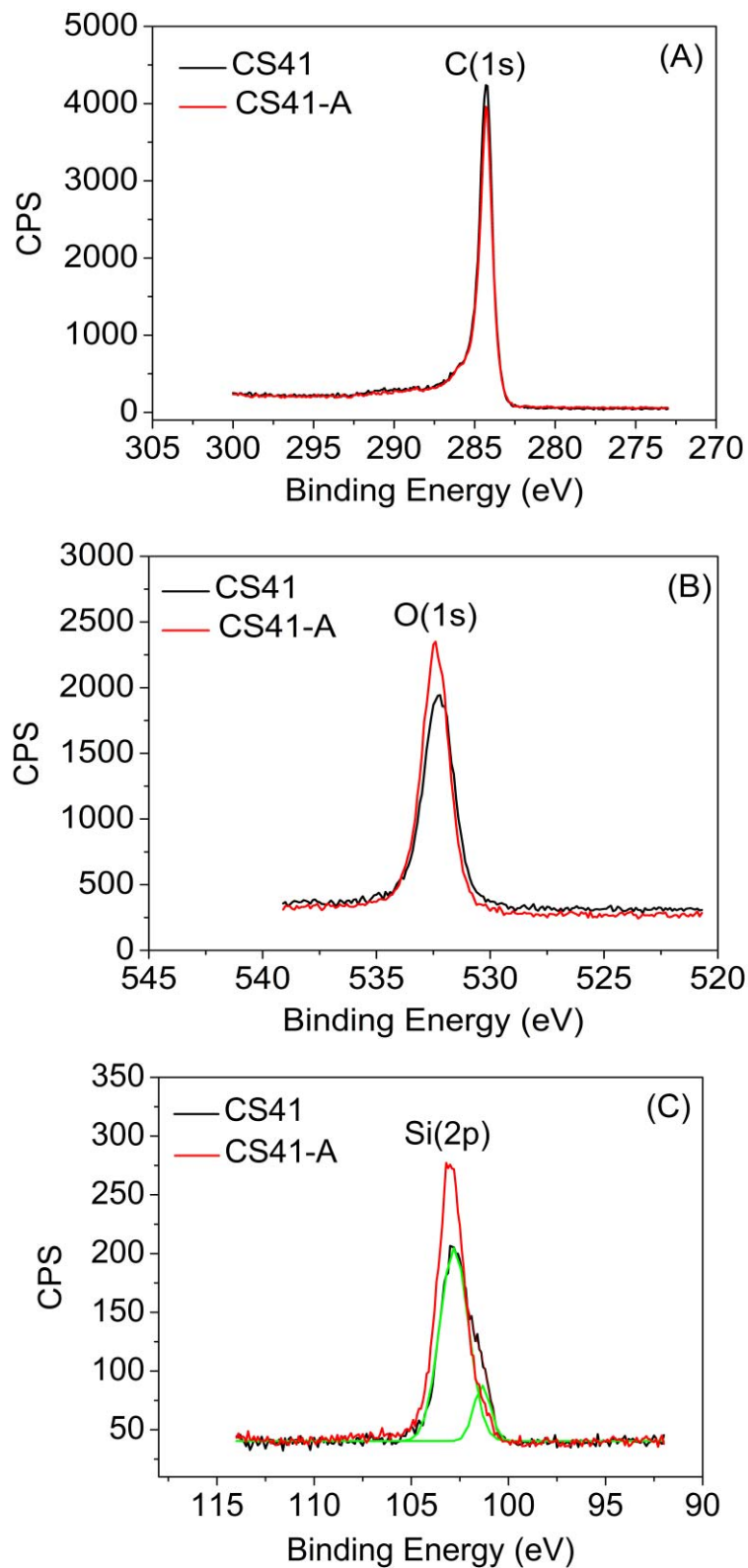


Figure 6.8. XPS spectra of CS41-A and CS41 films

However, there is one question that must be answered. Why does the system without acetic acid result in a C/SiO₂ film (CS41) with somewhat lower content of SiO₂ on the surface? We think it may be associated with the gelation processes of resorcinol/formaldehyde/APTES in both systems.

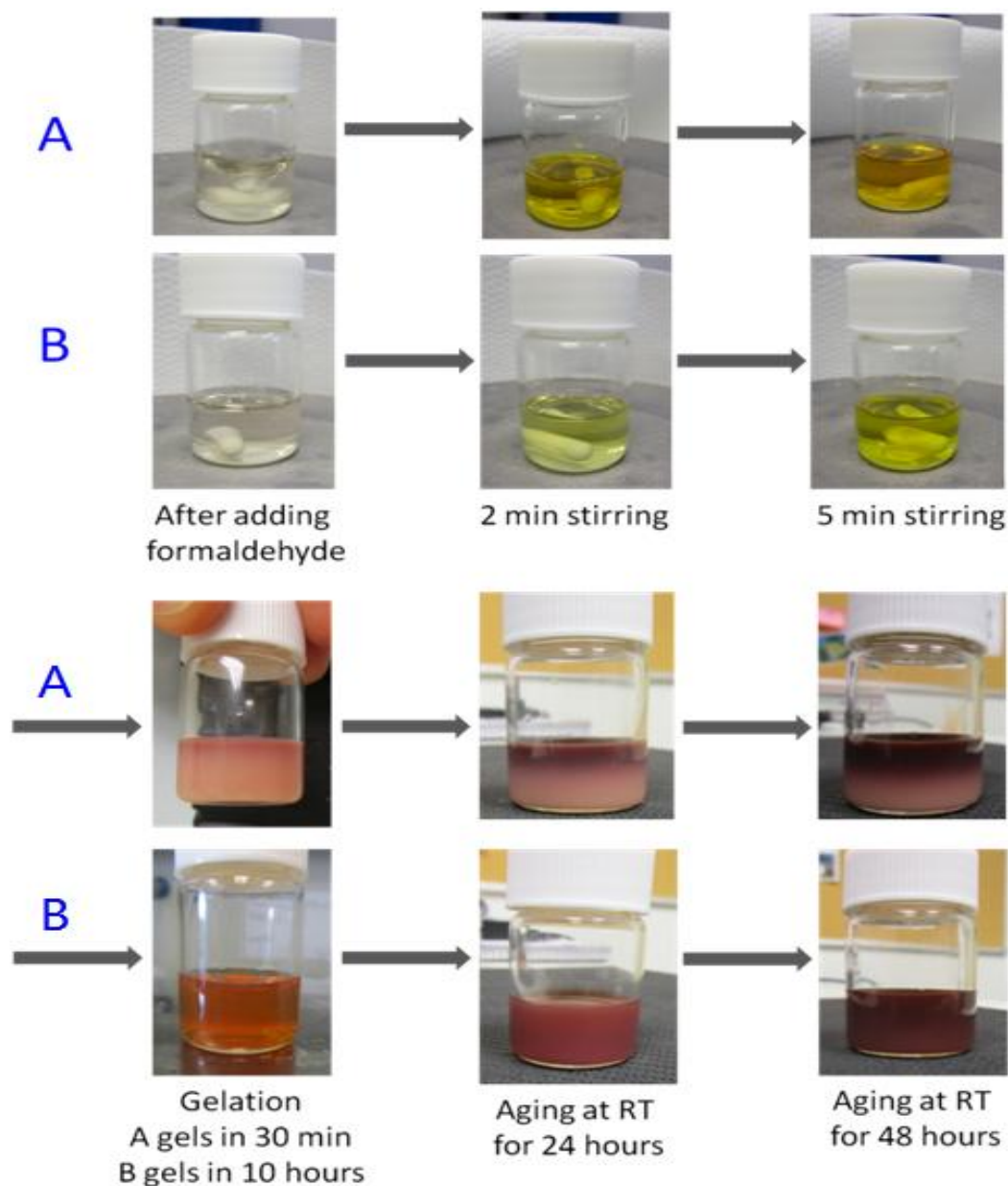


Figure 6.9. Images of CS41 (A) and CS41-A_l (B) gel preparation process, RT- room temperature

Gelation studies in films are very difficult and thus these were performed in bulk. Figure 6.9 shows the images of resorcinol/formaldehyde/SiO₂ gels prepared without (Figure 6.9 (A)) and with (Figure 6.9 (B)) acetic acid. The presence of acetic acid in the sol results in a more homogeneous gel than the ones synthesized without acetic

acid, which presented a lighter color at the bottom of the gel but darker color at the top. SiO₂ gels are normally white in color and resorcinol/formaldehyde gels are red in color. Therefore, it can be concluded that the amount of SiO₂ in the gel synthesized without acetic acid is somewhat rich at the bottom but a little bit poor at the top, showing a concentration gradient from the top to the bottom of the gel. This phenomenon could be extrapolated to the films. Consequently, the CS41 C/SiO₂ film contained a little bit lower amount of SiO₂ on the surface than CS41-A film, resulting in the more conductive film surface.

However, what is the reason behind the inhomogeneity of the gel synthesized from a sol without acetic acid? As can be seen in Figure 6.9, the color of the gel prepared in the presence of acetic acid was always homogeneous during the whole gelation and aging process, revealing the simultaneous gelation of resorcinol/formaldehyde and APTES. However, with respect to the gel made from a sol without acetic acid, the gel color was white firstly and then turned to be red but showing a color ramp from the top to the bottom of the gel. We think that in a sol solution without acetic acid, APTES gelled faster than resorcinol/formaldehyde and therefore the SiO₂ clusters moved towards the bottom of the gel due to its higher density.

6.4. Electrochemical Performance of C/SiO₂ Thin-films

Before patterning C/SiO₂ films by standard photolithography, their electrochemical properties were firstly investigated by cyclic voltammetry. The supporting electrolyte was a 0.1 M KNO₃ solution containing 1 mM ferri/ferrocyanide redox species.

In order to carry out these measurements, the film area to be used as the working electrode was defined by attaching an open plastic cuvette with a diameter at the bottom of 3 mm. This was glued to the film surface using silicone. The set-up is shown in Figure 6.10. In order to contact the film electrically, an Al wire was fixed onto one corner of the C/SiO₂ substrate with the aid of silver paste. When carrying out the measurements, a silver wire pseudo-reference electrode and a stainless steel wire counter electrode were immersed in the cuvette to complete the electrochemical cell.

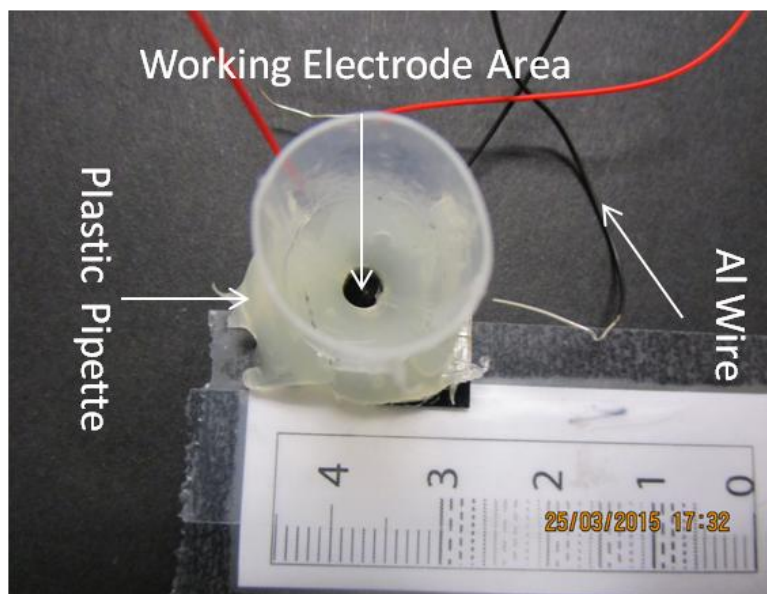


Figure 6.10. Image of the home-made electrochemical cell for carrying out the electrochemical characterization of the films

6.4.1. Cyclic Voltammetric Studies of the Responses of C/SiO₂ Films with Different SiO₂ Content

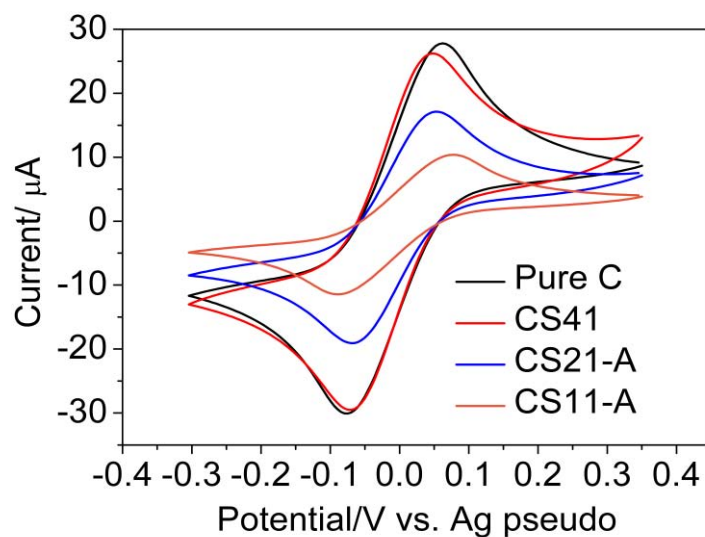


Figure 6.11. Cyclic voltammograms recorded with C/SiO₂ films with different silica content, in a 0.1M KNO₃ solution containing 1mM ferri/ferrocyanide redox couple. Scan rate: 50mV/s.

Figure 6.11 displays typical cyclic voltammograms recorded with these C/SiO₂ films containing different silica contents. Overall, quasi-reversible electrochemical responses were recorded that show an anodic to cathodic peak current ratio of

around 1. A comparative study of the responses of all the films having different SiO₂ content (i.e. CS11-A, CS21-A, and CS41), show that the peak to peak potential separation (ΔE_p) appreciably decreases from ca. 167 to 137 mV when the SiO₂ content decreases whereas the faradic peak currents increase from 10/-11 μ A to 26/-29 μ A. The higher peak current and lower ΔE_p values indicate a larger active surface area and a faster electron transfer at the liquid C/SiO₂ film interface. This is the expected behavior taking into account the lower sheet resistance of films with higher carbon content. Surprisingly, pure carbon films showed a similar peak current but larger ΔE_p compared to those recorded with CS41 films. This might be related to its surface defects, such as holes and cracks presented in the films (as shown in Figure 6.2) that negatively affected the film electrochemical performance.

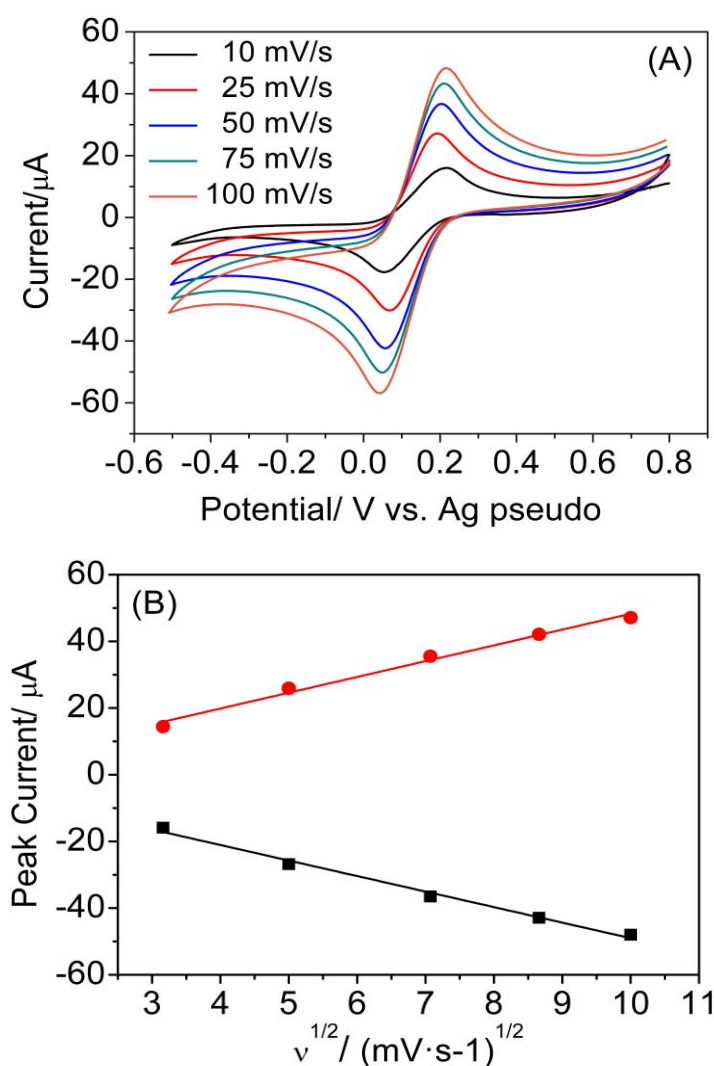


Figure 6.12. Cyclic voltammograms recorded with CS41 films at different scan rates, in a 0.1 M KNO₃ solution containing 1mM ferri/ferrocyanide redox pair (A) and plots of anodic peak and cathodic peak current vs. scan rate (B).

The mechanism of the electrochemical reaction at the surface of these C/SiO₂ films electrodes was also investigated. To this aim, the influence of the scan rate on the peak currents was studied with the CS41 film. The recorded peak currents in ferri/ferrocyanide system as shown in Figure 6.12 are proportional to the square root of scan rate in the range of 10 to 100mV/s. This is the usual behavior of a diffusion controlled electrode process.

6.4.2. Estimation of the Electron Transfer Rate at the Film/Electrolyte Interface

Figure 6.13 compares the cyclic voltammetric responses recorded at bismuth/carbon nanocomposite paste electrode (Bi-C CPE) as prepared in Chapter 4, screen printed graphite electrodes from DropSens (SPGE with reference catalogue number - DRP 110), and CS41 film electrode. At a scan rate of 50mV/s, ΔE_p values of around 254, 181, and 137 mV were obtained, respectively. The smaller ΔE_p value indicates a faster electron transfer at CS41 film/electrolyte interface. The heterogeneous electrochemical rate constant k^0 was also calculated for a direct comparison of CS41 C/SiO₂ film with the Bi-C CPE and SPGE using the Nicholson method (eq.1) [15],

$$\varphi = k^0 [\pi D n \nu F / (RT)]^{-1/2} \quad (\text{eq.1})$$

where D is the diffusion coefficient of potassium ferricyanide in 0.1 KNO₃ (ca. 7.01 x 10⁻⁶ cm²·s⁻¹) [16], n is the number of electrons involved in the electrochemical reaction, which in the case of potassium ferricyanide reaction is equal to one, ν is the scan rate in V/s, F is the Faraday constant, R is the universal gas constant and T the absolute temperature. As dimensionless kinetic parameter, φ is first determined using the following analytical equation.

$$\varphi = (-0.6288 + 0.0021 * \Delta E_p) / (1 - 0.017 * \Delta E_p) \quad (\text{eq.2})$$

As a consequence, in 1 mM potassium ferricyanide solution, the k^0 for CS41 C/SiO₂ film was calculated to be 0.0510 cm/s, demonstrating a favorable electron transfer rate compared with SPGE and Bi-C CPE, whose estimated k^0 values were 0.0278 cm/s and 0.0138 cm/s, respectively. In addition, the calculated k^0 values for CS21-A

and CS11-A C/SiO₂ films were estimated to be 0.0486 cm/s and 0.033 cm/s, respectively. These values indicate a slower transfer kinetics of films having an increase of SiO₂ content. It is known that the electron transfer rate at carbon based electrodes depends on the structure and morphology of carbon materials, and k^0 value typically ranges from 10^{-4} to 10^{-2} cm/s [17]. In comparison with Bi-C CPE and SPGE, these C/SiO₂ films do not incorporate any extra additives to the functional materials such as paraffin (CPE) or curing binders (SPE) and offer an enhanced performance as electrochemical sensing platforms.

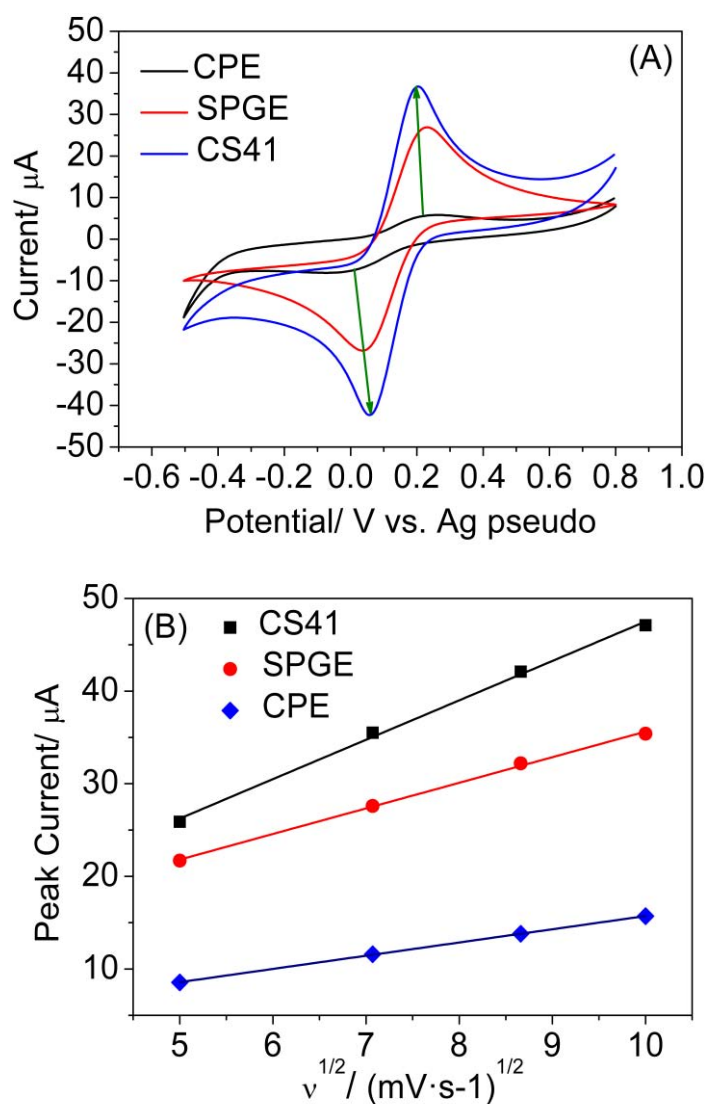


Figure 6.13. Cyclic voltammograms recorded in 0.1M KNO₃ solution containing 1mM ferro/ferri-cyanide redox couple at CPE, SPGE, and CS1 at a scan rate of 50mV/s (A), and plots of anodic peak current vs. scan rate (B).

Besides ΔE_p values, another difference among the voltammograms shown in Figure 6.13 is the peak area, which is proportional to the active surface area of the working electrode. Normally, electrochemical areas can be calculated according to the Randles-Sevcik equation as presented below:

$$i_p = 2.69 \times 10^5 n^{3/2} v^{1/2} D^{1/2} AC \quad (\text{eq.3})$$

Where i_p is the peak current value, n is the number of electrons involved in the reaction, v is the scan rate, A is the active area, D is the diffusion coefficient ($7.01 \times 10^{-6} \text{ cm}^2 \cdot \text{s}^{-1}$ for potassium ferricyanide), and C is the bulk concentration of this species solution.

However, here it must be emphasized that results of the active area cannot be accurately obtained because of the uncertainty of the physical area delimited by the plastic cuvette of the C/SiO₂ films. Because it should be taken into account that the sol-gel derived C/SiO₂ films present an open porous structure, which allows water solution to spread outside that defined film area. In order to give more insight about these wetting properties, a measurement of the porosity of this C/SiO₂ films was attempted but the N₂ adsorption desorption technique could not be carried out because the C/SiO₂ film could not be peeled off from the SiO₂/Si substrate. Other alternative techniques are being sought for carrying out such measurements.

6.5. Doping C/SiO₂ Films with Bi or Au Nanoparticles

From the discussion above, we have shown that conductive C/SiO₂ films were successfully prepared on SiO₂/Si substrates by a sol-gel approach and successfully performed in electrochemical experiments. In the following section, the studies directed towards the development of films containing Bi or Au nanoparticles to fabricate electrochemical sensors for heavy metal detection are presented.

6.5.1. Synthesis of Bulk Bi/C/SiO₂ Nanocomposite Materials

Keeping the molar ratio between resorcinol and APTES to 1, the composition of the sols used to prepare Bi/C/SiO₂ xerogel nanocomposite materials are presented in Table 6.5. Before synthesis, reagent miscibility must be considered. As we have mentioned in Chapter 3, Bi(NO₃)₃ is soluble in acetic acid but practically insoluble in

ethanol. Homogeneous resorcinol/formaldehyde gels containing Bi(III) could not be obtained by co-synthesis when using the ethanol solvent (Table 6.5) because of the precipitation of Bi(III) in this medium. However very surprisingly, with the presence of APTES in the mixture, a clear Bi(III) containing sol prepared in ethanol was obtained. This is likely related to the formation of some complex between Bi(III) and the amino groups of APTES molecules that prevents the precipitation of Bi. In addition, Bi(III) containing sol was found to gel much faster than that without Bi(III). This is probably because the addition of Bi(NO₃)₃ remarkably lowers the pH of the initial sol, and thus significantly accelerates the gelation process. In particular, the pH value was measured to be around 2-3 in B-C/SiO₂ sol but this value was lowered to around 1 after adding Bi(NO₃)₃. After leaving the homogeneous sol in an oven at 60°C for 24 hour to gel completely, these organic gels were carbonized at 900°C for 2 hours to produce Bi/C/SiO₂ xerogel nanocomposites.

Table 6.5 Composition of the sols for synthesizing Bi/C/SiO₂ composites by co-synthesis

Sample	R (g)	F (ml)	APTES (ml)	Bi(NO ₃) ₃ (g)	Acetic acid (ml)	Ethanol (ml)	Additional information
	1	1.36		0.2	5	25	Bi(NO ₃) ₃ not soluble in ethanol
B-C/SiO ₂	1	1.36	2.1		5	25	Gelation in 24 h
B-Bi/C/SiO ₂	1	1.36	2.1	0.6	5	25	Gelation in 4 h (silica gels firstly and then RF gels)

The structure of the resulting nanocomposite material was firstly characterized by SEM. Figure 6.14 (A) displays a representative backscattered electron SEM image of the material. It can be seen that spherical white Bi nanoparticles are uniformly dispersed in the C/SiO₂ matrix. The particle size distribution was measured from a detailed study of more than 10 SEM images using ImageJ software and results are displayed in Figure 6.14 (B). This shows that the Bi/C/SiO₂ nanocomposite presents a majority of particles with diameters comprised between 15 nm and 35 nm, which are smaller than those obtained in Bi/C nanocomposites (Chapter 3) also synthesized by a similar co-synthesis method. Quantitative calculation from EDS analysis (Figure 6.14 (C) and (D)) demonstrates that the addition of 0.6 g Bi(NO₃)₃·5H₂O per 1 g resorcinol resulted in a composite containing ~10 wt% of Bi.

The XRD analysis presented in Figure 6.15 shows the presence of metallic Bi in the Bi/C/SiO₂ nanocomposite as was also found in the co-synthesized Bi/C nanocomposite (Chapter 3).

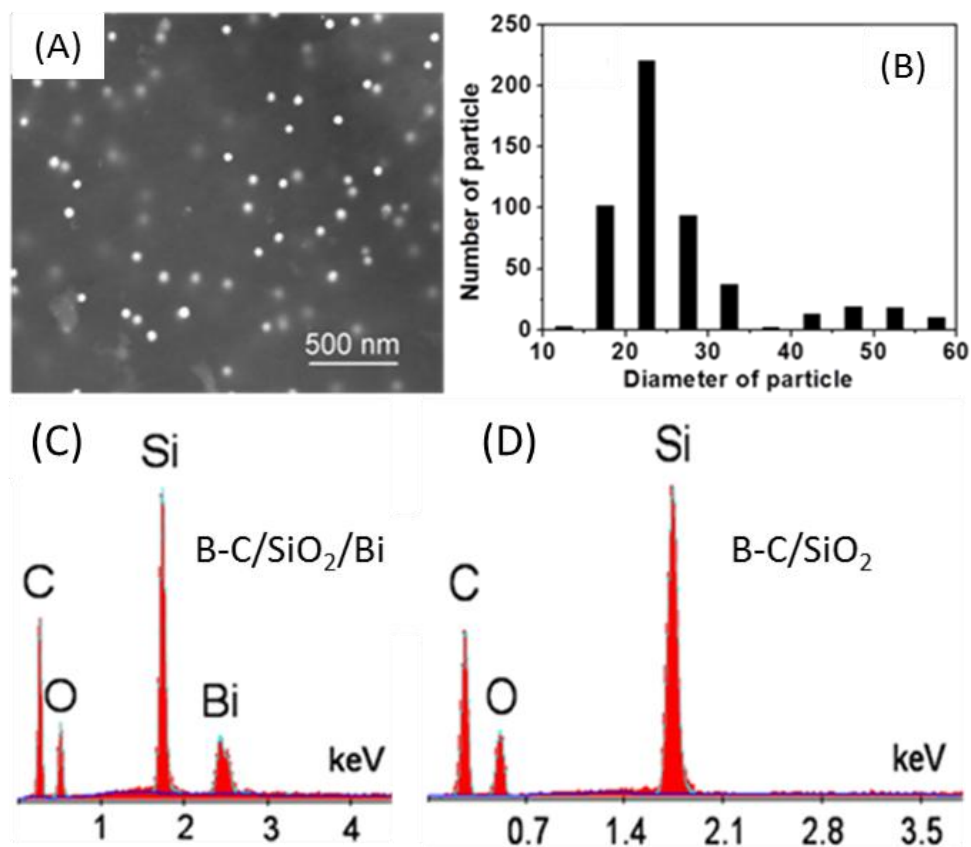


Figure 6.14. Backscattered electron SEM image of C/SiO₂/Bi xerogel nanocomposite (A) and corresponding Bi nanoparticle size distribution (B); SEM-EDS elemental analysis of C/SiO₂ xerogel nanocomposite with Bi (C) and without Bi (D).

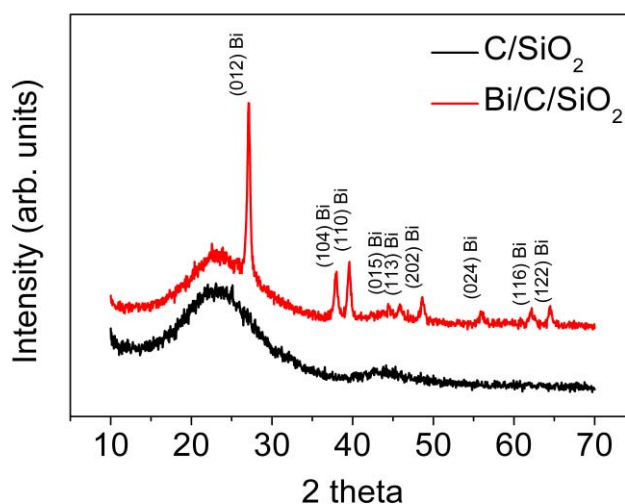


Figure 6.15. XRD patterns of C/SiO₂ and C/SiO₂/Bi composite

6.5.2. Deposition of Bi Doped C/SiO₂ Films on SiO₂/Si Substrates

Figure 6.16 displays a schematic drawing of targeted homogeneous nanocomposite film on SiO₂/Si substrate, comprising a uniform distribution of metal nanoparticles embedded in a porous C/SiO₂ composite matrix.

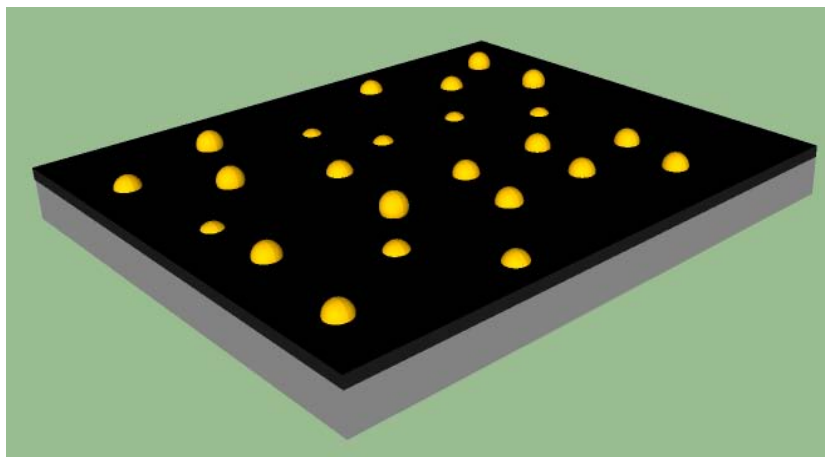


Figure 6.16. Schematic drawing of the desired nanocomposite film comprising C/SiO₂ matrix (black) doped with metal nanoparticles (yellow) on SiO₂/Si substrate (gray).

6.5.2.1. Co-synthesized Bi/C/SiO₂ composite film

1) Sol preparation and spin-coating process

Table 6.6 Recipe for the preparation of RF/silica/Bi(III) sol for spin-coating

Reagents	Amount	Stirring Time (min)	Adding order
Acetic acid	2 ml		1
Bi(NO ₃) ₃ ·5H ₂ O	0.35 g	10	2
Ethanol	5 ml	10	3
APTES	1.68 ml	20	4
Resorcinol	0.77 g	10	5
Formaldehyde	1.08 ml	10	6

RF/APTES sols containing Bi(III) were prepared similarly to that prepared for the synthesis of the nanocomposite in bulk (B-Bi/C/SiO₂) (see Table 6.6). As mentioned above, sol viscosity plays a decisive role in the success of film deposition by the spin-coating technique. We could obtain a sol with a suitable viscosity for spin-

coating by reducing the ethanol amount and keeping the sol in a hood at room temperature for 2 hours. After spin-coating at 4000 rpm for 45 s on a SiO₂/Si substrate, a continuous Bi(III)/RF/SiO₂/ film was obtained. Then, these films were kept in an oven set at 60°C for 24 hours during which the material films gelled and aged completely.

2) Loss of Bi after carbonization

Following a similar carbonization process as for the preparation of C/SiO₂ films, these films were firstly pyrolyzed at 900°C in Ar+H₂ (95%+5%) atmosphere for 2 hours. Figure 6.17 (A) shows a representative SEM image of the resulting nanocomposite film. Very surprisingly, no bismuth nanoparticles but many holes are observed. EDS technique further confirms the absence of Bi in this film. It was anticipated that some Bi could be lost after carbonization at 900°C when synthesizing bulk C/Bi nanocomposite, owing to the evaporation of liquid Bi at high temperatures. However we did not expect the total loss of this component. After this finding we wanted to check whether there was Bi(III) in RF/SiO₂ films. Hence, thermal treatment of RF/SiO₂ film at low temperatures for a shorter time (650°C for 1 min) was performed using an AS-micro rapid thermal annealing furnace, which can reach the set temperature in less than 2 min to avoid the influence of a long heating period (in general several hours to reach the set temperatures) using a conventional tubular furnace. As it can be seen in the SEM image of Figure 6.17 (B), plenty of white bismuth particles are observed dispersed in the C/SiO₂ matrix. This observation proves the presence of Bi in the RF/SiO₂ film before the pyrolysis process and also indicates the complete loss of this element after carbonization at 900°C for 2 hours. Why Bi was completely lost after the thermal treatment at high temperatures for Bi/C/SiO₂ films but not in the case of bulk Bi/C/SiO₂ composites?

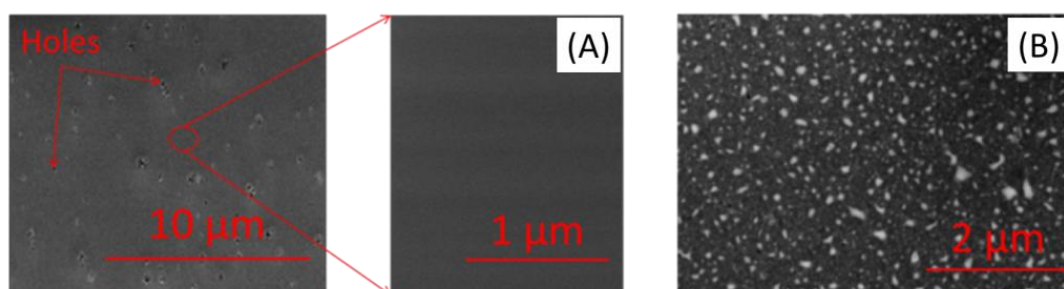


Figure 6.17. SEM image of C/SiO₂/Bi nanocomposite film carbonized at (A) 900°C for 2 hours, (B) 650°C for 1 min.

It is known that a liquid is in equilibrium with its own vapor which is at a certain pressure P_{vap} at temperatures below its boiling point. P_{vap} increases with temperature and equals the external pressure P_{ext} at the boiling point (i.e. the boiling point is dependent on the external pressure). The rate of evaporation in an open system is dependent on P_{vap} , P_{ext} and eventually on the existence of a convective flow that can accelerate the transport of vapor.

Table 6.7 Vapor pressure of Bi at different temperatures

Temperature (°C)	540°C	620°C	720°C	993°C
Vapor Pressure (mm Hg)	10^{-3}	10^{-2}	10	50

Table 6.7 lists the vapor pressures of Bi at temperatures between 500°C and 1000°C reported in [18]. The vapor pressure at temperatures below 620°C is relatively low. However it increases dramatically at higher temperatures. For instance, the reported vapor pressure at a temperature of 720°C is nearly 1000 times larger than that at 620°C. Moreover, this is worsened by the fact that the pyrolysis treatments are performed in an inert gas flow. Consequently, one can expect that the loss of Bi mainly occurs when the annealing temperature is higher than 720°C. In order to verify this hypothesis, Bi/RF/SiO₂ films were carbonized at 4 different temperatures (650°C, 800°C, 900°C and 1000°C). No Bi could be observed in samples pyrolyzed at temperatures higher than 800°C even when the annealing was carried out for only 1 min. RF/SiO₂ film carbonization process cannot be avoided in order to get a low enough sheet resistance for the films to be applied in electrochemistry, as shown in Table 6.8. Unfortunately, it is not possible to meet a compromise for achieving a suitable conductivity of the C/SiO₂ film while keeping the Bi content of the resulting films. Therefore, the co-synthesis approach could not be applied to produce the desired Bi/C/SiO₂ nanocomposite films on SiO₂/Si substrates.

Table 6.8 Sheet resistance of C/SiO₂ film pyrolyzed under various conditions

Carbonization Conditions	650°C ^a (1 min)	800°C ^a (1 min)	900°C ^a (1 min)	1000°C ^a (5 min)	900°C ^b (2 h)	1000°C ^b (2 h)
Sheet Resistance (Ω)	$>5 \times 10^4$	$>1 \times 10^4$	$>1 \times 10^4$	$\sim 1 \times 10^4$	$\sim 5 \times 10^3$	$\sim 5 \times 10^3$

Note: molar ratio between R and APTES being 1:1; a-pyrolysis was performed in a rapid thermal annealing furnace (heating rate 500°C/min), b-carbonization was done in a tubular furnace (heating rate 200°C/h).

Herein, there is another question that should be answered. Why not all the Bi was lost when synthesizing Bi/C/SiO₂ nanocomposite material in bulk, even though it was also pyrolyzed at 900°C for 2 hours under an inert gas flow? We believe that this is related with the size of the pieces of RF/SiO₂ xerogel being pyrolyzed, as indicated in Chapter 3. A large xerogel piece (of more than 0.1 cm length) appears to offer a matrix for semi-confining liquid Bi inside it, and as a consequence weaken the evaporation of Bi during pyrolysis.

6.5.2.2. Impregnation approach for synthesizing Bi/C/SiO₂ composite thin-film

We also tried to follow an impregnation route to prepare Bi/C/SiO₂ nanocomposite films. Two different approaches were performed: 1) impregnating a RF/SiO₂ film in a Bi(III) solution (0.2 M Bi(NO₃)₃ in CH₃COOH solution) for 1 hour and then pyrolyzing it at 900°C for 2 hours, 2) impregnating a conductive C/SiO₂ (previously carbonized at 900°C) in Bi(III) solution, followed by a second thermal annealing process at 600°C.

1) Impregnating RF/SiO₂ films

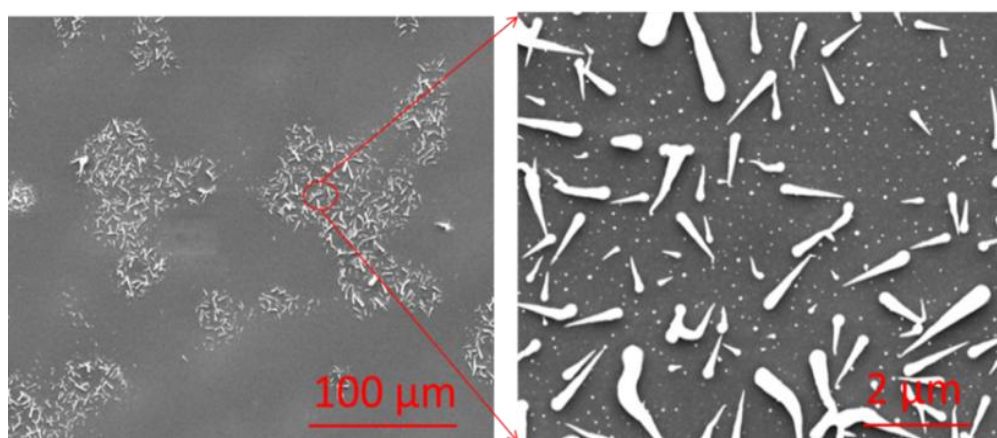


Figure 6.18. SEM image of a C/SiO₂/Bi film carbonized at 600°C for 30 min derived from Bi-impregnated RF/SiO₂ samples.

In the case of impregnated RF/SiO₂ film, as discussed in the previous section, no Bi could be detected after pyrolysis at 900°C. When pyrolyzing the films at 600°C, as shown in Figure 6.18, both irregular rods and spherical nanoparticles are observed simultaneously in some regions whereas only Bi nanoparticles embedded in C/SiO₂ matrix are found in other zones. The inhomogeneity of Bi dispersion in the C/SiO₂ film is not surprising because it is difficult to obtain a composite material with

homogeneous distribution of Bi by impregnation method as discussed in Chapter 3. These rods appear to be attached to the surface while nanoparticles seem to be embedded in the C/SiO₂ matrix. Regrettably, so far, we could not find an effective method to improve the homogeneity of the Bi distribution in impregnation process and it is not clear for us how these rods were formed. Nevertheless, there still exists a conflict between generating a conductive enough C/SiO₂ film and producing Bi nanoparticles.

2) Impregnating C/SiO₂ films

In order to overcome the impossibility of finding a pyrolysis treatment that would produce films with the required conductivity and at the same time generating Bi nanoparticles, we attempted another impregnation process consisting of soaking a previously pyrolyzed C/SiO₂ film in a Bi(III) solution, and then performing a thermal annealing process at low temperatures (600°C) to induce the formation of Bi nanoparticles. More specifically, a RF/SiO₂ film was firstly carbonized at 900°C for 2 hours in Ar+H₂ atmosphere. The pyrolyzed film was then immersed in a 0.2 M solution of Bi(III) in acetic acid. After 1 hour impregnation, the film was cleaned with distilled water and annealed at 600°C for 30 min. Instead of obtaining spherical nanoparticles, the annealed material presented rods with irregular shapes and lengths as can be seen in Figure 6.19. The formation of these structures was not further studied and remains an open question.

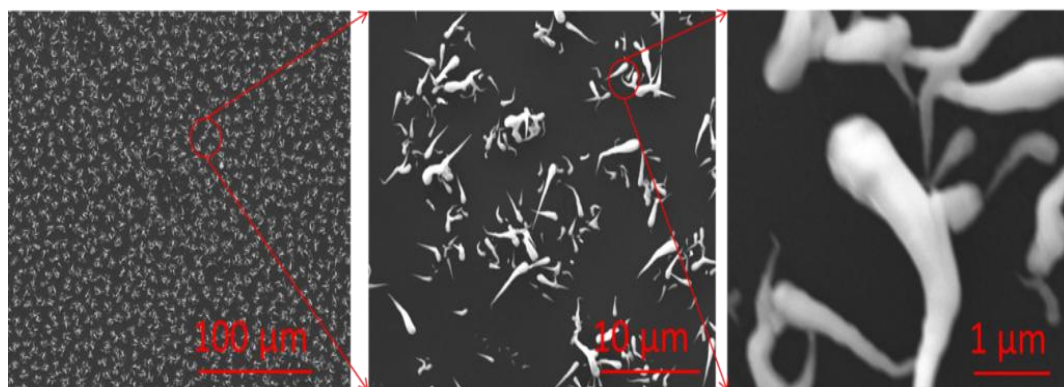


Figure 6.19. SEM image of Bi/C/SiO₂ films obtained from previously carbonized C/SiO₂ films impregnated in a Bi(III) solution and then carbonized at 600°C for 30 min in Ar+H₂ atmosphere.

From these results, it can be summarized that the generation of Bi/C/SiO₂ nanocomposite thin-films is still challenging.

6.5.3. Preparation of C/SiO₂ Films on SiO₂/Si Substrates with Gold Nanoparticles

Gold electrodes are also being widely used for the determination of heavy metals and are complementary to Bi-based electrodes because they allow the determination of analytes such as Hg(II) and As(III) [19] which are not efficiently detected with Bi-based electrodes. Gold has a melting point of 1064°C, which is not only much higher than that of Bi (270°C) but also higher than the required temperature to carry out the carbonization of the C/SiO₂ films (900-1000°C). Therefore, Au/C/SiO₂ nanocomposite films would be an appealing material for the fabrication of carbon microelectrodes for the detection of the above-mentioned heavy metals. However, we found that AuCl₃, a commonly used precursor for the synthesis of Au nanoparticles rapidly reacted with resorcinol in distilled water, causing the formation of black precipitates. A similar behavior was also found when trying to prepare Au(III) containing RF/APTES sol both using acetone or ethanol as a solvent, making the preparation of Au/C/SiO₂ films challenging by the co-synthesis approach.

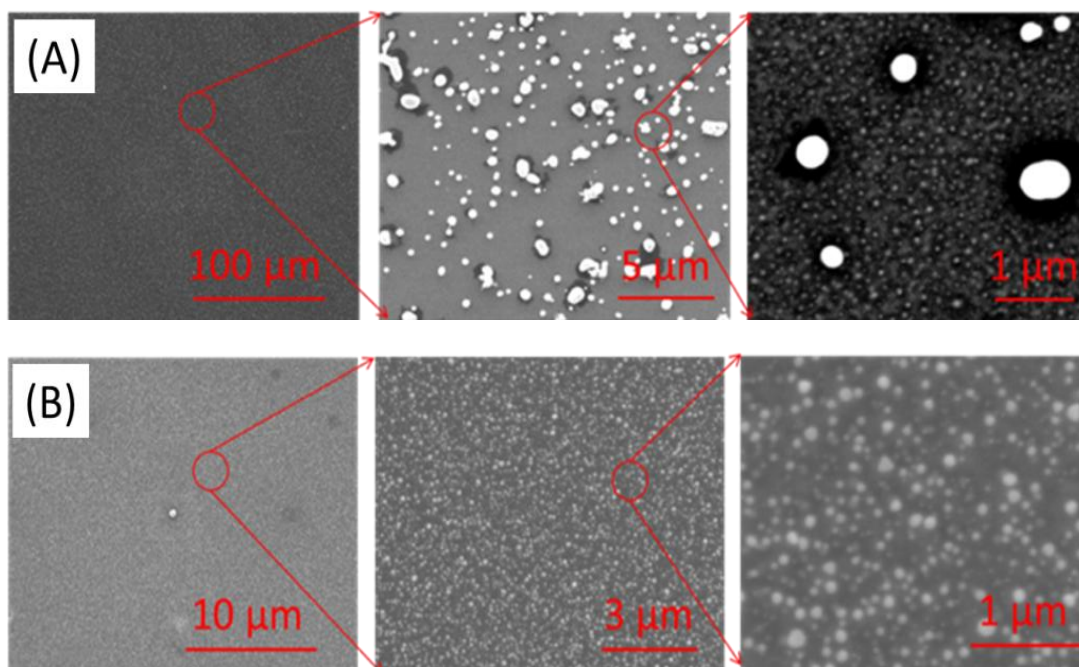


Figure 6.20. SEM image of Au/C/SiO₂ films carbonized at (A) 600°C for 2 hours and (B) 900°C for 2 hours in Ar+H₂ (95%+5%) atmosphere. The film is derived from impregnating RF/SiO₂ samples in AuCl₃ water solution (0.01 M) for 4 hours.

Therefore, Au/C/SiO₂ nanocomposite films were prepared by impregnating RF/SiO₂ films in a 5 mM HAuCl₄ water solution for 1 hour, followed by a carbonization step at 900°C for 2 hours under a Ar+H₂ flow of 100 cm³/min. Figure 6.20 shows representative SEM images of C/SiO₂/Au nanocomposite films carbonized at 600°C and 900°C. Both big and small particles coexist on Au/C/SiO₂ films carbonized at 600°C (see Figure 6.20 (A)). Big particles seem to attach on the surface of the film while smaller nanoparticles are embedded into the C/SiO₂ matrix. By increasing the carbonization temperature to 900°C, spherical gold nanoparticles with ~100 nm in diameter are found to be distributed uniformly in C/SiO₂ matrix (see Figure 6.20 (B)). The synthesis of this material is still under study.

6.6. Conclusion

In conclusion, a series of crack-free hybrid C/SiO₂ thin-film showing no macro-phase separation have been deposited on SiO₂/Si substrates by a one-pot sol-gel spin-coating approach. The interfacial adhesion between carbon films and SiO₂/Si substrates was significantly enhanced by the addition of a SiO₂ precursor to the sol formulation. The electrochemical characterization of these C/SiO₂ films demonstrates their prospective application as an electrochemical sensing platform. However the preparation of C/SiO₂ thin-films containing Bi nanoparticles is still challenging due to the loss of Bi by evaporation during the film carbonization at high temperatures. In contrast, Au/C/SiO₂ nanocomposite thin-films could be successfully prepared by an impregnation approach.

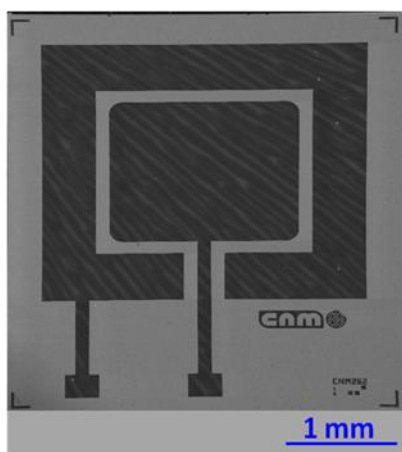
References

- [1] Chen C, Zhang J, Du Y, Yang X, Wang E. Microfabricated on-chip Integrated Au-Ag-Au Three-electrode System for in situ Mercury Ion Determination. *Analyst*. 2010;135:1010-1014.
- [2] Kokkinos C, Economou A, Raptis I, Speliotis T. Disposable Lithographically Fabricated Bismuth Microelectrode Arrays for Stripping Voltammetric Detection of Trace Metals. *Electrochemistry Communications*. 2011;13:391-395.
- [3] Kim J, Song X, Kinoshita K, Madou M, White R. Electrochemical Studies of Carbon Films from Pyrolyzed Photoresist. *Journal of The Electrochemical Society*. 1998;145:2314-2319.
- [4] Tao Y, Endo M, Inagaki M, Kaneko K. Recent Progress in the Synthesis and Applications of Nanoporous Carbon Films. *Journal of Materials Chemistry*. 2011;21:313-323.

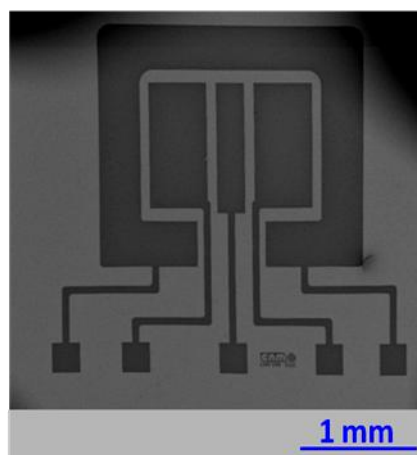
- [5] Obratsov AN, Obratsova EA, Tyurnina AV, Zolotukhin AA. Chemical Vapor Deposition of Thin Graphite Films of Nanometer Thickness. *Carbon*. 2007;45:2017-2021.
- [6] Hadi M, Rouhollahi A, Yousefi M. Nanocrystalline Graphite-like Pyrolytic Carbon Film Electrode for Electrochemical Sensing of Hydrazine. *Sensors and Actuators B: Chemical*. 2011;160:121-128.
- [7] Nolan H, McEvoy N, Keeley GP, Callaghan SD, McGuinness C, Duesberg GS. Nitrogen-Doped Pyrolytic Carbon Films as Highly Electrochemically Active Electrodes. *Physical Chemistry Chemical Physics*. 2013;15:18688-18693.
- [8] Schlesinger R, Bruns M, Ache HJ. Development of Thin-film Electrodes Based on Sputtered Amorphous Carbon. *Journal of The Electrochemical Society*. 1997;144:6-15.
- [9] Blackstock JJ, Rostami AA, Nowak AM, McCreery RL, Freeman MR, McDermott MT. Ultraflat Carbon Film Electrodes Prepared by Electron Beam Evaporation. *Analytical Chemistry*. 2004;76:2544-2552.
- [10] Jia J, Kato D, Kurita R, Sato Y, Maruyama K, Suzuki K, et al. Structure and Electrochemical Properties of Carbon Films Prepared by a Electron Cyclotron Resonance Sputtering Method. *Analytical Chemistry*. 2007;79:98-105.
- [11] Ye L, Ji Z-H, Han W-J, Hu J-D, Zhao T. Synthesis and Characterization of Silica/Carbon Composite Aerogels. *Journal of the American Ceramic Society*. 2010;93:1156-1163.
- [12] Asenath Smith E, Chen W. How to Prevent the Loss of Surface Functionality Derived from Aminosilanes. *Langmuir* 2008;24:12405-12409.
- [13] Spangler LL, Torkelson JM, Royal JS. Influence of Solvent and Molecular Weight on Thickness and Surface Topography of Spin-coated Polymer Films. *Polymer Engineering & Science*. 1990;30:644-653.
- [14] He JW, Xu X, Corneille JS, Goodman DW. X-ray Photoelectron Spectroscopic Characterization of Ultra-thin Silicon Oxide Films on a Mo(100) Surface. *Surface Science*. 1992;279:119-126.
- [15] Nicholson RS. Theory and Application of Cyclic Voltammetry for Measurement of Electrode Reaction Kinetics. *Analytical Chemistry*. 1965;37:1351-1355.
- [16] Griffiths K, Dale C, Hedley J, Kowal MD, Kaner RB, Keegan N. Laser-Scribed Graphene Presents an Opportunity to Print a New Generation of Disposable Electrochemical Sensors. *Nanoscale*. 2014;6:13613-13622.
- [17] Lee SH, Fang HY, Chen WC, Lin HM, Chang CA. Electrochemical Study on Screen-printed Carbon Electrodes with Modification by Iron Nanoparticles in Fe(CN)₆^{4-/3-} Redox System. *Analytical and Bioanalytical Chemistry*. 2005;383:532-538.
- [18] Johnston J. The Vapor Pressure and Volatility of Several High-Boiling Metals—A Review. *Journal of Industrial & Engineering Chemistry*. 1917;9:873-878.
- [19] Alves GM, Magalhaes JM, Salaun P, van den Berg CM, Soares HM. Simultaneous Electrochemical Determination of Arsenic, Copper, Lead and Mercury in Unpolluted Fresh Waters Using a Vibrating Gold Microwire Electrode. *Analytical Chimica Acta*. 2011;703:1-7.

Chapter 7

Fabrication of C/SiO₂ Thin-film Electrodes



C/SiO₂ thin-film electrode patterned by photolithography



C/SiO₂ thin-film electrode patterned by soft lithography

Summary

From the discussion in Chapter 6, it is clear that our proposed approach for the preparation of C/SiO₂ films shows enhanced interfacial adhesion to SiO₂/Si substrates. Also, the electrochemical characterization demonstrates the promising application of these C/SiO₂ films for the fabrication of carbon based thin-film electrochemical sensing platforms. Even though all the C/SiO₂ films developed in Chapter 6, which contain different amounts of SiO₂, can be patterned into thin-film electrodes, herein we only focus on CS41 C/SiO₂ film as an example to illustrate the application of standard photolithography in patterning these films into on chip thin-film electrodes. Besides photolithography, soft lithography was also applied to develop C/SiO₂ thin-film electrodes. The patterning process and the structures of the resulting electrodes are presented in this chapter.

Part of the work presented in this chapter is being included in one paper under preparation whose tentative title is "**Patterning Sol-gel Materials for Developing**

Carbon Thin-Film Based Electrodes", by Pengfei Niu, César Fernández-Sánchez, Martí Gich, and Anna Roig.

7.1. Patterning C/SiO₂ Films into Thin-film Electrodes by Photolithography

7.1.1. Patterning Process

A standard UV photolithographic process combined with a reactive ion etching process was used for patterning the C/SiO₂ films into various electrode geometries. Figure 7.1 illustrates the main steps of the overall process.

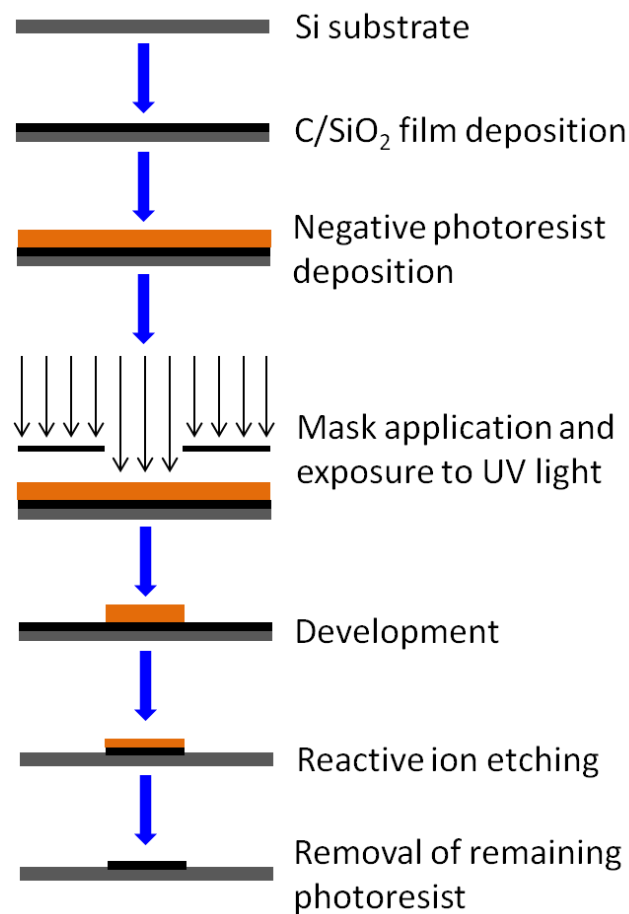


Figure 7.1. Schematic illustration for patterning C/SiO₂ films by standard photolithography and reactive ion etching processes

A standard photolithographic process was applied as follows. First, an AZ 5214 reversible photoresist layer with a thickness of around 1.7 μm was firstly spin-coated onto a C/SiO₂ film at 4500 rpm for 20 s. Then the photoresist was pre-baked at 90°C for 60 s. Afterwards, it was exposed to UV light through a photomask with the desired electrode pattern, followed by a second baking step at 120°C for 120 s.

After cooling down, a second UV exposure was done without photomask to reverse the photoresist and make it negative. Hereafter, the photoresist layer was developed in AZ 726 developer for 50 s and then the substrate was cleaned with distilled water, leaving the developed photoresist structures covering the C/SiO₂ film.

The C/SiO₂ zones that were not covered by photoresist were removed by CHF₃/O₂ (21%/6%) plasma using a Plasmalab 80 Plus reactive ion etching equipment. The etching rate was around 60 and 100 nm/min for C/SiO₂ film and photoresist, respectively. Therefore, working with an 800 nm thick CS41 C/SiO₂ film, it would take around 15 min to completely remove the exposed C/SiO₂ regions. However, using a photoresist layer of 1.7 μm, a photoresist layer of around 200 nm thick was still left protecting the electrodes patterns after the same etching time. The remaining photoresist layer was stripped off with acetone in an ultrasonic bath.

Figure 7.2 shows a representative image of the patterned C/SiO₂ thin-film electrodes on a 4-inch SiO₂/Si wafer. Around 400 electrodes were batch produced on the same substrate.



Figure 7.2. Image of a 4-inch wafer containing C/SiO₂ thin-film electrodes patterned by the standard photolithography process

Figure 7.3 (A) shows a detailed optical image of a pair of interdigitated electrode having 25 μm wide lines, separated 25 μm . An excellent resolution of the patterns was achieved that reveals the outstanding operability of this approach for the production of C/SiO₂ based thin-film electrodes. It can also be seen from the secondary electron SEM image in Figure 7.3 (B) that the wave-like surface morphology of the C/SiO₂ film as described in Chapter 6 is still present after photolithography.

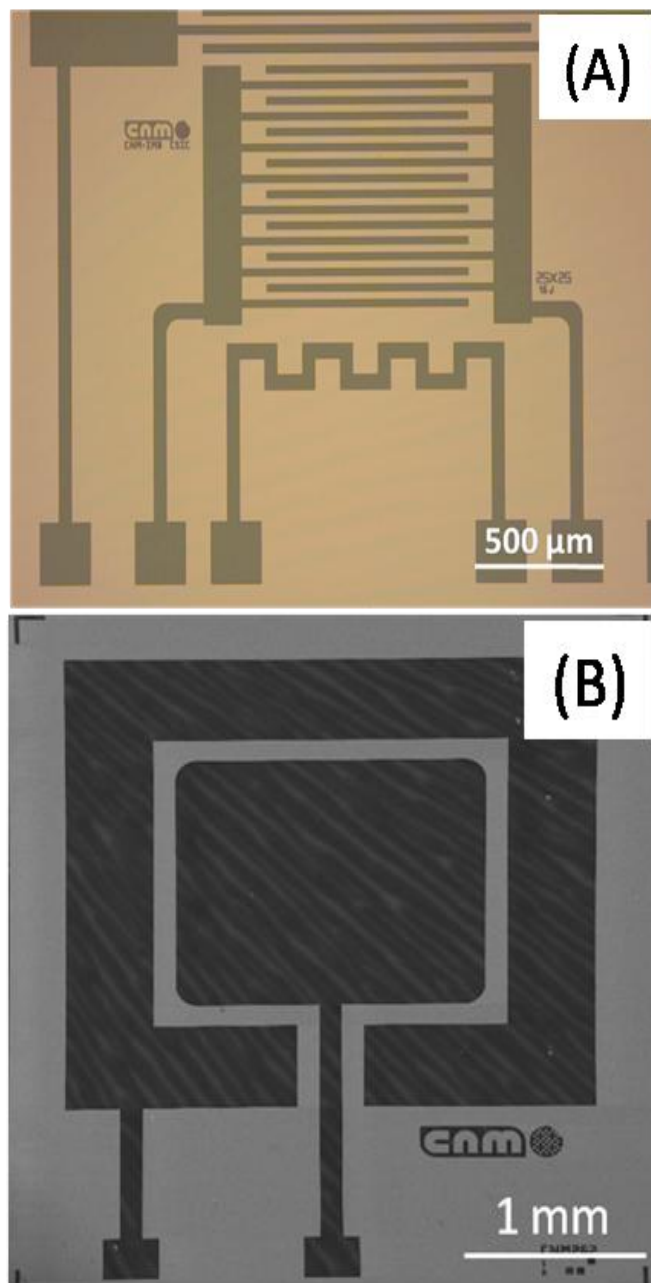


Figure 7.3. Typical pattern of C/SiO₂ thin-film electrodes patterned by photolithography

7.1.2. Effect of the photoresist coating on the C/SiO₂ Film

The photolithographic process involves working with different solvents and photoresists of different nature that could have an effect on the properties of the layer to be patterned. In this section, we present the results of our investigation on the influence of photoresist deposition on the structure and performance of C/SiO₂ films.

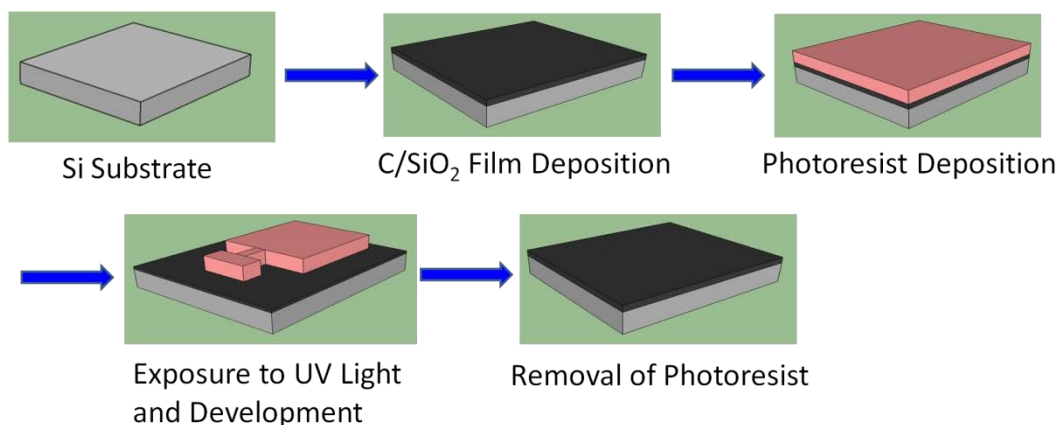


Figure 7.4. Incomplete photolithography process

To study this, an incomplete photolithography process on a C/SiO₂ film was carried out. As shown in Figure 7.4, the C/SiO₂ film was firstly coated with a photoresist layer which was then pre-baked and exposed to UV light through a mask. After that, the photoresist was developed. However, unlike in the entire patterning process displayed in Figure 7.1, herein the developed photoresist was cleaned in an ultrasonic acetone bath instead of undergoing an etching process to produce the corresponding C/SiO₂ film patterns.

7.1.2.1. Change in surface morphology

The surface morphology of C/SiO₂ film (original-film) was compared to that of a film that underwent incomplete photolithographic process as described in Figure 7.4 (photo-film) using AFM technique.

Figure 7.5 displays the topographic images of CS41 film with a thickness of around 800 nm and sheet resistance of ca. 510 Ω/□ (it corresponds to a resistivity of around 0.04 Ω/cm). As we mentioned above, in order to remove the remaining photoresist on C/SiO₂ film after reactive ion etching process, an ultrasonic cleaning of the

processed film with acetone was applied. For comparison, the original film was also treated in an ultrasonic acetone bath for 3 min (labeled as acetone-film). From Figure 7.5, it can be observed that a similar surface morphology is present in both the original-film (Figure 7.5 (A)) and acetone treated film (acetone-film Figure 7.4(B)). The corresponding mean surface roughness values are listed in Table 7.1, being around 0.20 and 0.22 nm, respectively, further confirming the similar topography of the films. However, the CS41 C/SiO₂ film that underwent photolithography (photo-film) shows an extremely different surface morphology with a much higher surface roughness (see Figure 7.5 (C) and Table 7.1).

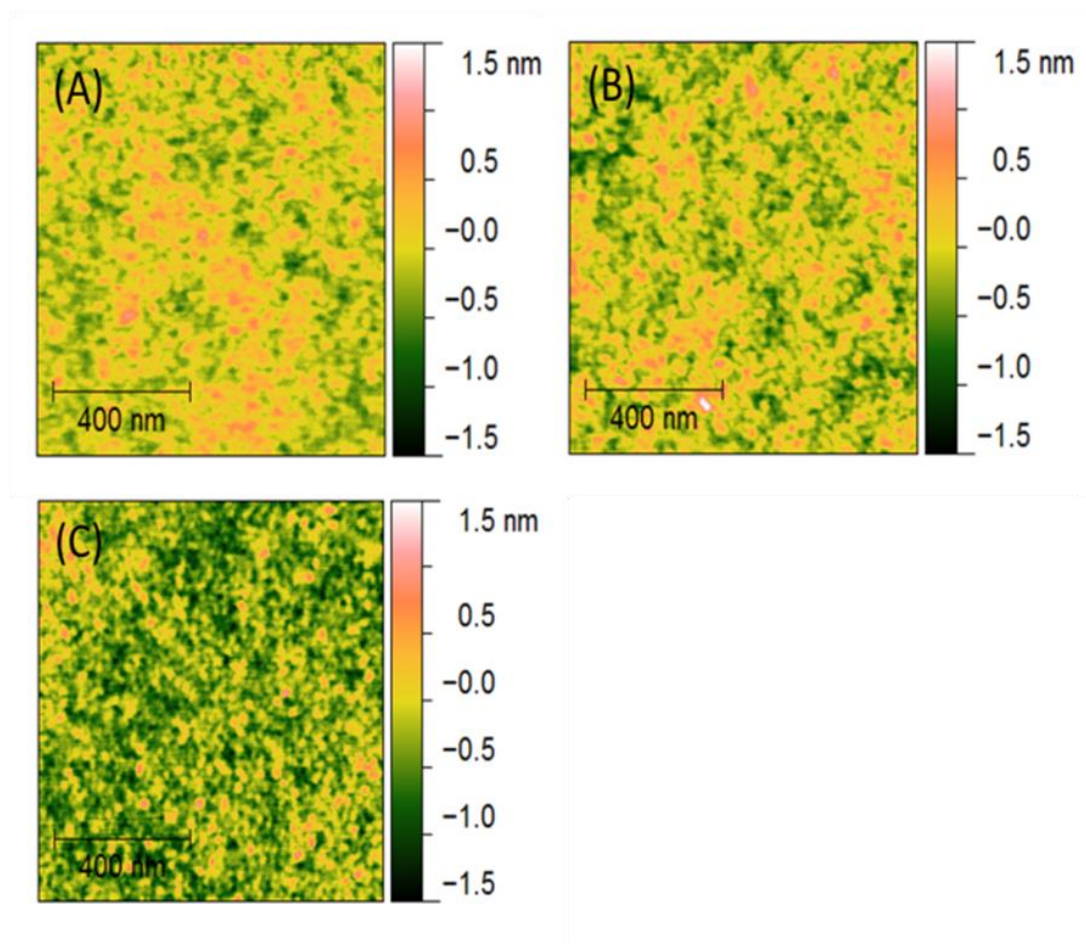


Figure 7.5. AFM images of C/SiO₂ CS41 film before and after photolithography process, (A) original-film, (2) acetone-film, (C) photo-film.

These results indicate that the contact with photoresist induced the modification of the surface structure of C/SiO₂ CS41 film. Further studies were performed with films containing a relatively higher amount of SiO₂ in order to ascertain whether the surface morphology of C/SiO₂ film was indeed modified by photolithography

process. Table 7.1 lists the surface roughness values of C/SiO₂ film containing different amount of SiO₂ before and after photolithography. The surface roughness increases with the SiO₂ content in the film. In addition, higher SiO₂ content in C/SiO₂ film appears to result in bigger increase in surface roughness by photolithography (Table 7.1).

Table 7.1 Roughness of C/SiO₂ films measured on 1 x 1 μm² square

Sample	Roughness (nm)		
	original-film	acetone-film	photo-film
CS41	0.20	0.22	0.29
CS21-A	0.62		1.44
CS11-A	1.05		3.01

7.1.2.2. Sheet resistance

Sheet resistance of C/SiO₂ film was measured using a four-point probe set-up. In comparison with the original C/SiO₂ CS41 film, a nearly 2 times higher sheet resistance was obtained with the photo-film (Table 7.2). In parallel experiments, we found that the increase in sheet resistance after photolithography also occurred to the other C/SiO₂ films with different SiO₂ content.

Table 7.2 Sheet resistances of CS41 film

Sample	CS41	
	original-film	photo-film
Sheet Resistance/ R/□ (Ω/□)	510±82	980±180

Note: the associated error corresponds to the standard deviation of 4 measurements

Then, what is the main reason causing the increase of film sheet resistance? During a photolithography process, on the one hand, the C/SiO₂ film was in direct contact with the photoresist. It is known that carbonized resorcinol/formaldehyde xerogel contains reactive C-O or C=O groups, which may interact with some active oxygen groups present in the photoresist. Thus it is possible that a monolayer of photoresist could not be removed from C/SiO₂ film by ultrasonically cleaning in acetone, due to a strong physical or chemical interaction. On the other hand, the developer is usually a strong basic solution, and this may react with the SiO₂ xerogel and thus

remove the SiO₂ network from C/SiO₂ film. In order to check this hypothesis, we carried out the following experiments. In the first one, a piece of SiO₂ aerogel of around 1 cm³ was immersed in the developer, and as a result the SiO₂ aerogel was decomposed in 5 min. In the second experiment, CS41 C/SiO₂ powder material (particle size around 30 μm in diameter) was immersed in the developer for only 3 min and its porosity measured by N₂ adsorption porosimetry, showing a significant increase compared to the material that has not been in contact with the developer. Nevertheless, it is important to point out that the part of C/SiO₂ film that remains on the SiO₂/Si substrate to form the electrode structures did not get in contact with the developer but just the areas being etched after carrying out the photolithography process. The photoresist was developed for only 50 s and lateral diffusion from the exposed areas to the photoresist coated C/SiO₂ film zones may take place, but its effect would be very small considering the significantly larger size of the electrodes compared to the thickness of the C/SiO₂ film. Therefore, we believe that the effect of the developer is not the main factor influencing the surface structure of C/SiO₂ film. It is the interaction of the photoresist with the film that mainly modifies the surface structure and the electrically conductive properties of the film.

7.1.2.3. Surface composition

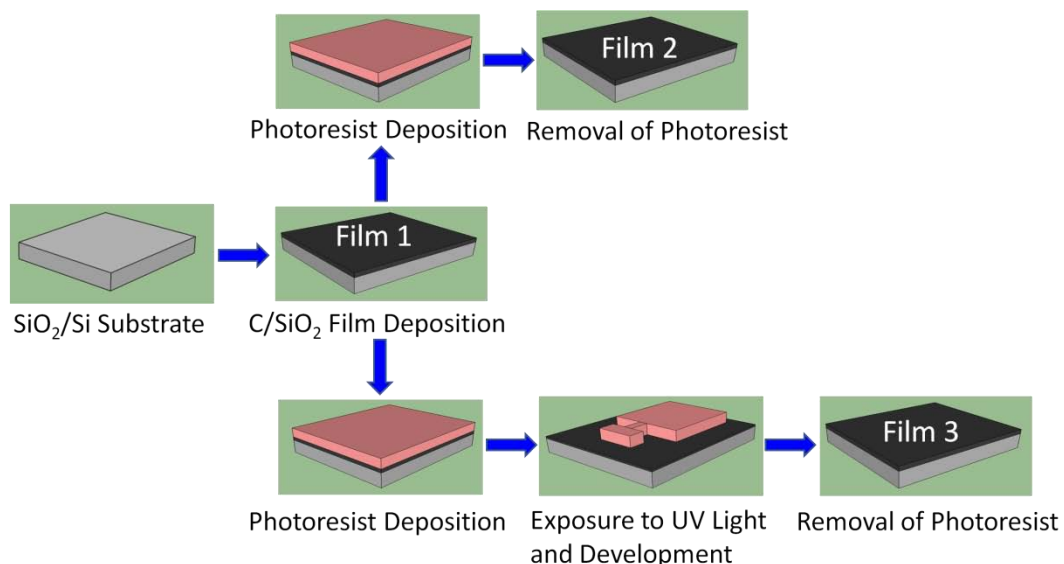


Figure 7.6. Schematic illustrate of the three CS41 films for XPS analysis

In order to give more insight about the effect described in the previous section, the

chemical composition of the surface of C/SiO₂ CS41 film was studied by XPS analysis. Herein, three samples as schematically illustrated in Figure 7.6 were tested, including original CS41 film (labeled as Film-1), CS41 film being coated with AZ5214 photoresist and then the photoresist being removed by acetone cleaning (named as Film-2), CS41 film being deposited with AZ5214 photoresist, exposed to UV, developed by AZ726 developer and then the remaining photoresist being removed by acetone cleaning (marked as Film-3).

Table 7.3 XPS analysis of surface chemical composition on CS41 film

Sample (CS41)	C (%)	O (%)	Si (%)
Film-1	78.9	17.0	4.2
Film-2	78.6	18.4	3.0
Film-3	78.6	18.4	2.9

The percentage of different chemical elements on the surface of the film was calculated from the corresponding area in the XPS spectra and is summarized in Table 7.3. In comparison with Film-1, an obvious difference is a slightly higher amount of oxygen (O) but lower amount of silicon (Si) both in Film-2 and Film-3. In addition, very similar surface chemical composition in Film-2 and Film-3 was calculated, revealing that the influences in film surface morphology as well as its electrical conductivity is mainly caused by its contact with photoresist.

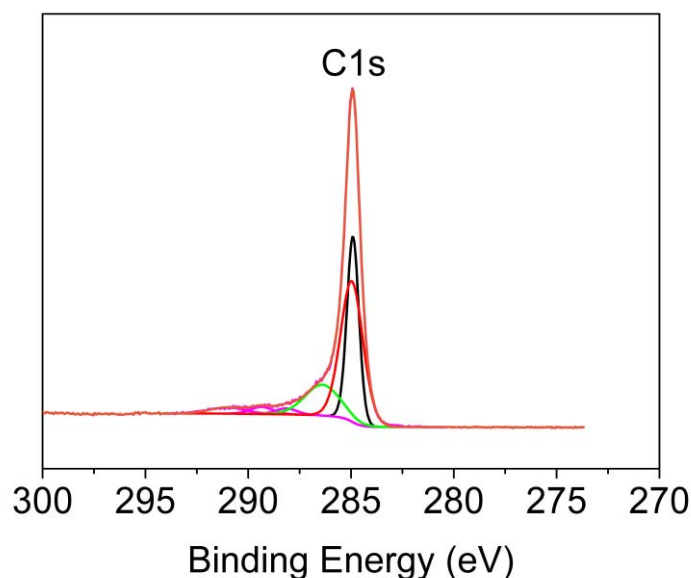


Figure 7.7. C peaks of an XPS measurement of a CS41 C/SiO₂ film

From Table 7.3, the carbon content in these films is similar. Then, what make the film after being contact with photoresist to be less conductive? It is well known that the electrical properties of carbon materials are sensitively dependent on the fraction of sp²-carbon. The de-convolution of the XPS C1s peak gives information on the different types of carbon bonds present in the films. Figure 7.7 shows the C1s XPS peak of the Film-1 which reveals the presence of five different contributions with those at 284.9 eV, corresponding to C-C, at 286.4 eV belonging to C-O bonds and at 288.1 eV, related to C=O bonds. A summary of the contribution of each C bond in these three films is displayed in Table 7.4. The analysis of these three components indicates that both Film-2 and Film-3 show a relatively lower content of sp²-carbon but an increased fraction of nonconductive C-O and C=O bonds.

Table 7.4 Surface carbon element allocation analysis on CS41 film

Allocation	C1s (%)					
	C-C sp ²	C-C	C-O	C=O	O-C=O	Shake up $\pi \rightarrow \pi^*$
Film-1	32.6	44.8	15.3	2.0	2.2	3.1
Film-2	26.6	50.5	15.1	2.6	1.8	3.4
Film-3	27.6	46.4	18.6	2.0	1.9	3.5

This may be related to the incomplete removal of the photoresist from C/SiO₂ film. The remaining photoresist monolayer would hinder the electron transfer at the electrode surface to some extent, and then limit the electrochemical processes to be measured at these electrodes. There are two options to completely remove the photoresist layer on the film. On the one hand, an additional plasma etching process can be applied after washing it with acetone. On the other hand, during the removal of the C/SiO₂ zones not protected by the photoresist, an etching period that is longer than it is needed can be used to entirely eliminate the photoresist.

7.2. On-chip C/SiO₂ Film Electrodes Fabricated by Soft lithography

7.2.1. Microtransfer Molding Procedure

Soft lithography represents a set of high resolution patterning techniques for generating micro- or even nanometer scale features using a mold [1, 2]. Figure 7.8 illustrates a concept drawing of the technique, microtransfer molding (μ -TM), used in this Thesis to develop thin-film electrodes. It comprises three main steps, namely, fabrication of master by standard photolithographic technique on SiO₂/Si wafer, generation of the PDMS mold, and production of the C/SiO₂ thin-film based electrode by μ -TM. These three steps are described in more detail below.

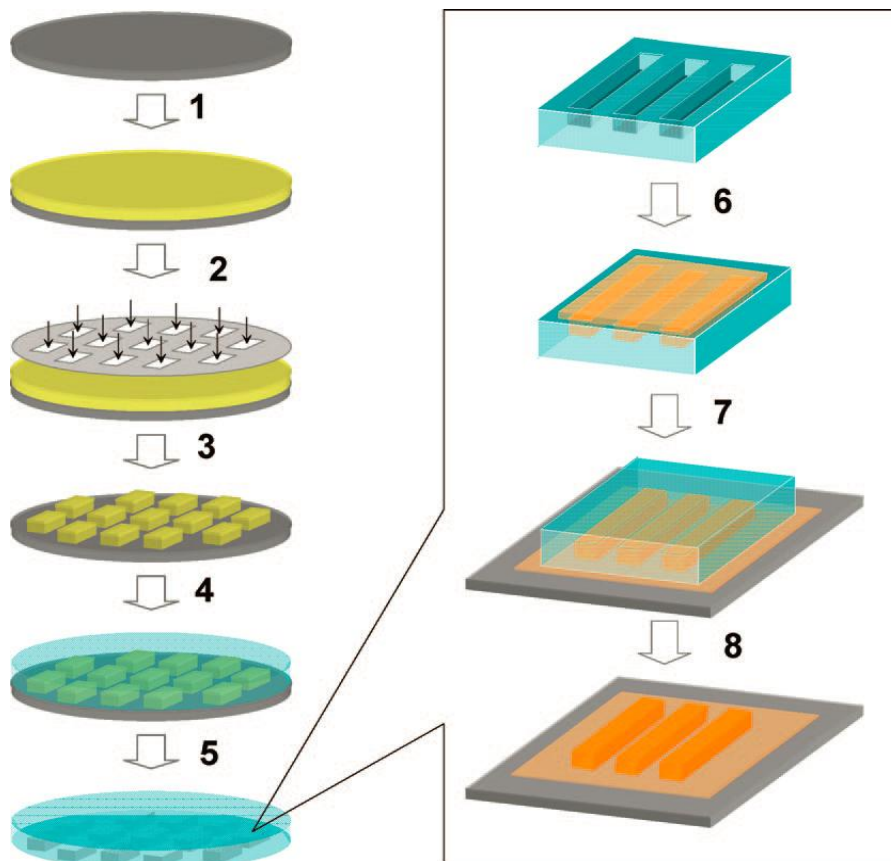


Figure 7.8. Concept drawing of microtransfer molding technique, (1) SU-8 spin-coated on wafer, (2) UV exposure through a mask, (3) SU-8 developed to release the patterns, (4) Master coated with PDMS, (5) PDMS peeled off the master, (6) Sol solution cast on the PDMS mold, (7) PDMS transferred to substrate, (8) PDMS peeled off the substrate after polymerization, reprinted from [3]

7.2.1.1. Fabrication of the master

A master with different electrode geometries was fabricated with the SU-8 negative photoresist by one photolithographic process on 4 inch SiO₂/Si wafer. To improve the adherence between SU-8 layer and SiO₂/Si wafer, a seed layer of MR-L 5005 was deposited by spin-coating at 4000 rpm for 15 s. It was then exposed to UV light without mask at 95°C for 6 min. After that, a 3.5 μm thick SU-8 5005 layer was deposited on top of MR-L 5005 layer. Following the step of exposure to UV light with a mask for 8 s, a post-exposure bake at 95°C for 5 min was carried out. Afterwards, the SU-8 layer was developed in PGMEA developer to obtain the master.

7.2.1.2. Generation of the PDMS mold

PDMS mold was prepared using Sylgard 184 elastomer. Firstly, Sylgard 184 and the curing agent in a volume ratio of 10:1 were thoroughly mixed in a plastic beaker. The mixture was then vacuum degassed and carefully poured onto the master. In order to remove the possible air bubbles that might be trapped in PDMS after pouring the solution, the master coated with the elastomer mixture was placed under vacuum for at least 1 hour. Then it was placed on a hot plate set at 80°C for 30 min. After curing, the generated PDMS stamp was peeled off the master with the aid of tweezers and stored in a closed container until use. Before application, the mold was cut into the desired pieces using a blade.

7.2.1.3. Microtransfer molding process

μ-TM process includes the following steps. Firstly, resorcinol/formaldehyde/APTES sol was poured onto a PDMS mold. To fill the mold cavities completely and remove air bubbles from the sol, the filled PDMS stamp was placed under a vacuum for a certain time. After taking the stamp out from vacuum chamber, a slightly scraping step on the surface of the stamp was performed with a PDMS piece to remove excess colloidal solution. The filled stamp was then brought into contact with a SiO₂/Si substrate. Afterwards, a constant pressure was uniformly applied to the stamp. The applied pressure should be large enough to maintain the mold and substrate in intimate contact in order to transfer the polymer sol solution to the substrate and also to minimize the thickness of the residual layer that is generated on the substrate around the patterns. However, the pressure cannot be too high

because it may cause mold deformation and even collapsing (when the upper part of the mold patterns contact the substrate) especially for those with low aspect ratio, which will result in the variation of the surface topography of the patterns. The compressed mold/substrate ensemble was left undisturbed for 24 h under room temperature conditions for the sol to gel and dry. Then, the applied pressure was released and the PDMS stamp was carefully peeled off, releasing the RF/SiO₂ patterns on SiO₂/Si substrate. Afterwards, these resulting gel patterned substrates were aged in an oven at 60°C for at least 6 hours.

7.2.2. Electrodes Prepared by μ -TM Procedure

7.2.2.1. Selection of the sol to be patterned

Selection of a suitable sol is of key importance for successfully carrying out μ -TM procedure. It has been shown in Chapter 6 that the CS41 C/SiO₂ film, derived from a RF/APTES sol with a molar ratio of 4:1 between resorcinol and APTES, already showed an enhanced interfacial strength with the SiO₂/Si substrate. Therefore, R/APTES molar ratio was also set to be 4:1 for carrying out μ -TM patterning procedure in order to prepare C/SiO₂ film electrodes with high electrical conductivity.

Table 7.5 Sol-gel composition for μ -TM fabrication of C/SiO₂ electrodes

Samples		R(g)	F(ml)	APTES (ml)	Molar Ratio (R:F:APTES)	Ethanol (ml)	Acetic Acid(μ l)
1	CS41	0.4	0.54	0.21	1:2:0.25	2	0
2	CS41-A _L	0.4	0.54	0.21	1:2:0.25	2	50
3	MCS41-A _L	0.4	0.54	0.21	1:2:0.25	1	50

Table 7.5 lists the three chemical compositions tested. The sols were prepared by successively adding ethanol, acetic acid, APTES, resorcinol and formaldehyde reagents in a glass bottle under vigorous stirring. After the addition of the final reagent (formaldehyde), stirring was kept for 5 min and then stopped. The mixture was placed in a fume hood for 10 min before carrying out the patterning process.

The first composition is exactly the same to the one used for spin-coating CS41 film on SiO₂/Si substrate described in Chapter 6. However, as discussed in Chapter 6, this

sol system gels quite rapidly (in less than 30 min), presenting many difficulties during the subsequent μ -TM operation. In addition, we have observed that the electrode patterns obtained from CS41 sol were not reproducible and exhibit highly macroporous surface structure as displayed in Figure 7.9.

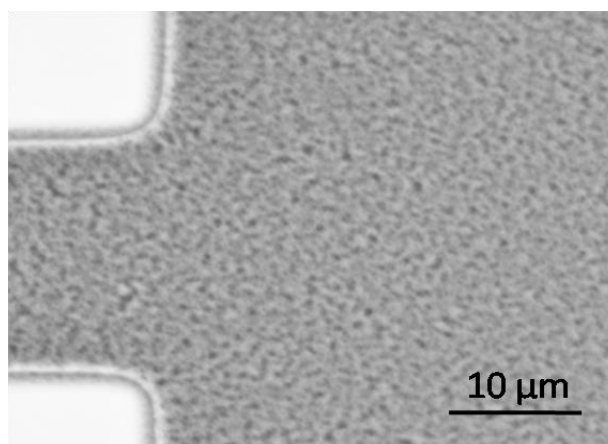


Figure 7.9. SEM image of μ -TM patterns derived from CS41 composition

As we also mentioned in Chapter 6, adding a few amount of acetic acid to the mixture greatly slows down its gelation speed. Therefore, 50 μ l of acetic acid were added to composition 1 to form composition 2. As a result, this resorcinol/formaldehyde/APTES sol system allowed more time to carefully operate all the transferring processes and resulted in relatively high fidelity and reproducible patterns. Figure 7.10 displays the representative images of part of the electrode patterns obtained by μ -TM procedure using composition CS41-A_L. The addition of acetic acid in the sol system not only made μ -TM procedure much easier but also produced electrode patterns with a much denser surface morphology as well as better defined microstructures.

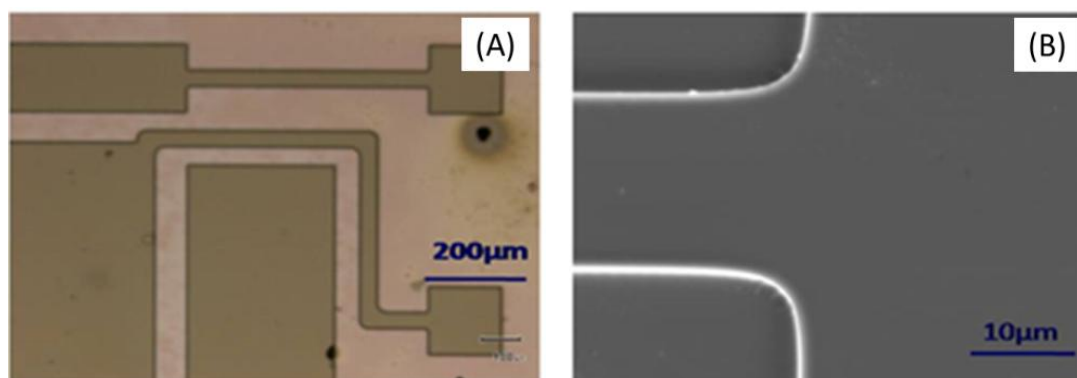


Figure 7.10. Microscopic images of μ -TM patterns derived from CS41-A_L material formulation

Composition 3 presents a higher density of reagents in the sol by decreasing the amount of solvent. This was intended to reduce the shrinkage of the patterns during solvent evaporation, as described in detail below.

7.2.2.2. Solid shrinkage and double peak topography

The fidelity of the patterns achieved by soft-lithographic processes is directly related to the liquid precursors, the polymerization conditions and their interaction with the mold. Sol-gel materials make use of a sol or colloidal suspension that contains a large amount of solvent being removed by evaporation. PDMS is permeable to organic and water vapors, enabling the evaporation of the solvent taking place through the mold during the overall polymerization process. As a result, shrinkage of the resulting patterns occurs to a certain extent and the generated solid structures do not keep the dimensions of the mold [4, 5].

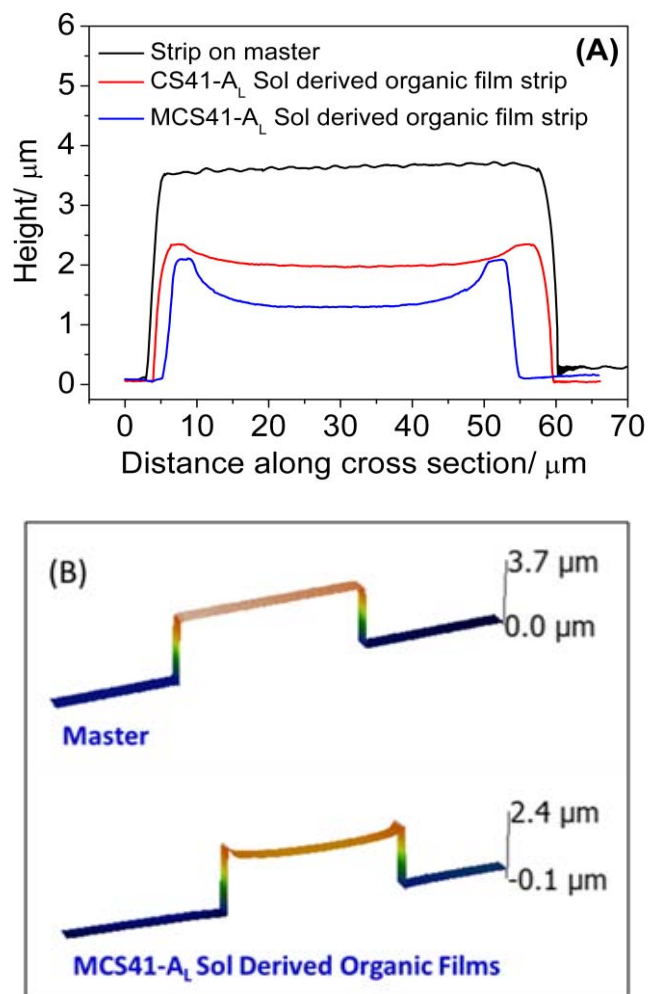


Figure 7.11. Extracted profiles (A) and representative 3D images (B) of 58 μm wide master film strip and RF/SiO₂ strip derived from μ -TM procedure.

Another drawback of patterning sol-gel materials by soft-lithography is the meniscus shape formed on the surface of the patterned features, that is, a larger thickness at the lateral edges than in the middle [6]. This is related to the capillary action of the liquid mixture and the relatively fast evaporation rate of organic and water vapors at the walls. Figure 7.11 shows the extracted profilometry profiles obtained from resorcinol/formaldehyde/SiO₂ pattern features. The height and width of this line on the master is around 3.5 μm and 58 μm , respectively. In the case of using composition 2, the replicated stripe shows heights of around 2.0 μm at the edges and 1.2 μm at the middle, with the highest shrinkage factor being around 65%. Dimension decrease was observed not only in vertical direction but dimension decrease was also observed in lateral direction, from 58 μm to 50 μm , with a shrinkage factor around 15%. Working with a sol containing less amount of solvent gives rise to a less pronounced shrinkage effect both in vertical and lateral directions. For instance, the shrinkage factors in these two directions were estimated to be around 44% vertically and 5% laterally, when patterning composition 3 (MCS41-A_L).

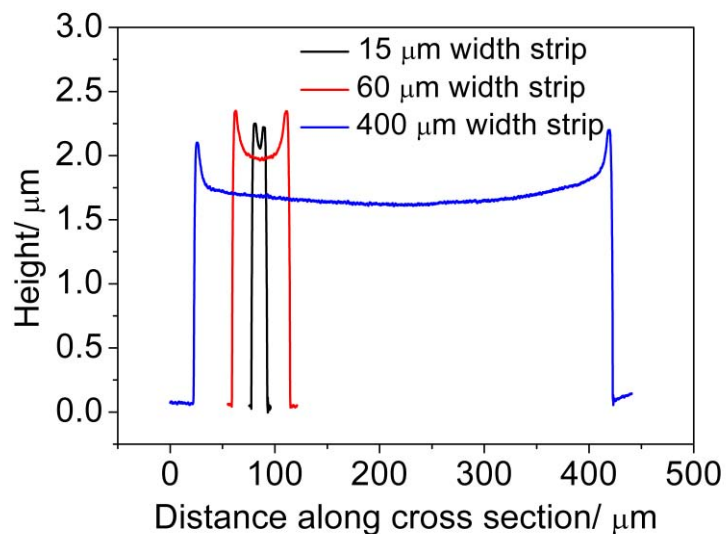


Figure 7.12. Extracted profiles of μ -TM generated RF/SiO₂ stripes with different widths using MCS41-A_L sol.

The influence of strip width on the replicated features was also studied. Figure 7.12 shows the extracted profiles with 15, 60 and 400 μm wide structures replicated from a 3 μm deep PDMS mold. The meniscus shape is observed for all the tested stripes. Interestingly, the height of the stripes decreases with the increase of strip width. Nevertheless, patterns with thickness above 1.8 μm could be generated for

the strip widths up to 400 μm .

From the discussion above, we know that the designed electrode patterns could not be completely replicated using this sol-gel approach, showing double-peak surface topography. Although meniscus formation should be taken into consideration, however it must be mentioned that meniscus structure does not significantly affect the eventual fabrication of C/SiO₂ electrodes and the electrochemical performance of the resulting devices. Therefore, this was not studied any further, and just the pressure applied to the PDMS mold during the μ -TM process was controlled to avoid the mold deformation and thus reproduce the features of the master as closely as possible.

7.2.2.3. Pyrolysis of the gel patterns and the resulting electrode structures

The patterned RF/SiO₂ features were transformed into conductive platforms by a carbonization step carried out in a tubular furnace at 1000°C for 2 h under a 100 cm³/min flow of Ar+H₂ (95% + 5%) mixture.

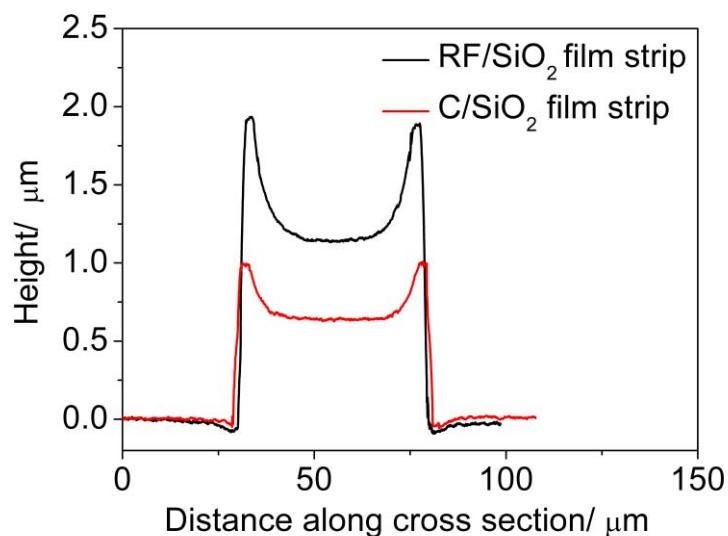


Figure 7.13. Extracted profiles of μ -TM generated RF/SiO₂ and C/SiO₂ film stripe derived from CS41-A₁ sol.

Figure 7.13 shows the size variation of μ -TM patterned lines after carbonization. It can be seen that this process resulted in an almost 45% reduction in height, but had nearly no effect in the lateral dimensions. This can be associated with the strong interfacial adhesion between C/SiO₂ film and SiO₂/Si substrate, limiting the shrinkage of resorcinol/formaldehyde xerogel and SiO₂ xerogel during carbonization

in the lateral direction. However, this strength is probably also responsible for the formation of cracks when working with thick films. In this research, crack-free electrodes were successfully generated when using a PDMS mold with a pattern depth of $3.5\ \mu\text{m}$. However, clearly visible cracks were observed in C/SiO₂ film electrodes developed with a $10\ \mu\text{m}$ deep PDMS mold.

Using the optimized experimental conditions, rectangular, round and ring shaped electrode patterns showing strip widths from $10\ \mu\text{m}$ to $1\ \text{mm}$ were simultaneously generated on a $2 \times 2\ \text{cm}^2$ SiO₂/Si substrate with acceptable reproducibility. Figure 7.14 presents the SEM images of some representative C/SiO₂ electrodes generated by μ -TM technique. Note that in Figure 7.14 (C1), the interdigitated electrodes indicated by an arrow present a width of only $10\ \mu\text{m}$, indicating the potential of μ -TM in the fabrication of patterned carbon-based microelectrodes.

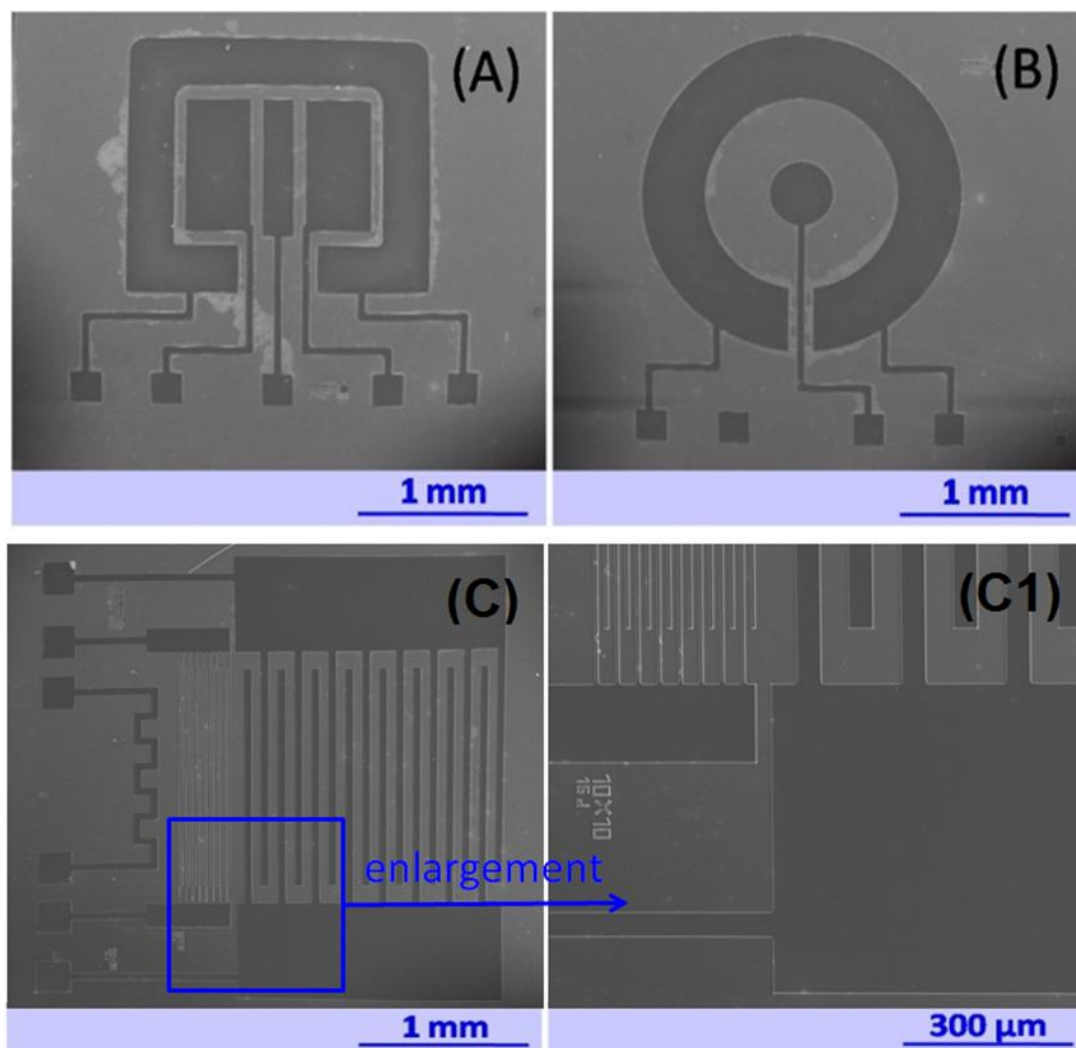


Figure 7.14. SEM images of typical μ -TM generated C/SiO₂ electrodes features

However, it is known that μ -TM process often leaves behind an undesirable thin residual layer connecting the patterns, since it is almost impossible to fully remove the liquid from the raised features of PDMS mold. In our case, a residual C/SiO₂ layer was also generated, which was subsequently removed using a CHF₃/O₂ plasma etching process.

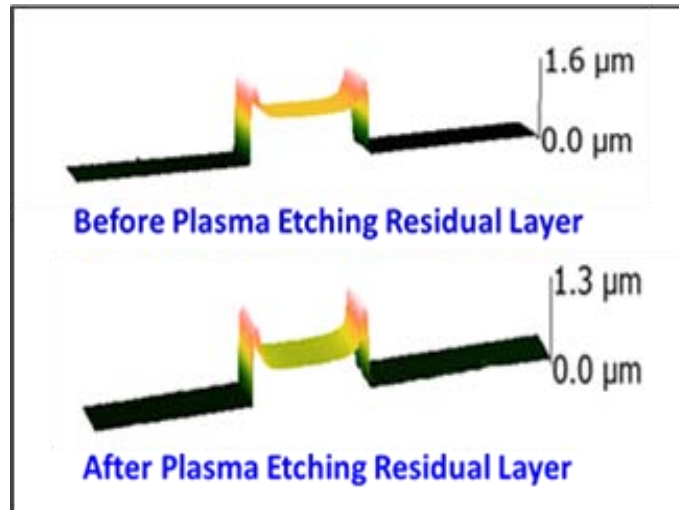


Figure 7.15. Representative 3D images of C/SiO₂ film stripe (lateral direction) before and after etching.

Figure 7.15 shows the cross-section 3D images of a patterned line before and after removing the residual layer. The thickness of the patterns decreased but the shape was almost unaltered. Also, as can be seen in Figure 7.16, no damage of the electrode structures was caused by the etching process.

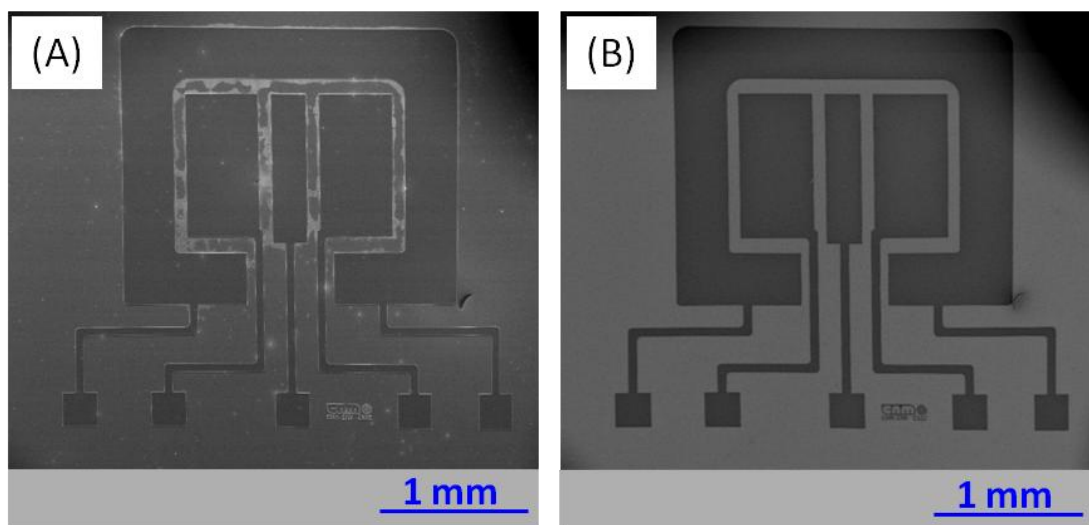


Figure 7.16. SEM images of a μ -TM C/SiO₂ electrode before (A) and after (B) etching the residual layer

7.3 Conclusion

In summary, C/SiO₂ thin-film electrodes derived from RF/APTES gels were successfully fabricated by both standard photolithography and soft-lithography techniques.

Regarding the photolithographic fabrication process, we have found that the contact of C/SiO₂ film with photoresist caused modification on the surface of the film, resulting in higher sheet resistance. This phenomenon is probably due to the incomplete removal of the photoresist layer by the acetone cleaning step of the film due to the chemical interaction of the photoresist with reactive carbon species present at the surface of the C/SiO₂ xerogel film. Therefore, a more effective cleaning process is probably required to get a pure C/SiO₂ patterned electrode surface.

With respect to the soft-lithographic approach, sols containing acetic acid are more suitable to carry out the μ -TM process because of the longer gelation time. A shrinkage effect took place, making the sol-gel patterns show smaller dimensions than those of the mold, wherein vertical shrinkage was more accentuated than the lateral one. Meniscus surface topography of the patterns was observed in the developed electrodes. Moreover, the fabrication of C/SiO₂ film electrodes using this approach required an etching process for the removal of a residual layer.

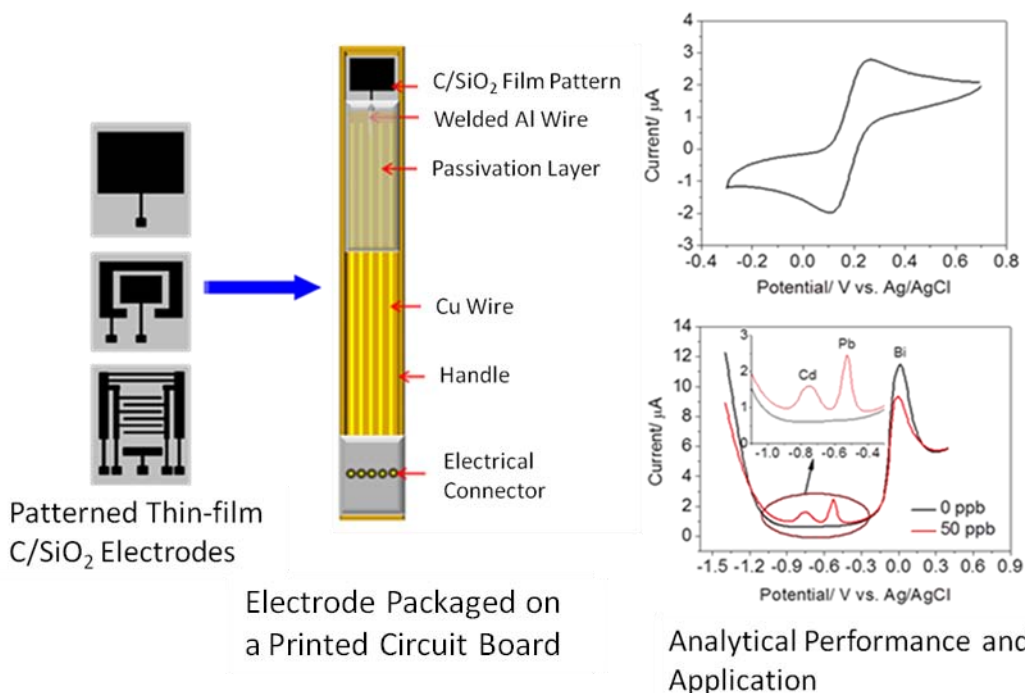
References

- [1] Xia Y, Whitesides GM. Soft Lithography. *Angewandte Chemie International Edition*. 1998;37:550-75.
- [2] Qin D, Xia Y, Whitesides GM. Soft lithography for micro- and nanoscale patterning. *Nat Protocols*. 2010;5:491-502.
- [3] Fernández-Sánchez C, Cadarso VJ, Darder M, Domínguez C, Llobera A. Patterning High-Aspect-Ratio Sol–Gel Structures by Microtransfer Molding. *Chemistry of Materials*. 2008;20:2662-8.
- [4] Sharma CS, Verma A, Kulkarni MM, Upadhyay DK, Sharma A. Microfabrication of carbon structures by pattern miniaturization in resorcinol-formaldehyde gel. *ACS applied materials & interfaces*. 2010;2:2193-7.
- [5] Seraji S, Wu Y, Jewell-Larson NE, Forbess MJ, Limmer SJ, Chou TP, et al. Patterned Microstructure of Sol–Gel Derived Complex Oxides Using Soft Lithography. *Advanced Materials*. 2000;12:1421-4.

[6] Martin CR, Aksay IA. Microchannel Molding: A Soft Lithography-inspired Approach to Micrometer-scale Patterning. *Journal of Materials Research*. 2005;20:1995-2003.

Chapter 8

Development and Characterization of Electrochemical Probes Based on C/SiO₂ Thin-film Electrodes



Summary

In Chapter 7, both conventional photolithography and soft-lithography were successfully employed to prepare C/SiO₂ thin-film electrodes from RF/APTES sols. This Chapter includes the post-processing steps carried out to package the electrodes and produce electrochemical probes that were further characterized by different electrochemical techniques. This work includes the generation of aluminum pads required for wire bonding of the thin-film C/SiO₂ electrodes to a printed circuit board, which in turn include the necessary Cu electrical pads that enable the connection of the fabricated electrodes to the measurement instrument (potentiostat). Electrode packaging was finished by coating and isolating the electrical wires with an epoxy resin. Thus the resulting electrochemical probes could

be immersed in water solutions. Afterwards, these fabricated probes were characterized by cyclic voltammetry in ferri/ferrocyanide inner-sphere and ferrocene outer-sphere redox probes. Preliminary studies on the electrochemical detection of heavy metals were also carried out by a Bi heavy metal co-deposition approach.

Part of the work presented in this Chapter is being included in one paper under preparation whose tentative title is "**Patterning Sol-gel Materials for Developing Carbon Thin-Film Based Electrodes**", by Pengfei Niu, César Fernández-Sánchez, Martí Gich, and Anna Roig.

8.1. Packaging C/SiO₂ Thin-film Electrodes

Once the C/SiO₂ thin-film was patterned into electrodes of different geometries and configurations onto SiO₂/Si substrates using either standard photolithography or soft-lithography techniques, as described in Chapter 7, they were diced into individual thin-film C/SiO₂ electrode chips having dimensions of 3 x 3 mm² or 3 x 3.5 mm². Then, each of them was packaged as an electrochemical probe for further characterization.

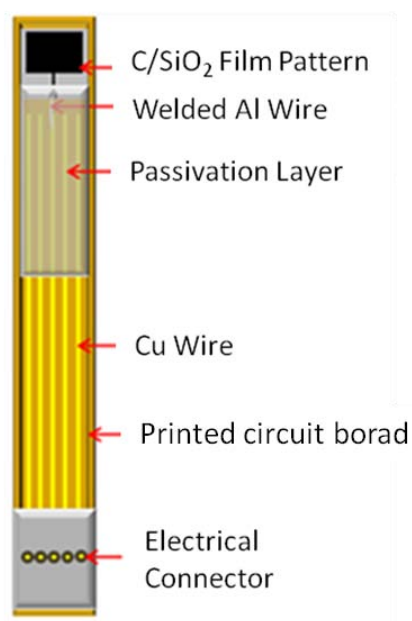


Figure 8.1. Schematic drawing of the fabricated electrochemical probes

Figure 8.1 shows the different components of the electrochemical probes produced with the C/SiO₂ electrode chips. The electrode chips were glued on a printed circuit board strip (PCB) in a recessed area defined at one end of each PCB. Then the electrodes were wire-bonded to the Cu electrical tracks also defined on the PCB. For that, an aluminum (Al) wire had to be bonded onto the contact pads, defined together with the electrodes, as shown in Figure 8.2 (A). This is a standard packaging process being carried out at the Chemical Transducers Group in IMB-CNM.

However, welding Al wire on the defined C/SiO₂ pad proved to be very difficult. The process yield was very low and although the wire bonding was successfully performed, the weld was not stable and easily came off the pad. A stable welded wire between the electrode pads and the Cu tracks is strictly required in order to get

robust electrochemical probes containing the fabricated thin-film C/SiO₂ electrodes.

In order to simplify the bonding process and make a stable interconnection, an additional aluminum layer was deposited over the defined C/SiO₂ pads by a shadow-mask lithographic approach, developed by the Power Devices group at IMB-CNM. Over 50 individual C/SiO₂ electrode chips were placed in recessed wells defined on a substrate that had the same dimensions of the chips. Then, the substrate was aligned against a mask containing the pad designs and through which a 1 μm-thick Al layer was deposited over the C/SiO₂ pads by a chemical vapor deposition process. Herein, it is worth mentioning that the alignment between the C/SiO₂ pads and the mask was critical for accurate deposition. No further details of this process were disclosed to us because it is proprietary information.

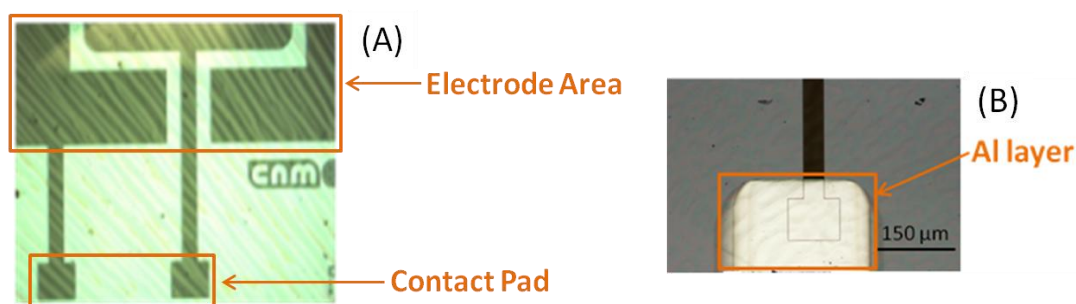


Figure 8.2. Contact pads connecting the electrodes (A) and deposited Al layer over the pad (B)

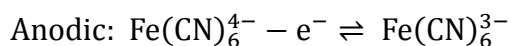
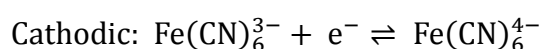
Figure 8.2 (B) shows the deposited Al layer that is larger than the C/SiO₂ pad. It is necessary to make the dimensions of the Al layer larger than those of the C/SiO₂ pad because of the weak interaction between Al and C/SiO₂ film. When the wire bonding was done on Al layer only covering the C/SiO₂ pad, the Al easily peeled off the C/SiO₂ pads. In order to solve this problem, we took advantage of the strong interfacial interaction between chromium/aluminum film and SiO₂/Si substrate and deposited a bigger Al layer with a seed layer of 10 nm thick chromium underneath it. Then, the wire bonding process was successfully performed on the metal film regions on SiO₂/Si substrate. Afterwards, an insulator layer of epoxy resin (EPOTEK H77) was coated on the electrical wires to isolate them from water solutions when carrying out electrochemical measurements. The curing process of epoxy was done at 120°C for 2 hours.

8.2. Electrochemical Characterization of the Electrochemical Probes

Cyclic voltammetry was firstly used to characterize the fabricated thin-film C/SiO₂ electrochemical probes. Before presenting the results obtained with these electrodes, some basic information about the commonly used electroactive species for demonstrating cyclic voltammetry is given below.

8.2.1. Common Electroactive Species

Ferri/ferrocyanide redox pair has been commonly used as a benchmark electroactive probe to study electron kinetics because of its ideal-like behavior. The corresponding electrochemical reaction is a reversible one electron transfer process. Depending on the electrode geometry, this process normally is governed by the diffusion of the ferri-/ferrocyanide species from the bulk of the solution to the electrode/solution interface. These reactions are shown below:



When considering the electrochemical process of ferri-/ferrocyanide redox pair, the composition of the electrode surface has to be taken into account because it often plays an important role during the process of electron transfer step at the electrode/electrolyte interface. This electron transfer can also be influenced by the electrolyte composition.

For instance, it is reported [1] that when sulfates are present in solution, reduction of $\text{Fe}(\text{CN})_6^{3-}$ to $\text{Fe}(\text{CN})_6^{4-}$ proceeds through an inner sphere reaction mechanism, that is, it involves a very strong interaction between $\text{Fe}(\text{CN})_6^{3-}/\text{Fe}(\text{CN})_6^{4-}$ species and the electrode surface. In other cases, this reaction follows an outer sphere mechanism in which $\text{Fe}(\text{CN})_6^{3-}/\text{Fe}(\text{CN})_6^{4-}$ species do not strongly interact with the electrode surface, and are kept separated from the electrode surface by one layer of solvent molecules.

However, Xiong et al. [2] have recently found that ferri-/ferrocyanide redox couple in

aqueous potassium chloride (KCl) electrolyte was not purely an outer sphere reaction in nature. The response for ferrocyanide was found to be strongly inhibited after exposing a graphite electrode surface to some organic solvents, which regularly would come into contact with graphite surface. Not only organic absorbents, but oxygen-containing organic groups on the electrode surface can inhibit the voltammetric response of ferrocyanide, as pointed by Lounasvuori et al. [3] who showed this effect with graphene based electrodes.

Besides ferri-/ferrocyanide redox couple, ferrocene is also widely used in cyclic voltammetric studies, because of its ideal reversible redox behavior (i.e. $\text{Fe}(\text{C}_5\text{H}_5)_2 \rightleftharpoons \text{Fe}(\text{C}_5\text{H}_5)_2^+$ ferrocene/ferrocenium) [4, 5]. Moreover, unlike the feasible inner sphere reactions of ferri-/ferrocyanide redox pair, which is highly dependent on the chemical nature of the electrode surface, ferrocene is known to follow an electron transfer process based on an outer sphere mechanism that is less influenced by the electrode material.

In this context, both ferri-/ferrocyanide and ferrocene electroactive species were employed to study the electrode responses to reversible inner- and outer redox species, respectively. Since ferrocene is insoluble in water but soluble in ethanol/methanol, the preparation of ferrocene solutions was carried out by firstly dissolving this probe in ethanol and then diluting it in 0.1 M aqueous KNO₃ solution. The results of these characterizations are presented in the next two sections for the electrodes prepared by photolithography (section 8.2.2) and those prepared by soft-lithography (section 8.2.3). Also, the electrochemical performance of these probes was compared with that of the original thin-films made by spin-coating process, which were implemented in custom-made electrochemical cells, whose design and measurement process were already described in Chapter 6. For carrying out cyclic voltammetric measurements with the patterned electrodes, we used a conventional three-electrode electrochemical cell, comprising the patterned C/SiO₂ working electrode, a platinum counter electrode and a Ag/AgCl reference electrode immersed into a plastic beaker with 10 mL of aqueous solution containing the respective electroactive species.

8.2.2. Electrochemical Devices Based on C/SiO₂ Thin-film Electrodes Patterned by Photolithography

8.2.2.1. Voltammetric response to inner- and outer-sphere species

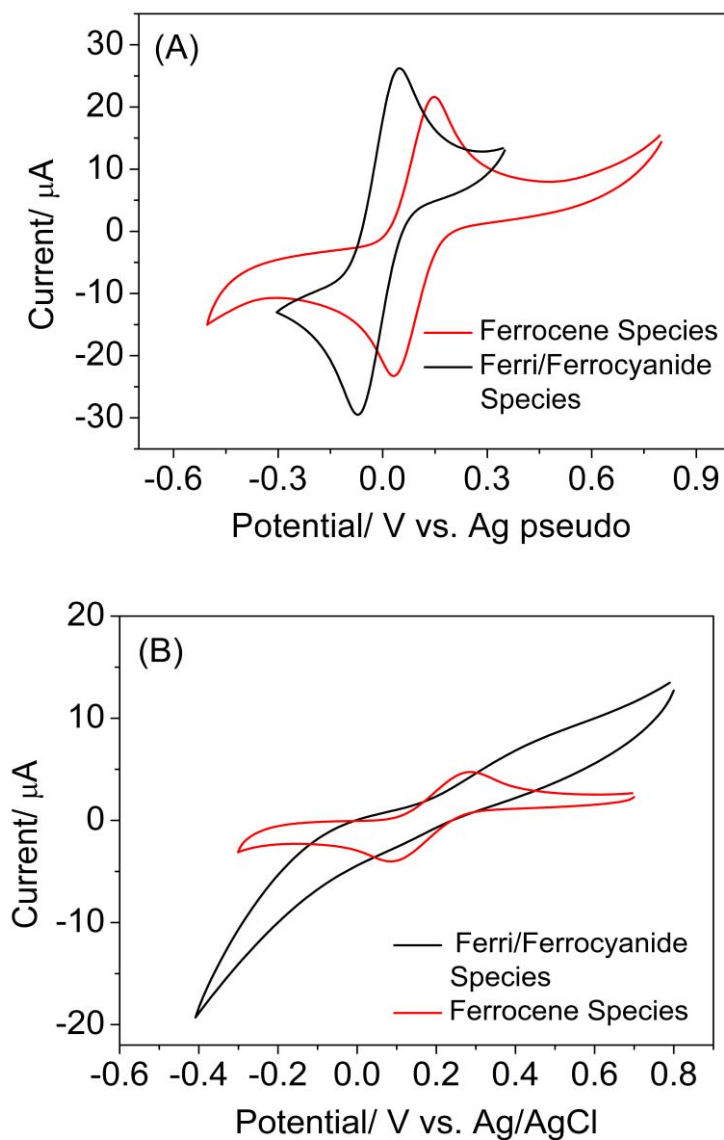


Figure 8.3. Cyclic voltammograms recorded in 0.1 M KNO₃ solutions containing 1 mM ferri/ferrocyanide (black curve) and 1 mM ferrocene-ethanol (red curve), using (A) original CS41 thin-film and (B) electrodes produced by photolithography from CS41 C/SiO₂ films. Scan rate was 50mV/s

Figure 8.3 shows the voltammograms recorded at original CS41 C/SiO₂ thin-films and the patterned C/SiO₂ electrodes in solutions containing either ferri-/ferrocyanide or ferrocene electroactive species. On the original film, quasi-

reversible voltammetric signals were recorded, showing oxidation and reduction peaks at around +75 mV and -62 mV for ferri/ferrocyanide and at around +150 mV and +25 mV and for ferrocene, respectively. Accordingly, peak to peak separations values (ΔE_p) of around 137 mV and 125 mV were obtained, respectively. However, using the patterned C/SiO₂ electrodes, a quasi-reversible signal was only recorded in the ferrocene solution and no apparent signal was recorded in the ferri-/ferrocyanide solution. Moreover, the ΔE_p obtained from the ferrocene voltammetric signal increased from 125 mV of the original film to 186 mV of the patterned electrodes. This demonstrates a slower electron transfer rate when using the patterned electrodes.

From these results, two questions were formulated. 1) Why the expected redox response for ferri-/ferrocyanide species could not be recorded with the patterned electrodes? 2) Why is the electron transfer slower in the patterned electrodes compared to the original films when working with ferrocene solutions?

As we discussed in Chapter 7, we have found that after photolithography process, the surface of the spin-coated C/SiO₂ film was modified, which is manifested by a higher sheet resistance. We think that this is probably related to the incomplete removal of the photoresist layer. Therefore, it is not so surprising that the response of the ferri-/ferrocyanide couple could not be recorded at the patterned electrodes, since it has been proved that organics can strongly inhibit the inner-sphere electron transfer at carbon electrodes. In contrast, in the case of ferrocene, following an outer sphere electron transfer process, the expected redox signal is observed albeit with a slower charge transfer rate which is likely related to the higher sheet resistance after photolithography.

In this context, the effect of scan rate on the peak current is studied using ferrocene solutions. Figure 8.4 (A) shows the cyclic voltammograms recorded in 1 mM ferrocene solutions at scan rates varying from 10 to 100mV/s. The peak current responses increase with the scan rate and are directly proportional to the square root of the scan rate, as shown in Figure 8.4 (B). This behavior demonstrates a diffusion-controlled electrochemical process taking place at the electrode/solution interface. In addition, the ratio between anodic peak and cathodic peak currents is near one at all the tested scan rates and ΔE_p increases as a function of scan rate

(Table 8.1), revealing that the electrode reaction is a quasi-reversible process.

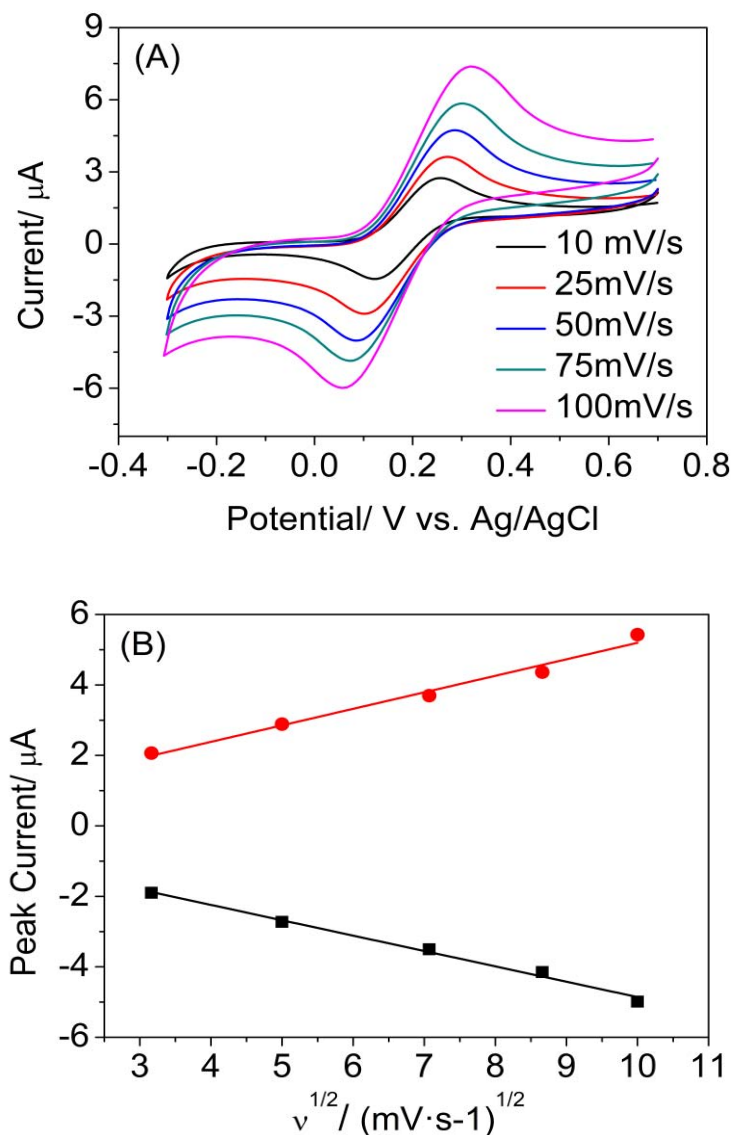


Figure 8.4. Cyclic voltammograms recorded in a 0.1 M KNO_3 solution containing 1 mM ferrocene redox species with the electrochemical device that integrates a CS41 C/SiO₂ thin-film electrode patterned by photolithography, at different scan rates (A) and linear plots of the recorded anodic and cathodic peak currents with the square root of the scan rate (B).

Table 8.1 Summary of ΔE_p at different scan rates

Scan Rate (mV/s)	10	25	50	75	100
$\Delta E_p / \text{mV}$	122	153	186	217	232

8.2.2.2. Electrochemical sensor for heavy metals using C/SiO₂ thin-film electrodes patterned by photolithography

Even though C/SiO₂ film chip electrodes show a slower electron transfer at electrode/electrolyte interface compared to original films, these electrodes can still be employed to produce an electrochemical sensing platform. In particular, we studied their performance in the determination of trace amounts of Pb(II) and Cd(II) ions in aqueous solutions. The detection approach was based on the co-deposition of Bi and the heavy metal ions on the electrode surface. The supporting electrolyte was 0.1 M H₂SO₄ solution containing 2 ppm Bi(III) ions.

Electrochemical measurements were carried out using the following procedure. Firstly, Pb(II), Cd(II) and Bi(III) were electrochemically reduced and co-deposited on a C/SiO₂ film chip electrode at -1.4 V under stirring for 3 min. After the stirring was stopped, the system was equilibrated for 20 s and then the voltammogram was recorded by sweeping the potential from -1.4 V to 0.4 V. After the recording of one measurement, the electrode was treated by applying a potential at +0.4 V for 30 s to completely remove the previously deposited metal for another measurement. Here it should be noted that the error bars are not given in the corresponding calibration curve because we just carried out one measurement for each concentration. This study is just to illustrate the possibility of using these C/SiO₂ thin-film electrodes as novel electrochemical sensing platforms.

Figure 8.5 (A) shows the recorded stripping voltammograms for the determination of Cd(II) and Pb(II) in a concentration range from 10 ppb to 100 ppb. The peaks at around -0.8 V, -0.5 V and 0 V are ascribed to the stripping process of Cd, Pb and Bi respectively. This platform shows high sensitivity for the determination of Pb as indicated by the good definition and sensitivity of the corresponding stripping signals, which is clearly differentiated from the blank signal (0 ppb of Pb) to the signal recorded at the tested concentration of Pb from 10 ppb to 100 ppb. The peak current of Pb increases linearly in the concentration range of 10 to 100 ppb as shown in Figure 8.5 (B). These results indicate the possibility of using these C/SiO₂ thin-film electrodes as novel carbon-based electrochemical platforms for Pb(II) sensing. Moreover, during these experiments, it was demonstrated that these electrodes can be used for many measurements, since no physical damage and drop

in the performance was observed after 20 measurements with the same chip.

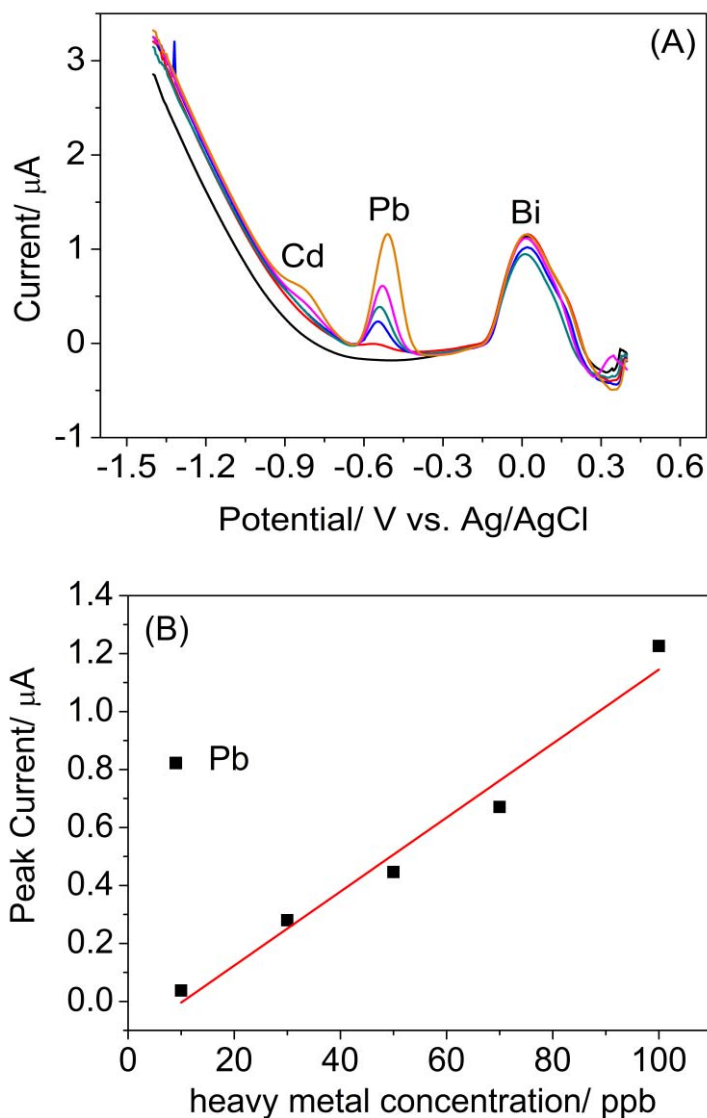


Figure 8.5. Square wave anodic stripping voltammograms for the determination of different concentrations of Pb(II), Cd(II) (from bottom to top, 0, 10, 30, 50, 70, 100 ppb) recorded with a C/SiO₂ thin film chip electrode patterned by photolithography. Accumulation was carried out at -1.4 V for 3min, Bi(III) concentration was maintained at 2 ppm in the solution for the in situ detection approach.

We also noticed the relatively poor analytical performance of these film electrodes for detecting Cd. This is likely to be related with the thin layer of organic photoresist that may be partially covering the electrodes, as described in Chapter 7. We believe that it should be possible to easily remove this layer by applying a subsequent plasma etching process. Unfortunately, further studies could not be carried out in this Thesis due to technical issues out of our control that kept the plasma etching

equipment out of work for several months. Further studies will be directed to deeply study the electrochemical properties of these C/SiO₂ thin-film electrodes fabricated by photolithography. These will include 1) optimization of an adequate surface cleaning process, 2) influence of electrode geometry design on the electrode performance, and 3) electrochemical application of these sensing platforms.

8.2.3. C/SiO₂ Film Chip Electrodes Fabricated by μ -TM Soft-Lithography

Approach

8.2.3.1. Voltammetric response to inner- and outer-sphere species

C/SiO₂ thin-film electrodes fabricated by μ -TM have not been contacted with any organics coming from a photoresist but exposed to CHF₃/O₂ plasma for the removal of residual C/SiO₂ layer. In the case of these electrodes, the expected redox process of out-sphere based ferrocene was just recorded because ferri-/ferrocyanide redox species did not produce any signal (Figure 8.6).

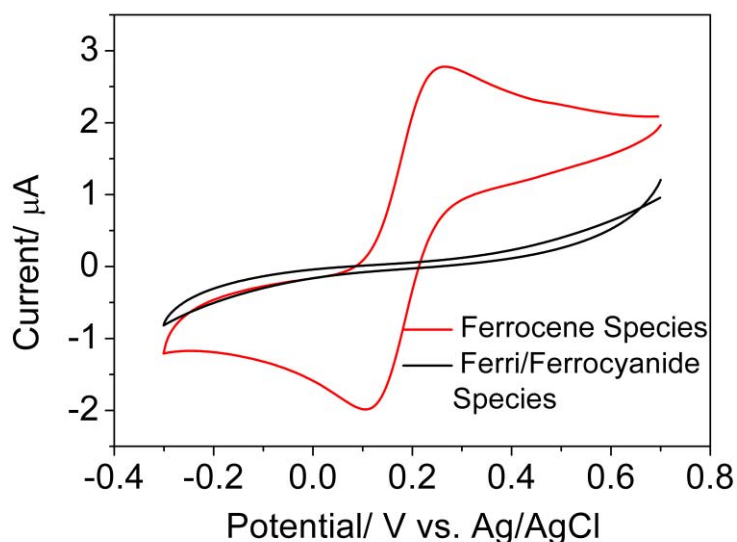


Figure 8.6. Cyclic voltammograms recorded on μ -TM generated C/SiO₂ film chip electrodes after CHF₃/O₂ plasma etching in 0.1 M KNO₃ solution containing 1 mM ferrocene-methanol (red curve) and 1 mM ferri-/ferrocyanide redox couple (black curve), respectively. Scan rate was 50mV/s

As mentioned above, surface oxygen functionalization would significantly inhibit the electrochemical response of ferri/ferrocyanide redox probe on carbon-based electrode. In order to ascertain if the electrode surface was modified during the

plasma etching process applied to remove the residual layer, cyclic voltammograms were recorded in ferri-/ferrocyanide solutions with electrodes fabricated by μ -TM but that did not go through the CHF_3/O_2 plasma etching step.

Figure 8.7 shows the corresponding voltammograms, where it can be seen the strong responses for this redox species. Here it must be mentioned that this measurement was done before we developed the standard packaging process, including Al pads deposition for obtaining a stable welded Al wire between the electrode and PCB. So, the contact between the C/SiO₂ electrode and the PCB was probably not very robust. Maybe this explains why the responses for ferri-/ferrocyanide are not reversible. Nevertheless, this result evidences the effect of the CHF_3/O_2 plasma etching process on the poor response of the resulting electrodes for the detection of inner sphere ferri-/ferrocyanide system. The creation of oxygen containing groups at the electrode surface is likely to account for this behavior, which is going to be studied by XPS analysis.

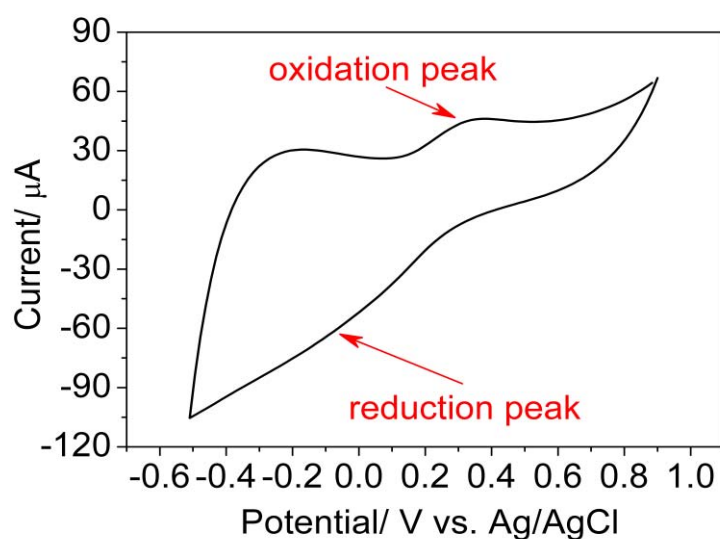


Figure 8.7. Cyclic voltammograms recorded on μ -TM generated C/SiO₂ thin-film chip electrodes before CHF_3/O_2 plasma etching in 0.1 M KNO_3 solution containing 1 mM ferri-/ferrocyanide redox couple. Scan rate was 50mV/s.

Regarding ferrocene system, the electrochemical responses of the electrodes fabricated by μ -TM were similar to that of the electrodes produced by photolithography. Figure 8.8 shows the voltammetric responses recorded at different scan rates and the linear relationship found between the corresponding peak currents and the square root of the scan rate in a range from 10 to 100mV/s.

This behavior unambiguously demonstrates the diffusion controlled process that also takes place when using these electrodes.

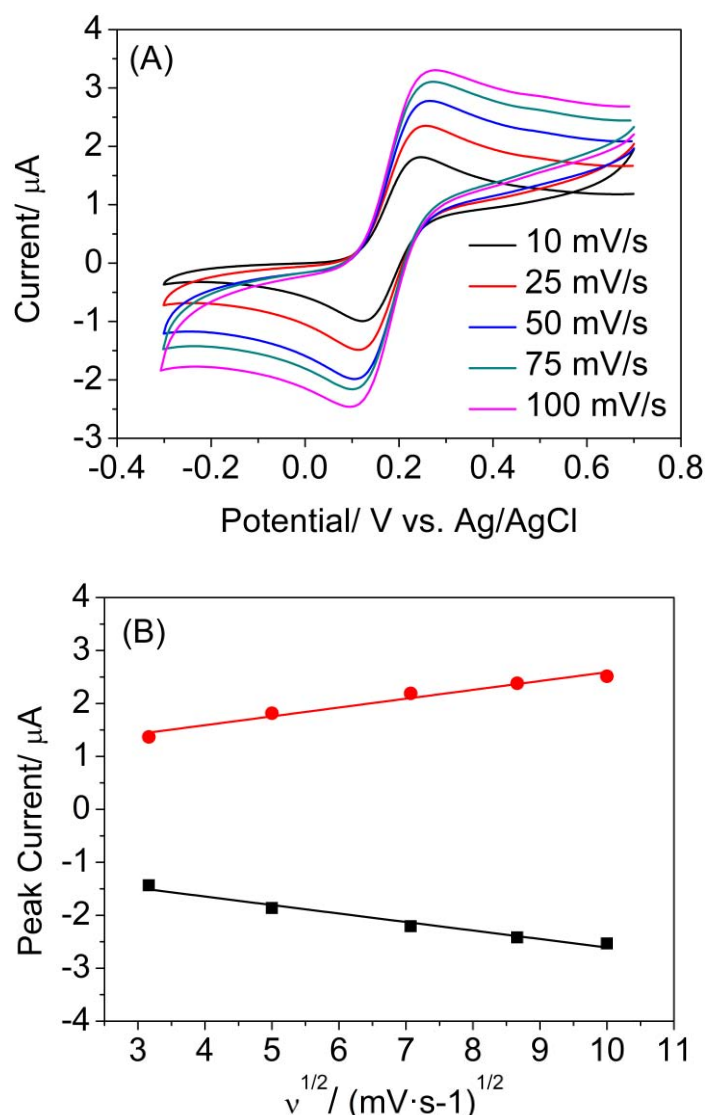


Figure 8.8. Cyclic voltammograms recorded in a 0.1 M KNO₃ solution containing 1mM ferrocene at μ -TM patterned C/SiO₂ film integrated electrode, under different scan rates (A) and plots of anodic and cathodic peak currents vs. scan rate (B).

The measured ΔE_p values are presented in Table 8.2. These values increase with the scan rate, which is an indication of the quasi-reversible behavior of this redox process. Also, they are smaller than those obtained with the electrodes patterned by photolithography, shown in Table 8.1. This indicates a relatively faster electron transfer rate at the electrode/electrolyte interface.

It is also worth mentioning that the ΔE_p value of 131 mV recorded at the scan rate

of 50 mV/s is comparable to that recorded with the original spin-coated film of around 125 mV (Figure 8.3(A)). This shows that the C/SiO₂ thin-films are less affected by the whole soft lithography process including the plasma etching of the residual layer, than by standard photolithography process. Therefore, it can be predicted that these electrodes can show better electrochemical performance than those produced by photolithography, as is shown below for the detection of heavy metals.

Table 8.2 Summary of ΔE_p at different scan rates recorded with μ -TM derived electrode

Scan Rate/ mV/s	10	25	50	75	100
$\Delta E_p / V$	106	119	131	135	141

8.2.3.2. Electrochemical sensor for heavy metal detection using thin-film C/SiO₂ electrodes patterned by μ -TM

The C/SiO₂ electrodes produced by μ -TM were also used for measuring heavy metals following the same approach as for the electrodes produced by photolithography.

Figure 8.9 (A) shows the stripping voltammograms for the determination of Cd(II) and Pb(II) in a concentration range from 10 ppb to 50 ppb. The corresponding stripping peaks for Cd, Pb and Bi are clearly visible in all the tested concentrations, and are located at around -0.75 V, -0.5 V and 0 V, respectively. The variation in peak current with increasing Cd(II) and Pb(II) concentration is shown in Figure 8.9 (B). A linear increase is observed for both heavy metals. The recorded stripping peaks for both analytes are much larger than those recorded with the electrodes produced by photolithography, thus confirming the better electrochemical performance of the soft-lithography electrodes. Also, it should be mentioned that the electrochemical devices were robust and could be used repeatedly without showing any loss of its performance.

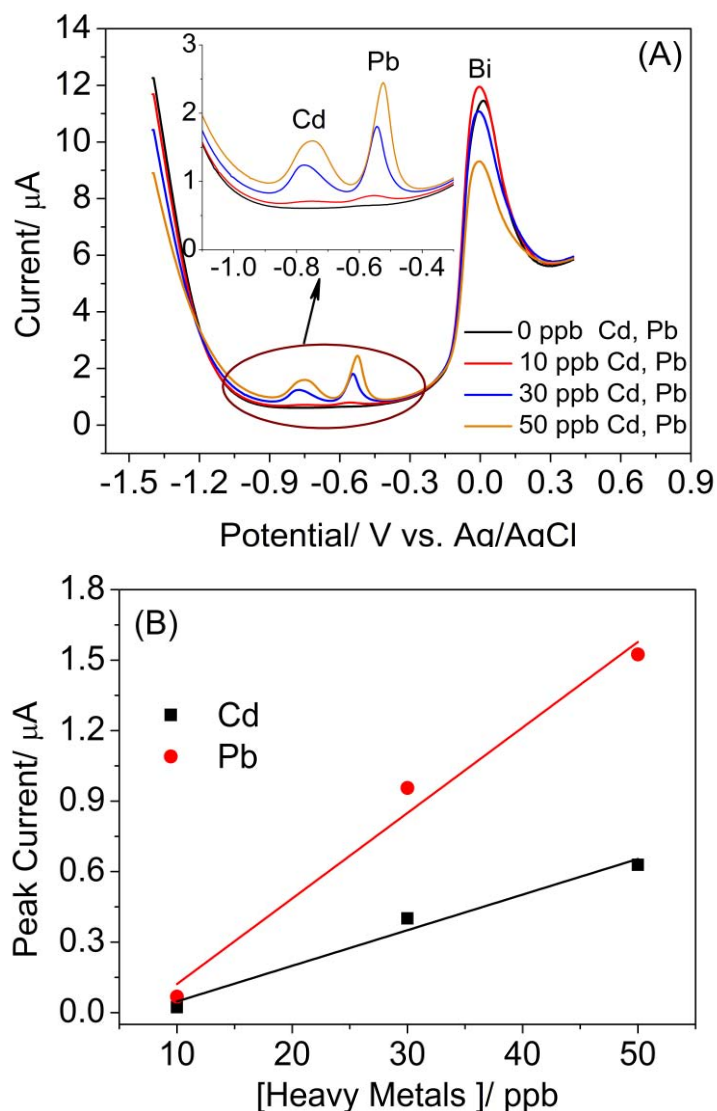


Figure. 8.9. Square wave anodic stripping voltammograms recorded in solutions containing different concentrations of Pb(II), Cd(II) (from bottom to top, 0, 10, 30, 50 ppb) and 2 ppm Bi(III) with the C/SiO₂ electrodes fabricated by μ -TM. Accumulation was carried out at -1.4 V for 3 min.

8.3 Conclusion

In this chapter, thin-film C/SiO₂ electrodes fabricated by both photolithography and μ -TM soft lithography was electrochemically characterized. Electrodes were successfully integrated in a PCB and robustly packaged to be repeatedly used in the analysis of target analytes in aqueous solutions. The entire fabrication process includes the deposition of aluminum pads required to carry out the wire bonding of the electrodes to the PCB. The C/SiO₂ thin-film electrodes fabricated by both

lithographic techniques do not provide any electrochemical signal in inner-sphere ferri-/ferricyanide solutions, this being likely related to the interaction of this species with the electrode surface. Nevertheless, the electrodes could be characterized in solutions containing outer-sphere redox probes such as ferrocene and proved to perform successfully as novel electroanalytical probes to be applied in chemical sensing. Thus, they were applied to the detection of heavy metals and preliminary results showed their feasible application to monitor these pollutants in water.

References

- [1] Vazquez-Arenas J, Pritzker M. How to Relate Experiments and Theory for Electrochemistry? Linear Sweep Voltammetry for the Reduction of $\text{Fe}(\text{CN})_6^{3-}$. *Education for Chemical Engineers*. 2010;5:e78-e86.
- [2] Xiong L, Batchelor-McAuley C, Ward KR, Downing C, Hartshorne RS, Lawrence NS, et al. Voltammetry at Graphite Electrodes: The Oxidation of Hexacyanoferrate (II) (ferrocyanide) Does not Exhibit Pure Outer-sphere Electron Transfer Kinetics and is sensitive to Pre-exposure of the Electrode to Organic Solvents. *Journal of Electroanalytical Chemistry*. 2011;661:144-149.
- [3] Lounasvuori MM, Rosillo-Lopez M, Salzmann CG, Caruana DJ, Holt KB. Electrochemical Characterisation of Graphene Nanoflakes with Functionalised Edges. *Faraday Discussions*. 2014;172:293-310.
- [4] Sieben JM, Ansón-Casaos A, Montilla F, Martínez MT, Morallón E. Electrochemical Behaviour of Different Redox Probes on Single Wall Carbon Nanotube Buckypaper-modified Electrodes. *Electrochimica Acta*. 2014;135:404-411.
- [5] Griffiths K, Dale C, Hedley J, Kowal MD, Kaner RB, Keegan N. Laser-Scribed Graphene Presents an Opportunity to Print a new Generation of Disposable Electrochemical Sensors. *Nanoscale*. 2014;6:13613-13622.

Chapter 9

Conclusions and Further Work

9.1. General Conclusions

This Thesis aimed at developing environmentally-friendly electrochemical devices for the sensitive analysis of trace concentrations of heavy metal ions in aqueous solution. The main achievements and conclusions of this Thesis are summarized below:

1- Based on resorcinol/formaldehyde sol-gel chemistry, we have synthesized bulk composites of porous carbon with bismuth nanoparticles both by impregnation and co-synthesis procedures. These materials consist of an open porous structure of carbon matrix with well distributed bismuth nanoparticles.

2- Conventional carbon paste sensors prepared with the nanocomposites displayed performances beyond the state-of-the-art in the sensitive stripping voltammetric detection of heavy metals in both buffered and real water samples. Very low limits of detection and wide linear calibration ranges were obtained for cadmium, lead and nickel in waters, which are targeted by the EU and US-EPA regulations as priority water pollutants. In addition, the minimum concentration detected for cadmium and lead was 0.6 ppb using an overall analysis time shorter than 4 min, which is well below the threshold concentrations established for drinking water quality. The electrodes also show high accuracy in the analysis of real water samples of different nature containing these pollutants at different concentrations.

3- The bismuth nanoparticle/porous carbon nanocomposite material powders were successfully applied to the fabrication of disposable miniaturized thick-film electrodes by screen-printing technique. The resulting electrochemical devices offer very competitive analytical performance for the detection of both cadmium and lead. In addition, these sensors show other advantageous features such as 1) easy-of-operation, by avoiding an extra step to incorporate Bi onto the electrodes, and 2) high sensitivity and accuracy for heavy metal determination.

4- The scaling up production of bulk bismuth nanoparticle/porous carbon nanocomposites by co-synthesis revealed that the use of glycerol formal solvent and bismuth nitrate as Bi source had a risk of explosion during the pyrolysis process.

5- Large scale uniform and continuous carbon films were deposited on 4-inch SiO₂/Si substrates by spin-coating resorcinol/formaldehyde based sols. The interfacial adhesion between carbon films and SiO₂/Si substrates is significantly enhanced by the addition of a SiO₂ precursor to the sol formulation and these C/SiO₂ films were conductive enough to be used as novel electrochemical sensing platforms. The incorporation of bismuth nanoparticles into C/SiO₂ thin-films during the sol-gel deposition stage is challenging due to the loss of bismuth by evaporation during the film carbonization step. C/SiO₂/Au nanocomposite thin-films could be successfully prepared by an impregnation approach.

6- Thin-film C/SiO₂ electrodes derived from RF/APTES sol-gels were successfully fabricated by both standard photolithography and soft-lithography techniques. Regarding the photolithographic fabrication process, we have found that the contact of C/SiO₂ film with the photoresist caused modifications on the surface of the film, resulting in higher sheet resistance. With respect to the soft-lithographic approach, sol solutions containing acetic acid are more suitable to carry out the μ -TM process because of the longer gelation time. A shrinkage effect took place resulting in the patterns fabricated by soft-lithography showing smaller dimensions than those in the mold and also a meniscus-like surface topography. The vertical shrinkage was more accentuated than the lateral one. In addition, a subsequent step to remove a residual layer was required for the eventual fabrication of thin-film C/SiO₂ electrodes using this technique.

7- Thin-film C/SiO₂ electrodes were successfully integrated into a printed circuit board (PCB) and robustly packaged to be repeatedly used in the analysis of target analytes in aqueous solutions. The entire fabrication process required the deposition of aluminum pads to carry out the wire bonding of C/SiO₂ film electrodes to the PCB. The thin-film C/SiO₂ electrodes fabricated by both lithographic techniques do not provide any electrochemical signal in inner-sphere ferri-/ferricyanide solutions. Nevertheless, they could be characterized in solutions containing outer-sphere redox probes such as ferrocene and proved to perform

successfully as novel electroanalytical probes to be applied in chemical sensing.

8- In spite of the impossibility of preparing porous C/SiO₂ films with Bi nanoparticles by a one-pot synthesis, the successful determination of heavy metals using C/SiO₂ thin-film electrodes fabricated by both lithographic approaches have been accomplished by co-deposition of Bi and the heavy metal target analytes.

9.2. Ongoing and Further Work

1- Regarding bulk bismuth/carbon nanocomposite materials, alternative syntheses that avoid the use of glycerol formal or bismuth nitrate for materials preparation are being investigated.

2- Screen-printed bismuth/carbon electrodes did not perform as good as conventional carbon paste electrodes made by the same bismuth/carbon nanocomposite. Further investigation should be directed towards the optimization of bismuth/carbon nanocomposite ink preparation to improve the analytical performance of these disposable devices and the integration of the electrodes into an automatic system for on-line analysis of trace heavy metals.

3- For thin-film C/SiO₂ electrodes, a detailed study of these novel electrochemical sensing platforms should be carried out, including the influence of the different electrode geometries on the electrochemical performance, and the sensing properties towards different electroactive species.

4- It would be very useful to find a way to incorporate bismuth nanoparticles onto the thin-film C/SiO₂ electrodes in order to avoid Bi deposition step during the heavy metal analysis.

5- Another development that would be interesting to undertake is the further integration of thin-film C/SiO₂ working electrode, reference and counter electrodes on the same SiO₂/Si chip for the fabrication of lab-on-chip devices based on these C/SiO₂ thin-film electrodes for heavy metal analysis.

6- The approach followed in this work to prepare bismuth nanoparticle/porous carbon composites can be extended to obtain similar composites but with other types of nanoparticles such as Au, Fe₃O₄ or TiO₂ that can be relevant in other

sensing applications. Similarly, it would be interesting to explore other routes to the formation of the porous carbon matrix that could bring advantages such as low-cost or more versatility in the synthesis of nanocomposites.

Conferences and Publications of This PhD Thesis

Conferences and Workshops

1) June 11th – June 15th 2014, 15th International Conference on Electroanalysis, Malmö, Sweden (**Oral Presentation**)

Title: Highly Sensitive Electrochemical Analysis of Heavy Metals with Bismuth Nanoparticle Porous Carbon Composite Electrodes

Pengfei Niu, César Fernández Sánchez, Martí Gich, and Anna Roig

2) August 25th – August 30th 2013, 17th International Sol-gel Conference, Madrid, Spain (**Poster**)

Title: Sol-gel Derived Bismuth-Carbon Nanocomposite for the Detection of Heavy Metals

Pengfei Niu, Martí Gich, César Fernández Sánchez, and Anna Roig

3) September 17th 2013, Biosensors for a Better Environment, IRTA, Barcelona, Spain (**Poster + Flash Presentation**)

Title: Bismuth-Carbon Nanocomposite Electrodes for the Simultaneous Detection of Heavy Metals

Pengfei Niu, Martí Gich, César Fernández Sánchez, and Anna Roig

4) April 2nd 2013 – April 5th 2013, Training School: Characterization Techniques for Interfaces in Hybrid Materials, Bordeaux, France (Poster)

List of Publications

Book Chapter

1) **Pengfei Niu**, Martí Gich, César Fernández-Sánchez, Anna Roig, Sol-Gel Nanocomposite for Electrochemical Sensor Applications, p. 1413-1434, in The Sol-Gel Handbook: Synthesis, Characterization and Application, Editor David Levy and Macros Zayat, Wiley-VCH books;

Review Paper

1) María Díaz- González, Manuel Gutiérrez-Capitán, **Pengfei Niu**, César Fernández-Sánchez, Electrochemical Devices and Processes for Detection and Remediation of Priority Pollutants Included in the EU Water Framework Directive, Submitted to Trac Trend in Analytical Chemistry;

Research Papers

1) Martí Gich, César Fernández-Sánchez, Liviu Cosmin Cotet, **Pengfei Niu**, Anna Roig, Facile Synthesis of Porous Bismuth-Carbon Nanocomposites for the Sensitive Detection of Heavy Metals, Journal of Materials Chemistry A, 2013, 1, 11410-11418;

2) **Pengfei Niu**, César Fernández-Sánchez, Martí Gich, Carlos Ayora, Anna Roig, Electroanalytical Assessment of Heavy Metals in Waters with Bismuth Nanoparticle-Porous Carbon Paste Electrodes, Electrochimica Acta, 2015, 165, 155-161;

3) **Pengfei Niu**, César Fernández-Sánchez, Martí Gich, Carla Navarro-Hernández, Pablo Fanjul-Bolado, Anna Roig, One-step Fabrication of Screen-Printed Bismuth Nanoparticle-Carbon Nanocomposite Electrodes for Heavy Metal Detection, Submitted to Sensors and Actuators B: Chemical;

4) **Pengfei Niu**, Martí Gich, César Fernández-Sánchez, Anna Roig, Deposition of Carbon Films on SiO₂/Si Substrates with Enhanced Interfacial Adhesion, in Preparation;

5) **Pengfei Niu**, César Fernández-Sánchez, Martí Gich, Anna Roig, Patterning Sol-gel Materials for Developing Carbon Thin-Film Based Electrodes, in Preparation;

Facile synthesis of porous bismuth–carbon nanocomposites for the sensitive detection of heavy metals†

Cite this: *J. Mater. Chem. A*, 2013, **1**, 11410

Martí Gich,^{*a} César Fernández-Sánchez,^{*b} Liviu Cosmin Cotet,^c Pengfei Niu^a and Anna Roig^a

This article describes the facile and scalable synthesis of carbon xerogel–bismuth nanoparticle composites using two different approaches. It also demonstrates the high potential of these materials for developing electrochemical sensors, which could simultaneously analyze in a rapid test very low concentrations (<1 ppb) of heavy metals in water. The microstructural characterization of the composites by different techniques revealed a microporous carbon structure with evenly dispersed spherical Bi nanoparticles whose dimensions depend on the synthesis conditions. Sensors prepared with the nanocomposites were used to test the electrochemical performance of the materials for the detection of several heavy metal ions in water such as cadmium and lead, which are included in the list of priority substances of most water policies. The minimum concentration detected for these two species was 0.6 ppb for an overall analysis time of below 5 min. This concentration is well below the maximum limits allowed in drinking water according to the most stringent regulations, and of the order of the maximum allowance concentration of environmental quality standards.

Received 5th June 2013

Accepted 23rd July 2013

DOI: 10.1039/c3ta12190a

www.rsc.org/MaterialsA

1 Introduction

Sensors find widespread uses in modern societies from industrial production and security to food analysis or environmental monitoring. The innovation in this area is currently driven by the development of systems which can provide real-time on-site measurements operated by non-specialists, not to mention the deep-rooted search for lower detection limits, improved sensitivity levels and wide spectrum of target analytes. Electrochemical sensors are especially suitable to meet these requirements because of their fast response, high sensitivity, simplicity of the instrumentation, as well as their relatively low cost and low power consumption. To respond to the market demands for disposable electrochemical sensors for the analysis of a variety of pollutants, it is necessary to solve technological issues to enable the fabrication of inexpensive, robust, reliable and efficient miniaturized sensors free from hazardous elements.¹

The increase in the environmental concentrations of heavy metals as a result of anthropogenic activities represents a serious health threat that requires a continuous monitoring of these pollutants. Regardless of the use of bench-top techniques such as ICP-MS or atomic absorption spectroscopy,² applied in standardized laboratories, sensitive electrochemical techniques have been shown to be suitable for the decentralized detection and remediation studies of these metals in water environments.^{3,4} Anodic stripping voltammetry (ASV) has been widely applied because it enables the pre-concentration/accumulation of the target analytes and their further stripping to get the corresponding analytical signal.⁵ In this context, for over two decades mercury has been the material of choice for the fabrication of electrochemical sensors for heavy metal detection. Because of its ability to amalgamate with many of these heavy metals, its low background current over a large potential window and a reproducible and renewable surface, products that make use of hanging mercury drop electrodes for the on-site analysis of these pollutants were developed.⁶ Paradoxically, mercury is one of the most hazardous heavy metals and thus the EU regulations will ban its use by 2020. In this context, the search for alternative materials applied to the fabrication of heavy metal electrochemical sensors has spurred considerable research during the last decade.^{7–9} Among them, bismuth,⁷ whose applications in the field was pioneered by Wang's group^{7,10} appears to be the ideal metal of choice to replace mercury because of its similar electrochemical behavior and additional biocompatibility. Bi-based electrodes based on

^aMaterials Science Institute of Barcelona (ICMAB-CSIC), Campus UAB, 08193 Bellaterra, Spain. E-mail: mgich@icmab.es; Fax: +34 935805729; Tel: +34 935801853

^bInstituto de Microelectrónica de Barcelona, IMB-CNM (CSIC), Campus UAB, 08193 Bellaterra, Spain. E-mail: cesar.fernandez@imb-cnm.csic.es; Fax: +34 935801496; Tel: +34 9355947700

^cFaculty of Chemistry and Chemical Engineering, "Babes-Bolyai" University, 11 Arany Janos, 400028 Cluj-Napoca, Romania

† Electronic supplementary information (ESI) available. See DOI: 10.1039/c3ta12190a

electrodeposited Bi films,^{11–14} Bi and Bi₂O₃ powder modified carbon pastes^{15,16} or carbon inks for screen-printed sensors,^{17,18} Bi nanomaterials^{19–21} and sputtered Bi thin-films²² have been shown to successfully perform in the detection of different heavy metals. However, these systems show fabrication and performance limitations to be commercially exploited as disposable electrochemical sensors. Among the former are the use of quite large volumes of Bi salt solutions to carry out the electrodeposition of Bi films or the mechanical incorporation of an amorphous or nanostructured Bi-based active powder into a carbon-based material, which make the sensor fabrication cumbersome and thus non-cost-effective. As a result, the reproducibility of the sensing response or the implementation of these devices into automatic analysis systems is often compromised.

The development and testing of new types of bismuth containing hybrid assemblies and the miniaturization of sensors in lab-on chip configurations are considered to be two of the areas with the highest potential for future research in the field of bismuth electrodes.⁷ It has been long recognized that carbon is a suitable material for ASV electrodes due to its low cost, wide potential window and relatively inert electrochemistry. In this context, inspired by our previous work on the synthesis of carbon aerogels and metal nanoparticle composites,²³ we have explored the potentiality of new Bi electrode composite materials prepared by sol-gel chemistry. Indeed, several characteristics of sol-gel technology can be advantageous for the fabrication of a new generation of bismuth electrodes: (i) Its chemical versatility allows modification of a particular synthesis to obtain materials with increased complexity or specificity such as organic-inorganic hybrids or composites of nanoparticles in a porous matrix; (ii) the intrinsic and tunable porosity of gels is important for controlling the porosity of the composite carbon xerogels, which is an important parameter for the heavy metal sensor application; (iii) the synthesis in solution ensures an excellent mixing of the reagents which results in a good homogeneity of the final material and opens the door to new processing routes for the fabrication of electrodes or electrode materials such as chemical solution deposition, soft lithography or electrospraying.

The synthesis of organic gels from the hydrolysis and condensation of resorcinol (R) and formaldehyde (F) by a mechanism analogous to the long-established sol-gel process of inorganic gel synthesis was first reported by Pekala.²⁴ This work opened a fruitful research field in the development and applications of the carbon xerogels and aerogels resulting from the drying and pyrolysis of resorcinol-formaldehyde (RF) gels.²⁵ These porous carbon materials were soon considered as attractive candidates for electrodes owing to their high surface area, low resistance and large voltage window without faradaic reactions, with applications in electrochemical double layer capacitors or electrosorptive devices.²⁶ The incorporation of metal or metal oxide nanoparticles into carbon xerogels and aerogels has been used to prepare supported catalysts²⁷ and electrodes²⁸ with increased functionalities/performance for electrochemical storage and conversion of energy: composite carbon aerogels with titania²⁹ (displaying photocatalytic

activity), with ruthenium oxide³⁰ (presenting an increased capacitance), with Pt³¹ (used as cathodes in proton exchange membrane fuel cells) or with cobalt oxide and vanadia³² (used as anodes in Li batteries).

So far, porous carbon nanocomposites have scarcely been exploited in the field of sensors,³³ in spite of their flexibility to be designed with the desired electrochemical properties and the benefits of sol-gel technology. Also, among the abundant literature on the synthesis of carbon aerogels and xerogels with nanoparticles of a diversity of metals,^{23,30,34,35} carbon xerogels nanocomposited with Bi have not been studied.

Here we report on the synthesis and characterization of carbon xerogels containing bismuth nanoparticles using commercial reactants such as resorcinol, formaldehyde, glycerol formal, water, acetic acid and bismuth nitrate. We describe two complementary preparation methods which differ in whether the Bi is incorporated into the system prior to or after the formation of the RF organic gel. The beyond the state of the art performance of these materials to construct sensor devices for the detection of heavy metals by ASV is demonstrated by the simultaneous detection of Pb and Cd at concentrations below 1 ppb in aqueous buffer solutions with an overall analysis time of below 5 min.

2 Experimental section

2.1 Reagents

The following chemicals were purchased from Sigma-Aldrich and used without any purification: resorcinol (*m*-C₆H₄(OH)₂, 99% pure), formaldehyde water solution (CH₂O, 37 wt%, methanol stabilized), glycerol formal (47% 5-hydroxy-1,3-dioxane, 33% 4-hydroxymethyl-1,3-dioxolane), bismuth nitrate pentahydrate (Bi(NO₃)₃·5H₂O, 98% pure), acetic acid (CH₃COOH, 99.7% pure), sodium carbonate (Na₂CO₃, 99.95% pure), ammonium hydroxide water solution (NH₄OH, 10 wt%), Pb, Cd, Cu, Hg, Ni standard solutions (1000 mg L⁻¹) and dimethylglyoxime (DMG). Deionised water was obtained from an in-house facility (conductivity 5 μS m⁻¹).

2.2 Nanocomposite synthesis

Our strategy to prepare composites of carbon xerogels with bismuth nanoparticles was to dry and pyrolyze previously synthesized RF gels containing homogeneously distributed Bi at a molecular scale.

These Bi-containing organic gels were obtained by following two approaches which differ in whether Bi is incorporated into the system prior to or after the formation of the RF gel. The first approach (impregnation route) consists of preparing a RF gel according to the convenient method of Pekala²⁴ that uses water as a solvent. Since common bismuth salts are not soluble in water, the incorporation of Bi can only be carried out after the gel formation by replacing the water contained in the gel pores with a liquid that dissolves bismuth nitrate. To this aim, the organic gels were washed in acetic acid and then soaked in a 0.2 M acetic acid solution of bismuth nitrate. The second approach (co-synthesis route) was

developed after successfully testing the materials prepared by impregnation in an attempt to simplify their preparation and increase the bismuth concentration in the gels. The Pekala method was modified to enable a one-step synthesis of Bi-containing RF gels by dissolving bismuth nitrate into the sol prior to gel formation. This was achieved by initially dissolving the bismuth nitrate in glycerol formal (GF), which is known to solubilize water insoluble compounds, and acetic acid and then incorporating R and F into the solution and finally adjusting the pH to 4 with NH_4OH .

In both preparation routes the organic wet gels containing bismuth were dried under ambient conditions in a fume hood for 24 h and pyrolysed in a tubular furnace under a N_2 flow ($120 \text{ cm}^3 \text{ min}^{-1}$). The pyrolysis treatment consisted of two isotherms of 30 min at $350 \text{ }^\circ\text{C}$ and 2 h at $900 \text{ }^\circ\text{C}$ with heating ramps of $100 \text{ }^\circ\text{C h}^{-1}$ up to $600 \text{ }^\circ\text{C}$ and $200 \text{ }^\circ\text{C h}^{-1}$ from $600 \text{ }^\circ\text{C}$ to $900 \text{ }^\circ\text{C}$, while the cooling ramp was set at $350 \text{ }^\circ\text{C h}^{-1}$. The details of the two methods adopted for the synthesis of bismuth-containing organic gels are indicated below.

A Impregnation route. Gels with a molar composition $\text{R} : \text{F} : \text{H}_2\text{O} : \text{Na}_2\text{CO}_3 = 1 : 2 : 18.9 : 0.01$ were synthesized by dissolving R and then Na_2CO_3 in deionised water and finally adding the F solution to the mixture. The above composition was selected in order to obtain gels in which $\sim 33\%$ of the mass corresponds to the cross-linked organic network. In a typical batch, $\sim 30 \text{ mL}$ of sol containing all the reagents were sealed in a glass container and placed in a stove at $60 \text{ }^\circ\text{C}$. Gelation occurred in about 1 h and the sealed containers were kept in the stove for 24 h. The wet gels removed from the containers and fragmented into irregular pieces of about 2 cm were soaked in acetic acid for at least one hour. The same washing process was repeated by soaking the pieces in a second acetic acid bath. The gels were subsequently transferred to a 4 M solution of $\text{Bi}(\text{NO}_3)_3 \cdot 5\text{H}_2\text{O}$ in acetic acid in which they were kept for 1 h before undergoing the drying and pyrolysis processes described above. The obtained composite xerogel materials were labeled $(\text{C-Bi})_{\text{IM}}$ and used for further analysis. A non-impregnated pyrolysed carbon xerogel (labeled (C-Blank)) was prepared for comparison purposes during the materials characterization. The Bi concentration of $(\text{C-Bi})_{\text{IM}}$ measured by EDX spectroscopy was $7.0 \pm 0.3 \text{ wt}\%$.

B Co-synthesis route. Gels with a molar composition $\text{R} : \text{F} : \text{CH}_3\text{COOH} : \text{NH}_4\text{OH} : \text{GF} = 1 : 2 : 3.84 : 0.57 : 6.35$ and Bi molar ratios of 0.0165 and 0.136 were prepared by first dissolving $\text{Bi}(\text{NO}_3)_3 \cdot 5\text{H}_2\text{O}$ in 5 mL GF with CH_3COOH and adding R and then F to the solution. The pH of this mixture was raised from ~ 2 to ~ 4 with a 10% aqueous solution of NH_4OH . The clear yellow sols were sealed in glass containers and placed in a stove at $60 \text{ }^\circ\text{C}$. Gelation occurred in about 15 h and the sealed containers were kept in the stove for 24 h. The wet gels removed from the containers were dried and pyrolysed as described above. The resulting composite xerogel materials exhibited low ($4.08 \pm 0.03 \text{ wt}\%$) and high ($16.4 \pm 0.5 \text{ wt}\%$) Bi concentrations as obtained by EDX spectroscopy and were labeled $(\text{C-Bi})_{\text{CS}_L}$, $(\text{C-Bi})_{\text{CS}_H}$, and used for further analysis. A xerogel containing no Bi was prepared according to the co-synthesis method and labeled $(\text{C-Blank})_{\text{CS}}$.

2.3 Microstructural characterization

Morphological and structural characterizations were performed using scanning electron microscopy (SEM), X-ray diffraction (XRD), X-ray photoelectron spectroscopy (XPS) and nitrogen adsorption porosimetry. SEM images were obtained with a Quanta FEI 200F microscope operating at 20 kV. Energy Dispersive X-ray (EDX) spectroscopy was used with the SEM to determine the elemental composition of the materials. For this study thick layers of the milled samples were supported on aluminium SEM holders by means of silver paint and 4 different zones of 500 by $500 \mu\text{m}$ were analyzed for each material. For the evaluation of the mean Bi particle size in the composites, particle size histograms were made out of over 150 particle counts from SEM images by using the imageJ software. Powder XRD patterns of the composites were measured with a Siemens diffractometer, with Bragg–Brentano geometry using a Cu anode with $\text{Cu}_{K\alpha 1} = 1.5406 \text{ \AA}$ and $\text{Cu}_{K\alpha 2} = 1.5444 \text{ \AA}$ in the 2θ range of 10 – 70° . The patterns were analyzed by Rietveld refinement with the Maud program.³⁶ Considering the structure of rhombohedral bismuth (space group $R\bar{3}m$, $a = b = 4.54 \text{ \AA}$, $c = 11.85 \text{ \AA}$ and an asymmetric unit with one Bi atom at fractional unit cell coordinates $x = 0$, $y = 0$, $z = 0.2333$) and defining the background by interpolation of about 20 data points selected from the patterns, an experimental resolution function was obtained from the refinement of a quartz reference in order to take into account the instrumental broadening and accurately determine the contributions of the studied materials microstructure to the diffraction peak broadenings (crystalline size and microstrain). XPS analyses were performed in an ultrahigh vacuum Kratos Analytical spectrometer using Al K_{α} X-rays of 1.48669 keV . The IMFPWIN software³⁷ of the National Institute of Standards and Technology was used to calculate the mean free path, λ_e , of 160 eV electrons in Bi_2O_3 from which a thickness of $3\lambda_e$ was taken of an estimate of a lower bound for the oxide thickness layer.³⁸ Z-contrast imaging of Bi nanoparticles in transmission electron microscopy was performed using a Tecnai F20 HRTEM/STEM. For these observations a thin lamella of the composite was embedded in a polymer and cut to an electron transparent thickness using microtomic techniques.

Nitrogen adsorption–desorption isotherms were recorded with Malvern Micromeritics equipment after degassing around 100 mg of the tested materials for 48 h at $150 \text{ }^\circ\text{C}$ in a vacuum ($<1 \text{ mPa}$). From nitrogen adsorption analysis we carried out determinations of specific surface areas using the BET (Brunauer–Emmet–Teller) method and pore size distributions, pore volume and mean pore diameters by the BJH (Barret–Joyner–Halenda) method.

2.4 Electrochemical characterization

Voltammetric measurements were performed using an Autolab PGSTAT30 potentiostat (EcoChemie, the Netherlands) controlled by Autolab GPES software version 4.3. All measurements were carried out at room temperature in a 10 mL plastic cell with a conventional three-electrode configuration. A 3 mm diameter working carbon paste electrode, homemade as described below, was used together with a platinum counter

electrode and a Ag/AgCl reference electrode (both from Metrohm AG). The preparation of working carbon paste electrodes to test the nanostructured carbon xerogels was carried out by firstly ball-milling the pyrolyzed materials using a Retsch Mixer Mill to obtain a powder with an average diameter of $\sim 5 \mu\text{m}$ (measured by optical microscopy image analysis with Morphologi G3 equipment by Malvern Instruments; see S1, ESI†). 1 g of this powder was thoroughly mixed with 0.4 mL of a spectroscopic grade paraffin liquid (Uvasol® from Merck), with the aid of a mortar, to produce a carbon paste. This was then packed into a 3 mm diameter well, defined at one end of a Teflon body, which also included a stainless steel rod to get the required electrical contact of the carbon paste material. The resulting carbon paste electrode (CPE) surface was eventually polished on a white paper sheet. The CPE surface was renewed after each measurement by polishing or packing a fresh carbon paste on the electrode body.

Square wave anodic and cathodic stripping voltammetric measurements (SWASV and SWCSV, respectively) were carried out for the detection of different heavy metals. The potential square wave showed a 25 mV amplitude and was applied with a 20 Hz frequency and a 5 mV step potential in the adequate potential window. A brief description of the working principle of SWASV and SWCSV is included in S7, ESI†.

3 Results and discussion

3.1 Structural and morphological characterization

XRD patterns of $(\text{C-Bi})_{\text{CS}_L}$ and $(\text{C-Bi})_{\text{IM}}$ nanocomposites and the calculated profiles obtained by Rietveld refinement are presented in Fig. 1. The patterns show the presence of an important background with broad bumps at $2\theta \sim 25^\circ$ and 45° typical of the scattering of amorphous carbon and diffraction peaks that were indexed with the structure of rhombohedral bismuth (ICSD PDF 044-1246). The relative intensities of the bump maximum at $2\theta \sim 25^\circ$ due to amorphous carbon with respect to the most intense (012) reflection of Bi at $2\theta = 27.16^\circ$

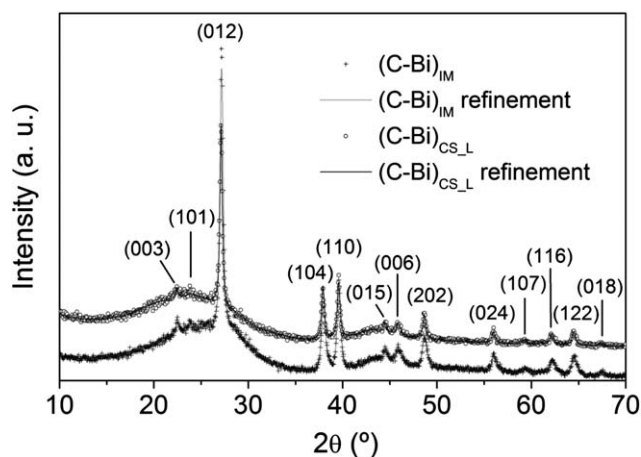


Fig. 1 X-ray diffraction patterns of carbon xerogel–bismuth nanoparticle composites prepared by impregnation, $(\text{C-Bi})_{\text{IM}}$, and co-synthesis, $(\text{C-Bi})_{\text{CS}_L}$. The solid lines correspond to the profiles obtained by Rietveld refinement.

and the visibility of small intensity reflections like the (003), (101), (107) and (018) indicate that the relative amount of Bi is slightly larger in $(\text{C-Bi})_{\text{IM}}$ than in $(\text{C-Bi})_{\text{CS}_L}$. This observation is in agreement with the larger Bi concentration found for $(\text{C-Bi})_{\text{IM}}$ ($7.0 \pm 0.3 \text{ wt\%}$) compared to $(\text{C-Bi})_{\text{CS}_L}$ ($4.08 \pm 0.03 \text{ wt\%}$) using EDX spectroscopy. The patterns could be satisfactorily refined ($R_{\text{wp}}/R_{\text{exp}} < 1.2$ for both materials) by considering exclusively the contribution of rhombohedral bismuth (Fig. 1) and the average crystallite size was found to be around 40 nm for both materials.

The surface of the Bi nanoparticles was studied by XPS (see S2, ESI†) which revealed the presence of Bi only in the form of Bi_2O_3 , with the Bi $4f_{7/2}$ and $4f_{5/2}$ photoelectron peaks found at 159 and 164 eV instead of the 157 and 162 eV peaks of crystalline Bi.³⁹ This indicates that the nanoparticle surfaces are covered by an oxide layer, which we can estimate to be at least 2 nm thick (see Section 2.3 for details). The absence of Bi_2O_3 reflections in the XRD patterns suggests that the Bi_2O_3 shell is amorphous, probably originating from the spontaneous surface passivation on contact with air. The core–shell nature of the nanoparticles was revealed by Z-contrast imaging in a transmission electron microscope using a high angle annular dark field detector. In this imaging mode differences in density are visualized as differences in brightness and from the image in Fig. S2b (ESI†) it is clearly observed that a less dense shell surrounds the nanoparticle core.

The SEM characterization revealed the presence of spherical Bi nanoparticles well dispersed in a porous carbon xerogel matrix in both composites (Fig. 2). The Bi particle size distributions were obtained from a detailed study of different SEM images (S3 and S4, ESI†). In the case of the materials prepared by co-synthesis, the distribution is clearly bimodal and can be fit by two Gaussians. For $(\text{C-Bi})_{\text{CS}_L}$ a relatively sharp Gaussian is centered at 29 nm with a full width at half maximum (FWHM) of 10 nm, which accounts for about two thirds of the measured particles, and a broader Gaussian (FWHM of 24 nm) is centered around 90 nm. The analysis of the SEM images shows that a higher Bi content results in larger particles: for $(\text{C-Bi})_{\text{CS}_H}$ both Gaussians are broader (FWHM above 30) and centered at about 85 and 155 nm. The nanocomposite prepared by impregnation (S4, ESI†) presents a majority of particles with diameters comprised between 15 and 50 nm and a broad distribution of particle sizes with larger diameters up to 250 nm. We ascribe

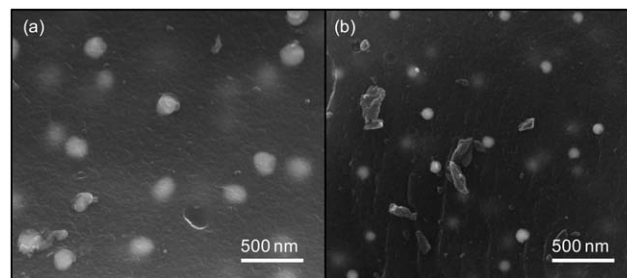


Fig. 2 Secondary electron SEM images of carbon xerogel–bismuth nanoparticle composites prepared by impregnation, $(\text{C-Bi})_{\text{IM}}$ in (a), and co-synthesis, $(\text{C-Bi})_{\text{CS}_L}$ in (b).

the increased polydispersity of (C-Bi)_{IM} to the preparation method that results in gradients of the Bi salt concentration from the surface to the core of the impregnated pieces of organic gel, which are dependent on parameters like the impregnation time or the size of the organic gel pieces.

The porosity of the composites was studied by nitrogen adsorption and desorption isotherms (S5a, ESI†). An evaluation of the specific surface area using the BET model gave values of the order of 200 m² g⁻¹ for (C-Bi)_{IM} and 400 m² g⁻¹ for (C-Bi)_{CS,L}. For both composites the measurements display a sharp increase in the adsorbed volume at low relative pressures indicating that the porosity is mainly due to micropores. However, the non-negligible slope of the curve at intermediate relative pressures and the increase in adsorbed volume at nitrogen relative pressures above 0.95 respectively indicate the existence of some mesopores and macropores. An analysis of the pore size distribution with the BJH model shows that most of the pores measured within the ranges measured by this technique have a mean diameter below 20 nm (S5b, ESI†). The adsorption measurements also revealed the absence of significant differences between the non-impregnated (C-Blank) and impregnated (C-Bi)_{IM} pyrolysed xerogels (S5b, ESI†), indicating that the Bi metal precursors did not affect the porosity of the carbon xerogel.

3.2 Electrochemical characterization and detection of heavy metals

The electrochemical performance of the synthesized materials was firstly assessed in a solution containing ferricyanide model electroactive molecules (S6, ESI†). A reversible cyclic voltammetric signal was recorded with both (C-Bi)_{IM} and (C-Bi)_{CS,L} showing the expected diffusion-controlled reduction/oxidation process of the Fe³⁺/Fe²⁺ redox pair. The peak potential separation was around 200 mV for both materials but the peak currents were sensibly smaller when working with the (C-Bi)_{IM} material. This behavior is indicative of a smaller electrochemical active area for the (C-Bi)_{IM} based electrode, which is in agreement with the smaller specific surface area measured by BET as discussed above (Section 3.1).

Fig. 3 shows the SWASV signals recorded in a 0.1 M acetate buffer solution pH 4.5 used as the background electrolyte for the detection of Zn, Cd and Pb, containing 0 and 50 ppb of these heavy metals and using carbon paste electrodes fabricated with (C-Bi)_{IM} and (C-Bi)_{CS,L} materials. An initial accumulation potential step was carried out by applying a constant DC potential of -1.4 V for 2 min, followed by an equilibration step for 10 s and the eventual potential scan from -1.4 V to +0.5 V. Voltammograms recorded in the background electrolyte show two peaks at around -0.10 V and +0.00 V. Both of them can be ascribed to the oxidation of the Bi nanoparticles exposed on the surface of the carbon paste electrode to generate different cationic Bi species. As described above, the Bi nanoparticles include a Bi₂O₃ shell which, upon the application of the cathodic potential during the accumulation step, underwent a reduction process to generate metallic Bi.¹⁶ Indeed, this effect was clearly visible by varying the accumulation time from 0 to

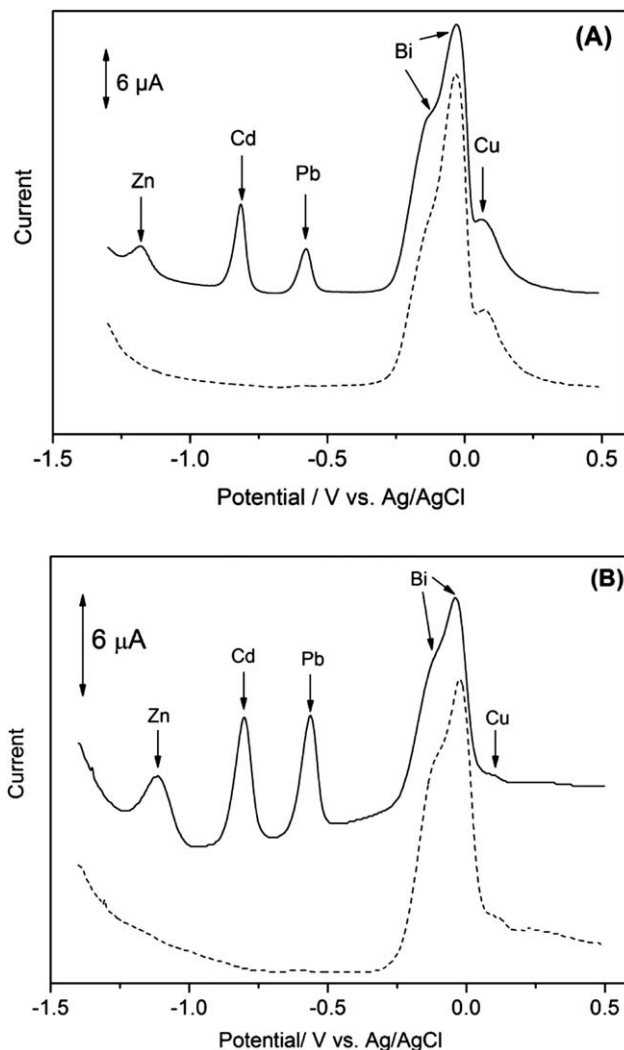


Fig. 3 SWASV signals recorded with carbon paste electrodes in 0.1 M acetate buffer solution of pH 4.5 containing 0 (dashed lines) and 50 ppb (solid lines) of Zn, Cd and Pb. (A) (C-Bi)_{IM} and (B) (C-Bi)_{CS,L}. Other conditions are detailed in the text.

180 s (Fig. S8, ESI†). Bi oxidation peaks increased up to a 120 s accumulation time, at which the Bi₂O₃ layer may be completely reduced. Then, accumulation times longer than 120 s were chosen for all the following electrochemical studies. It was previously reported that the oxidation process of electro-deposited metallic Bi films in acetate buffer of pH 4–5 shows a single peak, which was ascribed to the oxidation of Bi⁰ to Bi³⁺ and consequent stripping to the bulk solution.⁴⁰ Surprisingly, previous reports on the development of electrochemical sensors based on Bi nanomaterials for heavy metal detection did not show the Bi oxidation signals that we have observed during the stripping potential scan.^{19–21} No studies about the electrochemical oxidation of Bi nanoparticles in slightly acidic media like the one used in this work were found. However, related studies on the oxidation of Bi in alkaline solutions presented two anodic peaks ascribed to Bi³⁺ oxide and hydroxide species.^{41,42} Also, the electrochemical oxidation in strong acidic solution displays the formation of different Bi³⁺ species also

giving rise to two anodic peaks.⁴³ These studies may also explain the two peaks observed in our work. Voltammograms in Fig. 3 also present three additional peaks at -1.11 , -0.80 and -0.56 V, unambiguously related to the anodic stripping of Zn, Cd and Pb from the CPE, respectively. A peak at $+0.12$ V is also visible, this being related to the oxidation of metallic Cu that may be included in the electrode material and come from impurities of the $\text{Bi}(\text{NO}_3)_3$ salt used for the material synthesis. The peaks for each of the tested heavy metals recorded using $(\text{C-Bi})_{\text{CS}_L}$ show slightly higher intensities than the ones recorded using $(\text{Bi-C})_{\text{IM}}$. This appears to be related to differences in the active Bi area on the surface of the corresponding CPEs. In spite of the higher Bi content of $(\text{C-Bi})_{\text{IM}}$, its larger mean particle size and smaller C surface area result in a decreased sensitivity towards the detection of heavy metals. In addition, the amount of Bi required to carry out the impregnation process and the broader particle size distribution likely related to the existence of Bi salt concentration gradients, as explained above, have made the $(\text{C-Bi})_{\text{CS}}$ materials the ones chosen for all further experiments. Nevertheless, the impregnation approach could be useful when fabricating thin-films of these materials (Bi salt concentration gradients would be minimized) or for the fabrication of nanocomposites of porous carbon with other metal nanoparticles, because no modification of the sol-gel process for the preparation of the C matrix would be required.

As pointed out above, it would be expected that the peak current intensities of the different heavy metals were directly proportional to the amount of Bi in the form of nanoparticles present in the electrode material. Fig. 4(A) shows the voltammograms recorded under the same experimental conditions using $(\text{C-Bi})_{\text{CS}_L}$ and $(\text{C-Bi})_{\text{CS}_H}$ materials containing about 4 and 16 wt% Bi, respectively. The 4-fold increase in the Bi content results in an increased charge transfer related to the oxidation of the Bi nanoparticles (area under the Bi peaks) also by about 4-fold. The same effect was observed with the peaks of different heavy metals, but in this case the charge transfer increased by around 2-fold. These values indicate that the Bi active surface area directly depends on the amount of Bi in the C xerogel materials although this dependence is not strictly proportional. The reason for that is related to the fact that increasing the Bi concentration did not only result in an increase in the number of Bi nanoparticles by preserving its particle size distribution but also yielded larger particle sizes. From the analysis of SEM images of the materials $(\text{C-Bi})_{\text{CS}_L}$ and $(\text{C-Bi})_{\text{CS}_H}$ (S3, ESI†) the 4-fold increase of Bi content is roughly accompanied by a 2-fold increase of the mean nanoparticle diameter. Under such conditions it can be easily estimated that $(\text{C-Bi})_{\text{CS}_H}$ must have only half of the nanoparticles of $(\text{C-Bi})_{\text{CS}_L}$ but with a total surface area that is twice as large. Fig. 4(A) also shows the voltammogram recorded using a material synthesized without Bi. Very small peaks for just Cd and Pb are visible, thus demonstrating that the signals recorded with the Bi-containing materials are directly related to the presence of Bi nanoparticles on the surface of the CPE.

The enhancement of the electrode response for $(\text{C-Bi})_{\text{CS}_H}$ also had a direct influence on the limits of detection that could be achieved using the presented approach. Fig. 4(B)

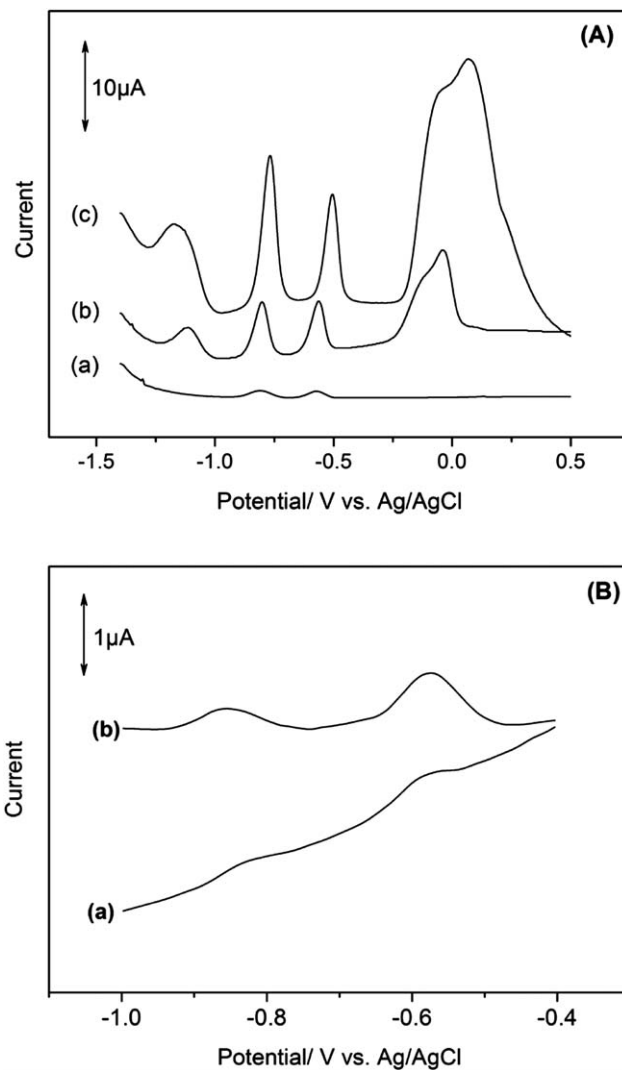


Fig. 4 (A) SWASV signals recorded in 0.1 M acetate buffer of pH 4.5 containing 50 ppb Zn, Cd and Pb, using CPEs prepared from $(\text{C-Blank})_{\text{CS}}$ without Bi (a), $(\text{C-Bi})_{\text{CS}_L}$ containing 4 wt% Bi (b) and $(\text{C-Bi})_{\text{CS}_H}$ containing 16 wt% Bi (c). Accumulation step: -1.4 V for 2 min. (B) SWASV signals recorded in 0.1 M acetate buffer of pH 4.5 containing 1 ppb Cd and Pb, using CPEs prepared with (b) and (c) as in (A). Accumulation step: -1.4 V for 3 min. Other conditions are detailed in the text.

shows the SWASV voltammograms recorded with $(\text{C-Bi})_{\text{CS}_L}$ and $(\text{C-Bi})_{\text{CS}_H}$ in a solution containing 1 ppb of Cd and Pb and evidences that for such low concentrations of pollutants the detection is more convenient with the material containing a higher amount of Bi. Indeed, the minimum concentration that was readily measured with CPEs based on $(\text{C-Bi})_{\text{CS}_H}$ was 0.6 ppb for both Cd and Pb using a 3 min accumulation time (Fig. 5). These values are considerably lower than most of those recorded with other reported Bi-based sensor approaches as summarized in Table 1. It is worth mentioning that the system displaying a performance comparable to that of the present work is made of a CNT based composite and relies on the electrodeposition of a Bi-film.¹⁴ The use of electrodeposited Bi films generated right before the heavy metal analysis has been commonly applied in the development of sensors previously reported.^{6–8} While these kinds of sensors showed the potential

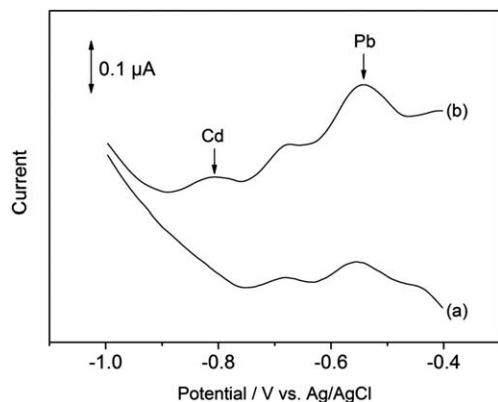


Fig. 5 SWASV signals recorded in a 0.1 M acetate buffer pH 4.5 background electrolyte (a) and in the same solution containing 0.6 ppb Cd and Pb (b). CPEs were prepared from the (C-Bi)_{CS,H} composite containing 16 wt% Bi. Accumulation step: -1.4 V for 3 min.

for the sensitive detection of heavy metals, they would be more difficult to implement and not so cost-effective to be applied as single-use devices in real applications.

The (C-Bi)_{CS,H} based electrode responded linearly to increasing concentrations of Pb and Cd in a range between 1 and 100 ppb, showing sensitivity values of 0.151 ± 0.003 and $0.200 \pm 0.004 \mu\text{A ppb}^{-1}$ (Pearson's $r = 0.999$), respectively (see calibration graphs S9, ESI†).

The good sensitivity of the (C-Bi)_{CS}-based electrodes can be understood from the microstructure of the material, consisting of Bi nanoparticles distributed in a carbon matrix with an open porosity. The large surface to volume ratio of the nanoparticles combined with the high porosity of the matrix result in a large area of Bi surfaces available for the interaction with the heavy metal analytes which is enhanced with respect to other common Bi electrode geometries. For instance, it can be easily estimated that a certain amount of metallic Bi in the form of a film with a thickness of 50 nm presents a surface area which is about one order of magnitude lower than if it is in the form of nanoparticles 50 nm in diameter.

The (C-Bi)_{CS} materials could also be applied for the detection of other heavy metals such as Ni. A SWASV study following previously reported approaches was carried out.⁴⁴ Ni²⁺ ions in an ammonia solution can be complexed using the DMG chelating agent, commonly applied in the gravimetric analysis of this heavy metal. The resulting complex is insoluble and is readily adsorbed on the surface of the CPE by applying a DC accumulation potential of -0.7 V. The adsorbed Ni²⁺ could then be detected by applying a cathodic potential scan between -1.00 and -1.25 V, where it underwent a reduction process to metallic Ni and gave rise to a voltammetric signal like the ones shown in Fig. 6.

Also, the C xerogel material synthesized with no Bi could be used for the detection of Cu and Hg. These two heavy metals show SWASV signals at potentials more positive than the one related to the Bi oxidation and do not require the presence of the nanoparticles to deposit on and further strip from the C electrode surface. Fig. 7 shows the SWASV signals at -0.15 and

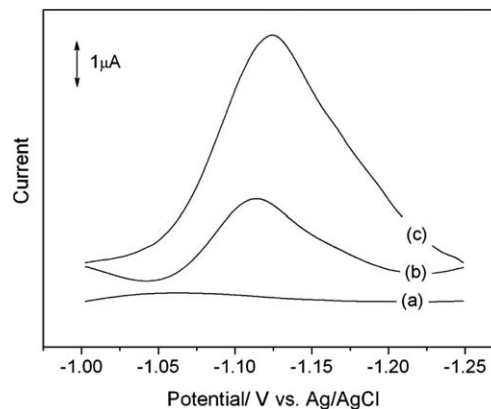


Fig. 6 (A) SWASV signals recorded in 0.1 M ammonia buffer of pH 9.2 containing 1 mM DMG and (a) 0, (b) 50, and (c) 100 ppb Ni, using the CPE prepared with 4 wt% (C-Bi)_{CS,L}. Activation step at -1.4 V for 3 min; accumulation step at -0.7 V for 3 min.

Table 1 Analytical performance of different Bi-based electrodes for the detection of Cd and Pb, reported in the recent literature^a

Bi structure	Electrode type	Minimum concentration measured/ppb		Accumulation time ^b /s	Ref.
		Pb	Cd		
Electrodeposited Bi films	Porous Bi film	20	20	90	13
	Bi film on CNT-PSS composite	0.5	0.5	120	14
Bi powder	Bi modified CPE	5	5	300	15
Bi ₂ O ₃ powder	Bi ₂ O ₃ modified CPE	5	5	240	16
	Bi ₂ O ₃ modified carbon inks for SPCE	5	5	120	17
Bi nanomaterials	Bi NP modified SPCE	10	10	120 ^c	19
	Bi NP graphene modified composite CPE	20	20	400 ^d	20
	Bi NP on SPCE	8	8	120	21
Sputtered Bi film	Bi microelectrode array	10	10	120	22
(C-Bi) nanocomposite	CPE	0.5	0.5	180	This work

^a CNT-PSS: carbon nanotube-poly(sodium 4-styrenesulfonate); CPE: carbon paste electrode; NP: nanoparticles; SPCE: screen-printed carbon electrode. ^b Measured in 0.1 M acetate buffer pH 4.5, if not stated otherwise. ^c 0.1 M NaAc + 0.025 M HCl pH 4.7. ^d 0.1 M acetate buffer pH 5.5.

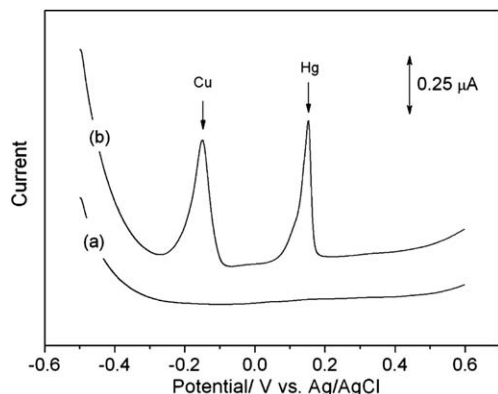


Fig. 7 SWASV signals recorded in 0.1 M sulfuric acid solution containing (a) 0 and (b) 50 ppb Cu and Hg, using the CPE prepared from the 0 wt% Bi (C-Blank)_{CS} material. Other conditions are detailed in the text.

+0.15 V, recorded in a 0.1 M H₂SO₄ solution containing 50 ppb of Cu and Hg. Both signals can be ascribed to the anodic stripping of both heavy metals, respectively, which were previously adsorbed on the electrode surface by applying a -0.5 V deposition potential for 2 min. The pH of the background electrolyte was important to record those signals. Voltammetric measurements carried out in 0.1 M acetate buffer of pH 4.5 (Fig. S10, ESI[†]), like those carried out with Zn, Cd and Pb, as well as in other diluted H₂SO₄ solutions showing pH values higher than 1, showed very small peaks for Hg, but this effect was not studied any further.

Finally, it is worth noting that the materials are very stable and can be kept under ambient conditions without any special care as no degradation of the composites was observed for more than a one year period following their synthesis.

4 Conclusions

We have presented two routes based on sol-gel chemistry to synthesize composites of porous carbon containing bismuth nanoparticles, demonstrating the potential of these materials for the fabrication of electrochemical sensors. These devices displayed performance beyond the state-of-the art in the sensitive stripping voltammetric detection of heavy metals in water targeted by the recent EU regulations. Specifically, for cadmium and lead, included in the list of priority substances, we achieved the detection of 0.6 ppb, which is of the order of the maximum allowance concentration following the environmental quality standards (MAC-EQS)⁴⁵ (*i.e.* between 0.45 ppb and 1.5 ppb Cd depending on water hardness class) and well below the threshold concentrations established for drinking water quality⁴⁶ (5 ppb of Cd and 10 ppb of Pb). The benefits of using this material with respect to other bismuth-based electrodes were reported. The excellent behaviour of the nanocomposites is reflected by the low heavy metal concentrations (0.6 ppb) measured for a short accumulation time (180 s) in an overall assay time of less than 300 s. Our approach can be compatible with different electrode fabrication technologies. The material can be powdered to prepare inks and fabricate

screen printed electrodes but can also be compatible with patterning deposition techniques based on lithographic approaches. We can anticipate that the latter approach and the versatility of sol-gel chemistry can open up new routes for the cost-effective fabrication of miniaturised heavy metal electrochemical sensors thus enabling the deployment of these kinds of devices for the simple and environmentally friendly detection of these pollutants.

Acknowledgements

Míriam Alejandra Garza and Ayman Zaheer are acknowledged for contributing to this work during their internship at ICMAB. G. Anantorrea is acknowledged for performing XPS measurements and J. Gàzquez for Z-contrast TEM images. This research was partially funded by the Spanish Government (MAT2012-35324, CONSOLIDER-Nanoselect-CSD2007-00041, TEC2010-17274 and RyC contract of M.G.), the Generalitat de Catalunya (2009SGR203), the Nanoaracat program of the Gobierno de Aragón and Generalitat de Catalunya and the European Commission (FP7-Marie Curie Actions, PCIG09-GA-2011-294168 grant of M.G. and the Sectoral Operational Programme “Human Resources Development 2007–2013” of the European Social Fund POSDRU 89/1.5/S/60189 grant of L.C.C.).

References

- 1 S. Su, W. Wu, J. Gao, J. Lu and C. Fan, *J. Mater. Chem.*, 2012, **22**, 18101–18110.
- 2 Strategic Document, 2001.
- 3 M. Taillefert, G. W. Luther and D. B. Nuzzio, *Electroanalysis*, 2000, **12**, 401–412.
- 4 F. Fu and Q. Wang, *J. Environ. Manage.*, 2011, **92**, 407–418.
- 5 K. Brainina and E. Neyman, *Electroanalytical stripping methods*, Wiley, 1994.
- 6 AML Heavy Metals Analyser, http://www.elta.fr/uk_doc/AML_ENG.pdf.
- 7 I. Švancara, C. Prior, S. B. Hočevár and J. Wang, *Electroanalysis*, 2010, **22**, 1405–1420.
- 8 A. K. Wanekaya, *Analyst*, 2011, **136**, 4383–4391.
- 9 G. Aragay, J. Pons and A. Merkoçi, *Chem. Rev.*, 2011, **111**, 3433–3458.
- 10 J. Wang, J. M. Lu, S. B. Hočevár, P. A. M. Farias and B. Ogorevc, *Anal. Chem.*, 2000, **72**, 3218–3222.
- 11 A. Economou, *TrAC, Trends Anal. Chem.*, 2005, **24**, 334–340.
- 12 K. E. Toghill, G. G. Wildgoose, A. Moshar, C. Mulcahy and R. G. Compton, *Electroanalysis*, 2008, **20**, 1731–1737.
- 13 V. Urbanová, M. Bartoš, K. Vytrás and A. Kuhn, *Electroanalysis*, 2010, **22**, 1524–1530.
- 14 X. Jia, J. Li and E. Wang, *Electroanalysis*, 2010, **22**, 1682–1687.
- 15 S. B. Hočevár, I. Švancara, K. Vytrás and B. Ogorevc, *Electrochim. Acta*, 2005, **51**, 706–710.
- 16 R. Pauliukaite, R. Metelka, I. Švancara, A. Krolicka, A. Bobrowski, K. Vytrás, E. Norkus and K. Kalcher, *Anal. Bioanal. Chem.*, 2002, **374**, 1155–1158.
- 17 R. O. Kadara, N. Jenkinson and C. E. Banks, *Electroanalysis*, 2009, **21**, 2410–2414.

- 18 R. O. Kadara and I. E. Tothill, *Anal. Chim. Acta*, 2008, **623**, 76–81.
- 19 N. A. Malakhova, A. A. Mysik, S. Y. Saraeva, N. Y. Stozhko, M. A. Uimin, A. E. Ermakov and K. Z. Brainina, *J. Anal. Chem.*, 2010, **65**, 640–647.
- 20 P. K. Sahoo, B. Panigrahy, S. Sahoo, A. K. Satpati, D. Li and D. Bahadur, *Biosens. Bioelectron.*, 2013, **43**, 293–296.
- 21 M. Á. Granado Rico, M. Olivares-Marín and E. P. Gil, *Talanta*, 2009, **80**, 631–635.
- 22 C. Kokkinos, A. Economou, I. Raptis and T. Speliotis, *Electrochem. Commun.*, 2011, **13**, 391–395.
- 23 L. C. Cotet, M. Gich, A. Roig, I. C. Popescu, V. Cosoveanu, E. Molins and V. Danciu, *J. Non-Cryst. Solids*, 2006, **352**, 2772–2777.
- 24 R. W. Pekala, *J. Mater. Sci.*, 1989, **24**, 3221–3227.
- 25 S. A. Al-Muhtaseb and J. A. Ritter, *Adv. Mater.*, 2003, **15**, 101–114.
- 26 R. W. Pekala, J. C. Farmer, C. T. Alviso, T. D. Tran, S. T. Mayer, J. M. Miller and B. Dunn, *J. Non-Cryst. Solids*, 1998, **225**, 74–80.
- 27 C. Moreno-Castilla and F. J. Maldonado-Hodar, *Carbon*, 2005, **43**, 455–465.
- 28 C. I. Fort, L. C. Cotet, V. Danciu, G. L. Turdean and I. C. Popescu, *Mater. Chem. Phys.*, 2013, **138**, 893–898.
- 29 C. Moreno-Castilla, F. J. Maldonado-Hódar, F. Carrasco-Marín and E. Rodríguez-Castellón, *Langmuir*, 2002, **18**, 2295–2299.
- 30 J. M. Miller and B. Dunn, *Langmuir*, 1999, **15**, 799–806.
- 31 A. Smirnova, X. Dong, H. Hara, A. Vasiliev and N. Sammes, *Int. J. Hydrogen Energy*, 2005, **30**, 149–158.
- 32 M. Dai, L. Song, J. T. LaBelle and B. D. Vogt, *Chem. Mater.*, 2011, **23**, 2869–2878.
- 33 X. L. Tang, L. S. Wang, S. T. Zhang, S. F. Zhang, X. R. Deng and X. X. Liu, *Chin. J. Anal. Chem.*, 2007, **35**, 216–220.
- 34 F. J. Maldonado-Hodar, M. A. Ferro-Garcia, J. Rivera-Utrilla and C. Moreno-Castilla, *Carbon*, 1999, **37**, 1199–1205.
- 35 F. J. Maldonado-Hódar, C. Moreno-Castilla, J. Rivera-Utrilla, Y. Hanzawa and Y. Yamada, *Langmuir*, 2000, **16**, 4367–4373.
- 36 H. R. Wenk, S. Matthies and L. Lutterotti, in *Proceedings of the 10th International Conference on Textures of Materials, Pts 1 and 2-Icotom-10*, ed. H. J. Bunge, 1994, vol. 157, pp. 473–479.
- 37 ed. C. J. Powell and A. Jablonski, N. I. o. S. a. Technology, Gaithersburg, 1.2 edn, 2010.
- 38 C. Klauber and R. St. C. Smart, in *Surface Analysis Methods in Materials Science*, ed. B. A. Sexton, D. J. O'Connor and R. St. C. Smart, Springer, Berlin, 2nd edn, 2003, ch. 1, pp. 25–26.
- 39 V. S. Dharmadhikari, S. R. Sainkar, S. Badrinarayan and A. Goswami, *J. Electron Spectrosc. Relat. Phenom.*, 1982, **25**, 181–189.
- 40 J. Wang, Ü. Anik Kirgöz and J. Lu, *Electrochem. Commun.*, 2001, **3**, 703–706.
- 41 A. M. Espinosa, M. T. San José, M. L. Tascón, M. D. Vázquez and P. Sánchez Batanero, *Electrochim. Acta*, 1991, **36**, 1561–1571.
- 42 G. H. Hwang, W. K. Han, S. J. Kim, S. J. Hong, J. S. Park, H. J. Park and S. G. Kang, *Journal of Ceramic Processing Research*, 2009, **10**, 190–194.
- 43 W. S. Li, X. M. Long, J. H. Yan, J. M. Nan, H. Y. Chen and Y. M. Wu, *J. Power Sources*, 2006, **158**, 1096–1101.
- 44 C. Kokkinos, A. Economou, I. Raptis and T. Speliotis, *Anal. Chim. Acta*, 2008, **622**, 111–118.
- 45 *Council Directive 92008/105/EC of 16 December 2008 on environmental quality standards in the field of water policy*, ed. E. Union, 1998, vol. OJ L 348/84 24.12.2008, ch. Annex 1.
- 46 *Council Directive 98/83/EC of 3 November 1998 on the quality of water intended for human consumption*, ed. E. Union, 1998, vol. OJ L 330/42 5.12.98, ch. Annex 1 Part B.



Electroanalytical Assessment of Heavy Metals in Waters with Bismuth Nanoparticle-Porous Carbon Paste Electrodes



Pengfei Niu^a, César Fernández-Sánchez^{b,*}, Martí Gich^{a,**}, Carlos Ayora^c, Anna Roig^a

^a Institut de Ciència de Materials de Barcelona, ICMA (CSIC), Campus UAB, 08193 Bellaterra, Spain

^b Instituto de Microelectrónica de Barcelona, IMB-CNM (CSIC), Campus UAB, 08193 Bellaterra, Spain

^c Institut de Diagnòsi Ambiental i Estudis de l'Aigua, IDAEA (CSIC), Jordi Girona 18, 08034 Barcelona, Spain

ARTICLE INFO

Article history:

Received 23 February 2015

Accepted 1 March 2015

Available online 3 March 2015

Keywords:

Bismuth nanoparticles
porous carbon
sol-gel
heavy metals
water analysis

ABSTRACT

This work reports on a detailed analytical assessment of a bismuth nanoparticle-porous carbon paste electrode working as an electrochemical sensor for the sensitive detection of Cd(II), Pb(II) and Ni(II) in water samples of different origin. Detection limits of 0.81, 0.65 and 5.47 ppb for Cd(II), Pb(II) and Ni(II), were achieved, respectively, keeping the overall analysis time below 240 s. This sensor device was employed in the analysis of several contrasting samples such as tap water, ground water, polluted waters from an influent and effluent of an urban wastewater treatment plant and polluted river water due to acid mine drainages, thereby covering a wide spectrum of matrices and absolute and relative heavy metal concentrations. Results were shown to be in good agreement with the reference values. The one-pot mass production of this composite material and the use of Bi in the form of nanoparticles result in sensitive, reproducible and cost-effective electrochemical devices. Moreover, the sol-gel synthesis technology applied to the production of the electrode material can be easily adapted to the fabrication of thick or thin films on planar substrates for the development of electrochemical sensors that could be of practical use for the on-site heavy metal analysis in diverse water sources.

© 2015 Elsevier Ltd. All rights reserved.

1. Introduction

The detection of heavy metal levels in natural or contaminated waters is of paramount importance because the persistence of these species in the environment can result in deleterious effects at different levels [1,2]. Anthropogenic activities have the potential to alter the natural concentrations of a variety of heavy metals in water, this posing a serious threat to the ecosystems and the human health. Indeed, an increasing number of regulations such as those set by the World Health Organization (WHO), the US Environmental Protection Agency (EPA) and the European Union, include heavy metals in the list of priority substances to be monitored [3–5], setting maximum concentration levels, guideline values or allowable concentrations in water following the environmental quality standards (EQS). Standard methods to analyze the presence and concentration of heavy metals in the environment include atomic absorption spectrometry (AAS) and

inductively coupled plasma mass spectrometry (ICP-MS) [6]. Both techniques make use of bulky and costly instrumentation operated by skilled personnel in dedicated centralized laboratories. Hence, the analyses are expensive and in practice these techniques cannot cope with the challenge of the semi-continuous monitoring of heavy metals in waters. The use of alternative reliable analytical tools such as chemical sensors is therefore highly desirable. These devices show the potential to be deployed and used on-site, providing real-time quantitative results. Electrochemical sensors require simple measurement protocols and employ a compact and low-power instrumentation that can be operated on-site. Among the different electrochemical devices, those based on a standard three electrode configuration, with the working electrodes showing a range of different materials and arrangements, and operated by the stripping voltammetry (SV) technique [7] have been long recognized to be an interesting alternative to be applied in this scenario.

Currently, many of the reported electrochemical sensor approaches make use of environmentally-friendly Bi-based electrodes [8–18]. These are increasingly replacing the highly hazardous Hg-based devices, which have long proved to be suitable for the sensitive detection of heavy metals. In this context, the generation of Bi films on the surface of carbon electrodes

* Corresponding author. Tel.: +34 9355947700; fax: +34 935801496.

** Corresponding author. Tel.: +34 935801853; fax: +34 935805729.

E-mail addresses: cesar.fernandez@csic.es (C. Fernández-Sánchez), mgich@icmab.es (M. Gich).

following a similar approach to that previously used with Hg, has been of widespread application in research. However, in order to become a real alternative to the standard analytical methods mentioned above, more progress is needed to improve the electrode analytical performance and avoid additional steps, such as those required for the *ex situ* plating to form a Bi film on the surface of the electrode [8], or the introduction of large amounts of Bi ions in the solution for the *in situ* plating of Bi film electrodes [16].

Several approaches that avoid additional processing steps have been reported to construct Bi electrodes showing different geometries. These include Bi rod-like electrodes [14], micro-fabricated thin-film Bi electrodes [11] and sputtered Bi screen-printed electrodes [17]. Also, electrochemical devices for heavy metal detection based on Bi nanoparticles (Bi NPs) have been developed aiming at reducing the amount of Bi and taking advantage of the superior analytical performance of nanomaterials [9,19]. The Bi NPs used in these systems were prepared by gas condensation [9] or chemical synthesis [19]. However, the corresponding sensors were fabricated by casting an aqueous solution containing Bi NPs on the surface of commercially-available standard electrodes, which still requires a second processing step to produce the final device.

In an effort to combine the benefits of both the one-step fabrication process and the application of Bi nanoparticles, our group is engaged in the one-step sol-gel synthesis of Bi nanoparticle porous carbon composite materials [20], which can be easily processed for the fabrication of different types of electrochemical devices from carbon paste to thick-film (screen printed) and thin-film planar electrodes. Conventional paste electrodes have been initially fabricated to analytically test these novel materials. Due to the high surface area of Bi NPs and the porosity of carbon, the resulting electrodes performed adequately in heavy metal detection, demonstrated by the simultaneous analysis of Pb(II) and Cd(II) at concentration levels below 1 ppb in aqueous standard solutions [20]. Such preliminary analytical results encouraged us to optimize the material synthesis process and then carry out an in depth analytical study of Bi NP porous carbon composite paste electrodes (Bi-CPEs) to fully demonstrate the potential of this material for heavy metal sensing. This work includes a thorough electroanalytical study for carrying out the detection of Cd(II), Pb(II) and Ni(II) in standard solutions using Bi-CPEs and its application to the rapid detection of these pollutants in water samples with significant differences in origin, composition and matrix complexity.

2. Experimental

2.1. Chemicals and solutions

The following chemicals were purchased from Sigma-Aldrich and used as received: resorcinol ($m\text{-C}_6\text{H}_4(\text{OH})_2$, 99% pure), formaldehyde water solution (CH_2O , 37 wt.%, methanol stabilized), glycerol formal (47% 5-hydroxy-1,3-dioxane, 33% 4-hydroxy-methyl-1,3-dioxolane), bismuth nitrate pentahydrate ($\text{Bi}(\text{NO}_3)_3 \cdot 5\text{H}_2\text{O}$, 98% pure), acetic acid (CH_3COOH , 99.7% pure); Cd(II), Pb(II), Ni(II), Cu(II), Zn(II), Co(II), Ga(III) standard solutions (1000 mg/L), dimethylglyoxime (DMG), potassium ferricyanide and potassium ferrocyanide ($\text{K}_3\text{Fe}(\text{CN})_6$ and $\text{K}_4\text{Fe}(\text{CN})_6$).

2.2. Preparation and Microstructural Characterization of the Nanocomposite

The porous Bi NPs-carbon composite (Bi-C) material was prepared in bulk as follows. Firstly 0.2 g $\text{Bi}(\text{NO}_3)_3 \cdot 5\text{H}_2\text{O}$ were dissolved in 5 mL glycerol formal containing 2 mL CH_3COOH . Then,

1 g of resorcinol and 1.36 mL of formaldehyde solution were added to it and stirred until a transparent *sol* was obtained. Gelation occurred by keeping the *sol* for 8 h at 60 °C. The wet gels were dried at ambient conditions under a fume hood for at least 48 h, and finally carbonized at 900 °C for 2 h in Ar or N_2 atmosphere. Microstructural characterization of the materials was performed using a FEI Quanta 200 F scanning electron microscope (SEM) with energy-dispersive X-ray microanalysis (EDX). Nitrogen adsorption-desorption isotherms were recorded with Malvern Micromeritics equipment after degassing around 100 mg of sample for 48 h at 150 °C in vacuum (pressure <1 mPa). Nitrogen adsorption analysis was carried out for the estimation of specific surface areas using the BET (Brunauer-Emmet-Teller) method while pore size distributions, pore volume and mean pore diameters were measured by the BJH (Barret-Joyner-Halenda) method.

2.3. Preparation of the Carbon Paste Electrode

The pyrolyzed Bi-C nanocomposite was firstly ball-milled in a Retsch Mixer Mill to obtain a powder with an average diameter of ca. 10 μm . Hereafter, 1 g of this powder was thoroughly mixed in a mortar with 0.4 mL of spectroscopic grade liquid paraffin (Uvasol® from Merck) to produce a carbon paste. This paste was then packed into a 3 mm-diameter well, defined at one end of a 6 mm-diameter Teflon body, into which a 3-mm diameter stainless steel rod was inserted to make the electrical contact. The surface of the resulting carbon paste electrode (Bi-CPE) was eventually polished on a white paper sheet. After each measurement the Bi-CPE was renewed by packing a fresh paste.

2.4. Electrochemical Analysis

Electrochemical measurements were performed at room temperature in a 10 mL plastic cell and using a conventional three-electrode configuration that included a 3-mm diameter CPE together with a platinum counter electrode and a Ag/AgCl reference electrode (both from Metrohm AG, Switzerland). Electrochemical analysis of Pb(II) and Cd(II) was carried out simultaneously by square wave anodic stripping voltammetry (SWASV) whereas Ni(II) was detected by square wave adsorptive cathodic stripping voltammetry (SWAdCSV). An Autolab PGSTAT30 potentiostat (EcoChemie, The Netherlands) was used for all the measurements. Selected square wave parameters were 20 Hz frequency, 25 mV amplitude and 5 mV step potential for all the analyses. The following supporting electrolytes were used: a 0.1 M acetate buffer solution pH 4.5 (Ac buffer), for the detection of Pb(II) and Cd(II), and a 0.1 M ammonia buffer solution pH 9.2 containing 1 mM (ca. 120 ppm) DMG chelating agent for the measurement of Ni(II) (NH_3 buffer). Calibration curves for the different heavy metals were constructed by plotting the stripping peak current versus the corresponding metal concentration. Each point in the calibration curves was the mean of three measurements with the error bars showing the corresponding standard deviation, unless stated otherwise.

2.5. Analysis of Real Water Samples

Water samples from different locations were collected and used to test the analytical sensor performance: Sample 1- Tap water from the Materials Science Institute of Barcelona (ICMAB, Bellaterra, Spain); Sample 2- Polluted water with a high organic load from an influent of an urban wastewater treatment plant (WWTP) located in Terrassa (Barcelona, Spain); Sample 3- Ground water certified reference material BCR[®] 610, purchased from Sigma-Aldrich; Sample 4- Treated water from an effluent of an urban WWTP located in el Prat (Barcelona, Spain); Sample 5-

Heavily polluted water from the Meca river due to acid drainages from Tharsis mine (Huelva, Spain). These samples were analyzed as follows. Sample 1 was analyzed immediately after collection. Sample 2 contained a high amount of organic matter in suspension and was stored in the freezer. In order to carry out the measurements, the sample was thawed and left for the organic matter to deposit before use. Sample 3 was stored in the fridge and analyzed as received. Samples 4 and 5 were filtered immediately after collection through 0.2 μm Millipore filters, acidified in the field to $\text{pH} < 2$ with Suprapur® HNO_3 and stored at 4 °C in sterile polypropylene containers until analysis.

Water sample analyses were carried out in triplicate with the Bi-CPE sensor. Prior to the electrochemical measurements they were diluted using the appropriate buffer. The degree of dilution necessary to obtain a heavy metal concentration falling within the range of the calibration curves was determined from the stripping currents and peak shapes in preliminary measurements. The analyses were carried out according to the standard addition method, unless stated otherwise.

Samples 1 and 2 did not contain any detectable concentration of the three heavy metals under study. Then, they were spiked with known amounts of the heavy metals and the recovery was calculated. Results obtained in Sample 3 were compared with those provided by the certificate of analysis of this reference material. Sample 4 and 5 contain different concentrations of heavy metals and results were compared with those obtained with the ICP-MS standard method performed by an external laboratory. ICP-MS analyses were carried out using a Thermo Scientific XSERIES II instrument with detection limits of about 1 ppb for all the tested heavy metals. Multi-element standard solutions prepared from single certified standards supplied by SCP SCIENCE were used for calibration and run at the beginning and at the end of each analytical series. Certified Reference Material SRM-1640 NIST fresh-water-type and inter-laboratory standard IRMM-N3 wastewater test material (European Commission Institute for Reference Materials and Measurements) were also intercalated in between the samples for accuracy checking. Precision error was higher than accuracy and was always around 5%.

3. Results and Discussion

3.1. Microstructural Characterization

The SEM image of the Bi-C nanocomposites shown in Fig. 1 reveals the presence of spherical Bi NPs homogeneously distributed in the carbon matrix. The Bi NPs has a size distribution between

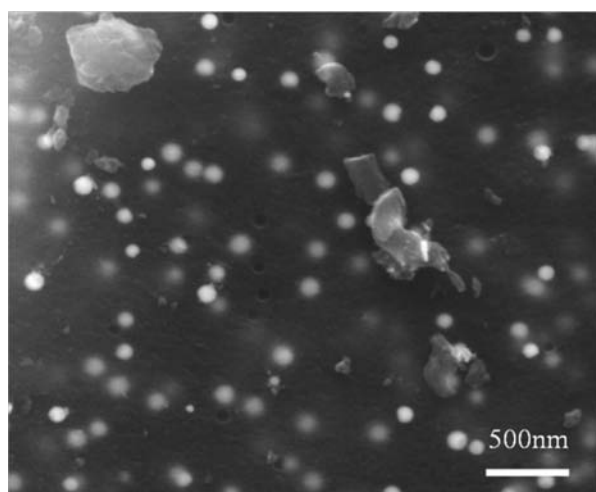


Fig. 1. SEM image of porous C-Bi nanocomposites.

30 nm and 200 nm and an average size around 100 nm. Using EDX analysis, the obtained Bi concentration in the nanocomposites was around 6 wt. %.

The porosity of the Bi-C nanocomposite was studied by nitrogen adsorption/desorption isotherms (Fig. 2). The adsorption uptake observed at low nitrogen relative pressures indicates that the porosity is mainly due to micropores. The non-negligible slope of the curve at intermediate relative pressures and the increase in the adsorbed volume at relative pressures above 0.9 indicate the existence of some mesopores and macropores, respectively. A surface area calculation using BET model gave a value of $71.5 \text{ m}^2 \cdot \text{g}^{-1}$, and the total pore volume was calculated to be $0.049 \text{ cm}^3 \cdot \text{g}^{-1}$ according to the amount adsorbed at a relative pressure P/P_0 of ca. 0.995. The inset of Fig. 2 shows the BJH pore-size distribution curve obtained from the adsorption branch that confirms the dominant diameters in the micropore region with the coexistence of small amount of mesopores and macropores. The lack of overlap of the adsorption and desorption branches at low pressures could be related to the interaction of nitrogen with the material surface or to the elastic deformation of the material at increasing pressures.

Compared to our previous report on this type of nanocomposite matrices [20], the lower pH of the sol, obtained by avoiding the use of NH_4OH , greatly accelerated the gelation process, resulting in materials with less surface area and porosity. However, as shown below, this decreased porosity is not detrimental to the performance of the nanocomposite in the electrochemical sensing of heavy metals.

3.2. Electrochemical Characterization

The large surface area of Bi NPs combined with the porosity of the carbon matrix results in an enlarged electroactive area available for the detection of heavy metals. The Bi-CPEs used in this work were single-use in order to make sure that the same working conditions were applied for all the analytical measurements. Generally, the surface of a CPE can be easily renewed by mechanical polishing after each measurement. However, since the electrode material under study is porous, it soaked up water solution and after the measurement most of the carbon paste packed inside the Teflon body was wet. Indeed, it was shown that a mechanical polishing renewal process did not result in a fresh CPE surface and as such could affect the reproducibility of the electrode signal. Figure S1 in the Supplementary Information (SI) shows that, even when the potential window at which the heavy metal

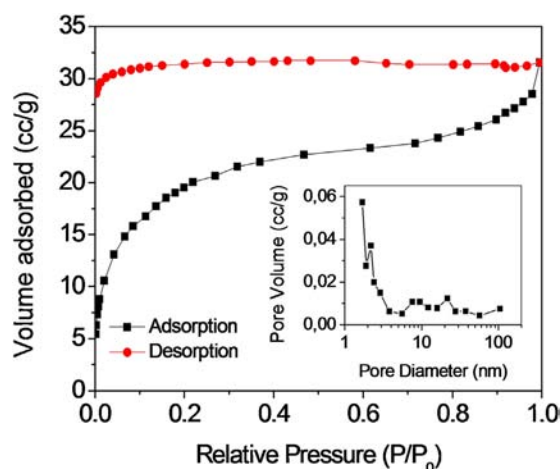


Fig. 2. N_2 adsorption/desorption isotherm of the porous C-Bi nanocomposite. Inset shows the pore size distributions calculated using the BJH method.

stripping process took place was narrowed to avoid the Bi oxidation, the recorded signals were not reproducible if the electrode surface was just renewed by mechanical polishing. Therefore, a new CPE was prepared by packing a fresh Bi-C paste following each measurement.

Figure S1 (SI) also indicates that the Bi-CPEs could be applied to the simultaneous detection of Zn(II), Cd(II) and Pb(II) in water solutions. The electrochemical measurement of these three heavy metals is commonplace and previous approaches have been reported on this matter [8,21]. However, the work presented here was focused on the detection of Cd(II), Pb(II) and Ni(II), taking into account that these are the heavy metals, together with Hg(II), included in the list of priority substances in the field of water policy compiled in the 2013/39/EU Directive [5]. The environmental quality standards expressed as the maximum allowable concentrations (MAC-EQS) in surface waters set up in this directive are 0.45 ppb Cd(II), 14 ppb Pb(II) and 34 ppb Ni(II). Other directives released by the US Environmental Protection Agency and the World Health Organization (WHO) set up concentration values in drinking water in a range of 3–5 ppb Cd(II), 10–15 ppb Pb(II) and 70–100 ppb Ni(II). None of these directives identifies Zn(II) as a primary substance to be monitored in water and just EPA includes it in the water secondary drinking water regulation, setting up a maximum allowable concentration of 5 ppm. Nevertheless, the measurement of Zn(II) was also carried out by our group in an effort to show the potential of our material for the detection of a wider range of heavy metals. Some drawbacks were found and the whole study is included in the SI (Figure S2).

Fig. 3(A) shows an example of the SWASV signals recorded for the determination of Pb(II) and Cd(II) in a concentration range from 1 ppb to 100 ppb after a 180 s accumulation step at -1.4 V in acetate buffer solutions. Two peaks at around -0.8 V and -0.5 V are clearly visible and can be ascribed to Cd(II) and Pb(II) stripping processes, respectively. The calibration curves shown in Fig. 3(B) were linear in the whole concentration range tested. Limits of detection (LOD) of 0.81 ppb and 0.65 ppb for Cd(II) and Pb(II), respectively, were estimated using the formula: $\text{LOD} = 3 \cdot (\text{SD}/S)$, where SD is the standard deviation of the intercept of three calibration curves, with S being the mean of the slopes of these calibration curves. These values are lower than those previously reported with Bi film based electrodes [22], a Bi powder modified carbon paste electrode [23], and a Bi NP modified screen printed carbon electrode [19], using similar or longer accumulation times. Among previously reported Bi NP based electrodes, Malakhora *et al.* [24] achieved similar detection limits (0.55 ppb for Pb(II) and 0.40 ppb for Cd(II)) after a 180 s accumulation time. Lee *et al.* [9] reported the lowest detection limit of 0.07 ppb and 0.15 ppb for Pb(II) and Cd(II) respectively, but using an accumulation time of 600 s. However, compared to our sol-gel approach, the Bi NP based electrodes used in those studies were prepared following a more complex and expensive gas condensation method. It is also worth noting that the LODs of the Bi-CPEs could be improved by increasing the Bi content in the nanocomposites and/or using longer accumulation times up to certain values without compromising the cost and the sensor response time.

The Bi-CPE sensor was then applied to the detection of Ni(II) by SWAdCSV in an ammonia buffer solution containing DMG as a chelating agent for this heavy metal. Here, an accumulation step was carried out at -0.8 V for 180 s, at which the corresponding Ni-DMG complex was adsorbed onto the electrode surface. Then, Ni(II) was reduced to metallic Ni by applying a negative potential scan from -0.8 V to -1.4 V. Reduction of Ni(II) induces fast desorption of the Ni-DMG complex from the electrode surface, as previously reported [18,25]. Fig. 4(A) shows the stripping voltammograms for different Ni(II) concentrations displaying a stripping cathodic peak at around -1.2 V. The absolute value of the

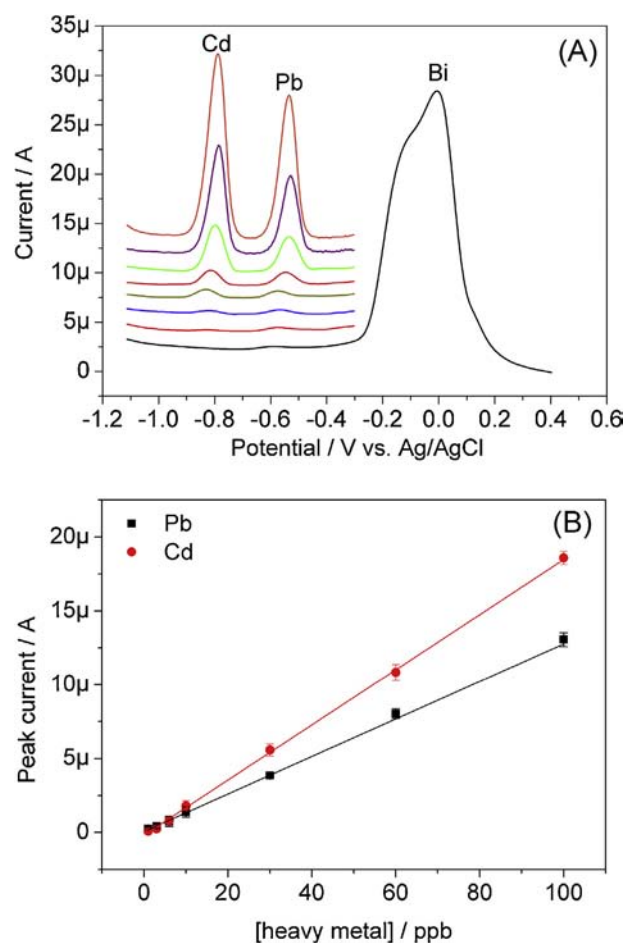


Fig. 3. (A) Square-wave anodic stripping voltammograms recorded in standard 0.1 M acetic buffer solutions pH 4.5 containing different concentrations of Cd(II) and Pb(II) (from bottom to top signals: 0, 1, 3, 6, 10, 30, 60 and 100 ppb). Electrodeposition was carried out at -1.4 V for 3 min. Potential was scanned from -1.4 V to $+0.4$ V. The potential windows of the different voltammograms shown in the figure were cut, and an offset was applied to them, for clarity of presentation. (B) Calibration curves for both heavy metals. Each point represents the mean value of three replicates. The error bars are the corresponding standard deviation.

stripping current increased linearly with the analyte concentration from 10 ppb to 150 ppb (see Fig. 5(B)) and a LOD of 5.47 ppb was estimated, using the criterion mentioned above.

Table 1 gathers all the analytical parameters extracted from the corresponding calibration curves for the three heavy metals tested. The small relative standard deviations of the electrode responses, indicated by the error bars of the calibration curves in Fig. 3(B) and 4(B), illustrate the good reproducibility and overall performance of the sol-gel derived nanocomposite electrodes.

Before undertaking the analysis of water samples, the effect on the electrochemical signal of possible interfering substances that may be present in water, should be considered. Apart from the organic matter, which has long been identified to mask to a certain degree the presence of heavy metals [26] and after carrying out a literature search, the effect of two metal ions was studied. From the chemical point of view, previous works on Bi film electrodes showed that one of the main interferences in the detection of Pb(II) and Cd(II) is Cu(II). For instance, Yang *et al.* [27] found that the presence of Cu(II) at concentration levels 10 times higher than those of Pb(II) and Cd(II) would result in an approximately 70% and 90% decrease in the peak signals of Pb(II) and Cd(II), respectively. They report that this effect was likely to be related to the formation of Cu(II)/Pb(II) and Cu(II)/Cd(II) inter-metallic compounds and the

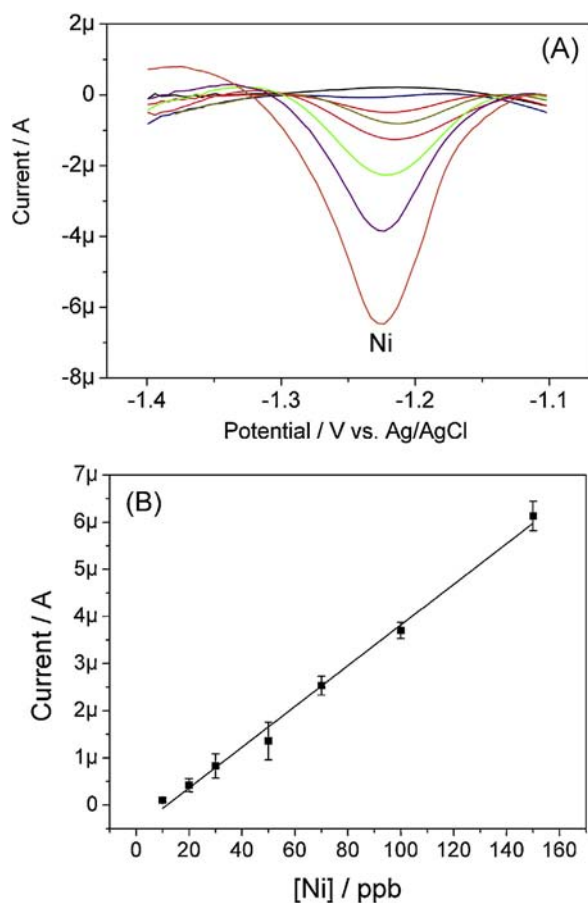


Fig. 4. (A) Stripping voltammograms recorded in standard 0.1 M ammonia buffer solutions pH 9.2 containing different concentrations of Ni(II) at (from top to bottom signals: 0, 10, 20, 30, 50, 70, 100, and 150 ppb) and 1 mM DMG. Activation step was carried out at -1.4 V for 3 min followed by electrodeposition at -0.8 V for 3 min. The potential windows of the different voltammograms shown in the figure were cut for clarity of presentation. (B) Calibration curve. Each point represents the mean value of three replicates. The error bars are the corresponding standard deviation.

deposition competition between Cu(II) and Cd(II), Pb(II) on the electrode surface. Jia *et al.* [28] reported that even a Cu(II) concentration only doubling that of Cd(II) and Pb(II) would affect the determination of these pollutants on CNTs-PSS/Bi composite film electrodes. Fig. 5(A) displays the SWASV signals recorded in solutions containing 50 ppb Pb(II) and Cd(II) and different concentrations of Cu(II). With increasing the Cu(II) concentration, the signals of Pb(II) and Cd(II) were rapidly attenuated and even no signals were recorded when 500 ppb Cu(II) were present in solution (i.e. 10 times higher than that of Pb(II) or Cd(II)). To alleviate this interference, potassium ferricyanide and potassium ferrocyanide were selected as masking agents for Cu(II). Both of them form relatively stable complexes with this metal ion and therefore may help neutralize its effect on the analyses of Pb(II) and Cd(II). The results show that potassium ferrocyanide is a more efficient masking agent than potassium ferricyanide. 100% and 70% signal recoveries for Pb(II) and Cd(II) were achieved, respectively. From the electrochemical point of view, other heavy metals that may simultaneously accumulate on the Bi-CPE surface and whose corresponding stripping signals are recorded at potentials lower than those of Cd(II) and Pb(II) could also interfere. Depending on the relative concentrations of the different heavy metals in solution, Mn(II) and Zn(II) have been identified as possible interferents and their effect should be studied for every particular sample to be analyzed.

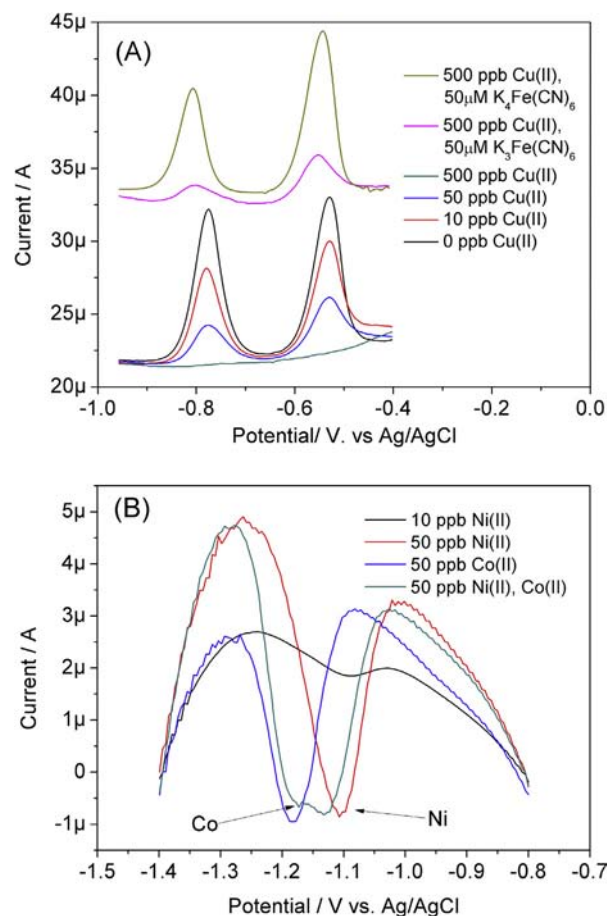


Fig. 5. (A) Stripping voltammograms showing the Cu(II) interference on Pb(II) and Cd(II) and the effect of the addition of ferricyanide or ferrocyanide to reduce this interference. Accumulation at -1.4 V for 3 minutes in 0.1 M pH 4.5 acetate buffer solution containing 50 ppb Cd(II) and 50 ppb Pb(II). An offset was applied to some voltammograms for clarity of presentation. (B) Stripping voltammograms showing the interference of Co(II) on the measurement of Ni(II). Activation at -1.4 for 2 min and accumulation at -0.8 V for 3 min in 0.1 M ammonia buffer pH 9.2.

Regarding the detection of Ni(II), and from the chemical point of view, other heavy metals that may be complexed by DMG could have a negative effect on Bi-CPE response to this target analyte. Divalent cations such as Co(II), Cu(II) and Zn(II) should be taken into account when present in the measuring sample. From the electrochemical point of view, the Ni(II) stripping voltammetric signal can be hampered by the presence of Co(II), which also forms a complex with DMG and whose stripping peak appears at a potential close to that of Ni. A study was conducted with the Bi-CPEs in ammonia buffer solutions containing different relative concentrations of Ni(II) and Co(II). Fig. 5(B) shows SWAdCV signals for Ni(II) or Co(II) recorded individually with the Bi-CPE and those recorded when both metals were present in the buffer solution. It is clearly observed that both signals are overlapped but the peak currents are similar to those of the individual signals. This behavior was observed in all the concentration range studied and should be taken into account when analyzing real water samples. Well-resolved peaks for both metals were previously reported using bismuth film modified glassy carbon electrodes [29], and macroporous bismuth modified screen printed carbon electrodes [18].

3.3. Analysis of Real Water Samples

To test the applicability of the Bi-CPEs, tap water and wastewater from an influent of a WWTP (named as Samples 1

Table 1
Parameters of calibration curves plotted for the different heavy metals.

Heavy metals	Linear range (ppb)	Sensitivity ($\mu\text{A/ppb}$)	Detection limit (ppb)	Number of points (n)	Correlation Coefficient (R)
Cd	1–100	0.19 ± 0.04	0.81	7	0.997
Pb	1–100	0.13 ± 0.02	0.65	7	0.999
Ni	10–150	0.04 ± 0.01	5.47	7	0.993

and 2 in the experimental section) were firstly analyzed. Different aliquots of both samples were diluted with either 0.2 M Ac buffer or 0.2 M NH_3 buffer, in a 1:1 volume ratio, depending on the heavy metal to be analyzed. No detectable amounts of the three heavy metals under study were found. Then, two aliquots of both samples diluted with 0.2 M Ac buffer were spiked with 10 ppb (Sample 1) and 5 ppb (Sample 2) of Cd(II) and Pb(II). The analysis was carried out by the standard addition method. Figures S3 and S4 (SI) show representative stripping voltammograms before and after the addition of different concentrations of Cd(II) and Pb(II) for the two samples, together with the corresponding calibration curves. In addition, two aliquots already diluted with 0.2 M NH_3 buffer, were spiked with 10 ppb Ni(II). Figure S5 (SI) shows the voltammograms of the standard addition method and the corresponding calibration curve carried out for the detection of Ni(II) in Sample 1. Table 2 shows the concentration values recovered for the three heavy metals in both samples. A good agreement between the added values and the estimated ones was found in all cases except for the Ni(II) in Sample 2. The detection of this heavy metal in the spiked sample did not produce any signal. As discussed in section 3.2., the presence in the sample of other divalent metal cations or a high content of organic matter, to which Ni(II) could be strongly adsorbed, may be the reason for this negative result. By contrast, the Cd(II) and Pb(II) detection was not affected by this.

Afterwards, the Bi-CPE was used to analyze two water samples containing the three heavy metals under study. Namely, Sample 3 is a certified reference groundwater with relatively high concentrations of the heavy metals under study and Sample 4 is another waste water collected in an effluent of a WWTP with relatively wide spectrum of heavy metals (Mn, Ba, Cu, Zn) but low amount of Cd(II), Pb(II) and Ni(II). Both samples were diluted and analyzed following the same protocol as with the previous samples. The concentration values measured with the Bi-CPE are shown in Table 2. The values of Pb(II) and Ni(II) in Sample 3 showed a good agreement with the reference values. Cd(II) detection proved to be more difficult. Figure S6 (SI) shows representative stripping voltammograms of Pb(II) and Cd(II) for Sample 3, recorded following the standard addition method. Although the Cd(II) concentration of 1.4 ppb after the 1:1 dilution was still slightly higher than the estimated LOD of Bi-CPE, the presence of 22 ppb Cu(II) negatively affected the Cd(II) determination, as shown below. Following the results of the interference study previously carried out, 0.1 mM $\text{K}_4\text{Fe}(\text{CN})_6$ was added to the solution in order to alleviate the Cu(II) interference. The recorded peak currents were significantly enhanced (see Figure S7, SI) but the recovery appeared to be well below the 100%, which still

resulted in the non-detectability of this analyte. The analyses of Sample 4 showed that the Bi-CPE detected Cd(II) and Pb(II) at very low concentrations, at which the ICP-MS standard technique just provided with estimated values below 2 ppb for both heavy metals. However, Ni(II) could not be measured with our device because its concentration appeared to be below the estimated LOD after carrying out the 1:1 dilution, required to pre-condition the sample.

Finally, the analysis of Sample 5, a heavily polluted river water sample due to acid mine drainages was attempted with the aim of assessing the potential of the Bi-CPEs in the analysis of very complex water samples. This sample contained ppm-levels of Zn(II), Cu(II) and Mn(II) but ppb-levels of Pb(II), Cd(II) and Ni(II). Sample dilution was adjusted to a 1:10 volume ratio with the corresponding buffer solution, this being the highest feasible dilution in an attempt to minimize the matrix effects while the target analytes could still be detected. Figure S8 shows the stripping voltammograms of Pb(II) and Cd(II) in this sample. They displayed a steep background signal at potentials below -0.6V that significantly reduced the potential window and hindered the detection of the stripping peak of Cd(II). This effect may be related to the presence of Mn(II) and Zn(II) at concentrations above 10 ppm in the original sample and whose stripping peaks are usually recorded at potentials lower than that of Cd(II). A Bi stripping peak at around 0 V was recorded, which is wider, rounder and much bigger than the Bi peak recorded in the solutions with a lower content of Cu(II). This peak shape is likely to be related to the overlapping of Bi(III) and Cu(II) stripping peaks. Cu(II) was present in the original sample at concentrations around 10 ppm and its interference on the detection of Cd(II) was described above. Surprisingly, the Pb(II) signals did not seem to be affected by the presence of Cu(II) and increased linearly with the standard additions of Pb(II) into the solution. Regarding the Ni(II) detection, DMG was added in the NH_3 buffered solution for the formation of the Ni(II)-DMG complex. However, DMG forms complexes with many metallic cations, such as Mn(II), Zn(II), Pb(II), Co(II), and Cu(II), some of which are also present at high concentrations in Sample 5. The Ni(II) current signals did not increase linearly with the standard additions of Ni(II) into the solution. We believe that all the DMG added to the solution was complexing the different heavy metals and then could not chelate the added Ni(II). However, increasing the concentration of DMG in the solution resulted in the production of a clearly visible white precipitate making the measurements unreliable. For all this, the Ni(II) concentration was measured by interpolating the signal recorded in the sample into the corresponding sensor calibration curve. From Table 1, the ICP-MS results and the values of the electrochemical analysis are in

Table 2
Results of the analyses of five water samples using the Bi-CPE.

Sample	Added/Reference/ICP-MS values (ppb)			Sensor values (ppb)		
	Cd(II)	Pb(II)	Ni(II)	Cd(II)	Pb(II)	Ni(II)
Tap water (1)	10	10	10	9.2 ± 1.0	9.1 ± 0.7	9.4 ± 0.9
Polluted water - influent (2)	5	5	10	4.7 ± 0.6	5.1 ± 0.8	$\leq \text{LOD}$
Certified water (3)	2.78	7.98	27	$\leq \text{LOD}$	7 ± 2	25 ± 4
Polluted water - effluent (4)	< 2	< 2	7.8	3.7 ± 0.8	1.3 ± 0.4	$\leq \text{LOD}$
Heavily polluted-mine drainages (5)	55 ± 3	38 ± 2	273 ± 14	$\leq \text{LOD}$	40.9 ± 0.6	$262 \pm 73^*$

*- analyzed by the interpolation method.

reasonable good agreement. However, this last analysis proves that the performance of electrochemical devices, such as the one presented here, for analysis of complex samples containing a variety of heavy metals in a wide range of concentrations, should be studied in detail for any particular case. Nevertheless, alarm systems based on this kind of sensors with the ability to detect increased concentrations of these pollutants due to sudden spills, could be implemented.

4. Conclusion

Bi-C nanocomposites prepared following a versatile soft chemistry approach successfully performed as working electrode materials for the electrochemical analysis of heavy metal pollutants in water. The materials consist of a highly porous carbon matrix with well-distributed Bi nanoparticles that provide a large active area for the electrochemical reduction of heavy metals in solution and are responsible for the superior electrode sensitivity.

Low detection limits and wide linear calibration ranges were obtained for Cd(II), Pb(II) and Ni(II). The electrodes were tested in the analysis of real water samples of different origin presenting complex and distinct heavy metals matrices. The results of the Cd (II), Pb(II) and Ni(II) analysis showed good recoveries in the spiked samples and were in good agreement with the reference values and those obtained by the standard ICP-MS method in samples of different nature containing these pollutants at different concentrations.

The C-Bi nanocomposite materials can be processed as inks for the fabrication of thick-film screen-printed electrodes and also as thin-films for the production of miniaturized electrodes. This opens the door to future developments of portable, low cost electrochemical sensors, which enabled a reliable on-site semi-continuous monitoring of heavy metals. Work is in progress in such direction.

Acknowledgements

This research was partially funded by the Spanish Government and cofounded by the European Social Fund (MAT2012-35324, TEC2010-17274, CGL2013-48460-C2), the Generalitat de Catalunya (2014SGR213, 2014SGR1645) and the European Commission (FP7-Marie Curie Actions, PCIG09-GA-2011-294168 grant and FP7-OCEAN-COMMON SENSE, as well as the COST Action MP1202). The Chinese Scholarship Council fellowship of P. N. is also acknowledged.

Appendix A. Supplementary data

Supplementary data associated with this article can be found, in the online version, at <http://dx.doi.org/10.1016/j.electacta.2015.03.001>.

References

- [1] H. Hu, Human health and heavy metals exposure, in: M. McCally (Ed.), *Life support The environment and human health*, MIT press, 2002, pp. 1–13.
- [2] L. Järup, Hazards of heavy metal contamination, *British Medical Bulletin* 68 (2003) 167–182.
- [3] WHO Guidelines for Drinking-water Quality, 4th edition, 2011.
- [4] U.S. EPA National Primary Drinking Water Regulations 2009.
- [5] Directive 2013/35/EU of the European Parliament and of the Council, 2013.
- [6] Standard methods for the examination of water & wastewater, 22nd Edition, American Public Health Association (APHA), American Water Works Association (AWWA) & Water Environment Federation (WEF) 2012.
- [7] J. Wang, Stripping-based electrochemical metal sensors for environmental monitoring, in: S. Alegret, A. Merkoci (Eds.), *Electrochemical sensor analysis*, Elsevier, 2007, pp. 131–140.
- [8] R. Pauliukaitė, C.M.A. Brett, Characterization and application of bismuth-film modified carbon film electrodes, *Electroanalysis* 17 (2005) 1354–1359.
- [9] G.-J. Lee, H.-M. Lee, C.-K. Rhee, Bismuth nano-powder electrode for trace analysis of heavy metals using anodic stripping voltammetry, *Electrochemistry Communications* 9 (2007) 2514–2518.
- [10] N.A. Malakhova, N.Y. Stojko, K.Z. Brainina, Novel approach to bismuth modifying procedure for voltammetric thick film carbon containing electrodes, *Electrochemistry Communications* 9 (2007) 221–227.
- [11] Z. Zou, A. Jang, P.M. Wu, J. Do, J. Han, P.L. Bishop, C.H. Ahn, Environmentally-friendly disposable heavy metal ion sensors using planar bismuth microelectrodes for in situ environmental monitoring, *Eleventh International Conference on Miniaturized Systems for Chemistry and Life Sciences Paris France (2007)*.
- [12] Z. Bi, C.S. Chapman, P. Salaün, C.M.G. van den Berg, Determination of lead and cadmium in Sea- and freshwater by anodic stripping voltammetry with a vibrating bismuth electrode, *Electroanalysis* 22 (2010) 2897–2907.
- [13] V. Urbanová, M. Bartoš, K. Vytrás, A. Kuhn, Porous bismuth film electrodes for signal increase in anodic stripping voltammetry, *Electroanalysis* 22 (2010) 1524–1530.
- [14] Z. Zhang, K. Yu, D. Bai, Z. Zhu, Synthesis and electrochemical sensing toward heavy metals of bunch-like bismuth nanostructures, *Nanoscale Research Letters* 5 (2010) 398–402.
- [15] N. Lezi, A. Economou, P.A. Dimovasilis, P.N. Trikalitis, M.I. Prodromidis, Disposable screen-printed sensors modified with bismuth precursor compounds for the rapid voltammetric screening of trace Pb(II) and Cd(II), *Analytica chimica acta* 728 (2012) 1–8.
- [16] C. Chen, X. Niu, Y. Chai, H. Zhao, M. Lan, Bismuth-based porous screen-printed carbon electrode with enhanced sensitivity for trace heavy metal detection by stripping voltammetry, *Sensors and Actuators B: Chemical* 178 (2013) 339–342.
- [17] V. Sosa, N. Serrano, C. Arino, J.M. Diaz-Cruz, M. Esteban, Sputtered bismuth screen-printed electrode: a promising alternative to other bismuth modifications in the voltammetric determination of Cd(II) and Pb(II) ions in groundwater, *Talanta* 119 (2014) 348–352.
- [18] S. Dal Borgo, H. Sopha, S. Smarzewska, S.B. Hočevar, I. Švancara, R. Metelka, Macroporous bismuth film screen-printed carbon electrode for simultaneous determination of Ni(II) and Co(II), *Electroanalysis* (2014) n/a–n/a.
- [19] M.Á.G. Rico, M. Olivares-Marín, E.P. Gil, Modification of carbon screen-printed electrodes by adsorption of chemically synthesized Bi nanoparticles for the voltammetric stripping detection of Zn(II), Cd(II) and Pb(II), *Talanta* 80 (2009) 631–635.
- [20] M. Gich, C. Fernández-Sánchez, L.C. Cotet, P. Niu, A. Roig, Facile synthesis of porous bismuth-carbon nanocomposites for the sensitive detection of heavy metals, *Journal of Materials Chemistry A* 1 (2013) 11410–11418.
- [21] G.-J. Lee, C.K. Kim, M.K. Lee, C.K. Rhee, Simultaneous voltammetric determination of Zn, Cd and Pb at bismuth nanopowder electrodes with various particle size distributions, *Electroanalysis* 22 (2010) 530–535.
- [22] A.A.A. Khan, M.A. Abdullah, Bismuth-modified hydroxyapatite carbon electrode for simultaneous in-situ cadmium and lead Analysis, *International Journal of Electrochemical Science* 8 (2013) 195–203.
- [23] S.B. Hočevar, I. Švancara, K. Vytrás, B. Ogorevc, Novel electrode for electrochemical stripping analysis based on carbon paste modified with bismuth powder, *Electrochimica Acta* 51 (2005) 706–710.
- [24] N.A. Malakhova, A.A. Mysik, S.Y. Saraeva, N.Y. Stozhko, M.A. Uimin, A.E. Ermakov, K.Z. Brainina, A voltammetric sensor on the basis of bismuth nanoparticles prepared by the method of gas condensation, *Journal of Analytical Chemistry* 65 (2010) 640–647.
- [25] G.M.S. Alves, J.M.C.S. Magalhães, H.M.V.M. Soares, Simultaneous determination of nickel and cobalt using a solid bismuth vibrating electrode by adsorptive cathodic stripping voltammetry, *Electroanalysis* 25 (2013) 1247–1255.
- [26] M. Ahmaruzzaman, Industrial wastes as low-cost potential adsorbents for the treatment of wastewater laden with heavy metals, *Advances in Colloid Interface Science* 166 (2011) 36–59.
- [27] D. Yang, L. Wang, Z. Chen, M. Megharaj, R. Naidu, Investigation of copper(II) interference on the anodic stripping voltammetry of lead(II) and cadmium(II) at bismuth film electrode, *Electroanalysis* 25 (2013) 2637–2644.
- [28] X. Jia, J. Li, E. Wang, High-sensitivity determination of lead(II) and cadmium(II) based on the CNTs-PSS/Bi composite film electrode, *Electroanalysis* 22 (2010) 1682–1687.
- [29] M. Morfobos, A. Economou, A. Voulgaropoulos, Simultaneous determination of nickel(II) and cobalt(II) by square wave adsorptive stripping voltammetry on a rotating-disc bismuth-film electrode, *Analytica chimica acta* 519 (2004) 57–64.

Sol-Gel Nanocomposites for Electrochemical Sensor Applications

Pengfei Niu¹, Martí Gich^{1*}, César Fernández-Sánchez^{2*}, Anna Roig^{1*}

¹*Institut de Ciència de Materials de Barcelona, ICMA B (CSIC), Campus UAB, 08193 Bellaterra, Spain*

²*Instituto de Microelectrónica de Barcelona, IMB-CNM (CSIC), Campus UAB, 08193 Bellaterra, Spain*

(*corresponding authors: mgich@icmab.es, cesar.fernandez@imb-cnm.csic.es, roig@icmab.es)

1. Introduction

Sensors find nowadays widespread use in many sectors, from traditional applications in research, to industrial production or environmental monitoring to an increasing deployment in everyday life such as in vehicles, domotics, security, healthcare or consumer technologies.

The current momentum of sensor applications and the prospects for new innovations has fueled this very active area of research in which the development of new materials plays a major role. On the one hand, these materials are expected to bring novel or enhanced responses to specific stimuli from the sampling milieu and eventually display all the functionalities required for the sensing and transduction processes, in order to improve the detection limits, the sensitivity or the selectivity of the sensor. On the other hand, alternative preparation approaches are being developed with the aims of decreasing fabrication costs or achieving the miniaturization of the sensor devices. Sol-gel synthesis is particularly appropriate to prepare materials facing those challenges thanks to the versatility of its chemistry and the myriad of structuring and processing alternatives compatible with the method. Indeed, because of the many possibilities of sol-gel methods it is relatively easy to obtain tailored hybrid materials or nanocomposites displaying the multifunctional properties required from a given sensing application. For instance, a transparent magnetic aerogel intended for real-time detection of current peaks in high-power lines via the Faraday effect can be readily prepared by supercritical drying of a silica/iron (III) composite gels¹. An initial solution with silica precursors, surfactants and an organic pH-sensitive molecule results in a pH sensor fabricated by an one-pot synthesis process². Dip-coated porous films of alkali-doped titania are the basis of a humidity sensor³ but vapor-surface sol-gel deposition of titania is better adapted to make composite films embedding horseradish peroxidase to be used as a H₂O₂ sensor⁴. These few examples serve to illustrate the potential of sol-gel chemistry to produce a broad range of sensing materials. In particular, chemical sensors are devices reporting a chemical concentration that, depending on the signal transduction mechanism, can be classified as optical, electrical (including electrochemical), mass sensitive or calorimetric sensors⁵. However, in the context of sol-gel chemistry, optical and electrochemical transduction modes are particularly relevant. Sol-gel materials applied to the fabrication of optical sensors for the detection of inorganic species has been addressed in two recent reviews^{6,7}. Other reviews have

focused on optical or electrochemical biosensors consisting of sol-gel matrices with entrapped biomolecules⁸⁻¹¹.

In this chapter an overview is given of the use of sol-gel nanocomposites in electrochemical sensors with emphasis in the detection of relevant chemical species. To this aim we will consider that a sol-gel nanocomposite consists of a distribution of a nanomaterial (typically carbon nanotubes, graphene, metallic or metal oxide nanoparticles, biomolecules) embedded in an open porous inorganic or hybrid organic-inorganic matrix obtained by sol-gel chemistry (most commonly being carbon, silica and other simple metal oxides). Figure 1 includes a schematic drawing of a sol-gel nanocomposite. The composition and porous microstructure of the matrices will obviously play a very significant role in the material performance for sensor applications. The use of nanomaterials as the active component of an electrochemical sensor is in several aspects advantageous because the high surface area to volume ratio of the nanomaterials provides fast mass transport and a large effective sensor surface area. Besides, materials often show particular properties in the nanoscale such as electrocatalytic activity towards a great variety of molecules. Furthermore, sol-gel matrices are interesting for its chemical inertness, mechanical stability, biocompatibility and high specific surface area provided by the porous open frame networks. All these features make sol-gel nanocomposite sensors to display improved sensitivity and low limits of detection towards a wide range of target analytes¹².

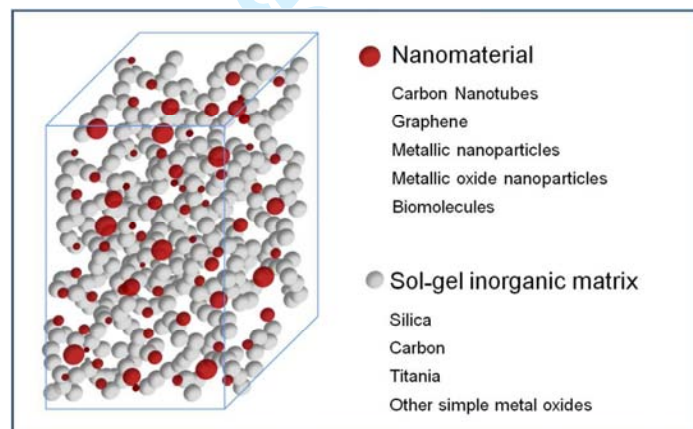


Figure 1. Scheme of the sol-gel nanocomposite basic structure.

The chapter is structured as follows: Section 2 includes a brief introduction to electrochemical sensors. Section 3 presents three different approaches to prepare sol-gel nanocomposites for electrochemical sensing applications, giving specific examples to each of them. In section 4 the different types of electrochemical transducers that can be prepared using the sol-gel material fabrication processes are described together with the electrochemical detection mechanisms applied. Section 5 gives an overview of recent literature on sol-gel nanocomposites as electrochemical sensors of different types of analytes. The chapter wraps up by summarizing the main conclusions and discussing some future prospects of sol-gel nanocomposites for electrochemical sensor applications.

2. Electrochemical Sensor

An electrochemical sensor is essentially a chemical sensor comprising a selective receptor to the target analyte to be measured and a transducer mainly formed by an electrode structure. The transducer transforms a chemical reaction commonly taking place between the target analyte and the receptor, into an electrical measurable signal. This electrical signal is usually an electron transfer process at the sensor solution interface, but could also be based on changes in the electrical properties of the measuring solution such as the conductivity or the capacitance induced upon the interaction of the sensor with the target analyte. In order to carry out the analyses, the electrochemical sensor should be integrated in an electrochemical cell comprising one electrode (reference/counter electrode) or two electrodes (separate reference and counter electrodes). The latter configuration is represented in Figure 2 together with the complete set-up required to carry out the sensor analysis. Based on the electrochemical transduction mode, electrochemical sensors can be mainly classified into the following categories: potentiometric, voltammetric (including amperometric) and impedimetric (including conductometric). For more details about the working principle of each type of electrochemical sensor, we refer the reader to references^{13, 14}. It is worth mentioning that most of the electrochemical sensors incorporating sol-gel derived nanocomposites employ voltammetric techniques to produce the analytical signals, which are typically cyclic voltammetry, differential pulse voltammetry or square wave voltammetry.

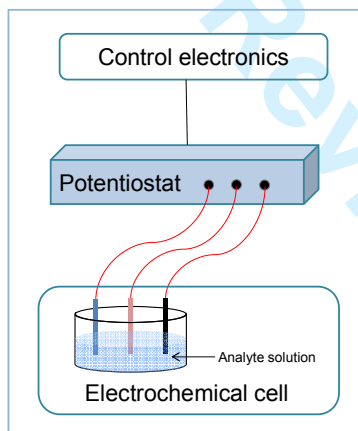


Figure 2. Schematic drawing of an electrochemical cell comprising the sensor (in red), counter (black) and reference (blue) electrodes and measurement set-up .

3. Sol-Gel Nanocomposites: Synthesis Routes

There are different strategies to encapsulate nanomaterials into a sol-gel matrix to obtain a nanocomposite. The simplest approach consists in dispersing in the initial solution a previously prepared nanomaterial,

which, upon gelation, will be retained within the gel matrix. This approach allows the inclusion of a wide range of different nanomaterials prior to their encapsulation¹⁵. Main drawbacks of this approach are possible agglomeration of the nanoparticles and the difficulty of obtaining a homogeneous dispersion. Thus material reproducibility might be an issue deserving attention. A second alternative is by co-synthesis, in which precursors of the sol-gel matrix and of the nanomaterials are introduced in the initial solution. This route can be considered as an easy one-pot and one-step synthesis allowing a fairly simple control of the nanomaterial load¹⁶. However, it should be noted that it is not always obvious to obtain the required degree of crystallinity or even the desired polymorph of the nanomaterial and that the matrix formation can be partially disrupted by the inclusion of a guest nanomaterial. The third route consists in impregnating the wet gel with a solution containing the nanomaterial precursors. This approach requires two differentiated synthetic steps and its major drawback is the limited control over the final nanomaterial load in the composite^{17,18}.

In all three cases, the final composite is usually formed after submitting the gel to a thermal treatment. Figure 3 depicts schematic representations of the approaches described above. Preparation details and a few representative examples of these approaches are given below.

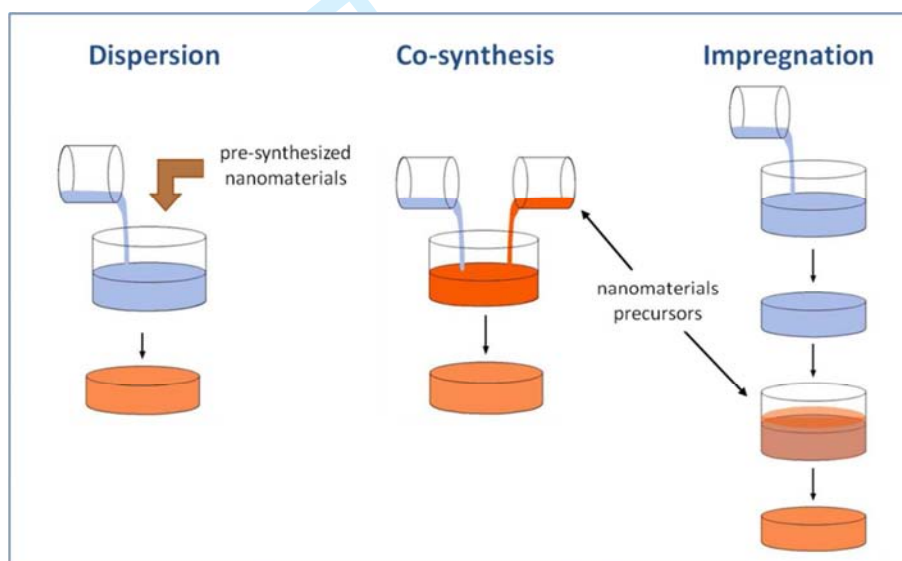


Figure 3. Three different strategies to encapsulate nanomaterials within a sol-gel matrix

3.1 Pre-synthesized nanomaterials dispersed in the matrix precursor solution

Carbon nanotubes dispersed in silica sol-gel nanocomposites. Carbon nanotubes can be incorporated in sol-gel matrices aiming to improve either the mechanical or conductive properties of the resulting materials. Lev's group¹⁹ employed a sol-gel silicate solution as a binder to be mixed with carbon (graphite powder or carbon black) to obtain bulk carbon/silica composite electrodes. The performance of this type of electrodes was further enhanced by using carbon nanotubes as²⁰. In another approach, Gong et al.²¹ described the incorporation of a relatively low content of carbon nanotubes into the starting silicate sol before depositing it onto Au or glassy carbon electrodes.

3.2 Co-synthesis of sol-gel nanocomposites

Metallic nanoparticles dispersed in sol-gel nanocomposites. This kind of nanocomposite material can be obtained incorporating metal salts to the starting sol²². In this case, an additional *in-situ* reduction step of metal ions to form metallic nanoparticles is required. For the stabilization of the metal ions and the subsequent formation of nanoparticles, monomers with functional chelating groups (e.g., amine, thiol) are commonly employed as the precursors of silica gel matrices. Lev *et al.*²² introduced H_{Au}Cl₄ to an amine functional silicate (aminopropyltrimethoxysilane) solution. Subsequently, gold nanoparticles were formed by *in-situ* reduction with NaBH₄ which could be initiated either before or after the condensation of the gels. Instead of NaBH₄, other organic reducing agents such as an aniline pentamer derivative²³ were also successfully used. In another example a Bi nanoparticle composite was prepared by adding bismuth nitrate to a resorcinol formaldehyde sol resulting Bi nanoparticles/carbon porous composite after a controlled pyrolysis of the organic gel²⁴.

3.3 Impregnation of the sol-gel matrices with nanomaterial precursors or pre-formed nanomaterials

Gels impregnated with metallic nanoparticles. Impregnation of metallic nanoparticles into a formed gel network is another approach to obtain sol-gel nanocomposites. The common strategy includes the initial synthesis of a porous three-dimensional gel network, which is further incubated in a metal nanoparticle suspension in order to introduce enough nanoparticles within the matrix²⁵. Impregnation success is dependent on the porosity of the gel and the relative affinity of nanomaterials with the gel network. Thus, the encapsulation of metallic nanoparticles by impregnation might require the use of an organically modified sol-gel network containing appropriate functional groups presenting an affinity with the nanoparticles.

Gels impregnated with metal salt solutions. To obtain composites of carbon with metal nanoparticles, organic gels can be impregnated with metal salt solutions before drying and pyrolysis processes^{18,24}.

Indeed, the above described approaches can be combined to obtain complex nanocomposite sensors. A nice example is the work by Lu *et al.*, combines in one material the excellent electrical conduction of graphene and the electrocatalytic properties and high surface area of metallic nanoparticles in a silica matrix²⁶. In this work graphene oxide was coated with silica and functionalized with a silicon alcoxide containing an amine in order to decorate it with silver nanoparticles. This last step was accomplished by two alternative approaches consisting in mixing a suspension of silica coated graphene oxide sheets either with a Ag nitrate solution followed by a reduction step or a suspension of Ag nanoparticles (see Figure 4). This electrode material was used for a highly efficient H₂O₂ and glucose sensing.

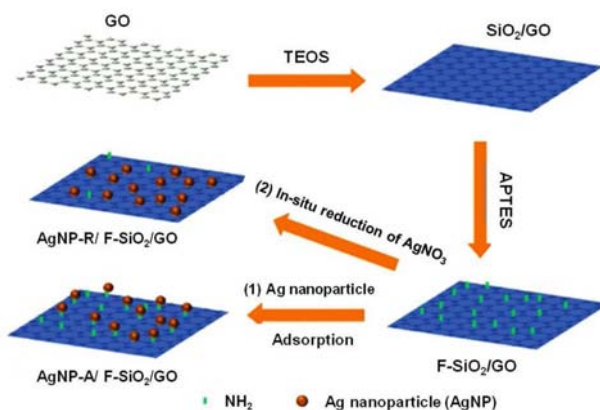


Figure 4. Schematic diagram of the formation procedure of Ag nanoparticles modified sol-gel silica@graphene oxide core/shell nanocomposites (adopted from Lu *et al.*, *Biosensors and Bioelectronics*, Volume 26, Issue 12, 2011, 4791 – 4797, with permission²⁶)

The preparation approaches described above are also convenient for the encapsulation of enzymes into the sol-gel nanocomposites to develop enzyme catalytic biosensors. For instance, Bharathi *et al.*²⁷ mixed glucose oxidase enzyme solution with gold nanoparticles in a methyl silicate sol and then coated the mixture suspension on a substrate for glucose sensing. In another example, silica matrices were impregnated with Au nanoparticles and horseradish peroxidase to obtain a glucose sensor²⁵.

4. Electrochemical Sensors Based on Nanocomposites by Sol-Gel

Electrochemical sensors based on sol-gel nanocomposites generally fall into three categories depending on the configuration of the working electrodes: 1) *bulk electrodes fabricated with conductive sol-gel nanocomposites*, 2) *films obtained by casting sol-gel nanocomposites on substrate electrodes* and 3) *molecularly imprinted sol-gel nanocomposite-based sensors*.

4.1 Bulk electrodes

A fabrication procedure of bulk electrodes was firstly proposed by Lev's group¹⁹ and subsequently widely employed for the development of carbon ceramic electrodes. The common feature of these electrodes is the high content of carbonaceous materials. Commonly, a sol is firstly mixed thoroughly with the desired amount of the carbon-based material. Then, the mixture is packed into one end of a plastic body which includes a stainless steel wire as electrical contact (Figure 5). After sol condensation, polymerization and gel drying, the resulting electrodes are polished to yield a smooth surface required for electrochemical measurements. In this set-up the sol-gel material, with or without nanomaterials, serves as a binder for the carbon-based conductive material.

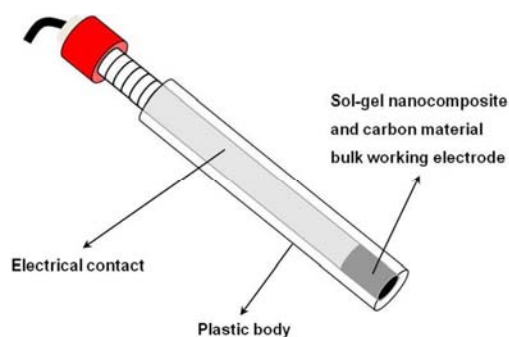


Figure 5. Schematic diagram of a conventional bulk sol-gel nanocomposite working electrode

Figure 6 shows a SEM image of the surface of a silica-carbon nanotube nanocomposite bulk electrode where the nanotube fibers and a porous structure are clearly visible²⁰.

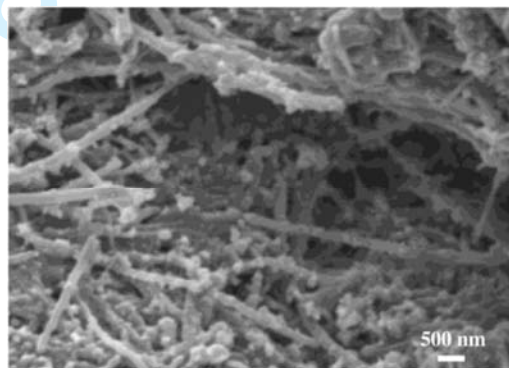


Figure 6. SEM image of the surface of sol-gel (MTMOS-derived) silica-carbon nanotube composites (44% w/w carbon nanotube) (adopted from Gavalas *et al.*, *Nano Letters*, Volume 1, Issue 12, 2001, 719-721, with permission²⁰)

4.2 Film electrodes

Sol-gel nanocomposite coated film electrodes were reported by Lev's group proposing a sol-gel silicate/gold nanoparticle composite biosensor for glucose detection²⁷. To fabricate a nanocomposite film electrode, one approach is casting a sol with the desired amount of the nanomaterial on a solid electrode, and then inducing gel polymerization and further drying. Another approach is by following a stepwise synthesis as shown in Figure 7²⁸. Here, a solid electrode is firstly dipped in a solution of silica monomers with chelating groups (e.g., thiol, amine). After gel film formation on the gold electrode, this is immersed in a metal nanoparticles suspension to achieve a nanocomposite film. Such impregnation method is an elegant alternative to construct enzyme catalytic biosensors based on sol-gel nanocomposites, since the influence of acidic or basic conditions, as well as the presence of alcohols in the initial solution or those generated during the monomer hydrolysis of the sol-gel synthesis can be avoided.

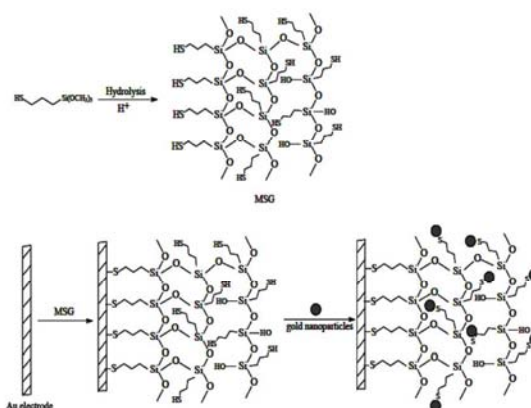


Figure 7. Stepwise assembly of a gold nanoparticle-derived organically functional sol-gels on a gold electrode (adopted from Wang *et al.*, *Electrochemistry Communications*, Volume 6, Issue 1, 2004, 49 - 54, with permission ²⁸)

4.3 Molecularly-imprinted electrodes

Molecular imprinting of polymer matrices (molecularly imprinted polymers - MIP) has emerged as an excellent strategy to produce stable selective receptors for electrochemical sensors. The porous structure of the sol-gel materials can be tuned to create MIPs and in turn its porosity can be modulated in order to enhance analyte diffusion penetration. One example is shown in Figure 8 ²⁹. It presents the fabrication steps of a MIP dopamine electrochemical sensor based on core(gold)/shell(silica) nanoparticles. The imprinted nanocomposite was synthesized by growing a silica shell by sol-gel in the presence of a template-analyte molecule (dopamine in this case) around a gold nanoparticle (core). After the silica shell is formed, the dopamine is eluted from the silica network leaving binding sites (cavities) complementary in size, shape and functional groups to the analyte to be sensed. Then, the core/shell nanoparticles are mixed with some film forming agent (i.e., chitosan, Nafion®) and cast on a solid glassy carbon electrode (GCE). The final electrode presents a large specific surface area, fast and easy diffusion and high binding capacity to dopamine.

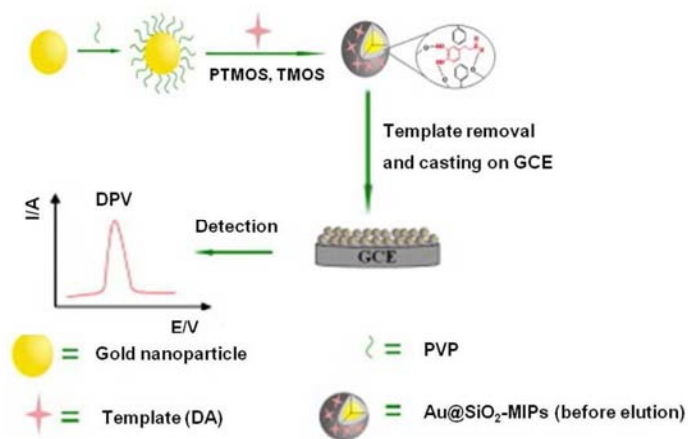


Figure 8. Preparation procedure of gold nanoparticles/silica core/shell MIPs (adopted from Yu *et al.*, *Biosensors and Bioelectronics*, Volume 38, Issue 1, 2012, 270 - 277, with permission ²⁹)

4.4. Aspects to be considered in the electrochemical performance of sol-gel nanocomposites

The performance of the sol-gel nanocomposites as a component of an electrochemical sensor is mainly directed towards either enhancing electron transfer between the electrode and the electrolyte and/or towards catalyzing electrochemical reactions. For instance, carbon nanotubes or graphene are incorporated with the main aim of enhancing the electron transfer rates at the transducer. In other approaches, metallic nanoparticles are mainly employed to catalyze different redox reactions. As catalysts, metallic nanoparticles generally act in one or more of the following directions: 1) providing active sites to bind metal ions (e.g., amalgam processes for the detection of heavy metals), 2) lowering the over-potential required to oxidize or reduce a chemical species without the need of using a bio-molecular catalyst (such as an enzyme) and thus improving the read-out signals and 3) offering biocompatible microenvironments to immobilize enzymes and enhance enzyme-catalyzed reactions.

In the following two examples of metal nanoparticles catalyzing chemical redox reactions are included. Maduraiveeran *et al.*³⁰ modified a glassy carbon electrode with a sol-gel silica/gold nanoparticle composite for the simultaneous detection of toxic N_2H_4 , SO_3^{2-} , and NO_2^- (Figure 9). The modified sensor displayed well-defined separated voltammetric peaks when compared to the ill-defined ones recorded with the bare glassy carbon electrode. This is due to a large decrease in the oxidation over-potentials (from higher than 0.8 V to 0.05 V, 0.2 V and 0.55 V for N_2H_4 , SO_3^{2-} and NO_2^- , respectively).

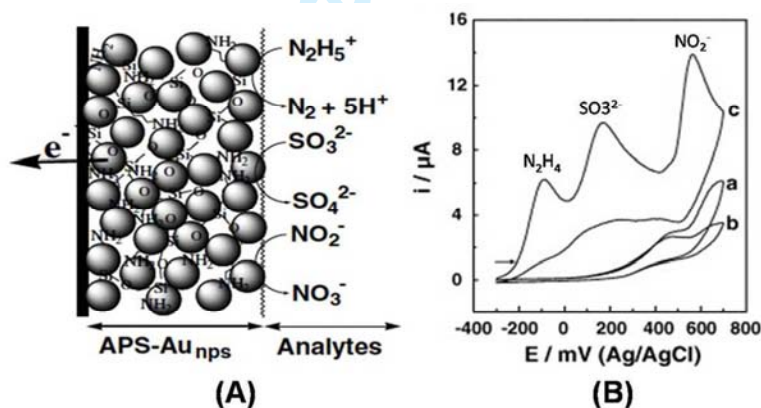


Figure 9. (A) Schematic representation of simultaneous electrocatalytic oxidation of N_2H_4 , SO_3^{2-} and NO_2^- on gold nanoparticles embedded in a sol-gel silicate matrix (B) the cyclic voltammograms recorded from a mixture containing each $250\mu\text{M}$ N_2H_4 , SO_3^{2-} and NO_2^- with (a) GCE, (b) GCE/ SiO_2 film, (c) GCE/ SiO_2 -gold nanoparticles film electrode (adopted from Maduraiveeran *et al.*, *Electrochemistry Communications*, Volume 9, Issue 8, 2007, 2051 - 2055, with permission³⁰).

On a different set-up, Du *et al.*³¹ cast sol-gel silica/gold nanoparticle nanocomposite films on a glassy carbon electrode and the electrode was then impregnated with an acetylcholinesterase (AChE) enzyme (Figure 10). The construct was used as a biosensor for organo-phosphorous (OP) pesticide detection. In this system, gold nanoparticles not only offered a biocompatible microenvironment to retain the activity of adsorbed enzyme molecules but also acted as a wire to enhance the direct electron transfer rate between the enzyme active centers and the electrode surface, which otherwise would be blocked by the thick protein shell of the enzyme chemical structure.

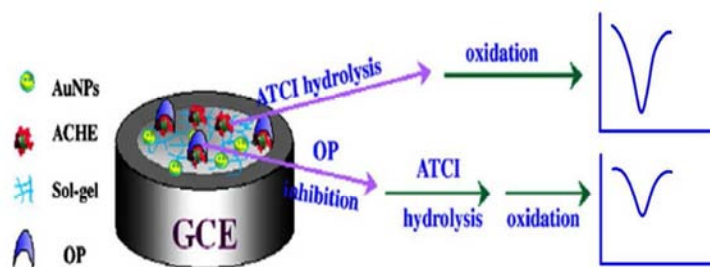


Figure 10. Principle of AChE biosensor on gold nanoparticles embedded in sol-gel silicate nanocomposites used for determination of OP compound (adopted from Du *et al.*, *Biosensors and Bioelectronics*, Volume 23, Issue 1, 2007, 130 - 134, with permission³¹).

5. Application of Sol-Gel Nanocomposites in Electrochemical Sensors

5.1. Detection of heavy metals

The detection of heavy metals, such as Pb^{2+} , Cd^{2+} , As^{3+} and Hg^{2+} is of paramount importance because of their toxicity to the environment and human health. Sensors employing stripping voltammetric detection modes have been demonstrated to be as reliable and cost effective devices for the analysis of heavy metals. Sol-gel nanocomposites are promising materials to construct high performance electrochemical sensors because they can be fabricated as films coating commercial electrodes, as conventional carbon paste electrodes and even as single-use screen printed electrodes. Sol-gel chemistry is also compatible with microfabrication and photolithographic methods facilitating pathways towards sensor miniaturization. For these types of sensors, the chemical composition and concentration of nanoparticles in the sol-gel matrix is critical for the success of heavy metals detection. Gold and bismuth are the most commonly used nanoparticles to sense heavy metals. Jena *et al.*³² reported on a modified solid gold electrode including a gold nanoparticle doped sol-gel silica matrix for the simultaneous detection of As^{3+} , Hg^{2+} , Cu^{2+} . The resulting sensor exhibited high sensitivity and well-defined stripping peaks for these three heavy metals with detection limits of 0.02 ppb (3σ) toward As^{3+} and Hg^{2+} . Dimovasilis *et al.*³³ modified a glassy carbon electrode with bismuth decorated (3-mercaptopropyl) trimethoxysilane silica gel and also demonstrated its application for heavy metals analysis. The obtained detection limits were 1.3 ppb and 0.37 ppb (3σ) for Pb^{2+} and Cd^{2+} , respectively. Fe_3O_4 nanoparticles are widely used in water treatment, due to the high adsorption capacity of these nanoparticles and ease of separating pollutant-loaded magnetic adsorbents from water solutions by using an external magnetic field³⁴. Wei *et al.*³⁵ developed a sensor for heavy metal detection based on the modification of a glassy carbon electrode with porous $\gamma\text{-AlOOH/SiO}_2\text{@Fe}_3\text{O}_4$ microspheres. The sensor was found to be very sensitive to simultaneous determination of Zn^{2+} , Cd^{2+} , Pb^{2+} , Cu^{2+} and Hg^{2+} , with reported lowest detection limits of 3.07, 1.75, 2.13, 0.93, and 2.87 ppt, respectively. Here, the high sensitivity for heavy metal analysis is likely related to the high adsorption capacity of the porous microspheres.

Metal nanoparticle doped sol-gel silica nanocomposites do not possess the required conductivity to fabricate bulk or screen printed electrodes. Inspired by the well-known resorcinol/formaldehyde sol-gel process, which can be pyrolyzed to get a conductive amorphous carbon matrix, we have synthesized a

nanocomposite material made of a carbon xerogel doped with bismuth nanoparticles and fabricated a carbon paste electrode for heavy metal analysis²⁴. The resulting sensor is very sensitive to several heavy metals. Extremely low detection limits for Pb^{2+} and Cd^{2+} around 0.5 ppb were achieved using a nanocomposite paste electrode containing 6 wt% of bismuth. This sensor approach has also been employed in the analysis of several relevant and contrasting water samples such as river water, acid mine drainages and treated urban water, thus covering a wide spectrum of matrices and heavy metal absolute and relative concentrations. Results are shown to be in good agreement with those obtained with the standard inductive coupled plasma mass-spectroscopy technique³⁶. Moreover, this sol-gel nanocomposite has been successfully employed for the construction of screen printed electrochemical sensors.

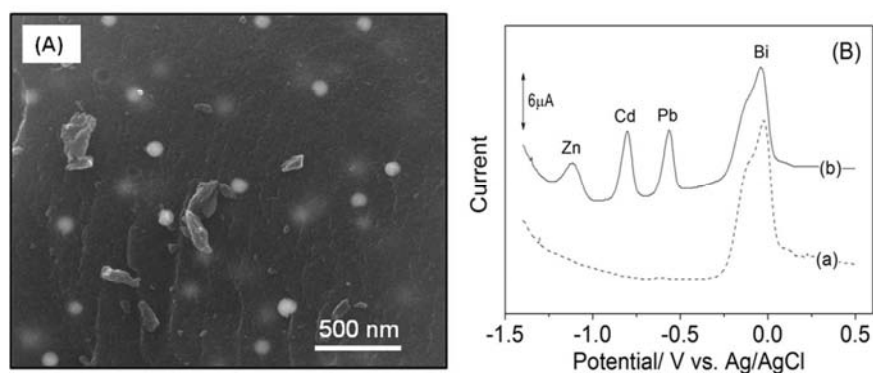


Figure 11. (A) SEM image of a carbon matrix/bismuth nanoparticle (C/Bi) composite, (B) Stripping voltammograms with C/Bi nanocomposite bulk paste electrode of (a) 0 ppb and (b) 50 ppb Zn (II), Cd (II), Pb (II) (adopted from Gich *et al.*, *Journal of Materials Chemistry A*, Volume 1, Issue 37, 2013, 11410-11418, with permission of The Royal Society of Chemistry (RSC) [35])

5.2 Detection of organic molecules

5.2.1 Ascorbic acid, dopamine and uric acid detection

Ascorbic acid, dopamine and uric acid are compounds of high biomedical interest, playing a relevant role in human metabolism. It is known that these three electroactive molecules always coexist in physiological samples and are oxidized at almost the same potential when trying to detect them using a conventional electrode, which results in the overlap of their respective voltammetric responses. Due to the easy preparation of sol-gel materials and the catalytic activities of different nanomaterials, tailor-made sol-gel nanocomposite based sensors can be developed for the simultaneous voltammetric detection of these molecules. Gavalas *et al.*²⁰ fabricated sol-gel carbon nanotube ceramic composite bulk electrodes and found that the oxidation of ascorbic acid shifted to lower over-potentials with the increase of the carbon nanotube content. Zhu *et al.*³⁷ compared the electrochemical behavior of a carbon nanotube ceramic composite bulk electrode and a graphite ceramic composite bulk electrode for the detection of some biological molecules, including ascorbic acid, uric acid, dopamine, and hydrogen peroxide. In all cases,

the carbon nanotube-ceramic bulk electrode provided better reversible signals with substantially decreased over-potential, better defined peak shapes and higher sensitivity.

Carbon nanotube ceramic composites could also be grounded into powder, and then mixed with water, chitosan or Nafion[®] to make a nanocomposite film-based solid electrodes to be used as electrochemical sensors. Canevari *et al.*³⁸ developed carbon nanotube/mesoporous silica nanocomposite film electrodes by casting a water suspension containing Nafion[®] and carbon nanotube/silica powder on a glassy carbon electrode for the determination of dopamine, uric acid and paracetamol. Compared to a bare glassy carbon electrode, the resulting electrode presented well-defined separated anodic peaks, and high sensitivity towards the determination of dopamine and uric acid. Surprisingly, the catalytic performance of carbon nanotubes can be modified by tuning its content in the gel network. Gong *et al.*²¹ casted a glassy carbon electrode with carbon nanotube doped silicate *sol* solution and observed different electrochemical performances of the resulting sensors depending on the carbon nanotube content within the gel matrix. A high content of carbon nanotube in the matrix (i.e., higher than 1.5mg/mL in the *sol*) was used to the formation of a conventional macroelectrode and the resulting sensor possessed remarkable electrocatalytic activity toward the oxidation of glutathione. By contrast, carbon nanotube low contents (typically lower than 0.1mg/mL in the *sol*) yielded nano-electrode ensembles and the resulting sensor exhibited good electrocatalytic activity towards the oxidation of ascorbic acid.

Metal nanoparticles are also good candidates for the modification of solid electrodes to detect ascorbic acid. Weng *et al.*²³ synthesized mesoporous silica doped with gold nanoparticles and thoroughly mixed them with graphite and paraffin oil to fabricate a carbon paste electrode for ascorbic acid sensing. The resulting sensor showed lower over-potential and 21-fold higher electrocatalytic activity towards ascorbic acid oxidation compared to the non-modified carbon paste electrode. In addition, carbon based nanomaterials and metal nanoparticles could be combined together to enhance the sensing performance of the sensor. Ragupathy *et al.*³⁹ coated a thin layer on a glassy carbon electrode with a *sol*-gel silica grafted carbon nanotube nanocomposite, and then introduced gold nanoparticles on the resulting nanocomposite film by electrodeposition. The thus fabricated sensor showed high sensitivity and excellent selectivity for ascorbic acid even in the presence of a large excess of dopamine. Liu *et al.*⁴⁰ introduced graphene oxide and gold nanoparticles into an amino functional silica *sol*-gel solution and then casted it onto a glassy carbon electrode to construct an electrochemical sensor for dopamine and uric acid detection. The sensor showed well-defined and separated voltammetric peaks for both analytes.

5.2.2 Organic pollutant detection

Environmental detection of toxic compounds harmful to human health such as dihydroxybenzene, nitrite, nitrobenzene, and nitroaromatics in water can also be carried out with *sol*-gel nanocomposite based sensors. The electrochemical determination of these target analytes on bare commercial solid electrode produces weak signals at high over-potentials. Taking advantage of the catalytic activity of metal nanoparticles, the sensitive electrochemical analysis of these compounds using *sol*-gel nanocomposite derived sensors is being widely studied. Canevari *et al.*⁴¹ synthesized Ag nanoparticle decorated *sol*-gel carbon nanotube/silica nanocomposites, and cast them on a glassy carbon electrode for the simultaneous

determination of dihydroxybenzenes isomers. The sensor exhibited high sensitivity for the simultaneous determination of hydroquinone and catechol in the presence of resorcinol. Maduraiveeran *et al.*³⁰ modified a glassy carbon electrode by casting an amino group functional sol-gel silica/gold nanoparticle composite and carried out the analysis of N_2H_4 , SO_3^{2-} , and NO_2^- . The use of this nanocomposite resulted in a large decrease of the applied over-potentials to values of ~ 750 mV, ~ 600 mV and ~ 250 mV for N_2H_4 , SO_3^{2-} , and NO_2^- oxidation, respectively. A sensitive nitrite sensor was also proposed by the same group in which a silver nanoparticle embedded thiol-silica matrix nanocomposite film was generated on the surface of a glassy carbon electrode to fabricate the working electrode⁴². The resulting sensor gave a detection limit of $4 \mu\text{M}$. Yang *et al.*⁴³ employed titania as the sol-gel matrix to encapsulate gold nanoparticles and coated the nanocomposite on a glassy carbon electrode to fabricate a nitrite sensor. The sensor showed excellent electrocatalytic activity towards nitrite, which was proved by a low detection over-potential and a low detection limit of $1.2 \mu\text{M}$. Manivannan *et al.*⁴⁴ also developed amino-silica/gold nanoparticle composites to coat a glassy carbon electrode and applied it as an electrochemical sensor for the determination of nitroaromatics. The same group reported the feasibility of electrochemically sensing nitrobenzene using an amino-silica/silver nanocomposite modified glassy carbon electrode⁴⁵. Taheri *et al.*⁴⁶ modified a gold electrode with a thiol-silica/silver nanoparticle composite for the detection of cyanide. The fabricated sol-gel nanocomposite sensor exhibited high sensitivity with a detection limit of 14 nM toward cyanide.

5.3 Biosensors

5.3.1 H_2O_2 and glucose detection

Hydrogen peroxide (H_2O_2) is a by-product of several enzyme-catalyzed reactions (e.g., glucose oxidase and horseradish peroxidase). The detection of H_2O_2 plays an important role in environmental protection and medical diagnostics. A great drawback for direct electro-reduction/oxidation of H_2O_2 is the high over-potential that has to be applied. Taking advantage of the catalytic activity of nanomaterials, sol-gel nanocomposite based amperometric sensors and biosensors have been constructed for the detection of H_2O_2 . Employing a sol-gel silica solution as a binder, Yang *et al.*⁴⁷ developed a carbon nanotube ceramic electrode for H_2O_2 determination and achieved a substantial decrease of the required over-potential (from 0.6V at conventional carbon paste electrode to 0.1V at this electrode) for the oxidation of H_2O_2 . To further improve the sensor performance, platinum nanoparticles were incorporated into the sol-gel matrix. The amperometric sensor exhibited highly enhanced signals due to the synergistic catalytic effect of platinum nanoparticles and carbon nanotubes (Figure 12). Enzymes could be easily introduced into the nanocomposites by doping them into the sol-gel *sol* solution or adsorbing them onto the carbon materials. Barbadillo *et al.*⁴⁸ incorporated gold nanoparticles into a silica *sol* solution which was further employed as a binder of graphite powder previously functionalized with glucose oxidase enzyme. The resulting carbon paste bulk electrode was successfully applied for glucose biosensing.

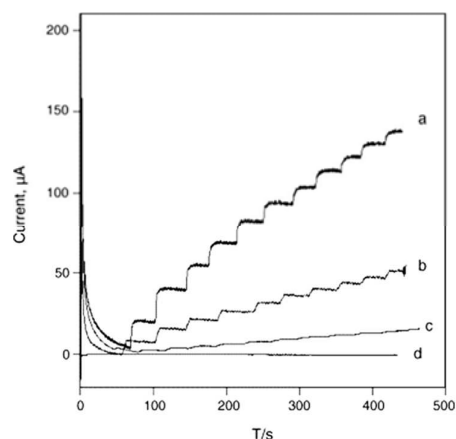


Figure 12. Typical current-time sensor responses to successive additions of 2mM H_2O_2 at the (a) Platinum nanoparticles (Pt)-Carbon nanotube (CNT) paste electrode, (b) CNT paste electrode, (c) Pt nanoparticle-graphite paste electrode (d) graphite paste electrode. (adopted from Yang *et al.*, *Biosensors and Bioelectronics*, Volume 21, Issue 7, 2006, 1125-1131, with permission)

For the construction of enzyme and nanoparticle co-doped nanocomposite film-based solid electrodes, the location of enzyme on the electrode surface is an important issue to be addressed. Wang *et al.*²⁸ stated that gold nanoparticles embedded in a sol-gel network could inhibit the adsorption of proteins onto a bare gold electrode and at the same time, acted as a wire to facilitate the electron transfer between the protein and electrode. Jia *et al.*²⁵ fabricated a horseradish peroxidase enzyme doped silica/gold nanoparticle composite based biosensor for the detection of H_2O_2 by a stepwise impregnation process carried out on a gold electrode. The resulting biosensor device showed a 2.5 s response time to H_2O_2 with a detection limit of 2.0 μM . Chen *et al.*⁴⁹ fabricated a carbon nanotube ceramic nanocomposite film sensor to monitor H_2O_2 by coating a glassy carbon electrode with a sol-gel silica/carbon nanotube/horseradish peroxidase nanocomposite. The sensor exhibited fast amperometric response for H_2O_2 and a detection limit of 12.89 μM .

Also, metal nanoparticles and carbon based nanomaterials could be combined together to yield a high performance sensor. Lu *et al.*²⁶ decorated a sol-gel SiO_2 coated graphene oxide nanosheet with silver nanoparticles and then cast the resulting nanocomposite on a glassy carbon electrode to fabricate H_2O_2 sensors. The sensor showed a detection limit of 4 μM to H_2O_2 .

5.3.2 Organic molecules detection

Du *et al.* proposed an amperometric AChE biosensor for pesticide determination³¹. The working principle is as follows. AChE catalyzes the hydrolysis of acetylcholine to acetate and choline which is electroactive and shows an irreversible anodic peak. The activity of AChE can be inhibited by some pesticides and drugs. By measuring the anodic peak of choline, one can follow the suppression of AChE activity and correlate it to the pesticide concentration. The biosensor was fabricated by coating a glassy carbon electrode with a homogeneous gold nanoparticle/sol-gel silica composite film and then immobilizing

AChE on the surface of the gold nanoparticles. The biosensor was also successfully employed to carry out a comparative study of the sensitivity towards different drugs against Alzheimer's disease⁵⁰.

5.4 MIP-based sensing

Molecularly imprinting technology is receiving more and more attention and being applied to the fabrication of selective receptors for electrochemical sensor applications. In this context, Prasad *et al.*⁵¹ deposited a dopamine imprinted film on the carbon nanotube ceramic composite bulk electrode that benefits from the enhanced electron transfer rate of the carbon nanotube ceramic composite material and the selectivity and stability of the MIP film. The resulting MIP-based sensor showed very high selectivity and sensitivity for sensing dopamine in aqueous, blood serum, cerebrospinal fluid and pharmaceutical samples and obtained detection limits of $0.143 \square 0.154 \mu\text{g L}^{-1}$ without any interference.

Imprinted nanocomposite microspheres with core/shell structures could be synthesized by growing the imprinted polymer on the surface of previously synthesized microparticles. An electrochemical sensor device was fabricated by casting a mixture of the imprinted microspheres and chitosan on the surface of a solid electrode. As described earlier, Yu *et al.*²⁹ coated imprinted core/shell silica@gold nanoparticle composites on a glassy carbon electrode for the determination of dopamine. The imprinted sensor exhibited not only high selectivity but also a wide linear range towards dopamine with a very low detection limit of 20 nM. Carbon nanotubes could be incorporated to enhance the electron transfer rate between the imprinted polymer film layer and the solid electrode. Hu *et al.*⁵² modified a glassy carbon electrode with a mixture of a benzylpenicillin imprinted core/shell silica@Fe₃O₄ nanoparticle composite, carbon nanotubes and chitosan in order to develop a device for benzylpenicillin determination. The imprinted sensor showed fast and sensitive voltammetric response for benzylpenicillin with a low detection limit of 1.5 nM.

5.5 Other approaches of sol-gel nanocomposite-based electrochemical sensors

Due to the excellent electronic, ionic conductivity and good extraction function, carbon nanotube/ion liquid nanocomposite bucky gels, prepared by mixing carbon nanotubes and various room temperature ion liquids (RTILs), are attracting great attention in electrochemical sensor applications. Xiao *et al.*⁵³ fabricated voltammetric nitrite sensors by coating a glassy carbon electrode with a hydrophobic RTILs/carbon nanotube gel using chitosan as a binder agent. The sensor exhibited very low over-potential for nitrite detection and a low detection limit of 10 nM. Chen *et al.*⁵⁴ employed hydrophilic RTILs being part of a bulky gel and casted them on a glassy carbon electrode with the aid of chitosan for the detection of 4-nitrophenol. The sensor gave significantly enhanced signals when compared with those of a bare glassy carbon electrode.

6. Conclusion and Prospects

To summarize, the different synthesis approaches of sol-gel nanocomposites, the configurations of sol-gel nanocomposite derived electrochemical sensors, the performance of the sol-gel nanocomposites in electrochemical devices and the various applications in environmental monitoring and biological

diagnosis fields are included in this chapter. Sol-gel nanocomposites, benefiting from the flexibility of the sol-gel process, the mechanical stability of the sol-gel matrices, the electric conductivity and catalytic functions of the nanomaterials, have been widely employed to develop versatile electrochemical sensor and biosensor devices. However, it is worth mentioning that the design of these attractive nanocomposites is sometimes an empiric and cumbersome process and their performance proved difficult to be fully predicted. Combinatorial analytical tools could help in the selection of the appropriate nanomaterials and of the sol-gel matrices as well as the best conditions in order to accelerate their preparation. Another important aspect to be tackled is the material mass-fabrication and its compatibility with other fabrication processes applied to produce analytical devices. Scaling-up the fabrication of nanocomposite sol-gel material formulations is currently carried out by only few companies. Sol-gel mass-production is critical for ensuring the production of large quantities of electrochemical devices at low cost. Such as those based on screen-printed technology and thus deploying such sensor for the chemical analyses in the environment or screening programmes in the biomedical field. Likewise, being compatible with microfabrication processes makes them amenable for the mass production of miniaturized electrochemical devices of highly added value that could also be applied in environmental monitoring or point-of-care applications. Therefore, it can be affirmed that its potential is huge and although the sol-gel technology has been known for more than four decades, the future of this technology and its particular application to the development of electrochemical sensors is undoubtedly secured for many years to come.

ACKNOWLEDGMENTS

This research was partially funded by the Spanish Government (MAT2012-35324, TEC2010-17274 and the RyC-2009-04335 contract of M. G.) and the European Commission (FP7-Marie Curie Actions, PCIG09-GA-2011-294168 grant) and cofounded by the European Social Fund. COST Action MP1202 and the Chinese Scholarship Council fellowship of P. N. are also acknowledged.

Reference

1. Maduraiveeran, G.; Ramaraj, R., Gold Nanoparticles Embedded in Silica Sol-gel Matrix as an Amperometric Sensor for Hydrogen Peroxide. *Journal of Electroanalytical Chemistry* **2007**, *608*, (1), 52-58.
2. Rottman, C.; Grader, G.; De Hazan, Y.; Melchior, S.; Avnir, D., Surfactant-Induced Modification of Dopants Reactivity in Sol-Gel Matrixes. *Journal of the American Chemical Society* **1999**, *121*, (37), 8533-8543.
3. Traversa, E.; Gnappi, G.; Montenero, A.; Gusmano, G., Ceramic thin films by sol-gel processing as novel materials for integrated humidity sensors. *Sensors and Actuators B: Chemical* **1996**, *31*, (1-2), 59-70.
4. Yu, J. H.; Ju, H. X., Preparation of porous titania sol-gel matrix for immobilization of horseradish peroxidase by a vapor deposition method. *Analytical chemistry* **2002**, *74*, (14), 3579-3583.
5. Gründler, P., Chemical Sensors. In *An introduction for scientists and engineers*, Springer, Ed. 2007; p 273.

6. Carrington, N. A.; Xue, Z.-L., Inorganic Sensing Using Organofunctional Sol–Gel Materials. *Accounts of Chemical Research* **2007**, *40*, (5), 343-350.
7. Urek, S. K.; Francic, N.; Turel, M.; Lobnik, A., Sensing Heavy Metals Using Mesoporous-Based Optical Chemical Sensors. *Journal of Nanomaterials* **2013**.
8. Walcarius, A.; Mandler, D.; Cox, J. A.; Collinson, M.; Lev, O., Exciting new directions in the intersection of functionalized sol-gel materials with electrochemistry. *Journal of Materials Chemistry* **2005**, *15*, (35-36), 3663-3689.
9. Walcarius, A.; Collinson, M. M., Analytical Chemistry with Silica Sol-Gels: Traditional Routes to New Materials for Chemical Analysis. In *Annual Review of Analytical Chemistry*, 2009; Vol. 2, pp 121-143.
10. Kandimalla, V. B.; Tripathi, V. S.; Ju, H., Immobilization of biomolecules in sol-gels: Biological and analytical applications. *Critical Reviews in Analytical Chemistry* **2006**, *36*, (2), 73-106.
11. Gill, I., Bio-doped nanocomposite polymers: Sol-gel bioencapsulates. *Chemistry of Materials* **2001**, *13*, (10), 3404-3421.
12. Luo, X.; Morrin, A.; Killard, A. J.; Smyth, M. R., Application of Nanoparticles in Electrochemical Sensors and Biosensors. *Electroanalysis* **2006**, *18*, (4), 319-326.
13. Liu, C. C., Electrochemical Sensors. In *The Biomedical Engineering Handbook: Second Edition*, Bronzino, J. D., Ed. CRC Press LLC: 2000.
14. Power, A. C.; Morrin, A., Electroanalytical Sensor Technology. In *Electrochemistry*, Khalid, M. A. A., Ed. InTech: 2013.
15. Gich, M.; Casas, L.; Roig, A.; Molins, E.; Sort, J.; Surinach, S.; Baro, M. D.; Munoz, J. S.; Morellon, L.; Ibarra, M. R.; Nogues, J., High-coercivity ultralight transparent magnets. *Applied Physics Letters* **2003**, *82*, (24), 4307-4309.
16. Casas, L. I.; Roig, A.; Molins, E.; Greneche, J. M.; Asenjo, J.; Tejada, J., Iron oxide nanoparticles hosted in silica aerogels. *Applied Physics a-Materials Science & Processing* **2002**, *74*, (5), 591-597.
17. Popovici, M.; Gich, M.; Roig, A.; Casas, L.; Molins, E.; Savii, C.; Becherescu, D.; Sort, J.; Surinach, S.; Munoz, J. S.; Baro, M. D.; Nogues, J., Ultraporous single phase iron oxide-silica nanostructured aerogels from ferrous precursors. *Langmuir* **2004**, *20*, (4), 1425-1429.
18. Cotet, L. C.; Gich, M.; Roig, A.; Popescu, I. C.; Cosoveanu, V.; Molins, E.; Danciu, V., Synthesis and structural characteristics of carbon aerogels with a high content of Fe, Co, Ni, Cu, and Pd. *Journal of Non-Crystalline Solids* **2006**, *352*, (26-27), 2772-2777.
19. Tsionsky, M.; Gun, G.; Glezer, V.; Lev, O., Sol-Gel-Derived Ceramic-Carbon Composite Electrodes: Introduction and Scope of Applications. *Analytical chemistry* **1994**, *66*, (10), 1747-1753.
20. Gavalas, V. G.; Andrews, R.; Bhattacharyya, D.; Bachas, L. G., Carbon Nanotube Sol–Gel Composite Materials. *Nano Letters* **2001**, *1*, (12), 719-721.
21. Gong, K.; Zhang, M.; Yan, Y.; Su, L.; Mao, L.; Xiong, S.; Chen, Y., Sol-Gel-Derived Ceramic-Carbon Nanotube Nanocomposite Electrodes: Tunable Electrode Dimension and Potential Electrochemical Applications. *Analytical chemistry* **2004**, *76*, 6500-6505.
22. Bharathi, S.; Lev, O., Direct Synthesis of Gold Nanodispersions in Sol–gel Derived Silicate Sols, Gels and Films. *Chemical Communication* **1997**, (23), 2303-2304.
23. Weng, C.-J.; Hsu, P.-H.; Hsu, S.-C.; Chang, C.-H.; Hung, W.-I.; Wu, P.-S.; Yeh, J.-M., Synthesis of electroactive mesoporous gold-organosilica nanocomposite materials via a sol-gel process with non-surfactant templates and the electroanalysis of ascorbic acid. *Journal of Materials Chemistry B* **2013**, *1*, (38), 4983-4991.
24. Gich, M.; Fernandez-Sanchez, C.; Cotet, L. C.; Niu, P.; Roig, A., Facile synthesis of porous bismuth-carbon nanocomposites for the sensitive detection of heavy metals. *Journal of Materials Chemistry A* **2013**, *1*, (37), 11410-11418.

25. Jia, J.; Wang, B.; Wu, A.; Cheng, G.; Li, Z.; Dong, S., A Method to Construct a Third-Generation Horseradish Peroxidase Biosensor: Self-Assembling Gold Nanoparticles to Three-Dimensional Sol-Gel Network. *Analytical chemistry* **2002**, *74*, (9), 2217-2223.
26. Lu, W.; Luo, Y.; Chang, G.; Sun, X., Synthesis of Functional SiO₂-Coated Graphene Oxide Nanosheets Decorated with Ag Nanoparticles for H₂O₂ and Glucose Detection. *Biosensor & bioelectronics* **2011**, *26*, (12), 4791-7.
27. Subramanian Bharathi, O. L., Sol-gel-derived nanocrystalline gold-silicate composite biosensor. *Analytical Communications* **1998**, *35*, 29-31.
28. Wang, L.; Wang, E., Direct Electron Transfer Between Cytochrome c and a Gold Nanoparticles Modified Electrode. *Electrochemistry Communications* **2004**, *6*, (1), 49-54.
29. Yu, D.; Zeng, Y.; Qi, Y.; Zhou, T.; Shi, G., A Novel Electrochemical Sensor for Determination of Dopamine Based on AuNPs@SiO₂ Core-Shell Imprinted Composite. *Biosensor & bioelectronics* **2012**, *38*, (1), 270-277.
30. Maduraiveeran, G.; Ramaraj, R., A Facile Electrochemical Sensor Designed from Gold Nanoparticles Embedded in Three-Dimensional Sol-Gel Network for Concurrent Detection of Toxic Chemicals. *Electrochemistry Communications* **2007**, *9*, (8), 2051-2055.
31. Du, D.; Chen, S.; Cai, J.; Zhang, A., Immobilization of acetylcholinesterase on gold nanoparticles embedded in sol-gel film for amperometric detection of organophosphorous insecticide. *Biosensors & bioelectronics* **2007**, *23*, (1), 130-134.
32. Jena, B. K.; Raj, C. R., Gold Nanoelectrode Ensembles for the Simultaneous Electrochemical Detection of Ultratrace Arsenic, Mercury and copper. *Analytical chemistry* **2008**, *80*, 4836-4844.
33. Dimovasilis, P. A.; Prodromidis, M. I., Bismuth-dispersed xerogel-based composite films for trace Pb(II) and Cd(II) voltammetric determination. *Analytica chimica acta* **2013**, *769*, 49-55.
34. Sun, L.; Li, Y.; Sun, M.; Wang, H.; Xu, S.; Zhang, C.; Yang, Q., Porphyrin-functionalized Fe₃O₄@SiO₂ core/shell magnetic colorimetric material for detection, adsorption and removal of Hg²⁺ in aqueous solution. *New Journal of Chemistry* **2011**, *35*, (11), 2697.
35. Wei, Y.; Yang, R.; Zhang, Y.; Wang, L.; Liu, J.; Huang, X., High Adsorptive Gamma-ALOOH(boehmite)@SiO₂/Fe₃O₄ Porous Magnetic Microspheres for Detection of Toxic Metal Ions in Drinking Water. *Chemical Communication* **2011**, *47*, (39), 11062-11064.
36. Niu, P.; Fernandez-Sanchez, C.; Gich, M.; Ayora, C.; Roig, A., Highly Sensitive, Fast Electrochemical Detection of Heavy Metals in Waters with Bismuth Nanoparticle-Porous Carbon Electrodes. *Submitted*.
37. Zhu, L. T., Chunyuan. Zhai, Jiangli. Yang, Ruilan, Sol-gel derived carbon nanotubes ceramic composite electrodes for electrochemical sensing. *Sensors and Actuators B: Chemical* **2007**, *125*, (1), 254-261.
38. Canevari, T. C.; Raymundo-Pereira, P. A.; Landers, R.; Benvenuti, E. V.; Machado, S. A., Sol-gel thin-film based mesoporous silica and carbon nanotubes for the determination of dopamine, uric acid and paracetamol in urine. *Talanta* **2013**, *116*, 726-35.
39. Ragupathy, D.; Gopalan, A. I.; Lee, K.-P., Electrocatalytic oxidation and determination of ascorbic acid in the presence of dopamine at multiwalled carbon nanotube-silica network-gold nanoparticles based nanohybrid modified electrode. *Sensors and Actuators B: Chemical* **2010**, *143*, (2), 696-703.
40. Liu, X.; Xie, L.; Li, H., Electrochemical biosensor based on reduced graphene oxide and Au nanoparticles entrapped in chitosan/silica sol-gel hybrid membranes for determination of dopamine and uric acid. *Journal of Electroanalytical Chemistry* **2012**, *682*, (0), 158-163.
41. Canevari, T. C.; Raymundo-Pereira, P. A.; Landers, R.; Machado, S. A. S., Direct Synthesis of Ag Nanoparticles Incorporated on a Mesoporous Hybrid Material as a Sensitive Sensor for the Simultaneous Determination of Dihydroxybenzenes Isomers. *European Journal of Inorganic Chemistry* **2013**, *2013*, (33), 5746-5754.

42. Maduraiveeran, G.; Manivasakan, P.; Ramaraj, R., Silver nanoparticles embedded three dimensional silicate sol-gel matrix modified electrode for nitrite sensor application. *International Journal of Nanotechnology* **2011**, *8*, (10), 925-934.
43. Yang, W.; Bai, Y.; Li, Y.; Sun, C., Amperometric nitrite sensor based on hemoglobin/colloidal gold nanoparticles immobilized on a glassy carbon electrode by a titania sol-gel film. *Analytical and bioanalytical chemistry* **2005**, *382*, (1), 44-50.
44. Manivannan, S.; Ramaraj, R., Synthesis of cyclodextrin-silicate sol-gel composite embedded gold nanoparticles and its electrocatalytic application. *Chemical Engineering Journal* **2012**, *210*, 195-202.
45. Manivannan, S.; Ramaraj, R., Silver nanoparticles embedded in cyclodextrin-silicate composite and their applications in Hg(II) ion and nitrobenzene sensing. *Analyst* **2013**, *138*, 1733-1739.
46. Taheri, A.; Noroozifar, M.; Khorasani-Motlagh, M., Investigation of a New Electrochemical Cyanide Sensor Based on Ag Nanoparticles Embedded in a Three-Dimensional Sol-Gel. *Journal of Electroanalytical Chemistry* **2009**, *628*, (1-2), 48-54.
47. Yang, M. H.; Yang, Y. H.; Liu, Y. L.; Shen, G. L.; Yu, R. Q., Platinum nanoparticles-doped sol-gel/carbon nanotubes composite electrochemical sensors and biosensors. *Biosensors and Bioelectronics* **2006**, *21*, (7), 1125-1131.
48. Barbadiillo, M.; Casero, E.; Petit-Dominguez, M. D.; Vazquez, L.; Pariente, F.; Lorenzo, E., Gold nanoparticles-induced enhancement of the analytical response of an electrochemical biosensor based on an organic-inorganic hybrid composite material. *Talanta* **2009**, *80*, (2), 797-802.
49. Chen, H.; Dong, S., Direct electrochemistry and electrocatalysis of horseradish peroxidase immobilized in sol-gel-derived ceramic-carbon nanotube nanocomposite film. *Biosensors & bioelectronics* **2007**, *22*, (8), 1811-1815.
50. Du, D.; Chen, S.; Cai, J.; Song, D., Comparison of drug sensitivity using acetylcholinesterase biosensor based on nanoparticles-chitosan sol-gel composite. *Journal of Electroanalytical Chemistry* **2007**, *611*, (1-2), 60-66.
51. Prasad, B. B.; Kumar, D.; Madhuri, R.; Tiwari, M. P., Sol-gel derived multiwalled carbon nanotubes ceramic electrode modified with molecularly imprinted polymer for ultra trace sensing of dopamine in real samples. *Electrochimica Acta* **2011**, *56*, (20), 7202-7211.
52. Hu, Y.; Li, J.; Zhang, Z.; Zhang, H.; Luo, L.; Yao, S., Imprinted sol-gel electrochemical sensor for the determination of benzylpenicillin based on Fe₃O₄@SiO₂/multi-walled carbon nanotubes-chitosans nanocomposite film modified carbon electrode. *Analytical Chimica Acta* **2011**, *698*, (1-2), 61-68.
53. Xiao, F.; Liu, L.; Li, J.; Zeng, J.; Zeng, B., Electrocatalytic Oxidation and Voltammetric Determination of Nitrite on Hydrophobic Ionic Liquid-Carbon Nanotube Gel-Chitosan Composite Modified Electrodes. *Electroanalysis* **2008**, *20*, (18), 2047-2054.
54. Chen, J. Y., G. Chen, M. Li, W., Sensitive determination of 4-nitrophenol based on multi-walled carbon nano-tube/ionic liquid/chitosan composite film modified electrode. *Russian Journal of Electrochemistry* **2009**, *45*, (11), 1287-1291.

The Author

Personal Information

Name: Pengfei Niu

Date of birth: 10/03/1985

Nationality: China

Email: niupengfei2012@gmail.com



Academic Records

09.2012-06.2015 **Ph.D. in Materials Science (Doctoral Student)**

Thesis topic: Carbon Xerogel Nanocomposite Materials for Electrochemical Devices: Application to Heavy Metals Detection

Group of Nanoparticles and Nanocomposite in ICMAB-CSIC and Group of Chemical Transducers in IMB-CNM-CSIC, Barcelona, Spain

Supervisors: Dr. César Fernández Sánchez and Dr. Martí Gich Garcia

09.2009-06.2012 **Master in Materials Processing Engineering**

Thesis topic: Preparation of Short Natural Fiber Reinforced Polypropylene (PP) Composite

College of Polymer Science and Engineering in Sichuan University, Chengdu, China,

Supervisor: Dr. Yang Jie

09.2005-06.2009 **Bachelor in Polymer Processing Engineering**

Final Project: Preparation of Poly(ether sulfones) Nanofibers via Electrospinning Technology

College of Polymer Science and Engineering in Sichuan University, Chengdu, China

Supervisor: Dr. Yang Jie

Languages

	<u>Reading</u>	<u>Writing</u>	<u>Conversation</u>
English	Excellent	Excellent	Fluent
Chinese	Excellent	Excellent	Excellent
Spanish	Basic	Poor	Basic

Technical Experience

1) **Sol-gel chemistry:** a) Synthesizing resorcinol-formaldehyde polymeric and

carbon xerogels both in acid and base catalysis system, b) Preparing metal nanoparticles modified porous carbon xerogels by both impregnation and co-synthesis methods, c) Depositing porous carbon/silica thin-films by spin-coating process and obtaining uniform carbon-silica film thinner than 500 nm on 4 inch wafer;

2) Micro-fabrication techniques: a) Spin-coating polymers on Si wafer, and physical vapor deposition of Al and SiO₂ layers on carbon films, b) Proficiently drawing by Pro/E to design microelectrodes features; c) Patterning carbon thin-films by both positive and negative photoresist based photolithography process, d) Fabricating carbon microelectrodes devices by sol-gel PDMS stamped soft-lithography; e) Removing residues carbon layer by reactive ions etching, f) ultrasonically bonding Al wire on Cu and Al;

3) Clean room experience: in my PhD, working in the clean room frequently for carrying out all the micro-fabrication processes;

4) Materials Characterization Techniques: a) self-operating SEM, optical microscopy, profilometer, nanoindenter; b) very familiar and often using the techniques of four-point probes equipment, TEM, AFM, XPS, BET, DSC, TGA, rheometer and XRD for materials characterization;

5) Electrochemistry: in my PhD, cyclic voltammetry and stripping voltammetry are employed for evaluating the performance of the fabricated carbon composite electrodes in heavy metals determinations.

6) In addition, I have a very strong background on conventional polymer processing techniques. During my master stage, I have carried out various polymers processing in different projects: a) Extrusion and injection molding of natural fiber, glass fiber, and carbon fiber reinforced polypropylene (PP), polyamide (PA) and polyphenylene sulfide (PPS) composites, b) Electrospinning of polymer nano-fibers.